# VARIABILITY AND TRENDS OF MEASURED AND SIMULATED ATMOSPHERIC AMMONIA OVER URBAN AND REMOTE REGIONS

by

Beatriz Adriana Herrera Gutierrez

A thesis submitted in conformity with the requirements for the degree of Doctor of Philosophy

Department of Physical and Environmental Sciences University of Toronto

© Copyright 2025 by Beatriz Adriana Herrera Gutierrez

Variability and Trends of Measured and Simulated Atmospheric Ammonia Over Urban and Remote Regions

> Beatriz Adriana Herrera Gutierrez Doctor of Philosophy

Department of Physical and Environmental Sciences University of Toronto 2025

### Abstract

Air pollution is one of the world's primary public health concerns, with 99% of the global population breathing polluted air, according to the World Health Organization. One key pollutant is ammonia (NH<sub>3</sub>), the most abundant alkaline compound in the atmosphere, with consequences for the environment and human health.

The temporal and spatial variability of NH<sub>3</sub> over Mexico City was studied using NH<sub>3</sub> total columns retrieved from Fourier transform infrared (FTIR) solar measurements at two sites (urban and remote). The columns were compared with satellite data from the Infrared Atmospheric Sounding Interferometer (IASI). Most of the NH<sub>3</sub> measured at the urban station was attributed to local sources, while the NH<sub>3</sub> observed at the remote site was transported from the city and surrounding areas. IASI measurements underestimated FTIR NH<sub>3</sub> total columns by an average of 32±27% but exhibited similar temporal variability. The NH<sub>3</sub> spatial distribution from IASI showed the largest columns in the northeast part of the city.

The seasonal and diurnal variability, along with long-term trends, of atmospheric NH<sub>3</sub> were assessed using measurements from 22 FTIR sites globally distributed between 45°S and 80°N. The mean NH<sub>3</sub> total columns from the FTIR time series ranged from (0.12 to 19.20)×10<sup>15</sup> molec. cm<sup>-2</sup>, with the smallest columns found at the Arctic and high-altitude sites, and the largest in urbanized areas. Significant NH<sub>3</sub> enhancements were attributed to biomass burning, and NH<sub>3</sub> emissions from volcanic eruptions were

also detected. Comparisons were made between the FTIR measurements and NH<sub>3</sub> simulations generated by the GEOS-Chem High-Performance (GCHP) model and the Tropospheric Chemistry Reanalysis (TCR-2) product. Most of the sites revealed increasing trends in NH<sub>3</sub> total columns, with a mean increase of 3.82 (3.29–4.35)% for the FTIR measurements, 3.66 (3.35–3.97)% for GCHP, and 6.49 (2.00–10.98)% for TCR-2.

A case study examined a pollution episode in Mexico City during May 2019, which was characterized by enhanced surface concentrations of  $PM_{2.5}$ . The analysis identified simultaneous enhancements in  $PM_{2.5}$  and  $NH_3$  using measurements and model simulations. Preliminary comparisons between high-resolution simulations of  $NH_3$  and  $PM_{2.5}$  revealed similar results, with more consistent simulations of  $NH_3$  than those for  $PM_{2.5}$ .

### Acknowledgements

First, I would like to acknowledge my supervisor, Kimberly Strong. I have no words to describe my gratitude for her continuous support, guidance, and motivation during this journey. From the moment I joined the group, she has always shown professionalism, dedication, and kindness. I would also like to acknowledge my doctoral committee members, Dylan Jones, for his support, endless patience, and useful insight when interpreting the models' results, and Jennifer Murphy for her accurate feedback and support; as well as Karen Smith, Debra Wunch, and Eloise Marais for their feedback to improve this thesis. I would also like to thank Ramina, Erik, Tyler, Ellen, Jinwoong, Shoma, Kristof, Erin, Victoria, Joseph, Orfeo, Christian, Anas, Fabiola, and Sabrina for enriching my graduate life experience. I want to thank my colleagues, Michel, Wolf, Ivan, Enrico, Camille, Corinne, Marina, Kazu, Dara, and Blanca, for the prolific conversations that helped improve this research. I would like to acknowledge the assistance of Elaine, Liz, Julie, Annie, Ayesha, Adam, Tom, CC, Gisela, and Katherine from the Department of Physical and Environmental Sciences, and Fatima, Ana, NuRee, and Greg from the Department of Physics, who made navigating this PhD easier. I want to thank my friends and family, especially Alison, Nave, Camel, Cipri, Mirna, and Biaanni, for their continuous motivation and support. I also want to give special thanks to my parents, who keep inspiring me from wherever they're watching, and to my dogs Hansel and Huesos. Finally, thanks to Victor, my husband, for his unconditional support and love; I couldn't have asked for a better partner through this journey, and to Victoria, my world.

This research has been supported by the Consejo Nacional de, Ciencias y Tecnología (CONACYT, now SECIHTI) (PhD grant no. 665043), and by the Natural Sciences and Engineering Research Council of Canada (NSERC).

## Contents

A	bstra	nct		ii
A	ckno	wledge	ements	iv
Li	ist of	Table	S	ix
Li	ist of	Figur	es	xi
Li	ist of	Abbre	eviations	xx
1	Inti	roduct	ion	1
	1.1	Introd	luction	1
	1.2	Overv	iew of Atmospheric Ammonia (NH <sub>3</sub> )	3
		1.2.1	Molecular Characteristics and Chemical Reactions	4
		1.2.2	Sources and Pathways of Atmospheric NH <sub>3</sub>	5
		1.2.3	Remote Sensing Measurements	10
		1.2.4	Modeling	13
	1.3	Thesis	s Overview	14
		1.3.1	Significance	14
		1.3.2	Scientific Objectives	14
		1.3.3	Outline	15
		1.3.4	Contributions	16
2	Me	thods		18

	2.1	Measu	rements of $NH_3$	18
		2.1.1	Vibrational Spectroscopy	18
		2.1.2	Atmospheric Spectroscopy	23
		2.1.3	Fourier Transform Technique	24
		2.1.4	Fourier Transform Spectrometers	26
		2.1.5	NH <sub>3</sub> FTIR Retrieval	30
		2.1.6	Satellite Data: IASI	43
	2.2	Simula	ations of NH <sub>3</sub>	45
		2.2.1	GEOS-Chem	45
		2.2.2	TCR-2	49
		2.2.3	WRF-Chem	51
3	Evo	lution	and Distribution of NH <sub>3</sub> Over Mexico City	53
	3.1	Introd	uction	53
	3.2	Metho	odology	54
		3.2.1	Study Site: Mexico City	54
		3.2.2	Ground-based FTIR Stations and $\mathrm{NH}_3$ Retrieval	56
		3.2.3	IASI-NH $_3$ Data Product and Comparison	58
		3.2.4	Back-Trajectory Analysis	59
	3.3	Result	s and Discussion	59
		3.3.1	FTIR $NH_3$ Time Series and Variability	59
		3.3.2	Satellite Observations and Comparison with FTIR	66
		3.3.3	Back-Trajectory Analysis and Origin Observed $\mathrm{NH}_3$ in Mexico	
			City	72
	3.4	Conclu	asions	73
4	Var	iability	$\gamma$ and Trends of $\mathbf{NH}_3$	<b>7</b> 5
	<i>1</i> 1	Introd	uction	75

6	Con	clusio	ns and Future Work	132
	5.4	Summ	ary	129
		5.3.3	GCHP-SF vs. GCHP-C48	125
		5.3.2	Spatial Distribution of $NH_3$ and $PM_{2.5}$	119
		5.3.1	Pollution Events	116
	5.3	Result	as and Discussion	116
		5.2.2	Modeled $NH_3$ and $PM_{2.5}$	115
		5.2.1	Pollution Events	114
	5.2	Mater	ials and Methods	114
	5.1	Introd	luction	112
5	NH	$_3$ and	$\mathrm{PM}_{2.5}$ over Mexico City	112
	4.5	Concl	usions	110
		4.4.4	Trend Comparison	105
		4.4.3	Sensitivity Tests	102
		4.4.2	Diurnal Variability	100
		4.4.1	Seasonal Variability	97
	4.4	Comp	arison of Simulated NH <sub>3</sub> Total Columns	93
		4.3.4	FTIR Trends	88
		4.3.3	Diurnal Variability	86
		4.3.2	Seasonal Variability	83
		4.3.1	Time Series	80
	4.3	FTIR	Results	80
		4.2.3	Trend Analysis	79
		4.2.2	Simulations of $NH_3$	79
		4.2.1	Ground-based FTIR $NH_3$ Observations	76
	4.2	Mater	ials and Methods	76

	6.1	Conclusions	132
	6.2	Future Work	136
A	Sup	plemental Figures and Information for Chapter 2	138
	A.1	$NH_3$ Retrieval	138
	A.2	Total Columns From GCHP	141
	A.3	Total Columns From TCR-2	142
В	Sup	plemental Figures for Chapter 4	143
$\mathbf{C}$	Sup	plemental Figures for Chapter 5	151
Bi	bliog	raphy	156

## List of Tables

1.1	The vibrational modes of the NH <sub>3</sub> molecule (Hargreaves et al., 2011).	4
1.2	Principal chemical reactions involving NH <sub>3</sub>	5
1.3	NH <sub>3</sub> lifetime estimates reported in the literature. Modified from Van Dan	nme
	et al. (2018)	S
2.1	Summary of fitting parameters for $NH_3$ retrievals at the 22 FTIR sites	
	used in this thesis.	37
2.2	Summary of mean parameters for $\mathrm{NH}_3$ retrievals at the 22 FTIR sites	
	used in this thesis.	40
3.1	Mean $\mathrm{NH}_3$ total columns reported from ground-based FTIR stations.	61
4.1	FTIR sites used in this study.	77
4.2	$\mathrm{NH_{3}}$ mean total columns and $\pm~1\sigma$ and absolute trends with 95%	
	confidence intervals for the FTIR sites. Bold indicates a significant	
	trend	90
4.3	Results of the $\mathrm{NH}_3$ total column comparisons of GCHP and TCR-2	
	with FTIR measurements	96
4.4	MRD for monthly means of GCHP and TCR-2 $\mathrm{NH_{3}}$ total columns	
	compared to FTIR measurements at each site	99
4.5	MRD for diurnal means of GCHP and TCR-2 $\mathrm{NH_{3}}$ total columns com-	
	pared to FTIR measurements at each site	102

4.6	GCHP-HTAP vs GCHP-CEDS NH <sub>3</sub> total columns and NH <sub>3</sub> total emis-	
	sions with HTAP and CEDS emissions based on Equation 4.5 during	
	February 2013	104
4.7	Trends in daily mean $\mathrm{NH}_3$ total column from GCHP and TCR-2 along	
	with the FTIR trends corresponding to the model time periods, and	
	95% confidence intervals. The model profiles were smoothed by the	
	FTIR AVKs prior to calculating total columns. Bold indicates a sig-	
	nificant trend	107
4.8	GCHP and TCR-2 trends in $\mathrm{NH}_3$ total columns derived from the full-	
	time series of each model along with 95% confidence intervals. Bold	
	indicates a significant trend	108
4.9	GCHP $\mathrm{NH_3/NH_4^+}$ total column ratio and correlation coefficients for	
	$\mathrm{NH_{3}}$ total columns vs. $\mathrm{SO_{2}},\mathrm{NO}_{x}$ total columns and surface tempera-	
	ture. The calculations were made using GCHP variables from 2003 to	
	2021	109
5.1	NH <sub>3</sub> pollution events over Mexico City during May 2019 from ground-	
	based measurements and model simulations	117
5.2	PM <sub>2.5</sub> pollution events over Mexico City during May 2019 from surface	
	measurements and model simulations	118
A.1	Summary of FTIR NH <sub>3</sub> retrieval parameters used at Eureka between	
	2006 and 2020	138
A.2	Summary of FTIR NH <sub>3</sub> retrieval parameters used at Toronto during	
	2021	138

# List of Figures

1.1	Spatial variability in global $\mathrm{NH}_3$ emissions based on the livestock, fertil-	
	izers, biomass burning and fuel consumption emissions from the Emis-	
	sion Database for Global Atmospheric Research (EDGARv4.2), and	
	seabirds emissions from Riddick et al. (2012). Figure taken from Sut-	
	ton et al. (2013)	6
1.2	The primary sources and chemical pathways for atmospheric $\mathrm{NH}_3$ .	
	Numbers indicate the global budget reported in Paulot et al. (2014),	
	and the global depositions and conversion to particulate $\mathrm{NH_4^+}$ percent-	
	ages are from model simulations reported in Khan et al. (2020)	8
1.3	Month of maximum NH3 total columns determined in 0.25° x 0.25° (lon-	
	gitude, latitude) cells from IASI $\mathrm{NH}_3$ measurements between 1 January	
	2008 and 31 December 2013. Monthly weighted columns associated	
	with a weighted relative error above $35\%$ have been set to zero. Figure	
	taken from Van Damme et al. (2015).	11
1.4	Diurnal variability in $\mathrm{NH}_3$ (upper panels) and $\mathrm{NO}_2$ (lower panels) from	
	2.5 years (between 2020 and 2022) of surface measurements over the	
	city of Paris. The diurnal variability is averaged by season, and the	
	hours are in local time. Blue lines represent all days, red lines repre-	
	sent weekdays, and black lines represent weekends. Figure taken from	
	Viatte et al. (2023)	13
2.1	The electromagnetic spectrum. Taken from Bernath (2025)	19

2.2	The elements of symmetry for the NH <sub>3</sub> molecule. Figure taken from
	Bernath (2025)
2.3	The vibrational modes of $\mathrm{NH}_3$ . For the degenerate modes, two orthog-
	onal components are depicted. Figure taken from Nguyen et al. (2021).
2.4	Schematic diagram of the a) Michelson interferometer. b) Phase of the
	electromagnetic waves from the fixed (solid line) and movable (dashed
	line) mirrors at different values of $\delta$ . Note that constructive interference
	occurs for $\delta = 0,  \delta = \lambda$ , and all other $\delta$ corresponding to integral num-
	bers of wavelengths. Modified from Griffiths and De Haseth (2007).
2.5	Schematic diagram of the Eureka Bruker IFS 125HR showing the opti-
	cal path of the solar beam (red arrows), and the internal components,
	which are labelled and indicated by the blue lines. Figure reproduced
	from Lutsch (2019)
2.6	Schematic diagram of the Mexico City Bruker Vertex 80 showing the
	optical beam path in orange, and the internal components which are la-
	belled and indicated. Figure reproduced from the user manual (Bruker
	Optics, 2006)
2.7	Mean retrieved $\mathrm{NH_{3}}$ VMR profiles (red) and a priori profiles (black)
	from 0 to 20 km at the 22 FTIR sites. The retrieved profiles are
	the means over the years indicated in Table 2.2. The circle markers
	indicate the layer centers of the FTIR vertical retrieval grid. A second
	version of this figure, from 0 to 120 km, is presented in Appendix A.
	For the Los Angeles site, only the a priori VMR profile is shown as
	GFIT scaling retrievals do not contain more vertical information than
	the total column amount.

2.8	Mean sensitivity for the NH <sub>3</sub> retrievals from 0 to 20 km at the 22 FTIR	
	sites taken over the years indicated in Table 2.2. The circle markers	
	indicate the layer centers of the FTIR vertical retrieval grid. A second	
	version of this figure, from 0 to above 100 km, is presented in the	
	Appendix A.2. The standard deviation (shade) for the Los Angeles	
	site was not available	42
2.9	Example of a GCHP C16 grid highlighting one face for illustrative	
	purposes. The highlighted face is a $16 \times 16$ grid that is regularly	
	spaced in a gnomonic projection centered on the face. Figure taken	
	from Bindle et al. (2021)	46
2.10	Illustration of the effect of increasing the stretch factor (S) on stretching	
	a C16 cubed sphere grid. Local scaling is the relative change to a grid	
	box's edge length induced by stretching. Figure taken from Bindle	
	et al. (2021)	49
3.1	Study area in central Mexico. Mexico City is shown in the middle,	
	with the red shading corresponding to NH <sub>3</sub> emissions reported in the	
	Mexico City Emissions Inventory 2016 (SEDEMA, 2018) in tonnes per	
	year. The stars indicate the location of the UNAM and Altzomoni	
	stations and the yellow shading indicates the extension of the MCMA.	56
3.2	Time series of retrieved FTIR-NH <sub>3</sub> data over (a) Altzomoni and (b)	
	UNAM, with a fitted Fourier series (red) to reproduce seasonality. Note	
	the differences in magnitude	60
3.3	Average diurnal evolution of NH <sub>3</sub> total columns over Mexico City at	
	(a) Altzomoni and (b) UNAM. Different years are shown in different	
	colours, the thick white line is the average for all years, and the blue	
	shading indicates $\pm 1\sigma$	62

3.4	Monthly averages showing the annual cycle of NH <sub>3</sub> over Mexico City	
	at (a) Altzomoni and (b) UNAM. The thick white line is the average	
	for all years and the shading indicates $\pm 1\sigma$ . (c) Monthly averages of	
	temperature at both stations between 2014-2018 for Altzomoni and	
	2012-2018 for UNAM. The shaded area indicates $\pm 1\sigma$	65
3.5	Snapshot of Mexico's City fire events on February 27, 2013, from	
	the Aqua MODIS instrument with true colour corrected reflectance	
	and resolution of 250 m, obtained from NASA Worldview Snapshots	
	(https://earthdata.nasa.gov). The red dots show the fire events.	
	The stars indicate the location of the UNAM and Altzomoni stations.	67
3.6	Correlation plot for IASI-A NH <sub>3</sub> vs. UNAM FTIR-NH <sub>3</sub> total columns,	
	with coincidence criteria of $<$ 20 km, $\pm$ 40 minutes, elevation (FTIR	
	station – IASI observation) < 300 m, IASI-NH $_3$ retrieval error < 100%	
	between November 2013 and December 2018	68
3.7	Spatial distribution of IASI-A NH <sub>3</sub> total columns for the morning over-	
	pass of MetOp-A over Mexico City, averaged over 2008-2018 for: (a)	
	the cold-dry season (November – February), (b) the warm-dry sea-	
	son (March-May), and (c) the wet season (June-October). HYSPLIT	
	back-trajectories for the UNAM site are shown in panel (d). The stars	
	indicate the locations of both stations, and Mexico City International	
	Airport is shown for reference	70
3.8	Spatial distribution of (a) IASI-A NH <sub>3</sub> total columns for the morning	
	overpass of MetOp-A over Mexico City, averaged over 2008-2018 (b)	
	altitudes in Mexico City from the Space Shuttle Radar Topography	
	Mission Global product (SRTMGL3) (Farr et al., 2007). The stars	
	indicate the location of ground-based stations, and Mexico City Inter-	
	national Airport is shown for reference	71

3.9	IASI and FTIR NH <sub>3</sub> total columns with coincidence criteria of $< 20$	
	km and $< 2$ hr: (a) monthly averages at UNAM, (b) annual averages	
	at UNAM and Altzomoni. The shaded area indicates $\pm 1\sigma$	72
4.1	Location of the 22 ground-based Fourier transform infrared spectrom-	
	eter sites used in this study.	78
4.2	Time series of $\mathrm{NH}_3$ total columns measured at the 22 FTIR sites	81
4.3	Monthly mean NH <sub>3</sub> total columns for each FTIR site. Different years	
	are shown in different colours, with the most recent years in pink shades	
	and older years in blue shades. The thick black line with error bars is	
	the mean for all years $\pm 1\sigma$	84
4.4	Hourly mean NH <sub>3</sub> total columns in local time (hours, with offset from	
	UTC for each site indicated on each panel) for each FTIR site. Different	
	years are shown in different colours with the most recent years in pink	
	shades and older years in blue shades. The thick black line with error	
	bars is the mean for all years $\pm 1\sigma$	87
4.5	Time series of FTIR daily mean NH <sub>3</sub> total columns with fitted third-	
	order Fourier series (solid blue line) and linear trends (dashed blue	
	line) for the sites with sufficient data density to derive trends	91
4.6	Scatter plots of GCHP and TCR-2 vs.FTIR NH <sub>3</sub> total columns. The	
	lines show the individual regression results for each dataset. Note	
	that for Porto Velho only the correlation between FTIR and GCHP is	
	shown, as there are no TCR-2 data available for this site	95
4.7	Monthly mean NH <sub>3</sub> total columns of FTIR (black), GCHP (blue), and	
	TCR-2 (green). The thick solid lines represent the temporally matched	
	FTIR measurements and GCHP and TCR-2 datasets; the dashed lines	
	represent the complete time series from each dataset. Vertical lines	
	represent the standard deviation $(\pm 1\sigma)$	98

4.8	Hourly mean NH <sub>3</sub> total columns of FTIR (black), GCHP (blue), and	
	TCR-2 (green) in local time (hours, with offset from UTC for each site	
	indicated on each panel) for each site. The thick solid lines represent	
	the temporally matched datasets between the FTIR measurements and	
	GCHP and TCR-2 datasets; the dashed lines represent the complete	
	time series from each dataset. Vertical lines represent the standard	
	deviation $(\pm 1\sigma)$	101
5.1	Daily mean NH <sub>3</sub> total columns in Mexico City from (a) ground-based	
	FTIR measurements and (b) GCHP-C48 simulations. In red are the	
	identified pollution events; note the spike in May. The blue shading	
	represents $2\sigma$ from the Fourier fit as described in Section 5.2.1	116
5.2	Daily mean surface $\mathrm{PM}_{2.5}$ in Mexico City from (a) in situ measurements	
	and (b) GCHP-C48 simulations. In red are the identified pollution	
	events; note the spike in May. The blue shading represents $2\sigma$ from	
	the Fourier fit as described in Section 5.2.1	118
5.3	(a) Snapshot of Mexico's fire events on May 13, 2019, from the Aqua	
	MODIS instrument with true colour corrected reflectance and reso-	
	lution of 1 km, obtained from NASA Worldview Snapshots (https:	
	//earthdata.nasa.gov). The red dots show the fire events. The lo-	
	cation of Mexico City is shown in red. (b) Hourly backward trajectories	
	from HYSPLIT on May 13, 2019, initiated in Mexico City at 100 m	
	(each dot corresponds to 1 h). Adapted from Rios et al. (2023)	120
5.4	Spatial distribution of mean $PM_{2.5}$ surface concentration during May	
	13, 2019, over central Mexico from the GCHP-SF stretched grid simu-	
	lation.	121
5.5	Spatial distribution of mean $PM_{2.5}$ surface concentration during May	
	13. 2019, over central Mexico from the WRF-Chem simulation.	122

5.6	Spatial distribution of daily mean NH <sub>3</sub> total columns during May 13,	
	2019, over central Mexico from the GCHP-SF stretched grid simulation	.123
5.7	Spatial distribution of mean $\mathrm{NH}_3$ total columns during May 13, 2019,	
	over central Mexico from the WRF-Chem simulation	123
5.8	Spatial distribution of $\mathrm{NH}_3$ total columns between 11 and 16 May 2019,	
	over central Mexico from (a) GCHP-SF, (b) WRF-Chem, and (c) IASI	
	A+B	124
5.9	Scatter plots of GCHP-SF vs. GCHP-C48 $\mathrm{NH_{3}}$ total columns for Mex-	
	ico City during May 2019	125
5.10	Scatter plots of GCHP-SF vs. GCHP-C48 surface $\mathrm{PM}_{2.5}$ for Mexico	
	City during May 2019	126
5.11	Scatter plots of GCHP-SF vs. GCHP-C48 $\mathrm{NH}_3$ total columns for Alt-	
	zomoni during May 2019	127
5.12	Scatter plots of GCHP-SF vs. GCHP-C48 surface $\mathrm{PM}_{2.5}$ for Altzomoni	
	during May 2019	127
5.13	Daily means of (a) $\mathrm{NH_{3}}$ , (b) $\mathrm{CO}$ , (c) HCHO total columns and (d)	
	surface $\mathrm{PM}_{2.5}$ for Mexico City during May 2019 from measurements	
	(FTIR and RAMA), GCHP-C48, and GCHP-SF	128
A.1	Mean retrieved $\mathrm{NH_{3}}$ VMR profiles (red) and a priori profiles (black) at	
	the 22 FTIR sites. The retrieved profiles are the means over the years	
	indicated in Table 2.2. The circle markers indicate the layer centers	
	of the FTIR vertical retrieval grid. The shaded region indicates $\pm$ the	
	standard deviation from the mean. For the Los Angeles site, only the a	
	priori VMR profile is shown as GFIT scaling retrievals do not contain	
	more vertical information than the total column amount	139

A.2	Mean sensitivity for NH <sub>3</sub> retrieval at the 22 FTIR sites taken over	
	the years indicated in Table 2.2. The circle markers indicate the layer	
	centers of the FTIR vertical retrieval grid. The shaded region indicates	
	$\pm$ the standard deviation from the mean. The standard deviation for	
	the Los Angeles site was not available	140
B.1	Comparison of $\mathrm{NH_{3}}$ and $\mathrm{CO}$ total columns measured at Porto Velho	
	between July and September 2019. Simultaneous enhancements can	
	be observed, attributed to biomass burning events	143
B.2	Comparison of $\mathrm{NH}_3$ and CO total columns measured at Reunion Maido	
	between August and November 2019. Simultaneous enhancements can	
	be observed, attributed to biomass burning events	144
B.3	Comparison of $\mathrm{NH}_3$ and $\mathrm{CO}$ total columns measured at Los Angeles	
	between July 2020 and August 2021. Simultaneous enhancements can	
	be observed, attributed to wildfires	144
B.4	Comparison of $\mathrm{NH_{3}}$ and $\mathrm{SO_{2}}$ total columns measured at Izana between	
	September and November 2021 during the Tarjogaite volcanic eruption	
	that reached the Izana site. Simultaneous enhancements can be observed	.145
B.5	Monthly mean GCHP surface temperature at each FTIR site between	
	2003 and 2021. Vertical lines represent the standard deviation $(\pm 1\sigma)$ .	146
B.6	Comparison of the time series of NH <sub>3</sub> total columns from FTIR mea-	
	surements (black) versus GCHP (blue) and TCR-2 (green) at the 22	
	FTIR sites	147
B.7	Scatter plot of GCHP and TCR-2 vs. FTIR temporally matched NH <sub>3</sub>	
	total columns. The lines show the regression results for each model	148
B.8	Time series of GCHP daily mean NH <sub>3</sub> total columns between 2003 and	
	2021 with fitted third-order Fourier series (solid red line) and linear	
	trends (dashed red line) for the 22 FTIB sites.	149

B.9	Time series of TCR-2 daily mean NH <sub>3</sub> total columns between 2005 and	
	2018 with fitted third-order Fourier series (solid red line) and linear	
	trends (dashed red line) for the 22 FTIR sites	150
C.1	Comparison of $\mathrm{NH}_3$ and $\mathrm{CO}$ total columns measured at Mexico City	
	during May 2019. Simultaneous enhancements can be observed, at-	
	tributed to biomass burning events	151
C.2	Comparison of NH <sub>3</sub> and CO total columns from GCHP-SF during	
	May 2019. Simultaneous enhancements can be observed, attributed	
	to biomass burning events	152
C.3	Spatial distribution of $\mathrm{NH}_3$ total columns during the May 11 to 16	
	2019, pollution event over Mexico from IASI A and B	153
C.4	Spatial distribution of mean $\mathrm{NH}_3$ total columns during May 13, 2019,	
	over Mexico from the target cube-face from the GCHP-SF stretched	
	grid simulation.	154
C.5	Spatial distribution of mean $PM_{2.5}$ surface concentration during May	
	13, 2019, over Mexico from the target cube-face from the GCHP stretched	
	grid simulation	155

#### List of Abbreviations

ALTZ Altzomoni

ANNI Artificial Neural Networks

AWB Autoregressive Wild Bootstrap

**BB** Biomass Burning

CANDAC Canadian Network for the Detection of Atmospheric Change

CEDS Community Emissions Data System

**CONACYT** Consejo Nacional de Ciencia y Tecnología (Mexico's National Council of Science and Technology)

CrIS Cross-track Infrared Sounder

CST Community Solar Tracker

CTM Chemical Transport Model

**DOFS** Degrees of Freedom for Signal

EDGAR Emissions Database for Global Atmospheric Research

**EMEP** European Monitoring and Evaluation Programme Inventory

EnKF Ensemble Kalman Filter

**EPA** Environmental Protection Agency

ESA European Space Agency

**EUMESAT** European Organization for the Exploitation of Meteorological Satellites

**FINN** Fire INventory from NCAR

**FOV** Field of View

**FRP** Fire Radiative Power

FTIR Fourier Transform InfraRed

FTS Fourier Transform Spectrometer

**GEIA** Global Emissions Inventory Activity

**GCHP** GEOS-Chem High Performance

GEOS-Chem Goddard Earth Observing System - Chemical transport model

**GFAS** Global Fire Assimilation System

**GFED** Global Fire Emissions Database

**GMAO** Global Modeling and Assimilation Office

GOCART Goddard Chemistry Aerosol Radiation and Transport

GOME-2 Global Ozone Monitoring Experiment

**HEMCO** Harmonized Emissions Component

HIRAS Hyperspectral Infrared Atmospheric Sounder

HITRAN High-resolution Transmission Molecular Absorption Database

**HRI** Hyperspectral Range Index

**HTAP** Hemispheric Transport of Air Pollution

**HYSPLIT** Hybrid Single-Particle Lagrangian Integrated Trajectory

IASI Infrared Atmospheric Sounding Interferometer

ILS Instrument Line Shape

IRWG Infrared Working Group

KOPRA Karlsruhe Optimized and Precise Radiative Transfer Algorithm

LBLRTM Line-By-Line Radiative Transfer Model

MAP Maximum A Posteriori

MCMA Mexico City Metropolitan Area

MCE2 Molina Center for Strategic Studies in Energy and the Environment

MCT Mercury Cadmium Telluride

ME Modulation Efficiency

MERRA Modern-Era Retrospective Analysis for Research and Applications

MetOp Meteorological Operational Satellite Program

MIR. Mid-InfraRed

**MODIS** Moderate Resolution Imaging Spectroradiometer

MOMO-Chem Multi-mOdel Multi-cOnstituent Chemical Data Assimilation

**MOPITT** Measurements of Pollution in The Troposphere

MOZART-4 Model for Ozone and Related chemical Tracers version 4

NASA National Aeronautics and Space Administration

NDACC Network for the Detection of Atmospheric Composition Change

**NEI** National Emissions Inventory

NCAR National Center for Atmospheric Research

NCEP National Centers for Environmental Prediction

**NH** Northern Hemisphere

NIR Near-InfraRed

NOAA National Oceanic and Atmospheric Administration

**OEM** Optimal Estimation Method

**OMI** Ozone Monitoring Instrument

**OPD** Optical Path Difference

PBL Planetary Boundary Layer

**PDF** Probability Density Function

**PEARL** Polar Environment Atmospheric Research Laboratory

PM Particulate Matter

 $PM_{2.5}$  Particulate Matter smaller than 2.5 microns

**PSR** Profile Scaling Retrieval

**QFED** Quick Fire Emissions Dataset

RAMA Red Automática de Monitoreo Atmosférico (Mexico City's Automatic Air Quality Monitoring Network)

RMS Root Mean Square

SCIAMACHY Scanning Imaging Absorption Spectrometer for Atmospheric Cartography

SECIHTI Secretaría de Ciencia, Humanidades, Tecnología e Innovación (Mexico's Ministry of Science, Humanities, Technology and Innovation)

**SH** Southern Hemisphere

SIA Secondary Inorganic Aerosols

SNR Signal-to-Noise Ratio

**TAO** University of Toronto Atmospheric Observatory

TCR Tropospheric Chemical Reanalysis

TCR-2 Tropospheric Chemical Reanalysis version 2

**TES** Tropospheric Emission Spectrometer

**TOA** Top of Atmosphere

TOMAS TwO-Moment Aerosol Sectional

TSV Total Spatial Variance

UNAM Universidad Nacional Autónoma de México (National Autonomous University of Mexico)

VMR Volume Mixing Ratio

 $\mathbf{WACCM}\ \ \mathrm{Whole}\ \mathrm{Atmosphere}\ \mathrm{Community}\ \mathrm{Climate}\ \mathrm{Model}$ 

WHO World Health Organization

 $\mathbf{WRF}$  Weather Research and Forecasting

WRF-Chem Weather Research and Forecasting coupled with Chemistry

**ZPD** Zero Path Difference

### Chapter 1

### Introduction

### 1.1 Introduction

"Of all man's recent interventions in the cycles of nature, the industrial fixation of nitrogen far exceeds all the others in magnitude" (Delwiche, 1970). Nitrogen-rich manure has been used as a fertilizer since before nitrogen was discovered as a chemical element. In the last century, the introduction of synthetic fertilizers and the invention of the Haber-Bosch process to industrially produce ammonia (NH<sub>3</sub>), a key chemical compound in nitrogen-based fertilizers, made possible the rapid increase in cultivation to keep up with the globally increasing food demand. Thus, nitrogen promoted the Agricultural Revolution, just as carbon promoted the Industrial Revolution (Paulot et al., 2014; Battye et al., 2017). However, a significant portion of NH<sub>3</sub> from fertilizers is lost to the environment (Galloway et al., 2004) and emissions of reduced N to the atmosphere are a key driver for atmospheric composition and chemistry in the twenty-first century (Fowler et al., 2013). In the atmosphere, NH<sub>3</sub> can participate in different reactions, such as the neutralization of atmospheric acidity and the formation of particulate matter (PM) (Behera et al., 2013), an air pollutant of great

concern (Fuzzi et al., 2015) consisting of especially fine particles with diameters of equal or less than 2.5 micrometres  $(PM_{2.5})$ . Because of their small size,  $PM_{2.5}$  particles can penetrate the lungs and even reach the bloodstream, contributing to several health conditions, including premature death (Paulot and Jacob, 2014; Giannakis et al., 2019; Vohra et al., 2021). NH<sub>3</sub> is the source of ammonium salts, which act as contributors of  $PM_{2.5}$  and can account for up to 50% of particulate matter mass (Behera et al., 2013). In addition,  $NH_3$  can be transported and deposited at considerable distances from emission sources, impacting ecosystems by contributing to forest decline, eutrophication of freshwater bodies, and soil acidification (Sutton et al., 2008; Behera et al., 2013). Deposition of reduced nitrogen, such as NH<sub>3</sub>, has increased over continental regions (Tan et al., 2020). As mentioned, the primary sources of NH<sub>3</sub> are related to agriculture; however, future increases in emissions from other sources are expected, for example, emissions due to the use of NH<sub>3</sub> as a hydrogen carrier for the production of renewable energy. This involves the industrial production of NH<sub>3</sub> with no, or almost no, co-production of carbon dioxide (green ammonia), and has seen more widespread use in recent years (Olabi et al., 2023).

Despite the importance of atmospheric NH<sub>3</sub>, there are still significant uncertainties regarding its emission budgets because of the limited availability of NH<sub>3</sub> observations (Luo et al., 2022) and the scarce regulation of its emissions (Paulot et al., 2014; Giannakis et al., 2019; Viatte et al., 2023). Accurate in situ samples of NH<sub>3</sub> are challenging because this gas is sticky and can interact with the surfaces of materials through adsorption and desorption processes, which can alter the instrumental response (von Bobrutzki et al., 2010). Satellite observations from the Infrared Atmospheric Sounding Interferometer (IASI) allowed for the first global NH<sub>3</sub> map (Clarisse et al., 2009); however, the frequency of these types of observations is limited to a few per day over a specific region, making it difficult to derive diurnal variabilities. Furthermore, NH<sub>3</sub> variability is difficult to model and predict using atmospheric chemical transport

models (Khan et al., 2020; Nair and Yu, 2020). Improvement in the knowledge of the spatial and temporal variability of NH<sub>3</sub> is equally as important as that of the total magnitude of emissions (Battye et al., 2003). This work focuses on obtaining and analyzing the variability and long-term trends of atmospheric ammonia using a combination of ground-based and satellite measurements, as well as simulations from chemical transport models and a reanalysis product.

### 1.2 Overview of Atmospheric Ammonia (NH<sub>3</sub>)

Nitrogen is the major component of the Earth's atmosphere (78.08 % of dry air), and it is essential for all living organisms. N<sub>2</sub> is stable and inert, and it needs to be chemically converted via nitrogen fixation to a form that organisms can assimilate. Natural nitrogen fixation occurs by the action of microorganisms and lightning, but it can also occur due to human activities. The nitrogen cycle has changed significantly since the introduction of the industrial fixation of nitrogen. It is estimated that the anthropogenic flux of fixed or reactive nitrogen to the biosphere is now roughly equivalent to the total flux from natural sources (Battye et al., 2017). Among the most relevant inorganic nitrogen-containing species in the atmosphere are nitrous oxide  $(N_2O)$ , nitric oxide (NO), nitrogen dioxide  $(NO_2)$ , the sum of NO and  $NO_2$ , which form the chemical family  $NO_x$ , nitric acid (HNO<sub>3</sub>), and ammonia (NH<sub>3</sub>). NH<sub>3</sub> accounts for almost half of all reactive nitrogen released in the atmosphere, with total emissions doubling from 1860 to 1993 and possibly doubling again by 2050 (Krupa, 2003; Galloway et al., 2004; Clarisse et al., 2009) and could reach 130 Tg  ${\rm NH_3}{-}N~{\rm yr}^{-1}$  by 2100 (Sutton et al., 2013), where ammonia nitrogen ( ${\rm NH_3}{-}N$ ) is the amount of N in NH<sub>3</sub>, 1 Tg NH<sub>3</sub>-N = 1.216 Tg NH<sub>3</sub> (Sheikh et al., 2023). Industrially, NH<sub>3</sub> is synthesized using the Haber-Bosch process, see (R1) in Table This method has helped expand the availability of nitrogen-based fertilizers since the early 1900s, contributing to increased agricultural outputs and population growth (Smil, 2000). Emissions of reduced N to the atmosphere are a key driver for atmospheric composition and chemistry in the twenty-first century (Fowler et al., 2013).

#### 1.2.1 Molecular Characteristics and Chemical Reactions

NH<sub>3</sub> is a molecule composed of one nitrogen atom and three hydrogen atoms. It is a volatile and highly water-soluble molecule. It has a tetrahedral electron geometry and a trigonal pyramid molecular geometry with  $C_{3\nu}$  symmetry. This molecule has six fundamental vibrational modes, two of them doubly degenerate, so in total, NH<sub>3</sub> has four different fundamental vibration frequencies in the infrared spectrum (Hargreaves et al., 2011) as illustrated in Table 1.1.

Table 1.1: The vibrational modes of the NH<sub>3</sub> molecule (Hargreaves et al., 2011).

Mode	Symmetry	Type	Frequency $\nu \ (\mathrm{cm}^{-1})$
$\overline{\nu_1}$	$a_1$	Symmetric stretch	3336.2
$ u_2$	$a_1$	Symmetric bend (umbrella)	932.5
$\nu_3$	e	Asymmetric stretch	3443.6
$\nu_4$	e	Asymmetric bend	1626.1

Chemically, NH<sub>3</sub> can donate electron density, and it can accept protons and release hydroxide ions in an aqueous solution (R2), so it is classified as a base with an acid-dissociation constant:

$$Ka = \frac{[NH_3(aq)][H^+(aq)]}{[NH_4^+(aq)]}$$
(1.1)

and pKa=9.2. In the atmosphere, NH<sub>3</sub> is the most abundant base, and it is involved in several chemical reactions either in the gas or aerosol phase (R2). Table 1.2 summarizes the main chemical reactions of NH<sub>3</sub> in the atmosphere (R3-R8). It predominantly reacts with sulfuric acid to form ammonium sulfate (R4) and bisulfate (R5). After the reaction with sulfuric acid, if there is still available NH<sub>3</sub>, the reaction with nitric acid proceeds to form ammonium nitrate (R6), and finally with

hydrochloric acid to form ammonium chloride (R7). NH<sub>3</sub> can also react with the hydroxy radical (OH) to form H<sub>2</sub>O and the NH<sub>2</sub> radical (R8), although this reaction is relatively slow (Finlayson-Pitts and Pitts, 2000). Reactions R3-R8 depend on the availability of NH<sub>3</sub>, ambient temperature, and relative humidity (Behera et al., 2013; Wen et al., 2013). The overall mass load of particulate matter in the air is generally composed of 10-30% of each of the following: sulfate, nitrate, ammonium, sea salt, mineral dust, organic compounds, and elemental carbon, with contribution from the products of reactions R4 and R6. Fine particulate matter refers to particles with diameters  $\leq 2.5 \,\mu\text{m}$  (PM<sub>2.5</sub>) (Pöschl, 2005). HNO<sub>3</sub> from NOx can produce secondary aerosols like NH<sub>4</sub>NO<sub>3</sub>, depending on the availability of atmospheric NH<sub>3</sub>, which serves as a precursor of Secondary Inorganic Aerosols (SIA) (Fuzzi et al., 2015).

Table 1.2: Principal chemical reactions involving NH<sub>3</sub>.

Reaction Details	Reaction Number
$N_2(g) + 3 H_2(g) \Longrightarrow 2 NH_3(g)$	R1
$NH_3(g) \rightleftharpoons NH_3(aq)$	R2
$NH_3(aq) + H_2O \Longrightarrow NH_4^+(aq) + OH^-(aq)$	R3
$2 NH_3(g) + H_2SO_4(aq) \longrightarrow (NH_4)_2SO_4(s) or (aq)$	R4
$NH_3(g) + H_2SO_4(aq) \longrightarrow NH_4H_2SO_4(aq)$	R5
$NH_3(g) + HNO_3(s) \Longrightarrow NH_4NO_3(s)$	R6
$NH_3(g) + HCl(g) \Longrightarrow NH_4Cl(s) \text{ or } (aq)$	R7
$NH_3(g) + OH(g) \longrightarrow NH_2(g) + H_2O(g)$	R8

### 1.2.2 Sources and Pathways of Atmospheric $NH_3$

The primary sources of atmospheric NH<sub>3</sub> are related to agricultural activities (mainly livestock and fertilizers), as well as natural sources, biomass burning, vehicular emissions, waste generated by humans and pets (Bouwman et al., 1997; Sutton et al., 2008, 2013). Figure 1.1 shows the global distribution of the primary sources of NH<sub>3</sub> and its

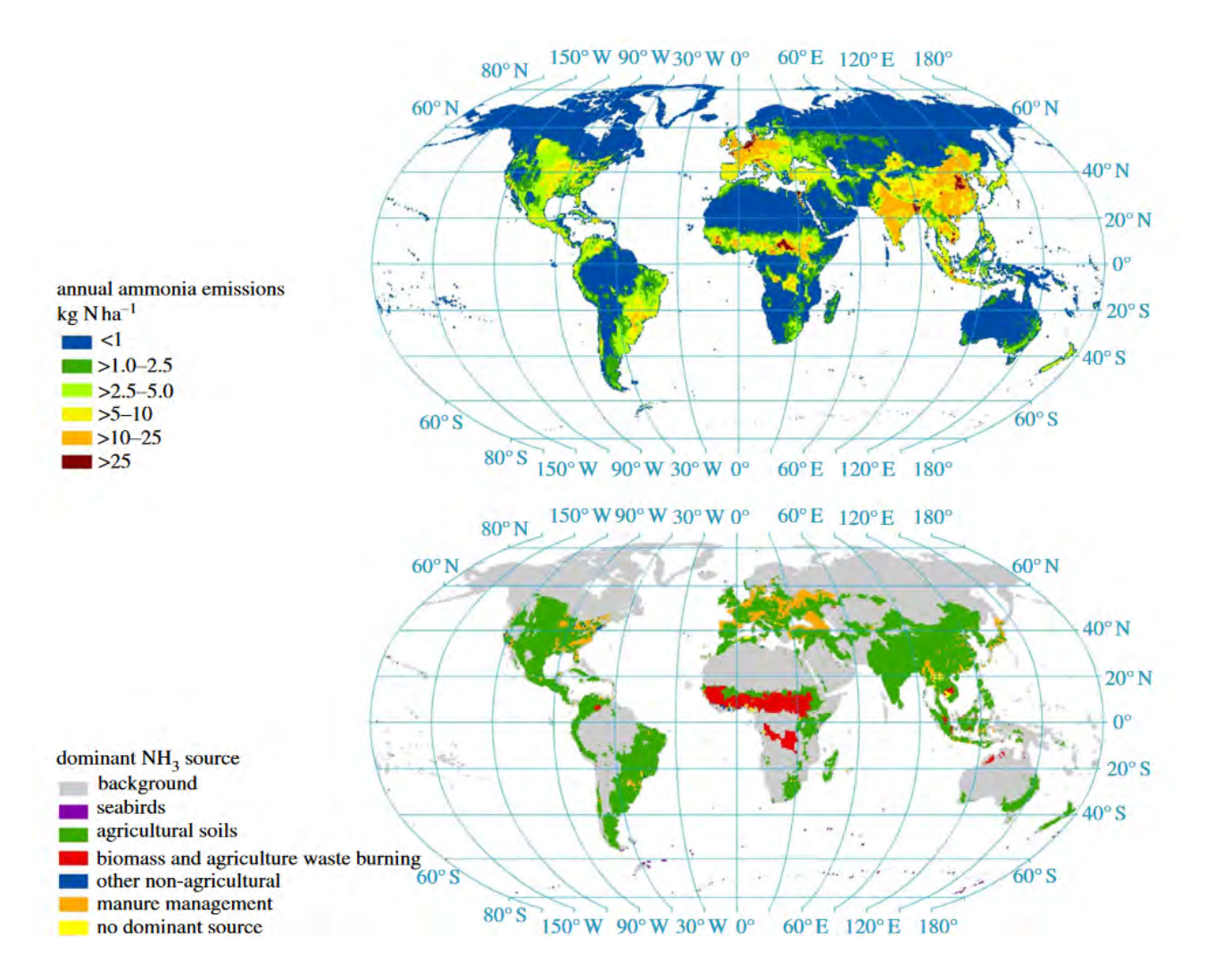


Figure 1.1: Spatial variability in global  $NH_3$  emissions based on the livestock, fertilizers, biomass burning and fuel consumption emissions from the Emission Database for Global Atmospheric Research (EDGARv4.2), and seabirds emissions from Riddick et al. (2012). Figure taken from Sutton et al. (2013).

annual emissions, with agricultural soils being the dominant source. In countries with intensive livestock production,  $NH_3$  is the main contributor to nitrogen fluxes. For example, according to an estimation made by Paulot et al. (2014), out of the global  $NH_3$  burden of 54 Tg  $NH_3-N$  yr<sup>-1</sup>, 34 Tg  $NH_3-N$ yr<sup>-1</sup> comes from manure and fertilizer applications, with the rest related to other natural and anthropogenic sources such as open fires or industry. Furthermore, wastewater streams are considered rich in N that contribute to  $NH_3$  emissions (Munasinghe-Arachchige and Nirmalakhandan,

2020; Sheikh et al., 2023).  $NH_3$  emissions from vehicles with catalytic systems have been reported (Cadle et al., 1979), mainly from vehicles using three-way catalytic converters (Fraser and Cass, 1998) or newer technologies, while NH<sub>3</sub> emissions are affected by the driving mode and are primarily generated during acceleration events (Huai et al., 2003). Human  $NH_3$  emissions strongly depend on temperature and skin exposure; for example, one adult can emit 0.4 mg of  $NH_3$  per hour at  $25^{\circ}C$  but 1.4mg of  $NH_3$  per hour at 29°C (Li et al., 2020). Although, due to geological reasons, not all volcanoes are a source of NH<sub>3</sub>, the volcanoes with surrounding sal ammoniac (NH<sub>4</sub>Cl) mineral or with accumulation of organic material that reacts with volcanic magma could be potential sources of NH<sub>3</sub> during volcanic activity, with reported NH<sub>3</sub> emissions up to  $\approx 0.003$  mg m<sup>-3</sup> 100 km downwind of the source (Uematsu et al., 2004; Sutton et al., 2008; Adams et al., 2017). In remote areas such as the Arctic, NH<sub>3</sub> emissions come from different sources, such as the hydrolysis of guano from migratory seabirds (Blackall et al., 2007; Riddick et al., 2012; Sutton et al., 2013; Croft et al., 2016), seal excreta (Theobald et al., 2006), and the ice-free and snow-free tundra (Croft et al., 2019). NH<sub>3</sub> enhancements in the Arctic due to boreal wildfires in the Northwest Territories have also been observed (Wentworth et al., 2016; Lutsch et al., 2019). Similarly, emissions from penguin guano have been reported as a significant source of Antarctic NH<sub>3</sub> (Boyer et al., 2025).

Emitted NH<sub>3</sub> can react, be transported by winds, or be removed from the atmosphere by wet or dry deposition (Neirynck and Ceulemans, 2008; Behera et al., 2013). Figure 1.2 shows the primary sources and chemical pathways of atmospheric NH<sub>3</sub>. Both gas and particles can be deposited on Earth's surface. Dry deposition consists of the removal of atmospheric pollutants without significant interaction with atmospheric moisture and direct reaction or absorption at the Earth's surface. A wet deposition involves the interaction with atmospheric moisture and scavenging by precipitation (Finlayson-Pitts and Pitts, 2000; Behera et al., 2013). NH<sub>3</sub> exchange between the

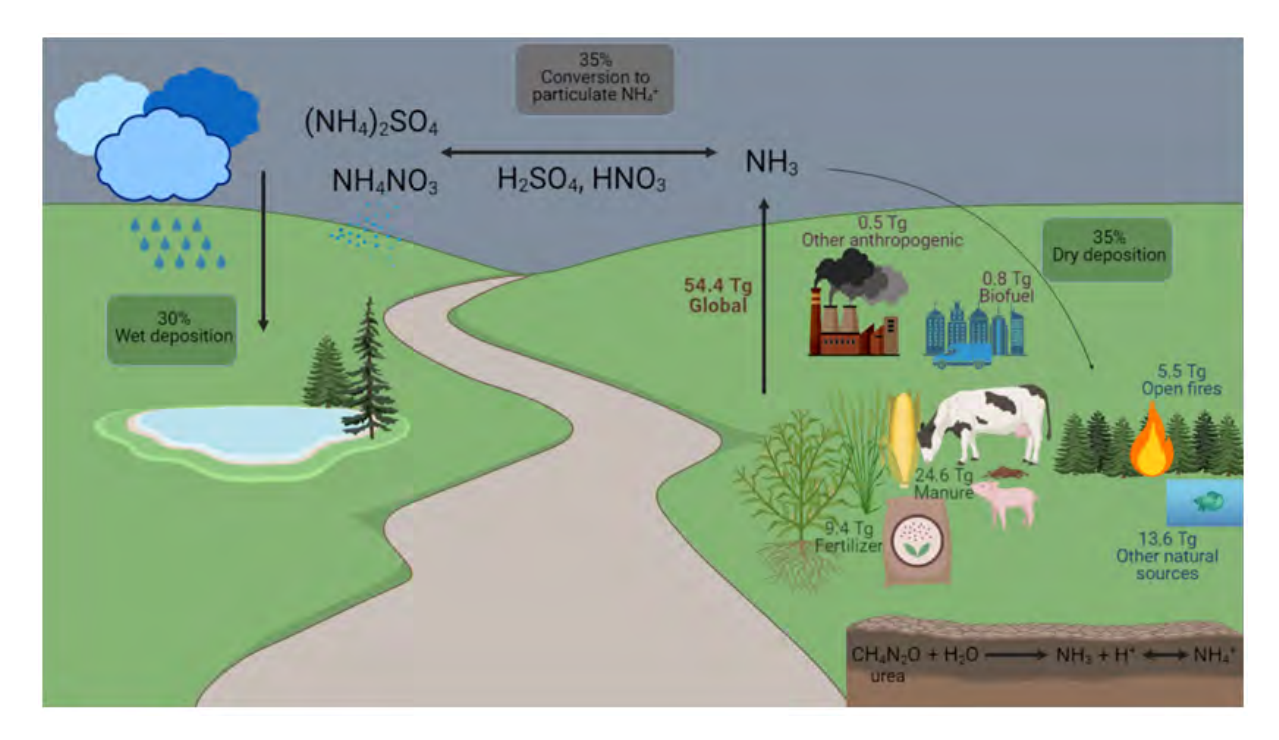


Figure 1.2: The primary sources and chemical pathways for atmospheric  $NH_3$ . Numbers indicate the global budget reported in Paulot et al. (2014), and the global depositions and conversion to particulate  $NH_4^+$  percentages are from model simulations reported in Khan et al. (2020).

atmosphere and the surface, where it is deposited, is bidirectional. This bidirectional exchange is particularly interesting when the surface involves vegetation, as NH<sub>3</sub> is present in the intracellular fluids of leaves. Therefore, plants can act as sinks of atmospheric NH<sub>3</sub>, and emissions will depend on the concentration, type of surface, and the NH<sub>3</sub> compensation point (Asman et al., 1998; Sutton et al., 2008). The NH<sub>3</sub> compensation point occurs when there is no net flux because the concentration of atmospheric NH<sub>3</sub> equals the concentration at the surface. When the atmospheric concentration of NH<sub>3</sub> is below the compensation point, NH<sub>3</sub> will be emitted from the surface (Farquhar et al., 1980). Usually, this bidirectional exchange is described with resistance models to represent the biosphere-atmosphere flux exchange (Nemitz et al., 2001; Sutton et al., 2013).

Table 1.3: NH<sub>3</sub> lifetime estimates reported in the literature. Modified from Van Damme et al. (2018).

Reference	Möller and Schieferdecker (1985); Sutton (1990) Oninn et al. (1990)	Dentener and Crutzen (1994)	Flechard and Fowler (1998)	Hertel et al. $(2012)$	Norman and Leck $(2005)$	Norman and Leck $(2005)$	Wallace and Hobbs $(2006)$	Hauglustaine et al. (2014)	Whitburn et al. (2016b)	Lutsch et al. (2016)	Van Damme et al. (2018); Clarisse et al. (2019)	Dammers et al. (2019)	Khan et al. (2020)	Evangeliou et al. (2021)	Xie et al. (2024)
Comments	Calculated using dry deposition rates Central Pacific Ocean	From a low resolution model	Scottish moorland site	Simulations over Europe	Clean remote ocean	Dust/Biomass plumes over ocean	Textbook calculation	Average global model	Fire plume	In a wildfire smoke plume	Conservative average used for satellite-derived fluxes	For large point sources of $NH_3$	Global model simulation	Calculated, ( $\sim 10$ hours for remote regions and $\sim 16$ hours for the Amazonian region	Urban areas
$\mathrm{NH_3}$ lifetime	10, 19 hours Order of hours	Order of hours	1-2 hours	24 hours	Few hours	Several days	2  to  10  days	15 hours	17-23 hours	48 hours	12 hours	$\sim 3 \text{ hours}$	1.1 days	$\sim 11, 10, $ and 16 hours	4, 9 hours

NH<sub>3</sub> deposition also plays a crucial role in the acidification and eutrophication of ecosystems (Krupa, 2003; Sutton et al., 2008), with multiple impacts on water, air, soil, climate, and biodiversity (Sutton et al., 2013). NH<sub>3</sub> has a short lifetime, on the order of hours to a few days (e.g., Dentener and Crutzen, 1994; Dammers et al., 2019; Nair and Yu, 2020; Evangeliou et al., 2021). Table 1.3 summarizes the different reported lifetimes of this gas. NH<sub>3</sub> lifetime can be extended by phase partitioning (Dentener and Crutzen, 1994) since NH<sub>4</sub><sup>+</sup> salts have lifetimes on the order of 1 to 15 days and can be transported and deposited at considerable distances from emission sources (Behera et al., 2013).

### 1.2.3 Remote Sensing Measurements

Remote sensing involves the collection of information about the interactions between electromagnetic radiation and the Earth's atmosphere or surface. In situ measurements of atmospheric NH<sub>3</sub> can be challenging due to several factors, such as the gas-particulate equilibrium, its wide range of ambient concentrations, and physical properties such as its high variability and the previously mentioned "stickiness" (von Bobrutzki et al., 2010). Using remote sensing techniques to measure NH<sub>3</sub> has the advantage of eliminating physical contact between NH<sub>3</sub> and an instrumental inlet or filter, avoiding the issues related to NH<sub>3</sub> adsorption. The vibrational modes of NH<sub>3</sub> shown in Table 1.1 are active in the infrared spectrum. The unique absorption bands of the NH<sub>3</sub> molecule can be used to identify it using spectroscopic techniques, employing both ground-based and satellite approaches. Measurements of vertical profiles and total columns of atmospheric NH<sub>3</sub> from ground-based Fourier transform infrared (FTIR) solar measurements have also been reported. This technique is explained in Chapter 2, as it is widely used in this thesis work.

Table 3.1 in Chapter 3 summarizes some NH<sub>3</sub> total columns reported from ground-based FTIR stations around the world. Ground-based FTIR measurements can be used to validate satellite observations (Dammers et al., 2016, 2017). Currently, there are several infrared spectrometers onboard satellite platforms that have reported top-down measurements of NH<sub>3</sub>. For example, the first successful observations of NH<sub>3</sub> from space were reported by Beer et al. (2008) using the Tropospheric Emission Spectrometer (TES) over the Beijing area. Later, Clarisse et al. (2009) reported the first global map using IASI satellite data. In addition, satellite data from IASI and the Cross-track Infrared Sounder (CrIS) have been used to localize global NH<sub>3</sub> hotspots globally (Van Damme et al., 2018; Dammers et al., 2019). More recently Zhou et al. (2024) reported a first global map, but using the Chinese Hyperspectral Infrared Atmospheric Sounder (HIRAS), with results similar to those of IASI (Zhou et al., 2024).

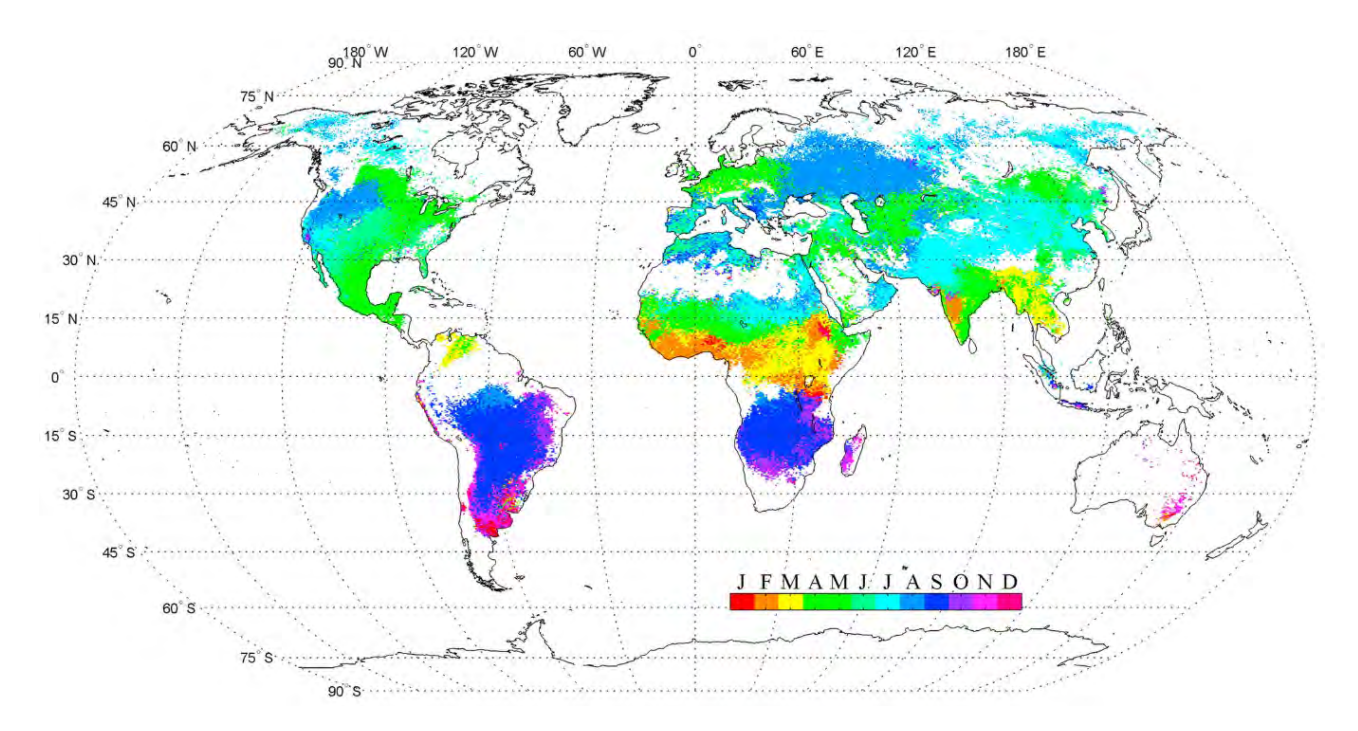


Figure 1.3: Month of maximum  $NH_3$  total columns determined in 0.25° x 0.25° (longitude, latitude) cells from IASI  $NH_3$  measurements between 1 January 2008 and 31 December 2013. Monthly weighted columns associated with a weighted relative error above 35% have been set to zero. Figure taken from Van Damme et al. (2015).

NH<sub>3</sub> emissions and depositions strongly depend on environmental conditions. Temperature and moisture play a crucial role in determining NH<sub>3</sub> concentrations on diurnal to annual scales (Sutton et al., 2013). NH<sub>3</sub> exhibits a strong temporal and spatial variability that ranges over three orders of magnitude near the surface (Shephard et al., 2011). Most studies of NH<sub>3</sub> variability have used satellite or in situ measurements. Van Damme et al. (2015) showed the worldwide spatiotemporal variability of atmospheric NH<sub>3</sub> using IASI's morning and evening measurements. They presented the global seasonal and monthly variability between 2008 and 2013, highlighting different variabilities across regions. Figure 1.3 shows the global distribution of the months of maximum  $NH_3$  column derived from Van Damme et al. (2015). The highest concentrations in Europe were during spring and summer, with columns around  $1.5 \times 10^{16}$  molec. cm<sup>-2</sup>; in Asia, the maximum is in July and the minimum in December with remarkable differences between the magnitude of the maximum columns in southwestern Asia  $(4 \times 10^{16} \text{ molec. cm}^{-2})$  and southeastern China  $(2 \times 10^{16} \text{ molec.})$  ${\rm cm}^{-2}$ ). In the northern central Africa region, the largest columns (1.5 – 2×10<sup>16</sup>  $\mathrm{molec.}$   $\mathrm{cm^{-2}})$  were in February; in South America, columns were enhanced from June to November, with a persistent peak in September. The central U.S. results resembled the European results, possibly due to similarities in agricultural practices. The highest monthly NH<sub>3</sub> total columns for Central America were during April and March, and for South America, during September and October, during the spring of the Southern Hemisphere.

In terms of diurnal variability, NH<sub>3</sub> is also influenced by meteorological factors, but local sources play a significant role, for example, road traffic in urban areas (Kutzner et al., 2021; Gu et al., 2022; Viatte et al., 2023). Figure 1.4 shows the diurnal variability of NH<sub>3</sub> and NO<sub>2</sub> in Paris, as in this city, NO<sub>2</sub> is considered a proxy for road traffic emissions. The variability of NH<sub>3</sub> and NO<sub>2</sub> surface measurements is influenced by the planetary boundary layer height (PBL).

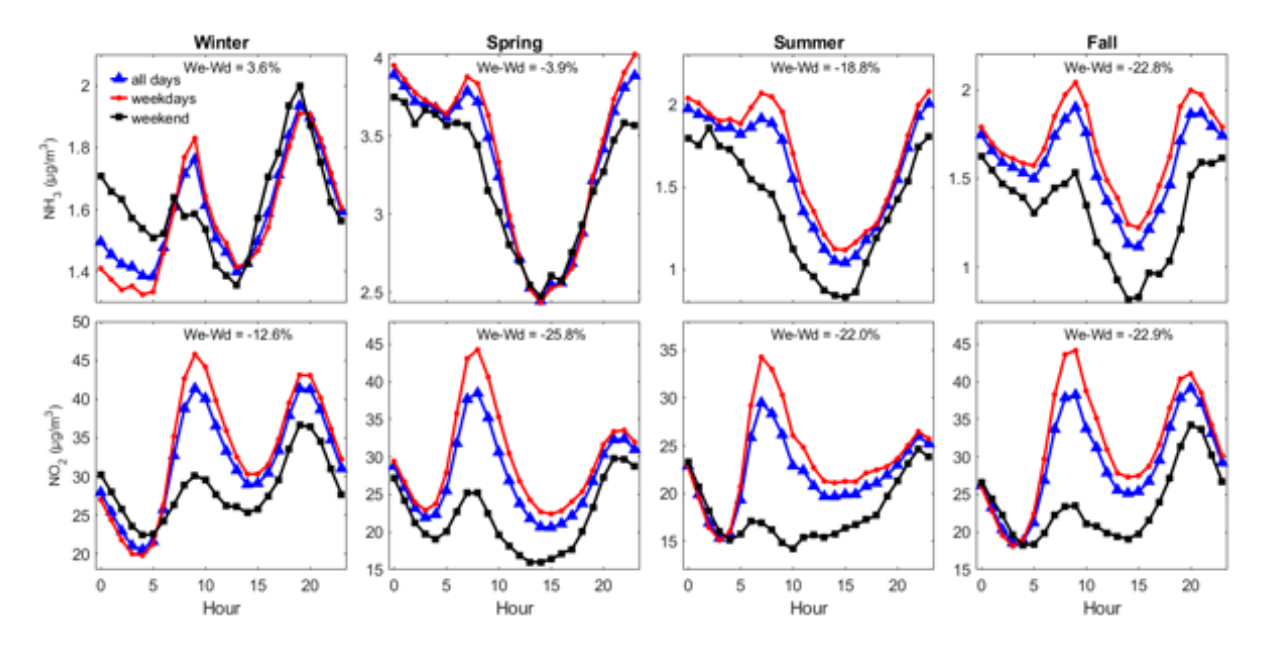


Figure 1.4: Diurnal variability in  $NH_3$  (upper panels) and  $NO_2$  (lower panels) from 2.5 years (between 2020 and 2022) of surface measurements over the city of Paris. The diurnal variability is averaged by season, and the hours are in local time. Blue lines represent all days, red lines represent weekdays, and black lines represent weekends. Figure taken from Viatte et al. (2023).

# 1.2.4 Modeling

Global Chemical Transport Models (CTMs) complement measurements of trace gases in the atmosphere, in addition to contributing to filling in gaps where measurements are scarce or unavailable. CTMs can be used to study the chemistry and transport of different species, analyze the impact of emissions, and improve the understanding of the processes controlling the atmospheric abundance of several species. Models require a number of parameters and inputs in order to simulate the desired atmospheric process; these parameters will impact the model's performance. In terms of modeling NH<sub>3</sub>, it is important to consider its emissions, deposition, and partitioning between gas-phase and particulate phase (Nair and Yu, 2020). The first simulation of NH<sub>3</sub> was made by Dentener and Crutzen (1994) using a 3-D model to derive the a global inventory of NH<sub>3</sub> emissions with a spatial resolution of  $10^{\circ} \times 10^{\circ}$ . Currently, several global and regional models have been used to study atmospheric NH<sub>3</sub>, with an

important increase in the model spatial resolution. For example, Khan et al. (2020) presented global and regional model simulations of NH<sub>3</sub> with a resolution as high as 15 km. A review of studies involving models of NH<sub>3</sub> is described by Nair and Yu (2020). More recent studies have used models to quantify NH<sub>3</sub> trends (e.g., Fortems-Cheiney et al., 2022). However, it is essential to compare the simulations with observations of atmospheric composition to assess the accuracy of the simulations and quantify the model's errors (Brasseur and Jacob, 2017).

### 1.3 Thesis Overview

## 1.3.1 Significance

This thesis provides information about the variability and trends of atmospheric NH<sub>3</sub> in urban and remote regions worldwide, including Mexico City and the Arctic. It uses a combination of NH<sub>3</sub> datasets, including ground-based measurements, satellite observations, atmospheric chemical transport models, and reanalysis products. The results of this work underscore the importance of NH<sub>3</sub> in the atmosphere and provide policymakers with information relevant to updating regulations and improving air quality, particularly in large cities.

## 1.3.2 Scientific Objectives

The primary scientific objectives of this thesis are as follows:

- 1. To investigate the spatial and temporal variability of  $\mathrm{NH}_3$  over Mexico City by using satellite data and ground-based measurements from remote and urban sites.
- 2. To quantify the variability and long-term trends of atmospheric NH<sub>3</sub> using measurements and model simulations at globally distributed sites.

3. To investigate simultaneous enhancements of NH<sub>3</sub> and PM<sub>2.5</sub> in Mexico City during an extreme pollution event, and to assess the ability of models to characterize this event.

#### 1.3.3 Outline

This chapter presents an overview of the current understanding of atmospheric NH<sub>3</sub> and the motivation and contributions of this work. The remaining chapters of this thesis are outlined as follows:

Chapter 2 provides an overview of atmospheric Fourier transform spectroscopy, retrieval theory in the context of trace gas retrievals, satellite observations, and simulations of NH<sub>3</sub> from a chemical transport model and a reanalysis product.

Chapter 3 presents the results of the inter-comparison of IASI satellite data with NH<sub>3</sub> total columns from two ground-based FTIR instruments located near Mexico City at remote and urban sites. This study provides insights into the NH<sub>3</sub> concentrations in two different environments as well as the temporal and spatial variabilities and influence of local sources.

Chapter 4 investigates the seasonal variability and long-term trends of NH<sub>3</sub> at 22 FTIR sites, most of them part of the Network for the Detection of Atmospheric Composition Change (NDACC). The seasonal and diurnal variabilities are also investigated using a long simulation of the GEOS-Chem High Performance (GCHP) model covering the period 2003–2021, and from the Tropospheric Chemical Reanalysis Product (TCR-2) between 2005-2018, providing an additional point of comparison with observations and allowing for an evaluation of the NH<sub>3</sub> simulations.

Chapter 5 describes a case study of simultaneous enhancements of NH<sub>3</sub> and

PM<sub>2.5</sub> during the May 2019 pollution events over Mexico City. This study utilizes NH<sub>3</sub> total columns from two models, the high-resolution configuration of GCHP and the regional model WRF-Chem, over this area, to explore the models' performance under these circumstances.

**Chapter 6** presents the conclusions of this thesis and provides suggestions for future work.

#### 1.3.4 Contributions

The work in this thesis was led by Beatriz Herrera, with contributions by others as described below.

The work in Chapter 3 was carried out by Beatriz Herrera, with input from Alejandro Bezanilla, Thomas Blumenstock, Enrico Dammers, Frank Hase, Lieven Clarisse, Adolfo Magaldi, Claudia Rivera, Wolfgang Stremme, Camille Viatte, Martin Van Damme, Michel Grutter, and Kimberly Strong. I designed the study in collaboration with Michel Grutter and Kimberly Strong, performed the main analysis and software development, implemented the PROFFIT retrieval algorithms at both sites with the support of Enrico Dammers and Wolfgang Stremme, and wrote up the results. All co-authors discussed the results and provided feedback on the study.

The work in Chapter 4 was carried out by Beatriz Herrera, with input from Enrico Dammers, Martine De Mazière, Omaira García, Michel Grutter, James W. Hannigan, Dylan Jones, Nicholas Jones, Emmanuel Mahieu, Maria Makarova, Kazuyuki Miyazaki, Isamu Morino, Isao Murata, Ivan Ortega, Mathias Palm, Anatoly Poberovskii, Takashi Sekiya, Hannah Still, Dan Smale, Wolfgang Stremme, Ralph Sussmann, Geoffrey Toon, Corinne Vigouroux, Tyler

Wizenberg, Debra Wunch, and Kimberly Strong. I designed the study with Kimberly Strong and Dylan Jones. I performed the analysis, software development, SFIT4 retrievals of the complete time series for the Mexico City, Altzomoni, Toronto, and Eureka sites, and writing up of the results. During the course of this PhD, I was also involved in the operation of the FTIR instruments located at the Polar Environment Atmospheric Research Laboratory (PEARL) in Eureka and the University of Toronto Atmospheric Observatory (TAO). I collaborated with Tyler Wizenberg to run the GCHP simulation. I analyzed the TCR-2 data that was provided by Kazuyuki Miyazaki. All co-authors discussed the results and provided feedback on the study.

The work in Chapter 5 was carried out by Beatriz Herrera, with input from Blanca Rios, Wolfgang Stremme, Dylan Jones and Kimberly Strong. All the authors designed the study. I performed the stretched-grid GEOS-Chem High-Performance model simulations, data analysis, software development and presentation of the results. Blanca Rios provided the WRF-Chem simulations for Mexico City. Wolfgang Stremme provided the CO and HCHO FTIR datasets for Mexico City for May 2019. All co-authors discussed the results and provided feedback on the study.

# Chapter 2

# Methods

## 2.1 Measurements of NH<sub>3</sub>

Spectroscopy is the study of the interaction of electromagnetic radiation with matter. Atmospheric remote sensing involves the use of spectroscopy to obtain information about atmospheric properties such as trace gas abundances. As mentioned in Chapter 1, in situ measurements of NH<sub>3</sub> are challenging; for this reason, remote sensing techniques are a good alternative to measure this gas. In this chapter, the focus will be on remote sensing of NH<sub>3</sub> in the infrared region.

# 2.1.1 Vibrational Spectroscopy

As quantum theory dictates, molecules interact only with light having the right amount of energy to move the molecule from one discrete energy level to another. This process is called a transition. The type of transition will depend on the energy in the photons. Figure 2.1 shows the different regions of the electromagnetic spectrum and their corresponding energy. The transitions can be rotational, vibrational, or electronic, and due to the Born-Oppenheimer approximation (Harris and

Bertolucci, 1978), can be treated separately from the nuclear motions. Thus, the energy in the molecule will be given by:

$$E_{tot} = E_{electronic} + E_{rot} + E_{vib}. (2.1)$$

If the light has infrared frequencies, it will usually promote a transition from one vibrational energy level to another. However, rotational transitions can occur at the same time as vibrational transitions. The spectroscopic study of these transitions is known as vibrational-rotational spectroscopy.

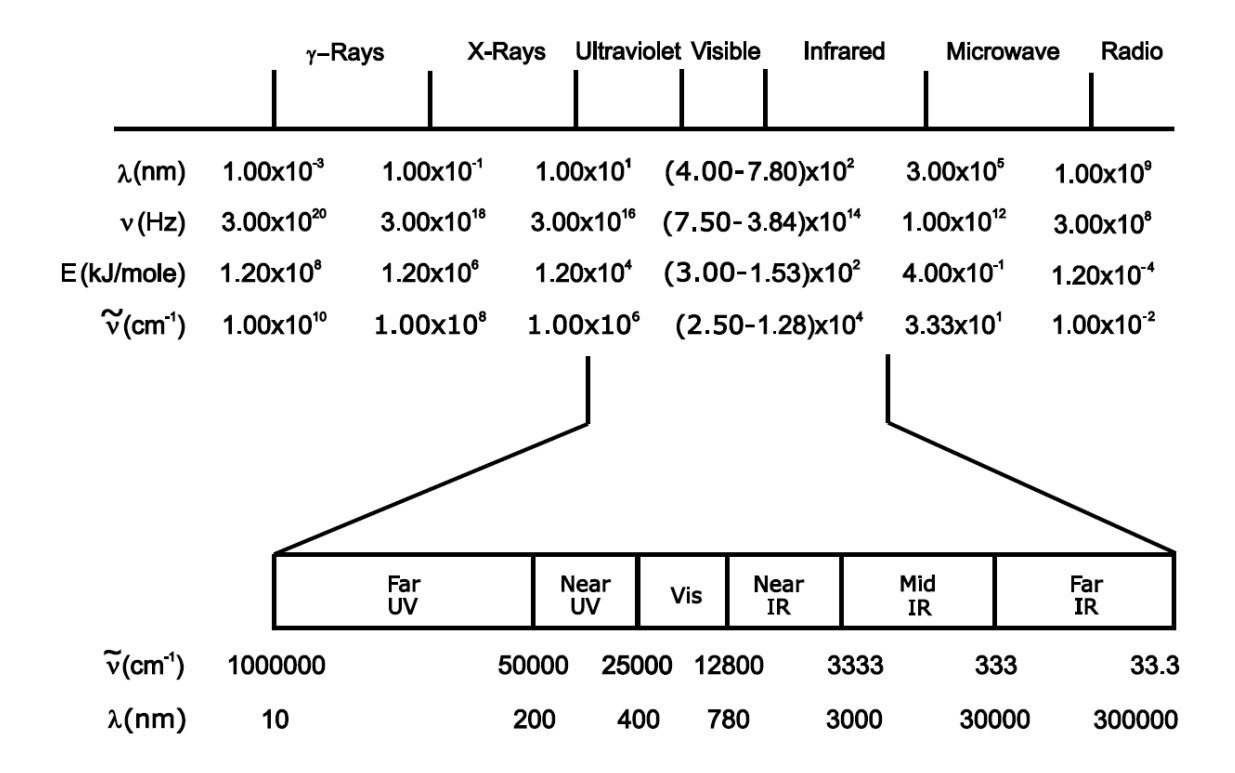


Figure 2.1: The electromagnetic spectrum. Taken from Bernath (2025).

The wavenumber unit  $\tilde{\nu}$ , given by Equation 2.2, is expressed in cm<sup>-1</sup>, and is usually used in this type of spectroscopy (Wartewig, 2003):

$$\tilde{\nu} = \frac{1}{\lambda} = \frac{\nu}{c} \tag{2.2}$$

where  $\lambda$  is the wavelength, c is the speed of light in vacuum, and  $\nu$  is the frequency. In addition, wavenumbers are linear or proportional to energy, as shown in Equation 2.3:

$$E_{photon} = hc\tilde{\nu} \tag{2.3}$$

where h is Planck's constant.

Assuming that a molecule behaves as a harmonic oscillator, its vibrational energy is given by Equation 2.4

$$E_{vib} = h\nu_0(v + \frac{1}{2}) \tag{2.4}$$

where  $\nu_0$  is the vibrational frequency of a particular mode and v is the vibrational quantum number (v = 0, 1, 2, 3, ...). The ground state is given by v = 0. However, in reality, vibrations in polyatomic molecules are better described as a system of coupled anharmonic oscillators (Wartewig, 2003). In addition, as molecules vibrate and rotate at the same time, the transitions between rotational energy levels are characterized by the rotational quantum number J, and given by the equation:

$$E_{rot} = E_J = \frac{h}{8\pi^2 cI} J(J+1) = BJ(J+1)$$
 (2.5)

where B is the rotational constant, I is the moment of inertia, and c is the speed of light.

In polyatomic molecules with N atoms, there are 3N degrees of freedom: 3 represent translational motion (x,y,z), 3 the rotational motion, and the last 3N-6 represent the number of vibrational modes in a nonlinear molecule (Griffiths and De Haseth, 2007). Each vibrational mode can be described in terms of normal coordinates  $Q_i$ , which have the same symmetry as the normal modes of vibration of the molecule. Molecular symmetry applied in the form of group theory is an important aspect of spectroscopy. For vibrational spectroscopy, symmetry can be used to understand

permitted and forbidden transitions, the description of vibrational modes, and the classification of individual rovibronic levels (Harris and Bertolucci, 1978; Bernath, 2025). However, only the vibrations that induce a change in the dipole moment vector  $(\mu)$  of the molecule  $(\frac{\partial \mu}{\partial Q_i} \neq 0)$  will be infrared active, and the intensity of the infrared band will be proportional to the square of the change in  $\mu$  (Wartewig, 2003; Griffiths and De Haseth, 2007). Usually, for many molecules, the fundamental transition, the transition between v=0 to the first excited state v=1, corresponds to energy between 400 and  $4000 \text{ cm}^{-1}$  (Wartewig, 2003; Griffiths and De Haseth, 2007). The vibrational transitions are accompanied by rotational transitions, that form two distinctive branches, P branch for lower energy  $(\Delta J = -1)$  and R branch for higher energy  $(\Delta J = +1)$ .  $\Delta J = 0$  is in general not allowed, but it would form a Q branch if there is additional angular momentum (Bernath, 2025). Thus, the selection rules for vibration-rotation transitions are  $\Delta v \pm 1$ ,  $\mu \neq 0$ , and  $\Delta J \pm 1$ . However, as a consequence of anharmonicity, transitions from v = 0 to v = 2, 3, 4 are also allowed and are called overtone transitions. Moreover, molecules with the presence of certain symmetry elements can have degenerate vibrational modes.

From the spectroscopic point of view, the NH<sub>3</sub> molecule is interesting because it can rapidly invert its geometry. The three H atoms can flip through the plane containing the N atom, perpendicular to the  $C_3$  symmetry axis, a threefold rotation axis, shown in Figure 2.2, basically a tunneling of the N atom through a plane formed by the H atoms. This "umbrella" motion is responsible for the splitting of rotational transitions of a certain symmetry, producing two energy states in the NH<sub>3</sub> molecule interconnected by the tunneling barrier with slightly different energy levels (Hauglustaine et al., 2014; Nguyen et al., 2021; Bernath, 2025). Thus, for NH<sub>3</sub> there are 3(4) - 6 = 6 vibrational modes, but two of them ( $\nu_3$  and  $\nu_4$ ) are doubly degenerate as presented in Table 1.1 of Chapter 1 and in Figure 2.3.

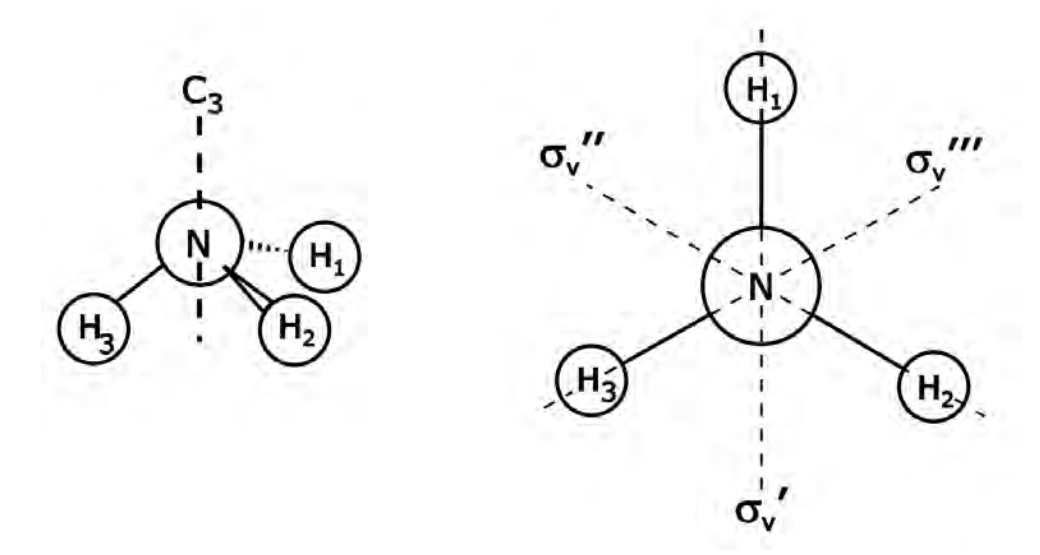


Figure 2.2: The elements of symmetry for the  $NH_3$  molecule. Figure taken from Bernath (2025).

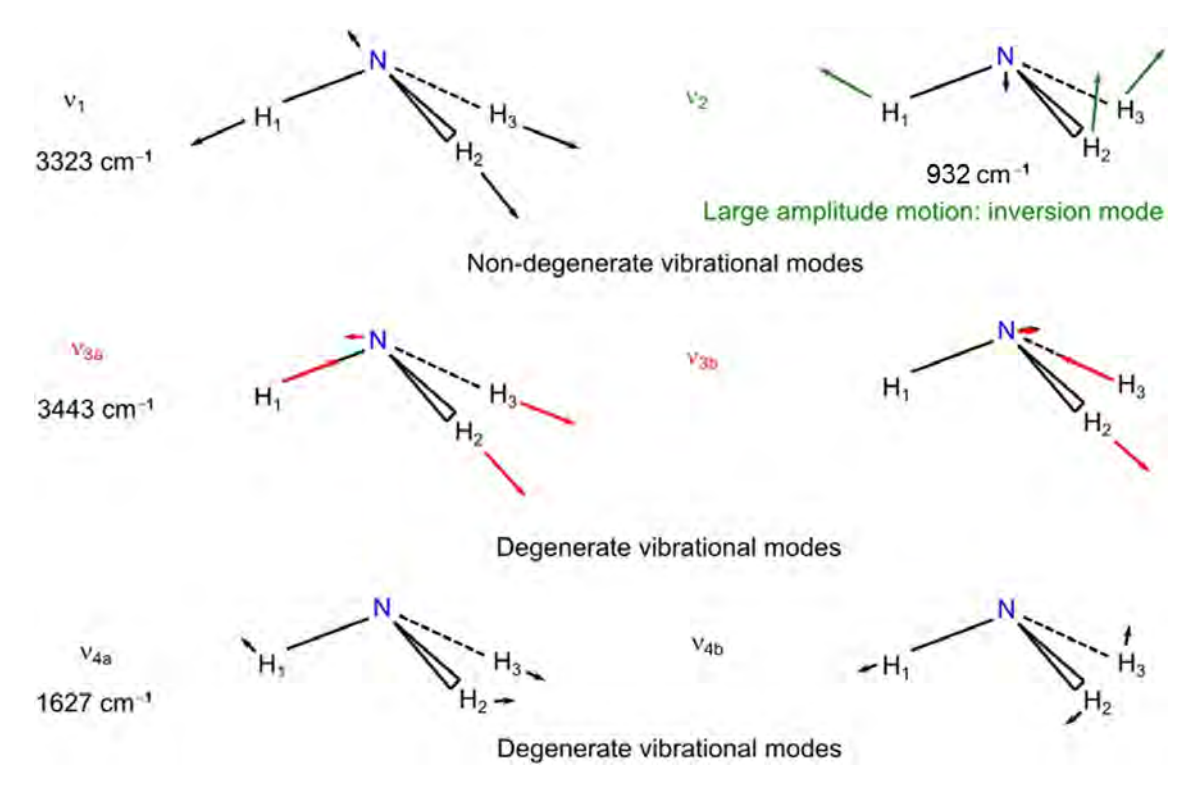


Figure 2.3: The vibrational modes of NH<sub>3</sub>. For the degenerate modes, two orthogonal components are depicted. Figure taken from Nguyen et al. (2021).

### 2.1.2 Atmospheric Spectroscopy

In the atmosphere, molecules of trace gases can be detected by their spectral signatures in different regions of the electromagnetic spectrum, including the infrared. Earth's atmospheric spectra show characteristic absorption and emission features that can be used for remote sensing. However, the presence of strong absorption lines of  $H_2O$ ,  $CO_2$ , and  $O_3$  can interfere with spectra of other trace gases (Bernath, 2025). The Sunlight that passes through the atmosphere can be absorbed by the gases. This absorption can be described using the Beer-Lambert Law:

$$dI_{\tilde{\nu}} = -I_{\tilde{\nu}}\sigma_{\tilde{\nu}}\rho ds \tag{2.6}$$

where I is the transmitted intensity,  $\sigma_{\tilde{\nu}}$  is the mass extinction cross-section for radiation of wavenumber  $\tilde{\nu}$  (in units of area per molecule),  $\rho$  is the density of the material, and ds is the thickness traversed (Liou, 2002).

The line strength S is related to the absorption coefficient  $k_{\tilde{\nu}}$  via the following equation (Liou, 2002):

$$S = \int_{-\infty}^{\infty} k_{\tilde{\nu}} d\tilde{\nu} \tag{2.7}$$

 $k_{\tilde{\nu}}$  (in cm atm<sup>-1</sup>) is related  $\sigma_{\tilde{\nu}}$  (in  $cm^{-2}$ ) through the Loschmidt's number  $N_o$  (=  $2.687 \times 10^{19}$  particles  $cm^{-3}$  at standard temperature of 273 K and standard pressure od 1013 mb) where  $k_{\tilde{\nu}} = \sigma_{\tilde{\nu}} \cdot N_o$ 

The broadening of spectral lines is caused by three main processes: natural broadening due to uncertainties in energy levels; pressure (or Lorentz) broadening due to reciprocal collisions between molecules; and Doppler effect broadening due to the differences in thermal velocities of atoms and molecules. Pressure broadening dominates in the lower atmosphere below 20 km, while between 20 and 50 km, there is a combi-

nation of Doppler and pressure broadening, with Doppler broadening dominating in the upper atmosphere. The natural broadening effect is negligible compared to the Doppler or pressure broadening (Liou, 2002). The Voigt line shape function results from a convolution of the Lorentz and the Doppler line shape, and it is useful when both broadening mechanisms are relevant.

## 2.1.3 Fourier Transform Technique

The heart of an FTIR instrument is the interferometer, such as the Michelson interferometer shown in Figure 2.4. In the Michelson interferometer, a beam of collimated light is divided by a beamsplitter, which reflects part of the beam to a fixed mirror and transmits the rest to a movable mirror. Both mirrors are mutually perpendicular; however, when the beams return to the beamsplitter and are recombined, an interference pattern is created due to the added optical path difference (OPD) from the movable mirror. The OPD, or retardation, is calculated as shown by Equation 2.8, where OM is the distance between the beamsplitter and the movable mirror and OF is the distance between the beamsplitter and the fixed mirror:

$$\delta = 2(OM - OF). \tag{2.8}$$

The recombined beam, modulated by the motion of the movable mirror, reaches the detector, registering the intensity of the combined beams as a function of OPD  $\delta$   $(I(\delta))$ , which is known as an interferogram. For a polychromatic source (such as the Sun), the interferogram is given by Equation 2.9. If the radiation source emits more than one wavelength, the measured interferogram is the resultant of the interferograms of all wavelengths (Griffiths and De Haseth, 2007) and the interferogram is given by

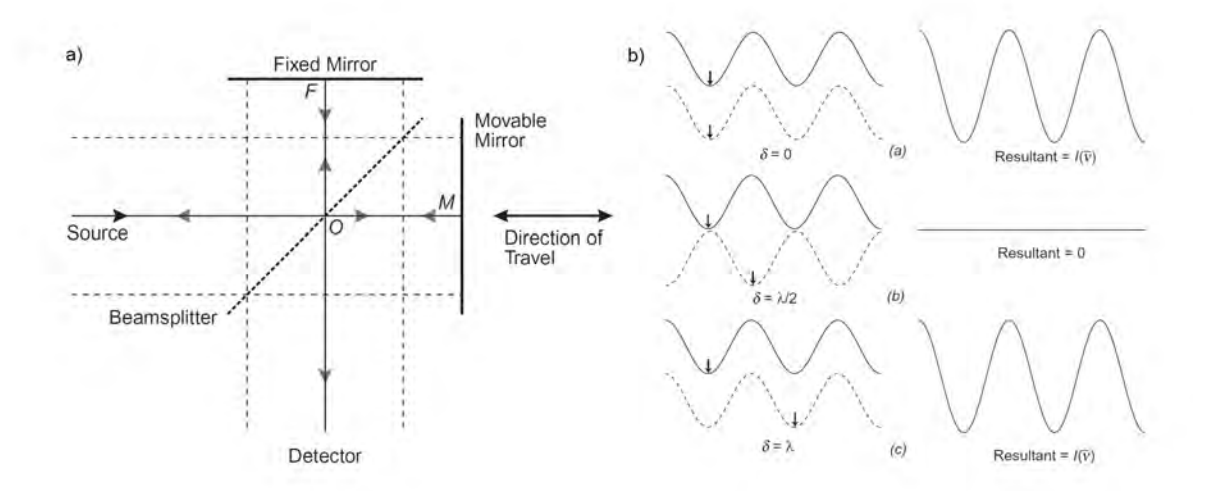


Figure 2.4: Schematic diagram of the a) Michelson interferometer. b) Phase of the electromagnetic waves from the fixed (solid line) and movable (dashed line) mirrors at different values of  $\delta$ . Note that constructive interference occurs for  $\delta = 0$ ,  $\delta = \lambda$ , and all other  $\delta$  corresponding to integral numbers of wavelengths. Modified from Griffiths and De Haseth (2007).

the integral (Wartewig, 2003):

$$I(\delta) = \int_{0}^{\infty} B(\tilde{\nu}) \cos(2\pi\delta\tilde{\nu}) d\tilde{\nu}$$
 (2.9)

where B is the spectral intensity at wavenumber  $\tilde{\nu}$ . The interference can be constructive or destructive, as shown in Figure 2.4. When  $\delta = 0$ , or at Zero Path Difference (ZPD), the two beams are perfectly in phase, producing the characteristic "centre burst" in the interferogram (Wartewig, 2003). The amplitude of the interferogram will depend on the source intensity, the beamsplitter efficiency, the detector response, and the amplifier characteristics (Griffiths and De Haseth, 2007). Then the spectrum B is calculated from the interferogram by applying a Fourier transform, described by (Wartewig, 2003):

$$B(\tilde{\nu}) = \int_{0}^{\infty} I(\delta) \cos(2\pi\delta\tilde{\nu}) d\delta.$$
 (2.10)

In an ideal interferometer,  $\delta$  varies between 0 and infinity; however, in practice, the optical path is finite, therefore, there will exist a  $\delta_{max}$ . To account for this limitation, the interferogram can be multiplied by a truncation function  $D(\delta)$ , known as apodization. The boxcar  $D(\delta)$  function describes the apodization that results from  $\delta_{max}$  and has the following form (Griffiths and De Haseth, 2007):

$$D(\delta) = \begin{cases} 0 & \text{if } \delta > \delta_{max} \\ 1 & \text{if } \delta \leq \delta_{max} \end{cases}$$
 (2.11)

Thus, as the Fourier transform of the product of two functions is the convolution of the Fourier transform of each function, the spectrum is given by the convolution of  $I(\delta)$  with  $D(\delta)$ . The Fourier transform of  $D(\delta)$ ,  $f(\tilde{\nu})$  is given by (Griffiths and De Haseth, 2007):

$$f(\tilde{\nu}) = 2\delta sinc(2\pi\tilde{\nu}\delta). \tag{2.12}$$

The spectral resolution of the spectrometer can be defined based on several criteria, but it will be affected by the selected apodization, as different apodization functions can be applied to reduce the side lobes of the sinc function, but also reduce the resolution. For the Bruker Fourier transform spectrometer (FTS) instruments, the spectral resolution is specified as  $0.9/\delta_{max}$ .

If the source of the interferogram is the Sun, a solar absorption spectrum can be measured and analyzed to derive the concentration of these trace gases in the atmosphere using retrieval methods as described in Section 2.1.5.

## 2.1.4 Fourier Transform Spectrometers

The Network for the Detection of Atmospheric Composition Change is an international global network that has performed high-quality ground-based remote sensing measurements of atmospheric composition since 1991, with the goal of acquiring longterm databases for detecting changes and trends in the chemical and physical state of the atmosphere (De Mazière et al., 2018). NDACC has several working groups categorized depending on the ground-based technique; for this work, the focus will be on the Infrared Working Group (IRWG) (https://www2.acom.ucar.edu/irwg) that includes more than twenty high-resolution Fourier-transform infrared spectrometers distributed from pole to pole. Most of the NH<sub>3</sub> datasets used in this work, especially in Chapter 4, are from FTIR instruments affiliated with NDACC, except for Garmisch, Mexico City, and Porto Velho. NH<sub>3</sub> is not one of the ten baseline IRWG species; however, it can be measured using the NDACC filter #6 to narrow the incoming spectral radiation in the wavenumber range of 700-1350 cm<sup>-1</sup> and increase the signal-to-noise ratio (SNR).

Figure 2.5 shows the internal components of the Bruker IFS 125HR instrument, which is the standard instrument across most NDACC-IRWG sites. A description of the experimental setup at Eureka will be used as a reference for the FTIRs used in NDACC. The Eureka 125HR FTIR at the Polar Environment Atmospheric Research Laboratory (PEARL) measures high-resolution solar absorption spectra under sunny and clear-sky conditions. Depending on the beamsplitter and detector used, it is possible to perform measurements in the near infrared (NIR) and in the mid-infrared (MIR) using the same instrument, however, this work focuses on the MIR. To acquire a solar absorption spectrum, a beam of Sunlight needs to reach the spectrometer, which is possible using a Sun-tracker capable of directing Sunlight into the instrument throughout the day. This tracker is usually housed in a dome or other enclosure to protect it from environmental conditions. There are commercially available Suntrackers and domes. Bruker sells a commercially available tracker, but Eureka uses a custom-built Community Solar Tracker (CST) and Robodome (Franklin, 2015).

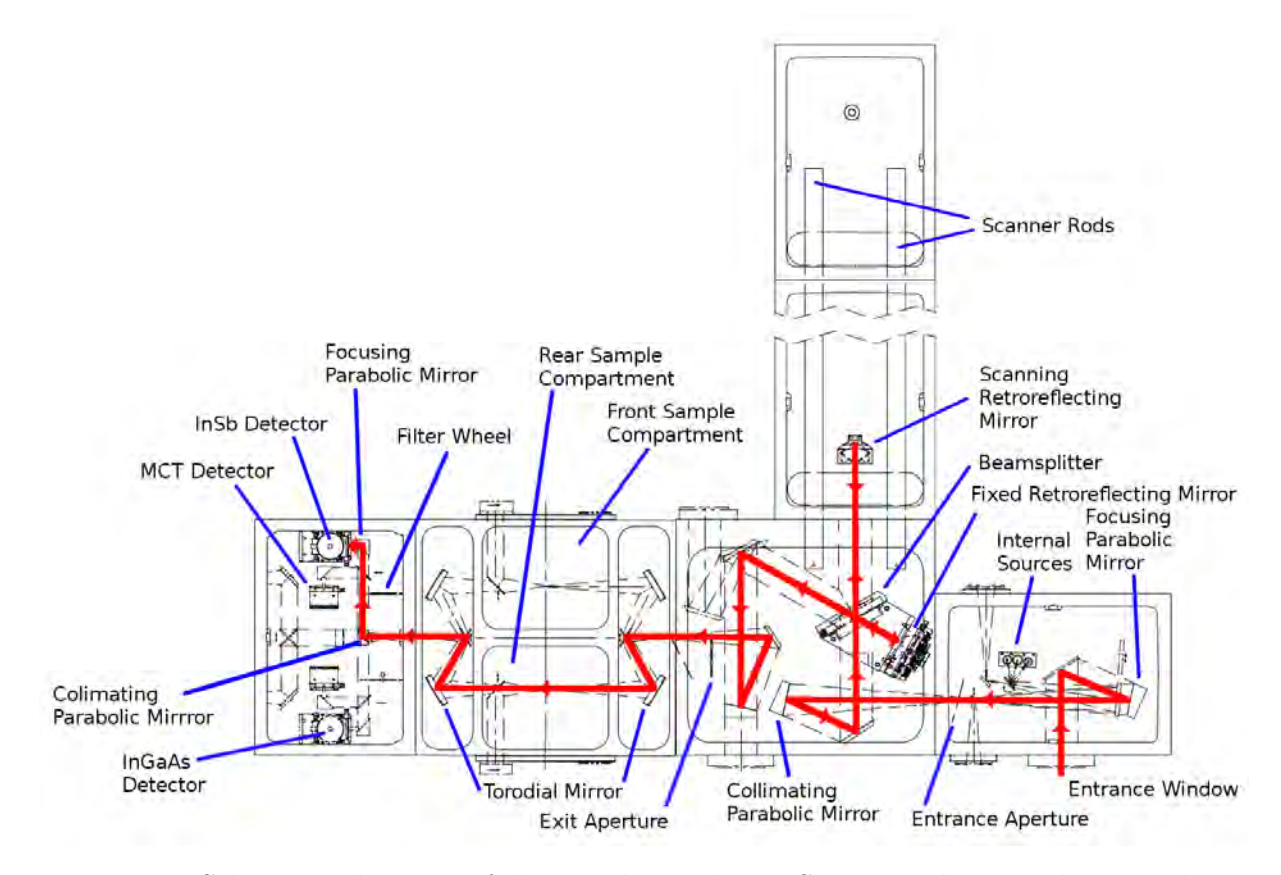


Figure 2.5: Schematic diagram of the Eureka Bruker IFS 125HR showing the optical path of the solar beam (red arrows), and the internal components, which are labelled and indicated by the blue lines. Figure reproduced from Lutsch (2019).

The general operation of the instrument for a filter #6 measurement is described as follows: once the solar beam reaches the entrance aperture in the source compartment of the 125HR, it passes into the interferometer compartment. The beam is collimated with a parabolic collimating mirror and then is directed to the potassium bromide (KBr) beamsplitter that divides the beam into the fixed and movable (scanning retroreflecting mirror) mirrors, with the reflected beams recombined as described in Section 2.1.3. The maximum OPD is 372 cm, corresponding to a maximum resolution of 0.0024 cm<sup>-1</sup>, however, for measurements using filter #6, the maximum OPD is set to 257 cm with a corresponding resolution of 0.0035 cm<sup>-1</sup> with boxcar apodization. The recombined beam is directed toward the exit aperture using a series of flat and parabolic mirrors. For this instrument, to control the amount of light

entering the instrument, the entrance and exit apertures are variable and controlled by an aperture wheel. For filter #6, the recommended aperture is 1.5 mm. The beam passes through the rear sample compartment because the front sample compartment contains a permanent HCl cell used for the NIR measurements; the beam path shown in Figure 2.5 accurately represents the path for MIR measurements except for the difference in the sample compartment. Finally, the beam passes through the rotating filter wheel, in this case filter #6, before reaching the photoconductive mercury-cadmium-telluride (MCT) detector, which is sensitive from 600 to 6000 cm<sup>-1</sup> and needs to be cooled with liquid nitrogen before starting the measurements. For each filter #6 measurement, two scans are co-added.

For efficient routine measurements, macro codes, which are commands written in the OPUS software, are used to run measurements semi-automatically; they usually cycle through the different NDACC filters until the Sun sets or clouds come into the field-of-view (FOV). For example, on a typical measurement sunny day with clear sky conditions, the FTIR instrument cycles through the different NDACC filters, usually seven narrowband filters, making a measurement with each before repeating the cycle, each measurement takes about 15 minutes. Usually 100-150 measurement days per year are common among the NDACC FTIR instruments (Yamanouchi, 2021).

Figure 2.6 shows the internal components of the Bruker Vertex 80 instrument, which is used in this thesis at the Mexico City FTIR site, and the optical beam path. This FTIR has fewer components than the Bruker 125HR; however, the principle is the same. For solar MIR measurements, the solar beam enters through IN1. The main difference compared to the Bruker 125HR is the resolution. The maximum OPD for the Vertex 80 is 15 cm, corresponding to a resolution of 0.06 cm<sup>-1</sup>.

For the Los Angeles site, the spectra were recorded using the high-resolution FTIR spectrometer MkIV (Toon, 1991; Sen et al., 1996; Toon et al., 2018). Information

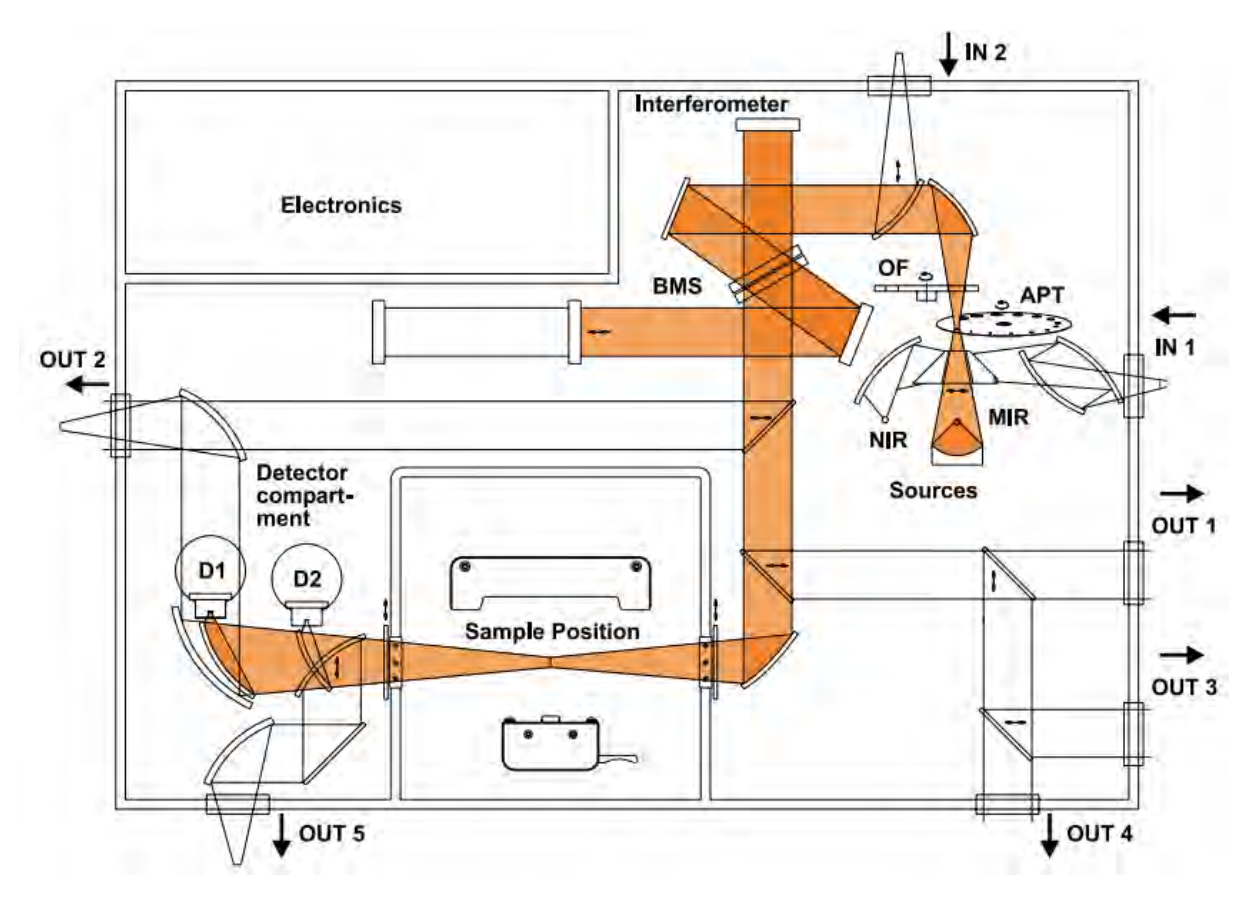


Figure 2.6: Schematic diagram of the Mexico City Bruker Vertex 80 showing the optical beam path in orange, and the internal components which are labelled and indicated. Figure reproduced from the user manual (Bruker Optics, 2006).

about this instrument can be found at https://www-air.larc.nasa.gov/pub/NDACC/PUBLIC/meta/ftir/Multi\_ftir\_gt\_2020.pdf and https://mark4sun.jpl.nasa.gov/ground.html.

## 2.1.5 NH<sub>3</sub> FTIR Retrieval

#### Retrieval Theory

The measured solar spectra are analyzed to obtain the concentration of trace gases in the atmosphere using a retrieval algorithm. For the NH<sub>3</sub> retrievals, the Optimal Estimation Method (OEM) is used. This method is described in detail in Rodgers (2000). In addition, a description of inverse modeling applied to atmospheric chem-

CHAPTER 2. METHODS

istry can be found in Brasseur and Jacob (2017). A summary of the key concepts is given below.

Inverse modeling provides a formal approach to quantify variables of interest in a system by using measurements of the system itself. This is done by statistically optimizing the variables using all the available information. The variables of interest to optimize are called state variables and are assembled in a state vector  $\mathbf{x}$ . The observations are assembled in a measurement vector  $\mathbf{y}$ . The relationship between them is given by:

$$\mathbf{y} = \mathbf{F}(\mathbf{x}, \mathbf{b}) + \boldsymbol{\varepsilon} \tag{2.13}$$

where  $\mathbf{F}$  is a model of the physical system called the forward model,  $\mathbf{b}$  is a parameter vector that includes all other model variables related to the measurement of interest that are not intended to be optimized, and  $\varepsilon$  is the observational error vector that includes contributions from errors in the measurements, forward model, and model parameters. Thus, the forward model  $\mathbf{F}$  predicts the effect  $\mathbf{y}$  as a function of cause  $\mathbf{x}$ , while the inverse model  $\mathbf{I}$  quantifies the cause  $\mathbf{x}$  from measurements of the effect  $\mathbf{y}$ . The solution to the inverse problem,  $\hat{\mathbf{x}}$ , can be called the optimal estimate, the posterior estimate, or the retrieval, and is the best estimate of  $\mathbf{x}$  with a statistical error  $\varepsilon \neq 0$ .

The constraints used to reduce the error on  $\mathbf{x}$  are called prior information, such as the prior estimate  $\mathbf{x}_a$ , which represents our best estimate of  $\mathbf{x}$  before the observations, and has an associated error,  $\boldsymbol{\varepsilon}_a$ . Likewise, the best estimate for  $\mathbf{b}$  is denoted by  $\hat{\mathbf{b}}$ , which includes the vector  $\mathbf{c}$  containing supplementary parameters that aren't in the forward model. In the context of FTIR remote sensing of the atmosphere, the state vector is the vertical concentration profile (e.g., the volume mixing ratio (VMR)), the measurements are the infrared solar spectra, the forward model is a radiative transfer

model, and the prior estimate is the a priori profile. Then  $\hat{\mathbf{x}}$  is given by:

$$\hat{\mathbf{x}} = \mathbf{I}(\mathbf{y}, \hat{\mathbf{b}}, \mathbf{c}) = \mathbf{I}(\mathbf{F}(\mathbf{x}, \mathbf{b}) + \boldsymbol{\varepsilon}, \hat{\mathbf{b}}, \mathbf{c}).$$
 (2.14)

By linearizing Equation 2.14 in terms of  $\mathbf{x}_a$  we obtain:

$$\hat{\mathbf{x}} = \mathbf{I}[\mathbf{F}(\mathbf{x_a}, \hat{\mathbf{b}}), \hat{\mathbf{b}}, \mathbf{c}] + \frac{\partial \mathbf{I}}{\partial \mathbf{y}} \frac{\partial \mathbf{F}}{\partial \mathbf{x}} (\mathbf{x} - \mathbf{x_a}) + \frac{\partial \mathbf{I}}{\partial \mathbf{y}} \frac{\partial \mathbf{F}}{\partial \mathbf{b}} (\mathbf{b} - \hat{\mathbf{b}}) + \frac{\partial \mathbf{I}}{\partial \mathbf{y}} \boldsymbol{\varepsilon}$$
(2.15)

where the gain matrix  $\mathbf{G}$ , that represents the sensitivity of the inverse model to the measurement, is given by:

$$\mathbf{G} = \frac{\partial \mathbf{I}}{\partial \mathbf{y}}.\tag{2.16}$$

The weighting function matrix  $\mathbf{K}$ , which is the sensitivity of the forward model to the state vector, is given by:

$$\mathbf{K} = \frac{\partial \mathbf{F}}{\partial \mathbf{x}} \ . \tag{2.17}$$

The averaging kernel  $\mathbf{A}$ , which is the sensitivity of the retrieved state to the true state, is given by:

$$\mathbf{A} = \mathbf{G}\mathbf{K} = \frac{\partial \hat{\mathbf{x}}}{\partial \mathbf{x}}.\tag{2.18}$$

The sensitivity of the retrieval may be defined as the sums of the rows of the averaging kernel and represents the fraction of the retrieved content that comes from the measurement rather than that from the a priori (Vigouroux et al., 2015). The vertical information content of the retrieval is quantified using the Degrees of Freedom Signal (DOFS), defined as the trace of **A**. The DOFS represent the number of independent quantities that can be retrieved from the measurement. A perfect observing system (**A** = identity matrix) will have  $\frac{\partial \hat{\mathbf{x}}_i}{\partial \mathbf{x}_i} = 1$  (Brasseur and Jacob, 2017).

The retrieved profile can be expressed as:

$$\hat{\mathbf{x}} = \mathbf{x_a} + \mathbf{A}(\mathbf{x} - \mathbf{x_a}) + \mathbf{G}\mathbf{K_b}(\mathbf{b} - \hat{\mathbf{b}}) + \mathbf{G}\boldsymbol{\varepsilon}. \tag{2.19}$$

To obtain the best estimate for  $\hat{\mathbf{x}}$  in Equation 2.19, Bayes' Theorem is used to find the maximum a posteriori (MAP) solution. Bayes' Theorem provides a systematic approach to combine prior knowledge with measurements. Basically, the optimal estimation weights the information from  $\mathbf{x}_a$  and the observations by incorporating the cost function and considering the errors statistically. Assuming a linear relationship between  $\mathbf{x}$  and  $\mathbf{y}$  (i.e.,  $\mathbf{y} = \mathbf{K}\mathbf{x}$ ), the solution is presented in the following equation:

$$\hat{\mathbf{x}} = \mathbf{x_a} + \mathbf{S_a} \mathbf{K^T} (\mathbf{K} \mathbf{S_a} \mathbf{K^T} + \mathbf{S_{\varepsilon}})^{-1} \mathbf{K} (\mathbf{x} - \mathbf{x_a})$$
 (2.20)

where  $\mathbf{S_a}$  and  $\mathbf{S_{\varepsilon}}$  are the a priori and measurement error covariance matrices, respectively. The error covariance matrix for a vector is equivalent to the error variance for a scalar, and it has as diagonal elements the error variances of the individual components of  $\mathbf{x}$ . In general, the diagonals of  $\mathbf{S}_a$  are given by:

$$\mathbf{S}_a = \mathbf{I} \cdot \sigma^2, \tag{2.21}$$

where  $\sigma$  is the standard deviation of the target species (in %), which may be derived from the variability in the mean a priori profiles. However, the estimation of  $\mathbf{S_a}$  often relies on simple estimates and expert judgment, as accurate knowledge is generally not available (Brasseur and Jacob, 2017).

From Equation 2.19, if we express  $\mathbf{A} = (\mathbf{S}_{\mathbf{a}}^{-1} + K^T \mathbf{S}_{\varepsilon}^{-1} K)^{-1} K^T \mathbf{S}_{\varepsilon}^{-1} K$ , Equation 2.20 becomes:

$$\hat{\mathbf{x}} = \mathbf{x_a} + \mathbf{A}(\mathbf{x} - \mathbf{x_a}) \tag{2.22}$$

where, for a perfect system, the best estimate of the retrieved state would be equal to the true state and A would be the identity matrix.

#### Retrieval Software

The main retrieval code used in this work was the SFIT4 spectral data analysis code (https://wiki.ucar.edu/spaces/sfit4/pages/217711301/Infrared+Working+Group+Retrieval+Code+SFIT), which is widely used in the NDACC-IRWG community to retrieve trace gases from solar absorption measurements. The SFIT4 algorithm is based on the SFIT2 (Pougatchev et al., 1995) retrieval code and uses the OEM to perform iterations to adjust trace gas profiles to minimize the difference between the measured and the calculated spectrum. The iteration process is repeated until the measured and calculated spectra converge, which means until the difference between subsequent iterations is smaller than a specified tolerance value. SFIT4 will attempt 17 iterations, and if the criterion is not met, then it is said that the retrieval has no convergence. Spectra with a low SNR, or inadequate selection of a priori profile and its corresponding error covariance matrix  $S_a$ , can lead to no convergence. The error covariance matrix  $S_c$  is derived from the SNR values estimated from the spectral data.

The forward model in SFIT4 consists of a line-by-line radiative transfer model (LBLRTM) that assumes a Voigt line shape for the absorbing gases. In SFIT4, the atmosphere is divided into layers from the top of the atmosphere to the surface; the number of layers will depend on the altitude of the measurement site location. Among the parameters required for the forward model to calculate the spectrum are: prior knowledge of the atmosphere's temperature and pressure profiles, spectroscopic parameters of the target gas and interfering species in the selected microwindows, an a priori profile of the target gas and an a priori error covariance matrix  $S_a$ . Parameters from the FTIR instrument, such as FOV, OPD, and ILS, are also required. The SFIT4 core code is

written in Fortran, but it can be run through a Python script called Layer 1.

Similar to SFIT4, PROFFIT (PROFILE FIT) (https://www.imk-asf.kit.edu/english/898.php) is a retrieval code used to analyze solar absorption spectra measured with ground-based FTIR spectrometers. This code is also used by the NDACC-IRWG community. PROFFIT performs iterations to minimize the difference between a calculated and measured spectrum, and can implement different retrieval methods, including OEM. The maximum number of iterations can be modified, and it is usually set to 20, with a convergence criterion that can also be modified; smaller values enforce more iterations. PROFFIT consist of two main algorithms, PROFFWD.INP, which contains the forward model, and PROFFIT9.INP, which is the inversion model. The forward model is the Karlsruhe Optimized and Precise Radiative Transfer Algorithm (KOPRA) LBLRTM (Stiller, 2000; Schreier et al., 2018) that requires input parameters similar to those of SFIT4. PROFFIT9.INP is written in Fortran and is available as an executable for Windows. The control files are written in ASCII and can be easily modified to customize the retrieval strategy. The retrieval can be run through batch processing.

Comparisons between the performance of SFIT and PROFFIT for analyzing ground-based FTIR measurements have been done by Hase et al. (2004). The profiles and total columns retrieved from both codes agreed within 1% despite different LBLRTM, and Hase et al. (2004) concluded that the codes were comparable.

In addition, the column abundances for the Los Angeles site were derived using the gas fitting software GFIT (https://www.atomic.physics.lu.se/fileadmin/atomfysik/AF\_Personal/Professors/download.html). GFIT is a non-linear least-squares spectral fitting algorithm that uses a profile scaling retrieval (PSR) to derive the total column abundances from solar absorption spectra (Roche et al., 2021; Zeng et al., 2021; Laughner et al., 2024).

#### Retrieval Parameters

The general retrieval strategy for NH<sub>3</sub> is based on the method of Dammers et al. (2015). Table 2.1 shows the main parameters used for the NH<sub>3</sub> retrievals at the different FTIR sites used in this work. For most FTIR sites, two main microwindows (MWs) were used (930.32-931.32 and 966.97-967.675 cm<sup>-1</sup>) to cover the NH<sub>3</sub> absorption lines from the  $\nu_2$  vibrational band in the mid-IR region. For sites with small concentrations of NH<sub>3</sub>, such as Arctic or high-altitude sites, a third MW, or wider MW can be used. The range of the microwindows was selected with the intention of minimizing the interference of other species. In the strategy, the interference of  $H_2O$ , O<sub>3</sub>, CO<sub>2</sub>, and N<sub>2</sub>O was taken into account. For some sites, additional minor interfering species were added, such as SF<sub>6</sub> or CFC-12, depending on the characteristics of the site. Spectroscopic parameters were obtained from the high-resolution transmission molecular absorption database HITRAN (Rothman et al., 2009). Temperature and pressure profiles were obtained from the US National Centers for Environmental Prediction (NCEP). The a priori profile information about the interfering gases was obtained from 40-year (1980-2020) averages of simulations from the Whole Atmosphere Community Climate Model (WACCM) (Eyring et al., 2007; Marsh et al., 2013).

NH<sub>3</sub> profiles are not available from WACCM for all sites; instead, scaled a priori profiles derived from the global chemical transport model GEOS-Chem v11 were used. The a priori scaling was performed empirically, and it was based on prior knowledge of the surface concentrations in the site or sites with similar characteristics. To test the a priori profile, retrievals were performed and compared; the final a priori was selected based on its performance to achieve better values for the DOFS, the errors, and the number of converged retrievals. Constructed scaled a priori profiles have been used previously from GEOS-Chem simulations for the retrieval of trace gases

Table 2.1: Summary of fitting parameters for NH<sub>3</sub> retrievals at the 22 FTIR sites used in this thesis.

Station	Spectroscopic $NH_3$	$c NH_3$	Retrieval	Microwindows	Other Interfering (S <sub>a</sub> calc.) <sup>e</sup>	$(S_a calc.)^e$
	$Database^a$	A priori $^b$ Code $^c$	$^{\circ}$ Code $^{c}$	$(cm^{-1})$	$Species^d$	
Eureka	HIT2008	Other	SFIT4	929.40-931.4, 950.2-952.2, 962.10-970.0	SF6, CFC-12	X
Ny Alesund	HIT2008	CC	SFIT4	930.32-931.32, 966.97-967.675		NA
Thule	HIT2008	CC	SFIT4	930.32-931.32, 966.97-967.675		NA
St. Petersburg	HIT2012	CC	SFIT4	930.32-931.32, 966.97-967.675		NA
Bremen	HIT2008	CC	SFIT4	930.32-931.32, 966.97-967.675		X
Garmisch	HIT2020	Other	PROFFIT	926.4-932.5, 964.1-968.4	SF6, CFC-12	NA
Zugspitze	HIT2020	Other	PROFFIT	926.4-932.5, 964.1-968.4		NA
Jungfraujoch	HIT2008	$GC \times 2.5$		929.4-931.4, 950.2-952.2, 962.1-970	SF6, CFC-12	NA
Toronto	HIT2008	$GC \times 3$		930.32-931.32, 966.97-967.675		Y
Boulder	HIT2008	CC	SFIT4	930.32-931.32, 966.97-967.675		NA
Tsukuba	HIT2008	CC	SFIT4	930.32-931.32, 966.97-967.675		Y
Los Angeles	$ATM2024^f$	Other	GFIT.	867.92-869.74, 930.45-932.65,966.20-970.60, CFC-11, CFC-12, NA	CFC-11, CFC-12,	ΝΑ
				1084.62 - 1089.96, 1103.30 - 1105.06	HCOOH, OCS	1 1 1 1 1 1 1 1 1 1 1 1 1 1 1 1 1 1 1 1
Hefei	HIT2008	CC	SFIT4	930.32-931.32, 966.97-967.675		NA
Izana	HIT2008	CC	PROFFIT	$929.40, 931.40,\ 950.20, 952.20,\ 962.10, 970.00$		NA
Mexico City	HIT2008	$GC \times 3$	SFIT4, PROFFIT $c'$	930.32-931.32, 966.97-967.675		Y
Altzomoni	HIT2008	$GC \times 3$	SFIT4, PROFFIT <sup>c'</sup>	929.4-931.4, 962.7-970.0		X
Paramaribo	HIT2008	CC	SFIT4	930.32-931.32, 966.97-967.675		NA
Porto Velho	HIT2012	CC	SFIT4	929.4-931.4, 950.2-952.0, 962.10-970.0	CFC-12	Y
Reunion St.Denis	s HIT2012	CC	SFIT4	929.4-931.4, 950.2-952.0, 962.10-970.0	CFC-12	Y
Reunion Maido	HIT2012	CC	SFIT4	929.4-931.4, 950.2-952.0, 962.10-970.0	CFC-12	Y
Wollongong	HIT2008	Other	SFIT4	930.32-931.32, 966.97-967.675		NA
Lauder	HIT2008	Other	SFIT4	930.32-931.32, 966.97-967.675		NA

<sup>a</sup> Version of HITRAN linelist used, indicated by the year.

<sup>b</sup> The GC a priori is based on GEOS-Chem profiles. For some sites, this profile was scaled by the mentioned factor. Other a priori profiles were not based on GEOS-Chem. For example, the Eureka a priori is described in Lutsch (2019) and for Lauder, the a priori is based on balloon measurements.

<sup>c</sup> SFIT refers to the retrieval code SFIT4 version 0.9.4.4. For PROFFIT, version 9 was used.

<sup>c</sup> For Mexico City and Altzomoni, PROFFIT was used for Chapter 3 and SFIT4 for Chapters 4 and 5. <sup>d</sup> Additional species to H<sub>2</sub>O, O<sub>3</sub>, CO<sub>2</sub>, and N<sub>2</sub>O and their isotopes.

<sup>e</sup> Y if the S<sub>a</sub> was calculated using Equation 2.23.

f Details about ATM2024 linelist can be found at Toon (2022).

(Shephard et al., 2011; Shephard and Cady-Pereira, 2015; Bader et al., 2017). A priori concentrations of NH<sub>3</sub> are mainly unknown at the different sites; for this reason, the choice of  $\mathbf{S_a}$  is particularly relevant, as it can improve the DOFS and minimize the RMS residuals of the fitted spectra. The recommendation for NH<sub>3</sub> retrievals is to scale the  $\mathbf{S_a}$  matrix diagonal elements by the corresponding layer thickness. Therefore, the diagonal elements of  $\mathbf{S_a}$  are given by:

$$\mathbf{S_{a,ii}} = 1/\sqrt{\Delta z} \tag{2.23}$$

where  $\Delta z$  is the thickness of the layer in km. The summary of mean parameters for NH<sub>3</sub> retrievals are shown in Table 2.2. The total statistical and systematic uncertainties are presented in the total error and were calculated as the square root sum of the squares of all statistical and systematic errors considered, as suggested in García et al. (2021). The mean a priori and retrieved NH<sub>3</sub> VMR for the 22 FTIR sites are shown in Figure 2.7. It can be observed that in most cases, the a priori VMR profiles are generally smaller than those of the retrieved VMR. In addition, in all sites, NH<sub>3</sub> is concentrated near the surface. The mean sensitivity of the NH<sub>3</sub> retrieval is shown in Figure 2.8, and it varies across the sites, but in all cases, the peak sensitivity is below 20 km.

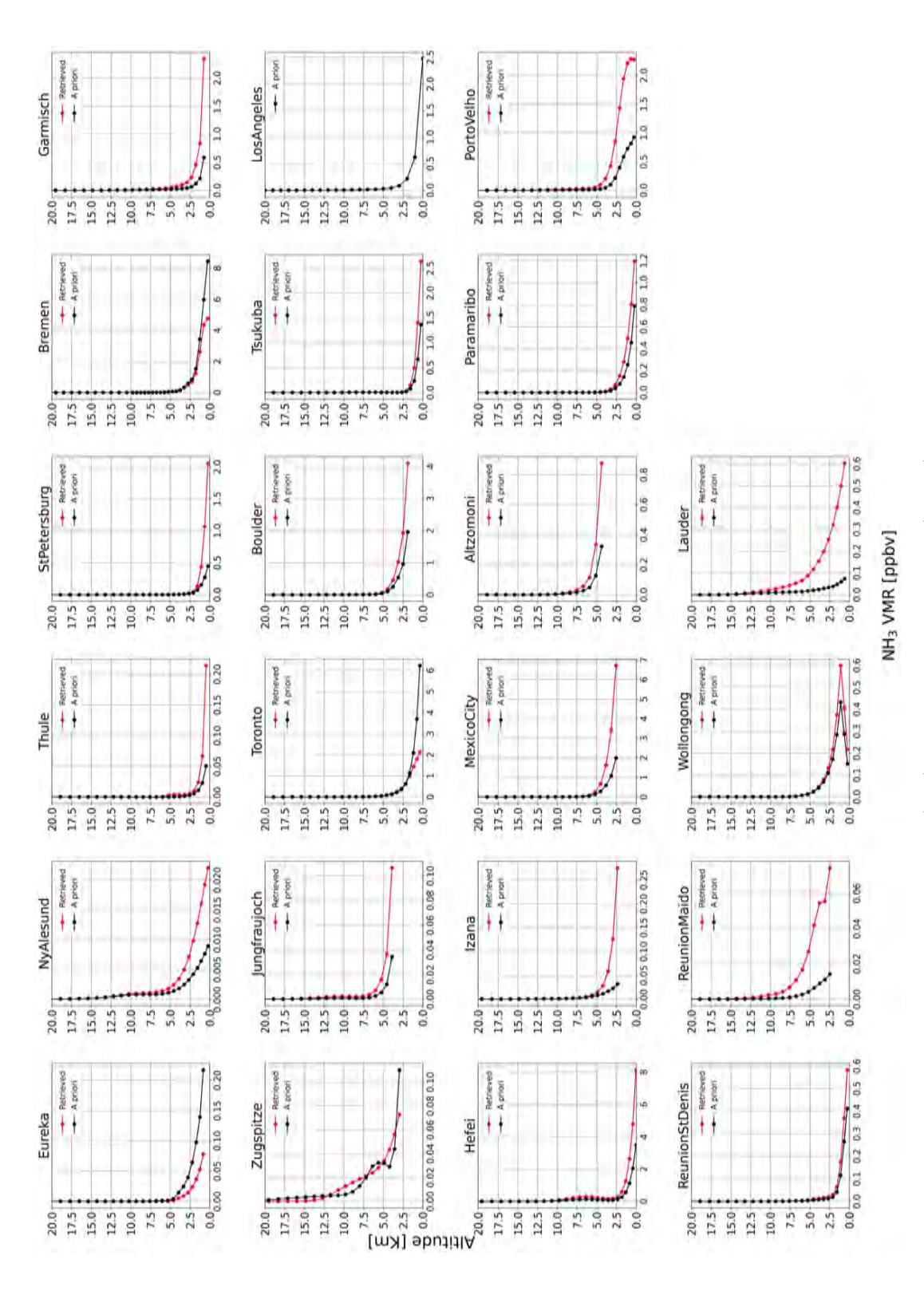
During the course of this work, the IRWG community made some efforts to "harmonize" the  $NH_3$  retrievals among the NDACC stations. One example was the recommendation of using the GEOS-Chem a priori profiles; however, these profiles can strongly underestimate  $NH_3$  at some sites. For Eureka, several tests were performed, finding that the GEOS-Chem a priori  $\times$  2.5 was the best option; however, the overall performance of this retrieval wasn't better than the results using the current a priori, which is derived from balloon-based measurements taken in Alaska, as described in Lutsch (2019). For Toronto, similar tests were performed, finding that for one year

of retrievals, by using the GEOS-Chem a priori scaled, there was an improvement in the DOFS compared to the strategy described in Yamanouchi (2021). Tests varying the version of HITRAN were also performed. For this work, most of the sites used HITRAN 2008, because this linelist was already available for all sites, the number of retrievals converged was higher, and it could run with SFIT4 v0.9.4.4. The use of HITRAN 2020 is still under discussion. This line list can only be adopted by sites that are currently using SFIT4 versions greater than version 1 due to the formatting of the hbin input file.

Table 2.2: Summary of mean parameters for NH<sub>3</sub> retrievals at the 22 FTIR sites used in this thesis.

Mean Relative Error $\%$	1.90	48.66	7.63	28.48	5.55	15.25	34.22	13.08	12.15	13.84	13.58	1.84	22.52	79.78	21.66	28.09	12.51	15.53	22.44	20.75	115.55	30.20
Mean Absolute Error (molec. $\text{cm}^{-2}$ )×10 <sup>15</sup>	0.00	0.00	0.03	0.87	0.93	0.54	0.11	0.03	0.97	1.25	0.63	0.21	4.32	0.34	3.14	0.46	0.38	1.83	0.27	0.07	3.03	0.95
Mean DOFS	1.01	0.35	1.01	0.93	1.86	1.61	1.00	1.02	1.43	1.03	1.12	$1.0^a$	1.37	1.18	0.96	0.92	0.51	1.09	0.98	0.95	1.11	1.19
$\rm NH_3$ Mean Total Column (molec. cm <sup>-2</sup> )×10 <sup>15</sup>	0.17	0.12	0.46	3.07	16.80	3.56	0.32	0.20	7.98	9.00	4.64	11.31	19.20	0.43	14.50	1.63	3.02	11.80	1.21	0.34	2.62	3.15
Measurement Period	2006-2020	2017 - 2019	1999-2022	2010 - 2022	2004-2018	2004 - 2007	1995-2023	2008-2023	2002 - 2023	2010 - 2022	2014 - 2022	1985 - 2024	2017-2022	2000-2022	2012 - 2022	2012 - 2022	2018 - 2019	2019	2009-2011	2013-2023	2007-2022	1996-2022
Station	Eureka	Ny Alesund	Thule	St. Petersburg	Bremen	Garmisch	m Zugspitze	Jungfraujoch	Toronto	Boulder	Tsukuba	Los Angeles	Hefei	Izana	Mexico City	Altzomoni	Paramaribo	Porto Velho	Reunion St. Denis	Reunion Maido	Wollongong	Lauder

 $^{\rm a}$  This site uses a profile scaling retrieval algorithm, DOFS = 1.0 were assumed.



vertical retrieval grid. A second version of this figure, from 0 to 120 km, is presented in Appendix A. For the Los Angeles Figure 2.7: Mean retrieved NH<sub>3</sub> VMR profiles (red) and a priori profiles (black) from 0 to 20 km at the 22 FTIR sites. The retrieved profiles are the means over the years indicated in Table 2.2. The circle markers indicate the layer centers of the FTIR site, only the a priori VMR profile is shown as GFIT scaling retrievals do not contain more vertical information than the total column amount.

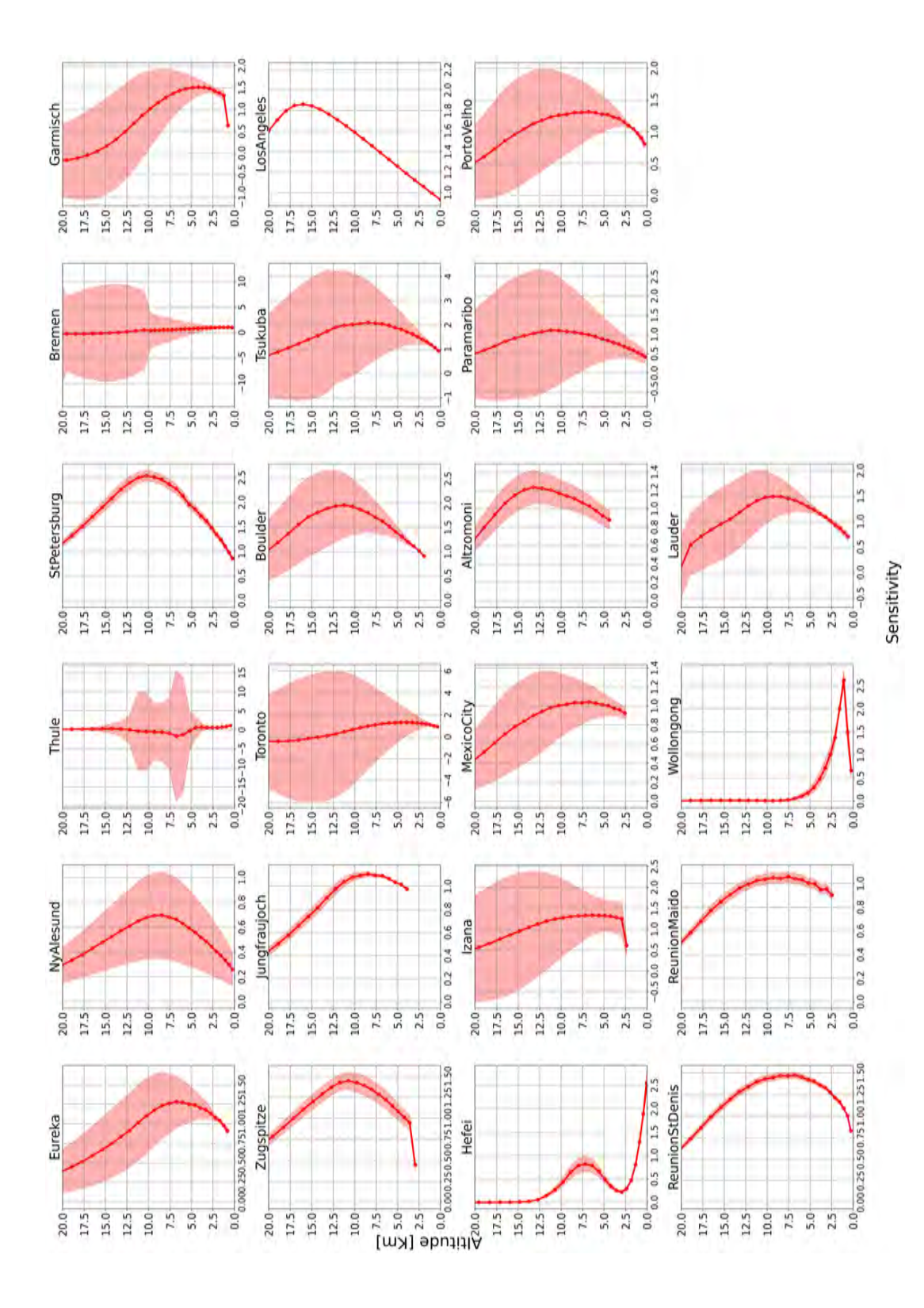


Figure 2.8: Mean sensitivity for the NH<sub>3</sub> retrievals from 0 to 20 km at the 22 FTIR sites taken over the years indicated in Table 2.2. The circle markers indicate the layer centers of the FTIR vertical retrieval grid. A second version of this figure, from 0 to above 100 km, is presented in the Appendix A.2. The standard deviation (shade) for the Los Angeles site was not available.

## 2.1.6 Satellite Data: IASI

IASI measures the infrared thermal radiation emitted by the Earth's surface and the atmosphere from a Sun-synchronous orbit on board the Meteorological Operational satellite program (MetOp) platform. MetOp is a collaboration between the European Organization for the Exploitation of Meteorological Satellites (EUMETSAT) and the European Space Agency (ESA). To date, there are three MetOp satellites identical in design: MetOp-A, launched in 2006 and retired in 2021, MetOp-B launched in 2012, and MetOp-C launched in 2018. IASI records spectra in the 645-2760 cm<sup>-1</sup> spectral range at a spectral resolution of 0.5 cm<sup>-1</sup> (Clerbaux et al., 2009). The instrument crosses the equator at mean local solar times of 09:30 and 21:30, providing global coverage of the Earth twice a day. IASI has a field-of-view composed of four circular footprints each with a diameter of 12 km at the nadir view and up to 20 km x 39 km elliptical pixels outside the nadir depending on the satellite viewing angle, complemented by scanning along a swath width of 2200 km off-nadir perpendicular to the ground track (Clarisse et al., 2009; Van Damme et al., 2014, 2015).

The IASI-NH<sub>3</sub> retrieval products are based on Artificial Neural Networks (ANNI) that link the Hyperspectral Range Index (HRI), a calculated dimensionless index that represents the amount of NH<sub>3</sub> in the column, to other input parameters such as temperature, pressure, water vapor profiles, and parametrized vertical profiles of NH<sub>3</sub> to derive the NH<sub>3</sub> total column. The algorithm maps the HRI to the NH<sub>3</sub> total column using a trained neural network; the uncertainty of each NH<sub>3</sub> column can be estimated by the propagation of the input parameters' uncertainties. However, large HRI values (more than  $3\sigma$ ) are associated with a confident detection of NH<sub>3</sub> (Van Damme et al., 2014, 2017; Whitburn et al., 2016a). The current spectral range for the retrieval process is set to 812-1126 cm<sup>-1</sup> to increase the sensitivity of NH<sub>3</sub> and reduce interferences (Van Damme et al., 2021). In addition, under conditions of

high NH<sub>3</sub> and when the thermal contrast is large, IASI has maximum sensitivity to NH<sub>3</sub> in the boundary layer (Clarisse et al., 2010). An error estimate is provided with each individual IASI observation. IASI's average detection limit for NH<sub>3</sub> under large thermal contrast is about 3 ppbv, and can be as low as 1 ppbv under conditions of well-mixed NH<sub>3</sub> throughout a thick boundary layer (Clarisse et al., 2010). The IASI Level 2 observations include quality flags that can be used to filter observations based on the quality and completeness of the IASI level 1 product. The retrieval scheme for version 3 of the product (ANNI-NH<sub>3</sub>-v3), used in Chapter 3, does not produce averaging kernels; however, previous studies comparing the IASI-NH<sub>3</sub> product with ground-based FTIR measurements have demonstrated good agreement (Dammers et al., 2016, 2017; Lutsch et al., 2019; Yamanouchi et al., 2021). To this date, the most recent version of the IASI NH<sub>3</sub> total column product (ANNI-NH<sub>3</sub>-v4, (Clarisse et al., 2023)) does include averaging kernels, and a more robust calculation of the HRI, resulting in NH<sub>3</sub> columns 10 to 20% larger than v3. ANNI-NH<sub>3</sub>-v4 NH<sub>3</sub> columns and were used in Chapter 5.

# 2.2 Simulations of NH<sub>3</sub>

The three pillars of atmospheric chemistry are atmospheric measurements, laboratory studies, and models (Brasseur and Jacob, 2017). Simulations of trace gases can be tested against observations to assess and improve our understanding of the current state of the atmosphere. A brief introduction to NH<sub>3</sub> simulations was presented in Chapter 1. In this section, the details of the models and reanalysis product used in this thesis are described.

#### 2.2.1 GEOS-Chem

GEOS-Chem is a global 3-D CTM (http://geos-chem.org) that is driven by assimilated meteorological fields from the NASA Global Modeling and Assimilation Office (GMAO). This model contains a chemical module with different configurations that updates column concentrations at each time step to account for the effects of emissions, deposition, chemistry, and aerosol microphysics (Bey et al., 2001); for this reason, it is widely used for atmospheric composition simulations on local and global scales. GEOS-Chem is one of the most widely used 3D-CTM for modeling NH<sub>3</sub> (Nair and Yu, 2020).

For this work, the high-performance version of GEOS-Chem (GCHP) was employed (Eastham et al., 2018; Martin et al., 2022). GCHP is highly parallelizable and designed to be efficient across several CPU cores, enabling faster and finer resolution simulations. This version of GEOS-Chem runs on the native Goddard Earth Observing System cubed-sphere model grid, allowing a more uniform grid box and accurate transport than regular latitude-longitude grids. A gnomonic cubed-sphere grid is a mosaic of six grids or faces, where each face is composed of a square grid divided into N equally sized segments. For this type of grid, the horizontal resolution is dictated by its size, where each face is an  $N \times N$  grid and it is denoted with the notation CN.

Figure 2.9 shows an example of a C16 grid. For this work, the model simulation was performed using GCHP version 14.1.1 at a horizontal resolution of C48 with 72 vertical layers from the surface to 0.01 hPa (approximately 80 km). The mean resolution for a C48 simulation is 192 km, which is similar to the resolution of a ~2° × 2.5° simulation in a regular latitude-longitude grid, which has a mean resolution of 198 km (Bindle et al., 2021). The analysis presented here uses a full-chemistry simulation that covers the period from 1 January 2003 to 31 December 2021. The model spinup was performed for the full year of 2002 to provide the initial conditions for the simulation. The model transport and chemical operator time steps were selected for 10 and 20 minutes, respectively, as recommended by Philip et al. (2016) to minimize simulation errors. More details and applications of this long-term GCHP simulation can be found in Wizenberg et al. (2024).

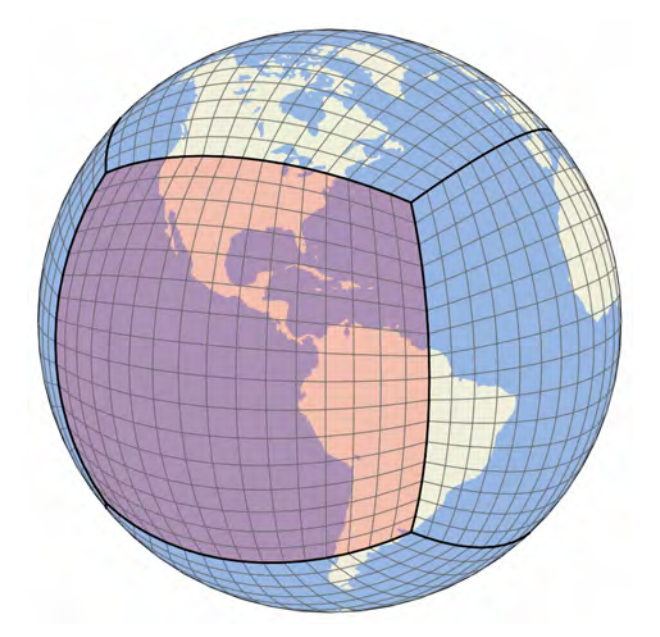


Figure 2.9: Example of a GCHP C16 grid highlighting one face for illustrative purposes. The highlighted face is a  $16 \times 16$  grid that is regularly spaced in a gnomonic projection centered on the face. Figure taken from Bindle et al. (2021).

The simulation is driven by Modern-Era Retrospective Analysis for Research and Applications, version 2 (MERRA-2) meteorological fields (Gelaro et al., 2017) provided

by GMAO at the NASA Goddard Space Flight Center. The microphysics used is from the TwO-Moment Aerosol Sectional (TOMAS) microphysics module (Trivitayanurak et al., 2008). The gas-aerosol equilibrium partitioning is represented using the ISOR-ROPIA II module (Fountoukis and Nenes, 2007). The PM<sub>2.5</sub> calculations were done following the recommendations from the GEOS-Chem website (https://wiki.seas.harvard.edu/geos-chem/index.php/Particulate\_matter\_in\_GEOS-Chem).

The model use emissions from different inventories that are configured at run-time using the Harmonized Emissions Component (HEMCO) (Lin et al., 2021). The emissions are re-gridded by HEMCO from their native resolution to the cubed-sphere grid, in this case to a C48 resolution. For this simulation, anthropogenic emissions are from the Community Emissions Data System (CEDS) v2 (Hoesly et al., 2018), biomass burning emissions from the Global Fire Assimilation System (GFAS) (Kaiser et al., 2012) v1.2 and natural emissions from the Global Emissions Inventory Activity (GEIA) (Graedel et al., 1993). CEDSv2 is a comprehensive global bottom-up emission inventory with a  $\sim 0.5^{\circ} \times 0.5^{\circ}$  resolution that accounts for eight anthropogenic emissions sectors, including agriculture, energy, industrial, transportation, residential, solvents, waste, and international shipping. The global anthropogenic emissions from CEDSv2 are between 1750 and 2019, and utilize regional and country-specific inventories, such as the European Monitoring and Evaluation Programme inventory (EMEP) for Europe, the Environmental Protection Agency (EPA) National Emissions Inventory (NEI) for the United States, and the Emissions Database for Global Atmospheric Research (EDGAR) for countries where national inventories are not available, to scale base emissions to produce trends over recent decades (Hoesly et al., 2018). For the 2020 and 2021 simulations, the CEDSv2 2019 emissions are applied. The GFASv1.2 inventory provides global fire emissions at a 3-hourly frequency on a  $0.1^{\circ} \times 0.1^{\circ}$  grid between for 2003 and 2021 (Kaiser et al., 2012), however, for the model spin-up in 2002, the Global Fire Emissions Database, version 4.1 (GFEDv4.1; Van Der Werf et al., 2017) was used. For NH<sub>3</sub> emissions, the GCHP simulation comprises five main emissions categories: total, anthropogenic, biomass burning, natural sources, ships, and seabirds, based on the previously mentioned inventories. The description of the calculation of the NH<sub>3</sub> total columns from GCHP is presented in Appendix A.

In addition to the 2003-2021 GCHP run, a one-month simulation for an arbitrary month (February 2013) was performed to explore the effect of changing the global emissions, by using the Hemispheric Transport of Air Pollution (HTAP) v3 emissions (Janssens-Maenhout et al., 2015), instead of CEDSv2, maintaining the same model configuration. The results of this simulation are discussed in Section 4.4.3.

Another advantage of the cubed-sphere model grid is its capability of finer resolution over a defined region by "stretching" a face (Bindle et al., 2021). The target face is centered on a target latitude and longitude and is stretched so that the grid resolution is finer. The degree of stretching is controlled by a parameter called the stretch-factor (S). The effect of S on stretching a cubed-sphere grid is seen in Figure 2.10, which shows that the refined domain decreases as S increases, and the grid boxes in the other faces outside the refined domain expand. The resolution at the target face ( $R_{TF}$ ) can be approximated by:

$$R_{TF} \approx \frac{10000 \text{ km}}{N \times S} \tag{2.24}$$

where N is the cubed-sphere size. For this work, a global full-chemistry GCHP stretched grid simulation for May 2019 centered over Mexico City was performed. The model configuration was the same as for the other simulations discussed. In addition, a one-month spin-up was performed for April 2019 using the regridded restart files produced from the 2003-2021 run. The target latitude was set to 19.2°N, and the target longitude to -99.0° with an S=6.5, which gives a resolution of approximately 32 km. The results of this simulation are discussed in Chapter 5.

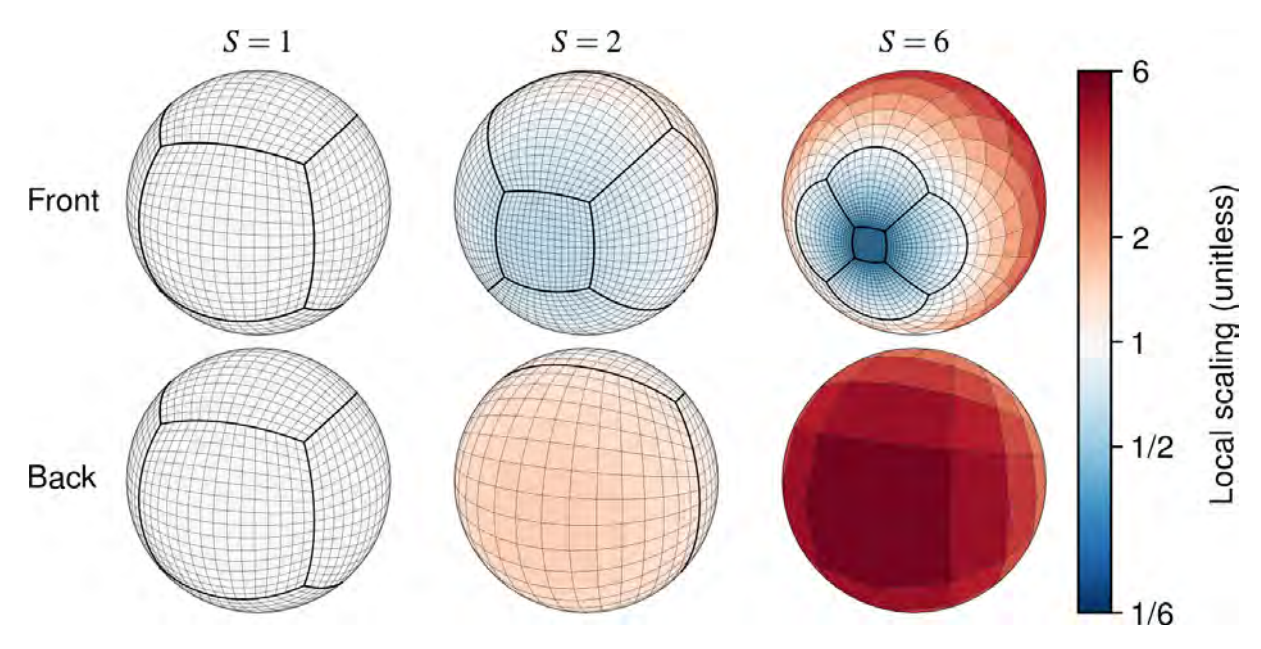


Figure 2.10: Illustration of the effect of increasing the stretch factor (S) on stretching a C16 cubed sphere grid. Local scaling is the relative change to a grid box's edge length induced by stretching. Figure taken from Bindle et al. (2021).

# 2.2.2 TCR-2

The Tropospheric Chemical Reanalysis (TCR-2) product (Miyazaki et al., 2020a) is a reanalysis product that consists of a global CTM and a data assimilation technique to optimize chemical concentrations and emissions of various chemical species. TCR-2 ozone product is very well known and has been compared with several ozone reanalysis products, showing improved agreements with independent ground and ozone-sonde observations (Huijnen et al., 2020). In this work the TCR-2 NH<sub>3</sub> product was evaluated. The reanalysis was produced using the MIROC-CHASER CTM (Watanabe et al., 2011) and an ensemble Kalman filter (EnKF) within the Multi-mOdel Multi-cOnstituent Chemical data assimilation (MOMO-Chem) (Miyazaki et al., 2020b) to assimilate observations of O<sub>3</sub>, CO, NO<sub>2</sub>, HNO<sub>3</sub> and SO<sub>2</sub> from multiple satellite instruments. The data assimilation system simultaneously updates tropospheric emissions and chemical concentrations of 35 chemical species described in Miyazaki et al. (2012, 2015, 2020a). The representation of tropospheric chemistry, including NO<sub>x</sub>

and SO<sub>2</sub> emissions is improved by assimilating NO<sub>2</sub> measurements from the Ozone Monitoring Instrument (OMI), the Global Ozone Monitoring Experiment (GOME-2), and the Scanning Imaging Absorption Spectrometer for Atmospheric Cartography (SCIAMACHY), and SO<sub>2</sub> from OMI.

Although NH<sub>3</sub> measurements were not directly assimilated in this product, the assimilation of NO<sub>x</sub> and SO<sub>2</sub> can influence the NH<sub>3</sub> analysis. For instance, an analysis of the COVID-19 lockdown period showed that while NO<sub>x</sub> and SO<sub>2</sub> emission reductions directly decreased nitrate and sulfate aerosols, they also led to a decrease in ammonium aerosols, even though NH<sub>3</sub> emissions remained unchanged in this analysis. This effect can be attributed to changes in NH<sub>3</sub> lifetime (Sekiya et al., 2023). The standard TCR-2 products publicly available at https://tes.jpl.nasa.gov/tes/chemical-reanalysis/ are regridded to 27 fixed pressure levels from 1000 to 60 hPa and don't always include surface level data. Different versions of the TCR-2 product were tested; however, due to the impact of surface data limitations on the NH<sub>3</sub> total columns, it was decided to use the product before the regridding that contains the vertical levels from the MIROC-CHASER.

The TCR-2 product used in this work has a horizontal resolution of  $1.1^{\circ} \times 1.1^{\circ}$  and consists of 32 vertical levels from the surface to 4.4 hPa. The TCR-2 fields were archived at a temporal resolution of 2 hours between 2005 and 2018. The gas-aerosol equilibrium partitioning is represented using the ISORROPIA module (Nenes et al., 1998). A priori anthropogenic emissions used in the reanalysis are from the HTAPv2 emissions (Janssens-Maenhout et al., 2015), biomass burning emissions from GFED v4 (Randerson et al., 2017), and soil emissions from GEIA (Graedel et al., 1993). The HTAP emission inventory has a  $0.1^{\circ} \times 0.1^{\circ}$  resolution between 2000 and 2018 and it is used to study trends and transport of air pollutants. Similarly to CEDSv2, HTAP accounts for eight sectors, which are agriculture, energy, industry, road transport,

residential, solvents, waste, and international shipping (Janssens-Maenhout et al., 2015). The description of the calculation of the NH<sub>3</sub> total columns from TCR-2 outputs is presented in Appendix A.

# 2.2.3 WRF-Chem

The Weather Research and Forecasting (WRF) model coupled with Chemistry (WRF-Chem) (https://www2.acom.ucar.edu/wrf-chem) was jointly developed by several research institutes led by the National Oceanic and Atmospheric Administration (NOAA). WRF-Chem is a regional fully coupled model that has the advantage of simultaneously solving chemistry and meteorology processes in the atmosphere, allowing for feedback between weather and air quality. Both components use the same horizontal and vertical grid, timestep, and transport scheme, without interpolations (Grell et al., 2005). To perform WRF-Chem simulations, the model has to be configured to include the initial and boundary conditions of the study area.

For this work, the output of a WRF-Chem version 4.2.2 simulation for May 2019 was compared with the performance of the GCHP stretched grid simulation. The simulation domain was centred over Mexico (22°N, 97°W) at a 32 km horizontal resolution, with 140 points in the horizontal dimension and 106 points in the vertical dimension. The temporal resolution of the output is 1 hour. For this simulation, the Goddard Chemistry Aerosol Radiation and Transport (GOCART) aerosol module (Chin et al., 2002) and the Model for Ozone and Related chemical Tracers, version 4 (MOZART-4) (Emmons et al., 2010) gas-phase module were used. The anthropogenic emissions were obtained from the EDGAR-HTAPv2 inventory at a 0.1° ×0.1° resolution between 2008 and 2010. The biomass burning emissions are from the Fire INventory from NCAR (FINN) version 1.5 (Wiedinmyer et al., 2011) that provides global fire estimations at a 1 km resolution. The initial and boundary meteorological

conditions were obtained from the NCEP Final Operational Global Analysis data https://rda.ucar.edu/datasets/ds083.2/ at a horizontal resolution of 1° every 6 h from 1000 to 10 mb. The initial and boundary chemical conditions were obtained from CAM-chem dataset simulation output (Buchholz et al., 2019; Emmons et al., 2020) that is intended to be used as boundary conditions for regional modeling. CAM-chem has a 0.9° ×1.25° horizontal resolution simulation with 56 vertical levels and a temporal resolution of 6 h. NH<sub>3</sub> and PM<sub>2.5</sub> are among the species simulated in the CAM-chem dataset. More details of the processes and setup for this simulation can be found in Rios and Estrada (2022).

# Chapter 3

# Evolution and Distribution of NH<sub>3</sub> Over Mexico City

# 3.1 Introduction

In this chapter, the diurnal and seasonal variability of NH<sub>3</sub> over Mexico City is investigated using datasets from two ground-based FTIR spectrometers, including an extension of the FTIR-NH<sub>3</sub> total column time series of the station in Mexico City used in Dammers et al. (2016), and of the FTIR-NH<sub>3</sub> total columns measured at Altzomoni, a remote high-altitude station close to Mexico City. The locations of these two sites are shown in Figure 3.1. The analysis is complemented with IASI satellite observations over the region, and back-trajectories that were constructed for anomalous NH<sub>3</sub> columns detected at the urban site to assess the influence of local and remote sources. This study is published in Herrera et al., Measurement report: Evolution and distribution of NH<sub>3</sub> over Mexico City from ground-based and satellite infrared spectroscopic measurements, *Atmos. Chem. Phys.*, 2022 (Herrera et al., 2022).

# 3.2 Methodology

# 3.2.1 Study Site: Mexico City

The number and size of the world's cities is increasing, with some of them becoming megacities, hosting more than 10 million inhabitants. The urban population worldwide is expected to continue this increase in the coming years, adding about ten more megacities by 2030 (United Nations, 2018). These massive concentrations of people and their activities present significant challenges for the global environment, especially in terms of air pollution, climate, and human health. One of the largest metropolitan areas in the world, and the largest in North America, is the Mexico City Metropolitan Area (MCMA), a megacity of more than 21 million inhabitants that presents poor air quality during many days of the year. It is located in a basin surrounded by mountains and volcanoes, complicating the ventilation of the polluted air (Molina et al., 2020) that is dominated by the dynamics of the boundary layer (Stremme et al., 2013; Dammers et al., 2016). The Mexico City Emissions Inventory (SEDEMA, 2021), reports that the MCMA hosts almost 6 million vehicles and 1900 regulated industries, and emits a total of 46,931 tonnes of NH<sub>3</sub>/yr, including part of the Estado de Mexico. According to this inventory, 0.3% of NH<sub>3</sub> emissions in Mexico City are coming from "point sources" such as industry, 5.5% from "mobile sources" such as vehicles, and 94.2% from "area sources" including urban waste (1.09%), agriculture (9.44%), livestock (13.92%) and other (69.75%); within the other category are: domestic emissions (69.73%) and forest fires (0.01%). The inventory strongly attributes domestic emissions of NH<sub>3</sub> to feces from domesticated animals; in Mexico, the estimated number of dogs and cats is around 23 million with 70% of them being homeless (Gomez, 2018). Despite the frequent pollution episodes due to PM, the local government has not implemented policies regulating NH<sub>3</sub> emissions.

A few studies have investigated atmospheric NH<sub>3</sub> in the Mexico City area. Surface

NH<sub>3</sub> concentrations between 10 and 40 ppbv were measured using an open-path FTIR spectrometer, with the highest mixing ratios observed in the morning hours during a two-month period (Moya et al., 2004). FTIR-NH<sub>3</sub> time series between 2012 and 2015 contributed to a validation study for IASI (Dammers et al., 2016) and CrIS (Dammers et al., 2017) NH<sub>3</sub> satellite products. In terms of NH<sub>3</sub> emissions in Mexico City, Yokelson et al. (2007) reported NH<sub>3</sub> emission factors from forest fires in the mountains surrounding Mexico City in 2006, and Christian et al. (2010) reported emission factors from garbage burning and domestic and industrial biofuel use in central Mexico. A more recent study by Cady-Pereira et al. (2017) investigated the impact of biomass burning events on pollution over the MCMA using trace gas data, including NH<sub>3</sub>, from the TES instrument onboard the Aura satellite. That study concluded that biomass burning events can impact pollution levels in Mexico City, specifically the south part of the MCMA and particularly during the March-April-May period. Recently, Clarisse et al. (2019) and Viatte et al. (2022) reported NH<sub>3</sub> hotspots near Mexico City at Tochtepec (18.84°N, 97.80°W), Ezequiel Montes (20.68°N, 99.93°W), and Tehuacan (18.45° N, 97.31° W), with all of them classified as agricultural sources. Finally, Van Damme et al. (2021) reported an increasing trend of NH<sub>3</sub> over Mexico of  $(2.5 \pm 1.5) \times 10^{13}$  molec. cm<sup>-2</sup> yr<sup>-1</sup> using 11 years of IASI satellite data (2008-2018).

In this work, the diurnal and seasonal variability of NH<sub>3</sub> over Mexico City is investigated using datasets from two ground-based FTIR spectrometers, including an extension of the FTIR-NH<sub>3</sub> total column time series of the station in Mexico City used in Dammers et al. (2016), and of the FTIR-NH<sub>3</sub> total columns measured at Altzomoni, a remote high-altitude station close to Mexico City, that are retrieved for the first time. The locations of these two sites are shown in Figure 3.1. The analysis is complemented with IASI satellite observations over the region, and back-trajectories that were constructed for anomalous NH<sub>3</sub> columns detected at the urban site to assess

the influence of local and remote sources.

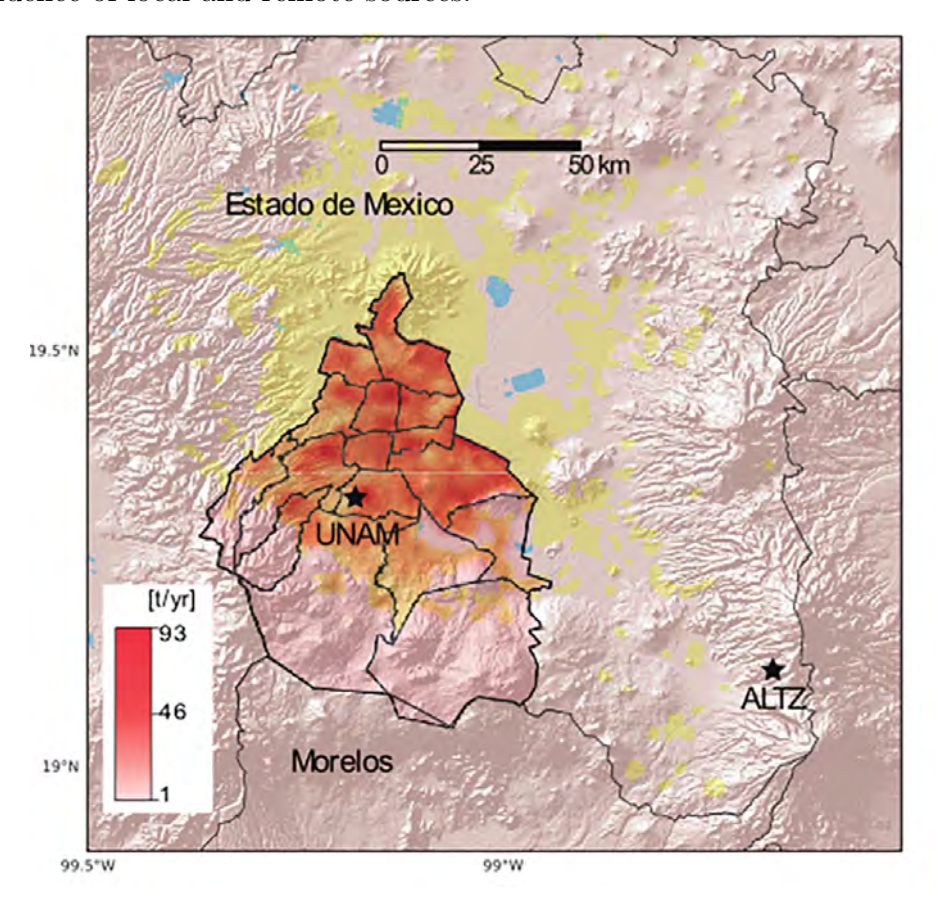


Figure 3.1: Study area in central Mexico. Mexico City is shown in the middle, with the red shading corresponding to NH<sub>3</sub> emissions reported in the Mexico City Emissions Inventory 2016 (SEDEMA, 2018) in tonnes per year. The stars indicate the location of the UNAM and Altzomoni stations and the yellow shading indicates the extension of the MCMA.

# 3.2.2 Ground-based FTIR Stations and NH<sub>3</sub> Retrieval

This study utilizes NH<sub>3</sub> total columns retrieved from solar absorption spectra measured with ground-based FTIR spectrometers at two sites in and around the MCMA. The urban FTIR station is located in the south of Mexico City within the campus of the Universidad Nacional Autónoma de Mexico on the rooftop of the Instituto de Ciencias de la Atmósfera y Cambio Climático (UNAM, 19.33°N, 99.18°W, 2280 m.a.s.l.). A custom-built solar tracker directs solar radiation to the entrance of the FTIR spectrometer (Bruker Optik GmbH model Vertex 80); see the diagram of the in-

ternal parts of the instrument in Chapter 2 (Figure 2.6). The instrument is equipped with a KBr beamsplitter and two detectors (MCT and InGaAs). For more details about this system, see Bezanilla et al. (2014). Measurements from the remote FTIR site were made at the Altzomoni Atmospheric Observatory (ALTZ, 19.12°N, 98.66°W, 3985 m.a.s.l.), a high-altitude station located 60 km from the UNAM urban site and within the Izta-Popo National Park, surrounded by nature. This site is part of the NDACC, contributing data from a high-resolution FTIR spectrometer since 2012. This instrument (Bruker Optik GmbH model IFS 120/125 HR), similar to the instrument described in Chapter 2 (Figure 2.5), can record solar spectra with a maximum spectral resolution of 0.0035 cm<sup>-1</sup>, and is equipped with KBr and CaF<sub>2</sub> beamsplitters and MCT, InSb, and InGaAs detectors. For details of the site and the instrument, see Baylon et al. (2017).

The FTIR spectra used for the retrieval of NH<sub>3</sub> were collected with the MCT detector at each site with a spectral resolution of 0.005 cm<sup>-1</sup> at Altzomoni, and 0.1 cm<sup>-1</sup> (prior to 2014) and 0.075 cm<sup>-1</sup> at UNAM, using an optical bandpass filter in the region between 700 and 1400 cm<sup>-1</sup>. In this study, we extend the UNAM time series used in a previous 2012-2015 comparison between IASI and FTIR (Dammers et al., 2016) with improvements to the retrieval, and we present for the first time, Altzomoni FTIR-NH<sub>3</sub> retrievals for the period between April 2012 and May 2020. The analysis presented here focuses on the region around the MCMA, also using the IASI satellite product and a back-trajectory evaluation, as described below.

For both sites, the solar FTIR spectra were analyzed using PROFFIT version 9.6 for the retrievals (Hase et al., 2004) to obtain the NH<sub>3</sub> total columns. The details of the parameters used for the retrieval strategy are described in Section 2.1.5. A total of 7992 NH<sub>3</sub> columns were retrieved for the UNAM station and 4031 for ALTZ. The resulting uncertainties obtained with PROFFIT averaged over the entire time series,

in molec. cm<sup>-2</sup>, were  $1.25\times10^{15}$  (random),  $8.40\times10^{14}$  (systematic), and  $1.52\times10^{15}$  or 11.50% (total) at UNAM; and  $3.09\times10^{14}$  (random),  $3.14\times10^{14}$  (systematic), and  $4.42\times10^{14}$  or 51.37% (total) at ALTZ. The average DOFS over the entire time series were 2.03 for UNAM and 1.04 for ALTZ.

# 3.2.3 IASI-NH<sub>3</sub> Data Product and Comparison

IASI measurements are described in Section 2.1.6. For this study, eleven years of the IASI-A NH<sub>3</sub> total columns (ANNI-NH<sub>3</sub>-v3) between 2008 and 2018 were used; details of this version 3 can be found in Appendix A of Van Damme et al. (2021), and was also used by Yamanouchi et al. (2021). IASI observations with adequate sensitivity to NH<sub>3</sub>, based on the quality flag of the product, and with errors less than 100% were used. The spatial distribution of NH<sub>3</sub> over Mexico City was obtained by averaging all the IASI-A morning observations between January 2008 and December 2018 over this region (latitude: 18.9°N to 19.9°N, longitude: 98.5°W to 99.5°W). The FTIR-NH<sub>3</sub> total columns at UNAM were compared against the IASI-NH<sub>3</sub> total columns over Mexico City to assess the agreement between both data sets.

Due to the high spatiotemporal variability of NH<sub>3</sub>, the temporal and spatial coincidence criteria were tested and assessed using the correlation coefficient R and the slope of the fitted line in the scatterplots. In addition, as suggested in Dammers et al. (2016), an elevation filter using the altitude difference between the location of the FTIR and the IASI pixel position (FTIR station altitude minus IASI observation < 300 m) was applied. The criteria resulting in the best correlations were elevation filter < 300 m, spatial sampling difference < 20 km, maximum temporal sampling difference  $\pm 40 \text{ min}$ , and maximum IASI-NH<sub>3</sub> retrieval error of 100%. The seasonal variability comparison and annual averages were performed using only FTIR-NH<sub>3</sub> retrievals between 9:00 and 10:59 a.m. (Local Time), corresponding to the IASI over-

pass time over Mexico City, and the < 20 km spatial criterion for IASI-NH $_3$  total columns. Altzomoni correlation plots with IASI-NH $_3$  data were not included due to the few coincidences between FTIR and IASI.

# 3.2.4 Back-Trajectory Analysis

To determine the primary sources of NH<sub>3</sub> measured at the UNAM station and to assess the dominant atmospheric transport pathways during the events with the largest hourly means of NH<sub>3</sub> columns in the time series, trajectory cluster analysis (Reizer and Orza, 2018) was applied. Eight-hour back-trajectories were selected to capture the air masses passing over the MCMA. Using the UNAM station as the receptor, back-trajectories were calculated using the Hybrid Single-Particle Lagrangian Integrated Trajectory (HYSPLIT) model (Stein et al., 2015; Draxler and Hess, 1997) at different altitudes above the UNAM station level (2280 m.a.s.l.). The HYSPLIT model can be run online at the following link https://www.ready.noaa.gov/HYSPLIT.php. The wind data used for the back-trajectories were derived from the NCEP North American Mesoscale (NAM) analysis product at 12 km and 1 hour spatial and temporal resolution, respectively. The cluster analysis is an embedded routine in HYSPLIT and is based on the Ward's agglomerative hierarchical clustering algorithm (Ward, 1963). Finally, the Total Spatial Variance (TSV) method (Draxler et al., 2021), included in HYSPLIT, was used to fit the number of clusters that represent the data.

# 3.3 Results and Discussion

# 3.3.1 FTIR NH<sub>3</sub> Time Series and Variability

The NH<sub>3</sub> total column time series retrieved at both FTIR stations are shown in Figure 3.2. The urban UNAM columns, shown in the top panel, are about one order of magnitude larger than the high-altitude Altzomoni columns. The mean NH<sub>3</sub> to-

tal columns  $\pm 1\sigma$  measured at UNAM is  $1.46 \pm 0.64 \times 10^{16}$  molec. cm<sup>-2</sup> and  $1.87 \pm 2.40 \times 10^{15}$  molec. cm<sup>-2</sup> at Altzomoni are compared to values reported for stations in other parts of the world in Table 3.1. The Mexico City NH<sub>3</sub> total columns are comparable with those reported in Bremen, while they are about twice as large as those measured at Toronto (Canada), Paris (France), and Lauder (New Zealand). Jungfraujoch, a remote high-altitude station in Switzerland with similar characteristics to Altzomoni, presents a significantly lower average NH<sub>3</sub> column and also has much lower variability. The reason for this might be that Altzomoni is impacted more frequently by biomass burning events in the dry season and also by the regional boundary layer, receiving polluted air from Mexico City and other large urban centres in the afternoon (Baumgardner et al., 2009).

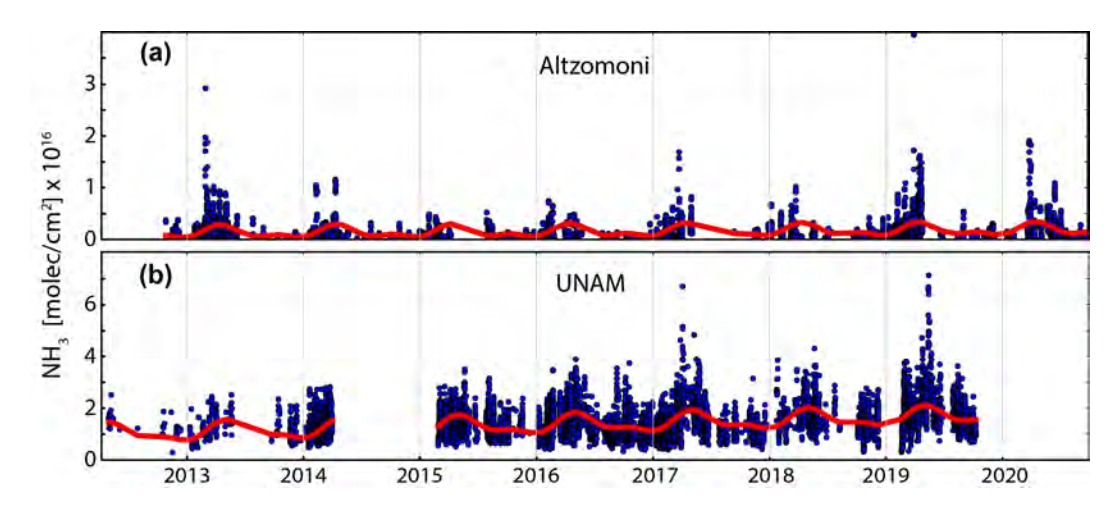


Figure 3.2: Time series of retrieved FTIR-NH<sub>3</sub> data over (a) Altzomoni and (b) UNAM, with a fitted Fourier series (red) to reproduce seasonality. Note the differences in magnitude.

Figure 3.2 also shows the fit of a Fourier series (Baylon et al., 2017) to represent seasonality at both stations. A clear cycle is seen at both locations, with a maximum between mid and late April, and a minimum in late December. However, the difference between the minimum and the maximum is larger at Altzomoni, with UNAM having greater NH<sub>3</sub> background concentrations. The average annual increase in the NH<sub>3</sub>

Table 3.1: Mean  $\mathrm{NH}_3$  total columns reported from ground-based FTIR stations.

Station	Location	Measurement	Measurement $NH_3$ total column <sup>a</sup>	Station	Reference
	Latitude, Longitude, Elevation	period	(molec. cm <sup>-2</sup> ) $\times 10^{15}$	Characteristics	
Bremen Germany	53.10°N, 8.85°E, 27 m.a.s.l	2004-2013	$13.7\pm4.24$	Urban, fertilizers, livestock	(Dammers et al., 2015)
Paris France	48.79°N, 2.44°E, 56 m.a.s.l	2009-2017	$8.4\pm 8.6$	Urban, fertilizers	(Tournadre et al., 2020)
Jungfraujoch Switzerland	46.55°N, 7.98°E, 3580 m.a.s.l	2004-2013	$0.18 \pm 0.07$	Remote, high altitude, transport, no large sources	(Dammers et al., 2015)
Toronto Canada	43.66°N, 79.40°W, 174 m.a.s.l	2002-2005	$5.94 \pm 5.14$	Urban, fertilizers,	(Yamanouchi et al., 2021)
		2015 - 2018	$8.13 \pm 7.88$	biomass burning	
UNAM Mexico	19.33°N, 99.18°W, 2280 m.a.s.l	2012-2019	$14.6\pm6.39$	Urban, large local sources	This study
Altzomoni Mexico	19.12°N, 98.66°W, 3985 m.a.s.l	2012-2020	$1.87 \pm 2.40$	Remote, high altitude, transport, no large sources	This study
Reunion Indian Ocean	20.90°S, 55.50°E, 85 m.a.s.l	2004-2012	$0.80\pm0.54$	Remote, fertilizers, biomass burning	(Dammers et al., 2015)
Lauder New Zealand	45.04°S, 169.68°E, 370 m.a.s.l	2004-2014	$4.17\pm1.40$	Remote, fertilizers, livestock	(Dammers et al., 2015)
a MIII	40401 0010000 1 1 -				

<sup>a</sup> NH<sub>3</sub> mean total column  $\pm 1\sigma$ .

columns obtained from the Fourier fit are  $92 \pm 3.9 \times 10^{13}$  molec. cm<sup>-2</sup> yr<sup>-1</sup> at UNAM (from 2012 to 2019) and  $8.4 \pm 1.4 \times 10^{13}$  molec. cm<sup>-2</sup> yr<sup>-1</sup> at (from 2012 to 2020). Van Damme et al. (2021) reported a trend from 2008 to 2018 of  $2.5 \pm 1.5 \times 10^{13}$  molec. cm<sup>-2</sup> yr<sup>-1</sup> for all of Mexico, which is closer to the Altzomoni value. The difference in magnitude can be attributed to the datasets and methodology as the present study uses ground-based FTIR measurements from two sites with higher values in 2019 and 2020, while Van Damme et al. (2021) used IASI satellite data over a wider region between 2008 to 2018.

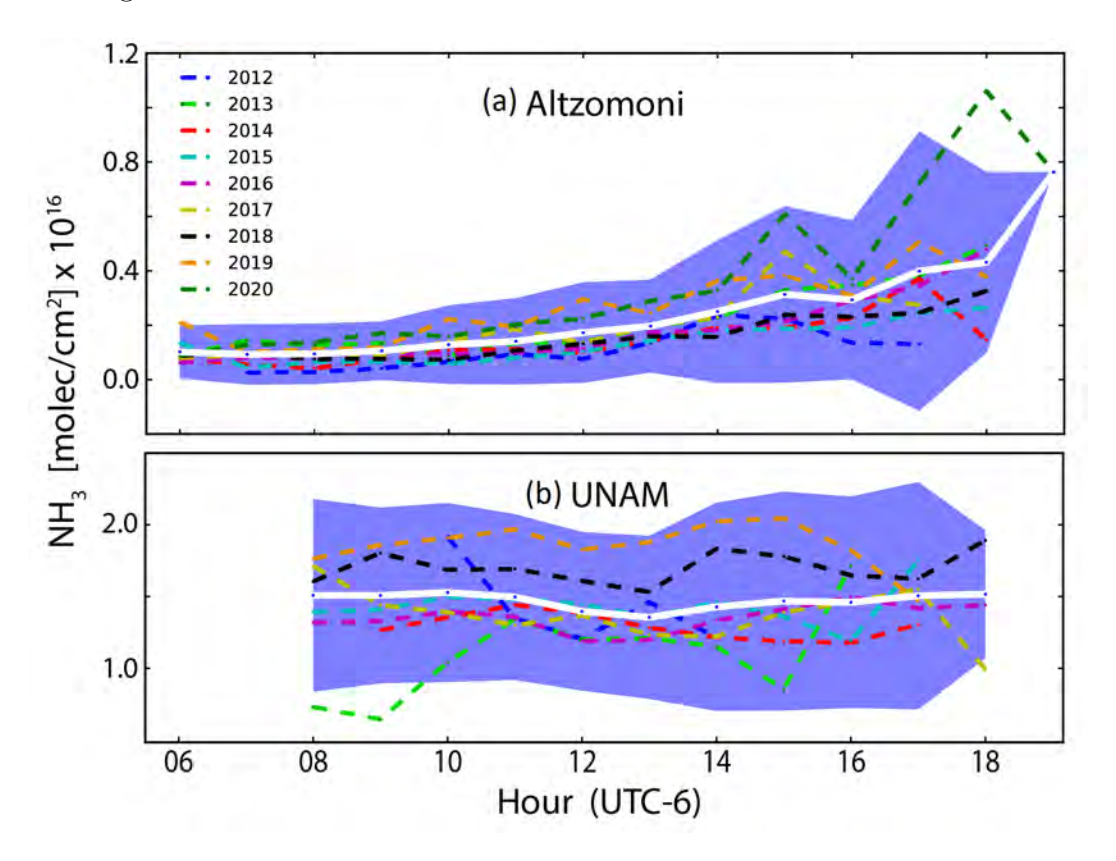


Figure 3.3: Average diurnal evolution of NH<sub>3</sub> total columns over Mexico City at (a) Altzomoni and (b) UNAM. Different years are shown in different colours, the thick white line is the average for all years, and the blue shading indicates  $\pm 1\sigma$ .

The average diurnal variability of the FTIR NH<sub>3</sub> total columns at both stations is displayed in Figure 3.3. The largest average NH<sub>3</sub> columns at the urban station are on the order of  $1.50 \times 10^{16}$  molec. cm<sup>-2</sup> and were observed during the morning and

the evening. Although the diurnal pattern is not as evident as in other cities where motor vehicles have been found to be a dominant source of urban NH<sub>3</sub> (Osada et al., 2019; Kotnala et al., 2019), traffic emissions in Mexico City still might play a role in conjunction with other urban sources of atmospheric NH<sub>3</sub>. The average NH<sub>3</sub> columns at UNAM have a minimum of  $1.35\times10^{16}$  molec. cm<sup>-2</sup> at 13 h, which can be attributed to the conversion to ammonium as was observed by Moya et al. (2004) when describing the evolution of the surface gas phase NH<sub>3</sub> and PM NH<sub>4</sub><sup>+</sup> evolution in Mexico City.

The diurnal cycle at the remote station (Figure 3.3a) is noticeably different, with NH<sub>3</sub> columns that increase systematically as the day progresses, with the largest variability in the afternoon hours. Altzomoni is located within a natural protected area with few local sources of NH<sub>3</sub>, and even less so during the morning hours when values are around  $0.10 \times 10^{16}$  molec. cm<sup>-2</sup> and when cooler temperatures do not favour the volatilization of NH<sub>3</sub>. The columns increase throughout the day, having the largest average values of  $0.76 \times 10^{16}$  molec. cm<sup>-2</sup> in the evening, probably transported from lower altitudes by the dynamics of the regional boundary layer (Baumgardner et al., 2009). This is supported by the large variability observed in the afternoon, since the probability that  $NH_3$  is transported > 1,700 m a.g.l. (above ground level) up to this site strongly depends on the meteorological conditions, which vary from day to day. Comparisons between daily average NH<sub>3</sub> columns and the daily averages of some meteorological variables, during the same measurement period as the FTIR data, from the RUOA Network (Red Universitaria de Observatorios Atmosféricos) such as temperature, relative humidity (RH), precipitation, and solar radiation, resulted in weak correlations (R between 0.1 and 0.3), and negative correlations with RH and precipitation (R between -0.1 and -0.3). The average wind speed for Altzomoni is 4.5 m/s, with dominant winds from the east-southeast and west-northwest, while the average wind speed for UNAM is 1.6 m/s, with dominant winds from the north and the north-northwest.

The seasonal variability of the FTIR NH<sub>3</sub> total columns is shown in Figure 3.4. In general, the pattern is similar at both stations, showing the NH<sub>3</sub> temperature dependence with larger NH<sub>3</sub> columns in the months of March, April, and May which correspond to the warm-dry season; this season usually has days with clear skies, weak winds, high pressure systems, and biomass burning events (Molina et al., 2020), and also corresponds to the most critical part of the fire season in Mexico City (Yokelson et al., 2007; CENAPRED, 2021). In addition, there are two agricultural seasons in the country, the first one from April to September and the second one from October to March. The fertilizer application combined with meteorological conditions could favour NH<sub>3</sub> volatilization from the agricultural sources contributing to the higher NH<sub>3</sub> spring columns observed in Figure 3.4. Smaller columns are clearly observed during the wet season (June to October), due to the increase in wet deposition, and during the cold-dry season from November to February, due to less favorable conditions for NH<sub>3</sub> volatilization. This is in agreement with Viatte et al. (2022).

The annual cycle of NH<sub>3</sub> columns at the urban UNAM station is similar to that observed at the background Altzomoni station but has a larger amplitude. A study by Sun et al. (2017) observed that the growing efficiency of three-way catalysts in motor vehicles is responsible for large NH<sub>3</sub> emissions detected in urban locations in the USA and China. These emissions are strongly dependent on traffic volume and, thus, should not have a strong seasonality. On the other hand, emissions originating from agricultural activity usually have a distinct seasonality that depends on the fertilizer application and temperature (Sun et al., 2017; Van Damme et al., 2015; Viatte et al., 2022). In the current study, the annual cycles follows the pattern of temperature (Figure 3.4c), indicating that emissions from other sources, such as fires, waste treatment, human or pets emissions, may be contributing significantly to the NH<sub>3</sub> detected over the MCMA.

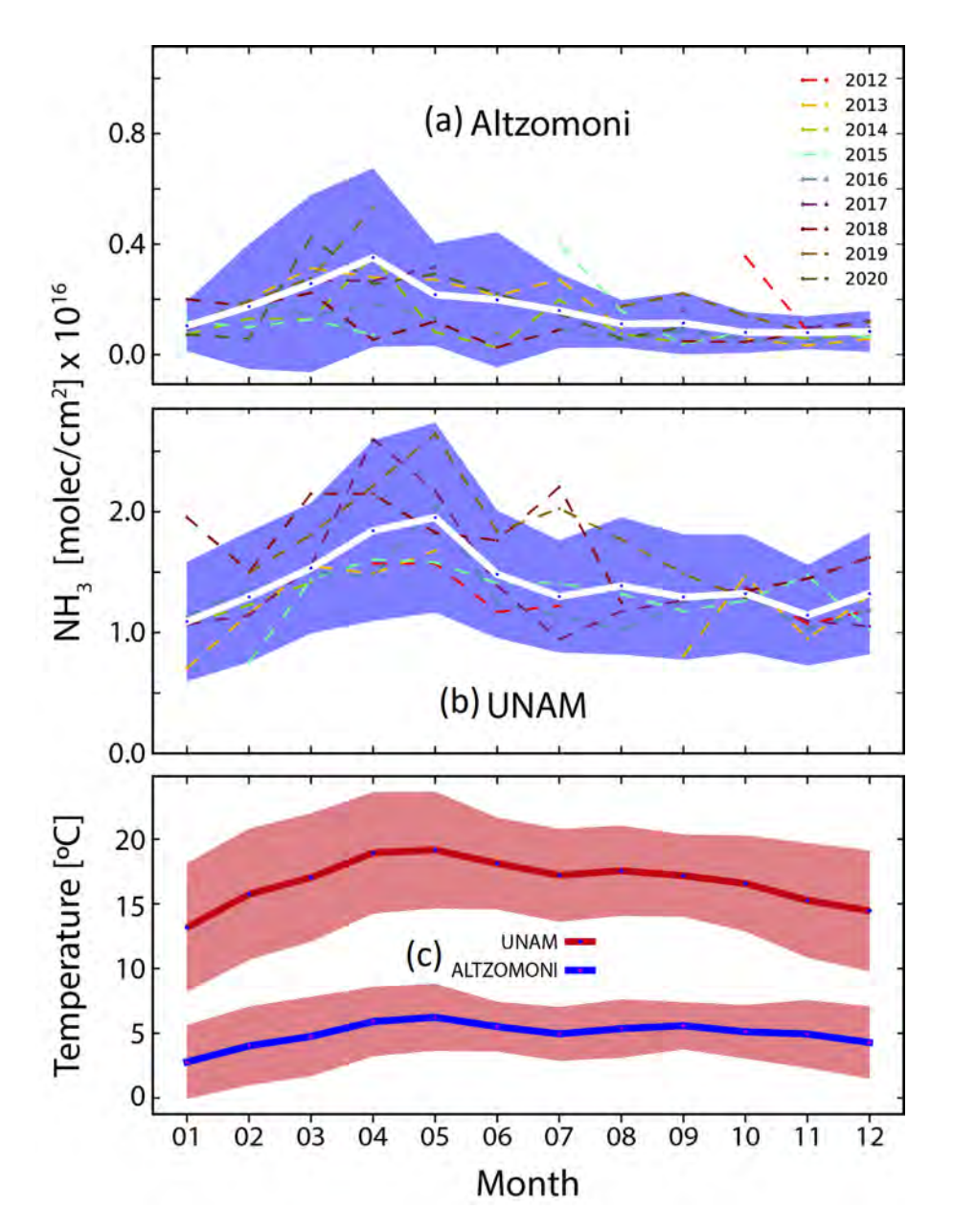


Figure 3.4: Monthly averages showing the annual cycle of NH<sub>3</sub> over Mexico City at (a) Altzomoni and (b) UNAM. The thick white line is the average for all years and the shading indicates  $\pm 1\sigma$ . (c) Monthly averages of temperature at both stations between 2014-2018 for Altzomoni and 2012-2018 for UNAM. The shaded area indicates  $\pm 1\sigma$ .

There are more features to note in Figure 3.4. While Altzomoni and UNAM NH<sub>3</sub> columns have similar annual cycles, those at Altzomoni have greater variability throughout the different years during the warm-dry season than during the rest of the year. This might be due to the strong relationship between pollutants reaching the high-

altitude station and the boundary layer dynamics and wind conditions, which are more variable during the warm-dry season. However, another contribution to this variability may be biomass burning activity, which has a maximum during the warmdry months as has been shown by Cady-Pereira et al. (2017). The 2013 pollution events presented by Cady-Pereira et al. (2017) are seen on April 23, May 9, and May 25 in Figure 3.2, with May 9 having the largest enhancements at Altzomoni; unfortunately, there are no coincident measurements for UNAM. At Altzomoni, the average NH<sub>3</sub> column for May 9, 2013 was  $2.39 \pm 0.53 \times 10^{15}$  molec. cm<sup>-2</sup>, which is 28% greater than the average column for the entire period (Table 3.1). However, in 2013, the largest NH<sub>3</sub> column measured at Altzomoni was on the evening of February 27 with an average value of  $17.4 \pm 0.58 \times 10^{15}$  molec. cm<sup>-2</sup>, almost ten times higher than the average column presented in Table 3.1. This enhancement on February 27, 2013 seems to be local and of short duration, most likely due to a nearby biomass burning event. This is supported by the detection of active fires northwest of the site on that date by the MODIS instrument on Aqua as shown on Figure 3.5. With its high altitude and few local sources, Altzomoni seems to be more sensitive for the detection of pollution events than UNAM. Even if the fires are not occurring nearby, the increased lifetimes of emitted pollutants at these altitudes may favour transport over longer distances to Altzomoni.

# 3.3.2 Satellite Observations and Comparison with FTIR

The correlation between IASI-NH<sub>3</sub> and the ground-based FTIR-NH<sub>3</sub> total columns at UNAM from November 2013 to December 2018 is shown in Figure 3.6. The coincidence criteria are described in Section 3.2.3, and are based on values used in previous validations of IASI products using ground-based FTIR data (Dammers et al., 2016), including an elevation correction using the Space Shuttle Radar Topography Mission Global Product at 3 arcsec resolution (SRTMGL3) (Farr et al., 2007) over

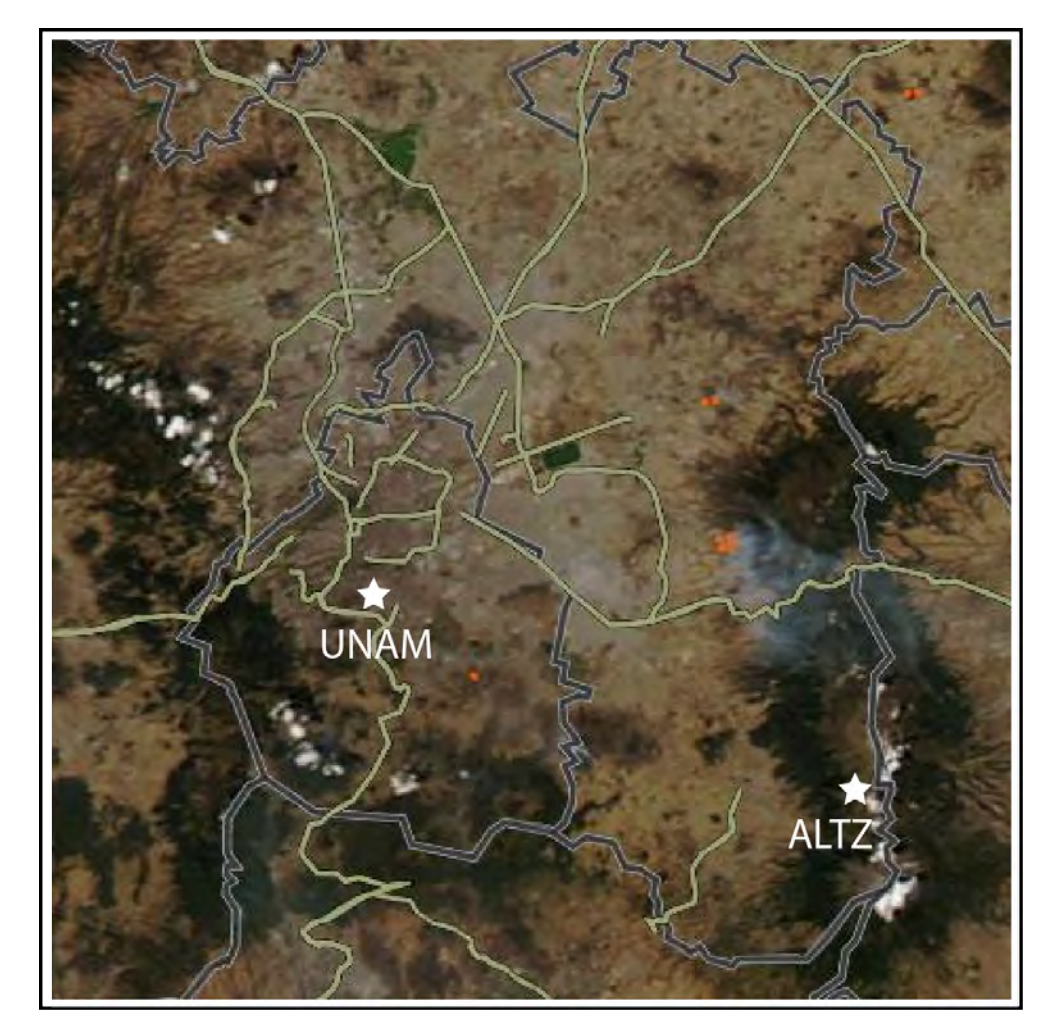


Figure 3.5: Snapshot of Mexico's City fire events on February 27, 2013, from the Aqua MODIS instrument with true colour corrected reflectance and resolution of 250 m, obtained from NASA Worldview Snapshots (https://earthdata.nasa.gov). The red dots show the fire events. The stars indicate the location of the UNAM and Altzomoni stations.

Mexico City. A total of 64 coincident data pairs were found, from which a correlation coefficient R=0.72 and a mean relative difference (MRD) of -32.2  $\pm$  27.5 % were obtained ( $\pm$  1 $\sigma$ ). These results are consistent with R=0.64 and MRD = -30.8  $\pm$  43.9 % reported by Dammers et al. (2016) for this region using an older version of the IASI-NH<sub>3</sub> product. The correlation is also similar to that of Tournadre et al. (2020), who obtained R=0.79, when comparing IASI-NH<sub>3</sub> to FTIR-NH<sub>3</sub> columns using a similar instrument (Vertex 80) in Paris, and to the R=0.80 and MRD = -32.4  $\pm$  56.3

% reported for 547 coincidences from several ground-based FTIR stations and IASI-NH<sub>3</sub> (Dammers et al., 2016). The IASI ANNI-NH<sub>3</sub>-v3 product is thus in agreement with the ground-based data and even presents an improved correlation compared to the previous result in Dammers et al. (2016). However, an underestimation in the IASI-NH<sub>3</sub> total columns of approximately 32% over Mexico City persists. Dammers et al. (2017), using an older version of the IASI ANNI-NH<sub>3</sub> product, attributed these differences to a combination of more randomly distributed error sources and large systematic errors, however, these reasons need to be investigated further.

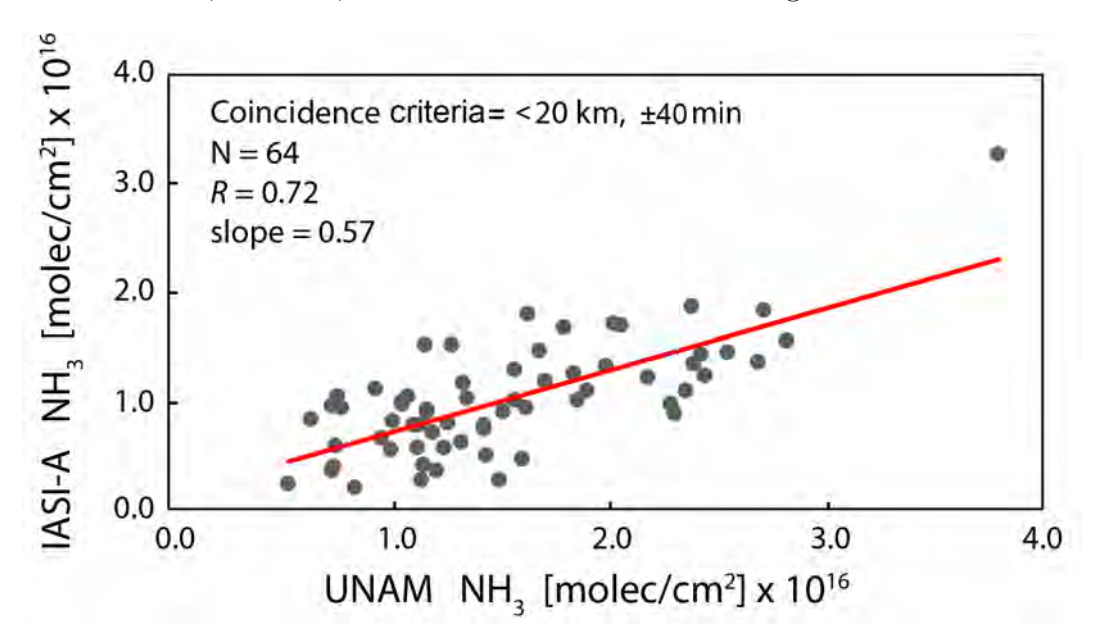


Figure 3.6: Correlation plot for IASI-A NH $_3$  vs. UNAM FTIR-NH $_3$  total columns, with coincidence criteria of < 20 km,  $\pm 40$  minutes, elevation (FTIR station – IASI observation) < 300 m, IASI-NH $_3$  retrieval error < 100% between November 2013 and December 2018.

The spatial distribution of NH<sub>3</sub> over MCMA as observed by IASI is presented in Figure 3.7. The distribution shows a clear NH<sub>3</sub> enhancement in the northeast section of Mexico City and in part of the Estado de México region. There are several potentially important sources located in this area: Mexico City International Airport, an area of continuous traffic emissions; the Bordo Poniente compost plant, which treats around 1500 tonnes of daily organic waste from the city; wastewater discharge and treatment

bodies with nearby bird colonies such as the regulation lagoon Cola de Pato; and the agricultural area at Texcoco. The combination of these factors, along with the high population density of this area, are likely to be the cause of the NH<sub>3</sub> enhancements observed in this part of the city. This enhancement is partially in agreement with the location of the larger NH<sub>3</sub> emissions reported in the Mexico City Emissions Inventory (SEDEMA, 2018, 2021) shown in Figure 3.1 in the northern part of the city, which is mainly associated with population activities and domestic animals' excreta. Figure 3.7d will be discussed in Section 3.3.3.

Figures 3.7a-c show the variations of NH<sub>3</sub> over the year, with the largest columns measured during the warm-dry season and to the northeast of UNAM. In contrast, the NH<sub>3</sub> columns are reduced in the wet season when wet deposition can occur and are smallest during the cold-dry season, when there are lower temperatures and less NH<sub>3</sub> volatilization. To investigate the influence of local topography on the NH<sub>3</sub> distribution, Figure 3.8 compares the average IASI-NH<sub>3</sub> total column spatial distribution (a) with altitude (b). The figure illustrates that the highest columns are located at the lowest altitudes while the lowest columns are at higher altitudes, reflecting the source locations and the boundary layer dynamics. The figure shows that the main NH<sub>3</sub> sources in MCMA are located in the most urbanized areas in Mexico City and Estado de Mexico at an altitude of around 2250 m. These urban emissions agree with the statement of Li et al. (2020) that human NH<sub>3</sub> emissions are contributing significantly to the total NH<sub>3</sub> emissions in hot and highly populated urban areas such as Mexico City. A rough estimation using 25 °C as an average diurnal temperature for Mexico City and the 0.4 mg of NH<sub>3</sub> per hour at 25 °C from Li et al. (2020) resulted in an estimate of 34 tonnes of NH<sub>3</sub> per year, a contribution of the same order of magnitude as all the "point sources" and "urban waste" combined according to the Mexico City Emissions Inventory (SEDEMA, 2018, 2021).

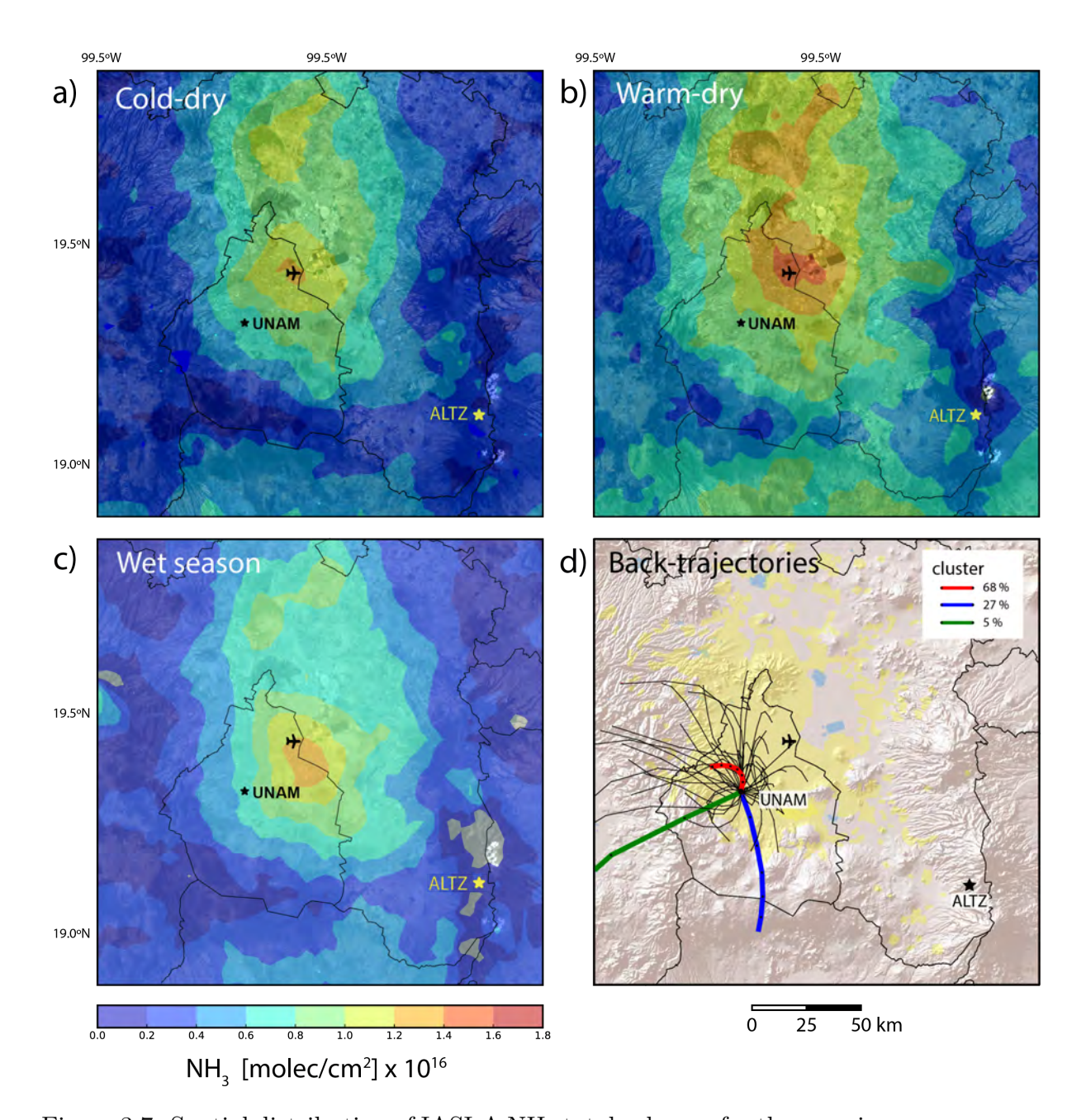


Figure 3.7: Spatial distribution of IASI-A NH<sub>3</sub> total columns for the morning overpass of MetOp-A over Mexico City, averaged over 2008-2018 for: (a) the cold-dry season (November – February), (b) the warm-dry season (March-May), and (c) the wet season (June-October). HYSPLIT back-trajectories for the UNAM site are shown in panel (d). The stars indicate the locations of both stations, and Mexico City International Airport is shown for reference.

Comparisons between the NH<sub>3</sub> seasonal variability and time evolution over the UNAM station in Mexico City were performed using morning (9-11 h) FTIR-NH<sub>3</sub> columns

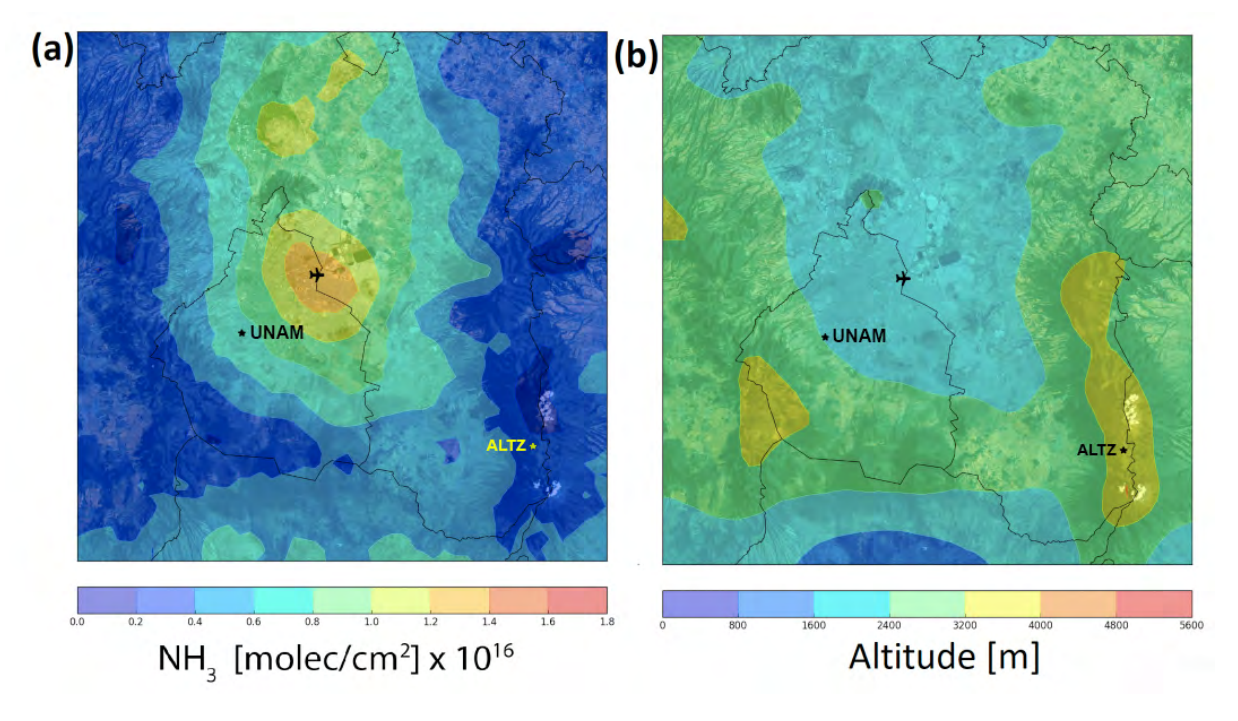


Figure 3.8: Spatial distribution of (a) IASI-A NH<sub>3</sub> total columns for the morning overpass of MetOp-A over Mexico City, averaged over 2008-2018 (b) altitudes in Mexico City from the Space Shuttle Radar Topography Mission Global product (SRTMGL3) (Farr et al., 2007). The stars indicate the location of ground-based stations, and Mexico City International Airport is shown for reference.

and IASI-NH<sub>3</sub> columns with a spatial criterion of < 20 km from the UNAM station (Figure 3.9a). The NH<sub>3</sub> seasonal variability over Mexico City in Figure 3.9a, is similar for both the IASI and ground-based FTIR NH<sub>3</sub> columns and is in agreement with Figure 3.4. However, the IASI-NH<sub>3</sub> shows a consistent negative bias. The time evolution is represented by the IASI-NH<sub>3</sub> and FTIR-NH<sub>3</sub> annual averages in Figure 3.9b. The datasets suggest an increasing trend in the annual averages of the NH<sub>3</sub> total columns, with larger columns observed in the most recent years, even in Altzomoni except for 2013, which was affected by the February 27 event as discussed previously.

The average annual increase of the IASI-NH<sub>3</sub> columns between 2008 and 2018 (using the < 20 km spatial criterion and the same Fourier fit as for the FTIR data) is  $38 \pm 7.6 \times 10^{13}$  molec. cm<sup>-2</sup> yr<sup>-1</sup> for Mexico City. This is a larger positive trend than that of  $2.5 \pm 1.5 \times 10^{13}$  molec. cm<sup>-2</sup> yr<sup>-1</sup> reported by Van Damme et al. (2021) for all of

Mexico over the same period, but lies between the values obtained in this study for the remote and urban FTIR measurements.

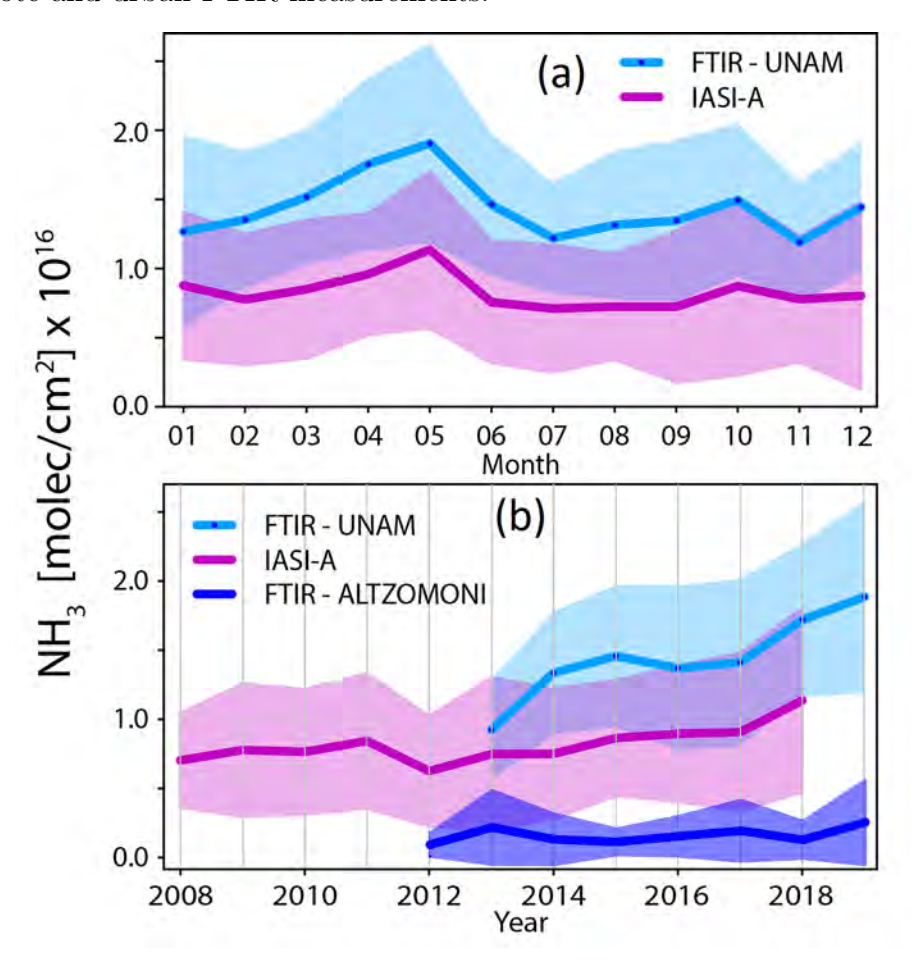


Figure 3.9: IASI and FTIR NH<sub>3</sub> total columns with coincidence criteria of < 20 km and < 2 hr: (a) monthly averages at UNAM, (b) annual averages at UNAM and Altzomoni. The shaded area indicates  $\pm 1\sigma$ .

# 3.3.3 Back-Trajectory Analysis and Origin Observed $NH_3$ in Mexico City

A cluster analysis was applied using 8-hour back-trajectories 100 m above UNAM station to identify the main transport pathways for air masses arriving at this station that correspond to the highest average hourly NH<sub>3</sub> total columns (Figure 3.7d). The 100 m cluster was considered the most representative because NH<sub>3</sub> is mostly concentrated near the surface. The TSV method was able to represent the primary

trajectories at 100m above UNAM with only three clusters. It was found that 68% of the trajectories originate from the north (red line with black dots), 27% from the west-southwest (green line), and 5% from the south (blue line). However, the individual back-trajectories that comprise the red cluster (the thin black lines in Figure 3.7d), indicate that most of the NH<sub>3</sub> detected at UNAM comes from a variety of local sources and does not originate exclusively from NH<sub>3</sub>-enriched air masses transported from the enhancement region to the northeast observed in Figures 3.7a-c. This is in agreement with Viatte et al. (2022). The relationship between the back-trajectories and measured NH<sub>3</sub> columns can be explained by the fact that Mexico City is located in a basin; the wind fields are constricted in this basin and in general they are breeze winds (6 km/h). Under these conditions, small locally distributed NH<sub>3</sub> urban emissions seem to be the main cause of the high column values of this pollutant measured at the UNAM station, this agrees with Figure 3.8, which shows that the main NH<sub>3</sub> sources in MCMA seem to be urban.

# 3.4 Conclusions

This work presented the temporal and spatial distribution of NH<sub>3</sub> total columns over the Mexico City Metropolitan Area derived from two ground-based FTIR spectrometers and IASI satellite observations. The average NH<sub>3</sub> total column at the urban UNAM site  $(1.46 \pm 0.64 \times 10^{16} \text{ molec. cm}^{-2})$  is considerably larger than that at the remote station Altzomoni  $(1.87 \pm 2.40 \times 10^{15} \text{ molec. cm}^{-2})$ , with a clear difference in the diurnal cycle but similar seasonal variability. The NH<sub>3</sub> spatial distribution from IASI shows the largest NH<sub>3</sub> columns in the northeast part of the city, an area surrounded by water bodies, a landfill, a compost plant for the treatment of all the organic waste, and the airport. The IASI ANNI-NH<sub>3</sub>-v3 data product underestimates the NH<sub>3</sub> total columns over Mexico City, with a mean relative difference of

32% over the period 2008-2018, but showed a similar temporal variability and a good correlation with FTIR measurements (R = 0.72).

The analysis of back-trajectories for the largest NH<sub>3</sub> enhancement events suggests that most of the NH<sub>3</sub> measured at the urban station is coming from local sources. The NH<sub>3</sub> observed at the remote site is most likely transported from the surroundings and it is influenced by biomass burning events. These results present evidence that sources other than from agriculture, such as motor vehicles, fires, human emissions, domestic animals, water discharge, and waste, have a significant contribution to the total NH<sub>3</sub> budget in the city. In general, an average annual increase is observed in Mexico City from both ground-based stations (92  $\pm$  3.9×10<sup>13</sup> molec. cm<sup>-2</sup> yr<sup>-1</sup> at UNAM, 8.4  $\pm$  1.4×10<sup>13</sup> molec. cm<sup>-2</sup> yr<sup>-1</sup> at Altzomoni) and IASI (38  $\pm$  7.6×10<sup>13</sup> molec. cm<sup>-2</sup> yr<sup>-1</sup>).

Based on the results of this chapter, two measurement campaigns were conducted by the Instituto de Ciencias de la Atmósfera y Cambio Climático (UNAM), using passive samplers to collect NH<sub>3</sub> in the northeast part of the city, reporting NH<sub>3</sub> concentrations within the range of 0.002 to 0.0622 mg m<sup>-3</sup>. These observations, together with model data, will examine the role of reactive nitrogen in the pollution of Mexico City. In addition, the results of this chapter were presented in the "Virtual Workshop: Diagnosis of current knowledge of the scientific bases for air quality management in the Megalopolis region", which was held on April 21 and 22, 2022. The workshop was jointly organized by the Molina Center for Strategic Studies in Energy and the Environment (MCE2) and the government of Mexico, and the results were summarized and published in Molina et al. (2023). A re-evaluation of the contribution of NH<sub>3</sub> emission sources to the Mexico City inventory is suggested. Measures to mitigate NH<sub>3</sub> emissions and reduce these positive trends are important, given that NH<sub>3</sub> is closely linked to secondary aerosol formation and the deterioration of ecosystems.

# Chapter 4

# Variability and Trends of NH<sub>3</sub>

# 4.1 Introduction

This chapter presents the variability and trends of NH<sub>3</sub> using total columns retrieved from spectroscopic solar absorption measurements performed at 22 ground-based FTIR sites. The sites are globally dispersed in both hemispheres, ranging from 45°S to 80°N, with most of them affiliated with NDACC. In addition, to complement the measurements and provide additional insight, the FTIR data are compared with simulated NH<sub>3</sub> from the GEOS-Chem High Performance CTM and the Tropospheric Chemistry Reanalysis product. Variability and trends from the FTIR measurements are first explored, followed by comparisons with the GCHP and TCR-2 NH<sub>3</sub> total columns. GCHP exhibited a better general agreement with the FTIR observations than TCR-2; potential reasons for this are explored in this work. A manuscript on this work titled Herrera et al., NH<sub>3</sub> variability and trends from globally distributed FTIR ground-based measurements and simulations, will be submitted to *Journal of Geophysical Research: Atmospheres*, (Herrera et al., 2025).

# 4.2 Materials and Methods

# 4.2.1 Ground-based FTIR NH<sub>3</sub> Observations

### FTIR Sites

Figure 4.1 shows the location of the 22 study sites used in this work. Most of the sites are affiliated with the Network for the Detection of Atmospheric Composition Change (De Mazière et al., 2018), contributing data from high-resolution FTIR spectrometers, mainly using the Bruker Optik GmbH IFS 120/125HR spectrometer that can record solar absorption spectra with a typical spectral resolution of 0.0035 cm<sup>-1</sup>, and is equipped with either KBr or CaF<sub>2</sub> beamsplitters, and MCT and InSb detectors. The Mexico City instrument is a low-resolution Bruker Optik GmbH Vertex 80, which was included in this study due to the relevance of the site, as it is located in the south of Mexico City, one of the largest metropolitan areas in the world, and the largest in North America. The Los Angeles instrument is the MkIV high-resolution FTIR spectrometer, which has been performing ground-based observations since the 1980s, mainly in California (Toon, 1991; Sen et al., 1996; Toon et al., 2018).

Table 4.1 presents the main characteristics of each of the 22 FTIR sites. Eureka, Thule, and Ny Alesund are Arctic sites where NH<sub>3</sub> sources are limited. Zugspitze, Jungfraujoch, Izana, Altzomoni, and Reunion Maido are high-altitude stations, with generally smaller NH<sub>3</sub> columns. St. Petersburg, Toronto, Los Angeles, Hefei, and Mexico City are sites located in heavily urbanized areas with populations of millions. Bremen, Boulder, Tsukuba, Paramaribo, Porto Velho and Wollongong are located in less urbanized areas, while Garmisch, Reunion St. Denis, and Lauder are more remote sites. Data from the NDACC FTIR instruments have been used to accurately document trends of many stratospheric and tropospheric gases (De Mazière et al., 2018).

Table 4.1: FTIR sites used in this study.

Station	Latitude	Longitude	Elevation	Measurement	Primary NH <sub>3</sub> Sources
			m.a.s.l.	Period	
Eureka	80.05°N	86.4°2W	610	2006-2020	Seabirds, biomass burning
Ny Alesund	78.92°N	$11.93^{\circ}E$	20	2017-2019	Seabirds, biomass burning
Thule	76.53°N	68.74°W	225	1999-2022	Seabirds, biomass burning
St. Petersburg	59.90°N	$29.80^{\circ}$ E	20	2010 - 2022	Biomass burning, local sources
Bremen	53.10°N	$8.80^{\circ}$ E	27	2004-2018	Fertilizers, livestock
Garmisch	50.01°N	$14.45^{\circ}$ E	302	2004 - 2007	Fertilizers, transport
Zugspitze	47.42°N	10.98°E	2694	1995-2023	High altitude, fertilizers, transport
Jungfraujoch	46.55°N	7.98°E	3580	2008 - 2023	High altitude, no large sources, transport
Toronto	43.66°N	$79.40^{\circ}$ W	174	2002-2023	Fertilizers, biomass burning
Boulder	39.99°N	$105.26^{\circ}\mathrm{W}$	1634	2010 - 2022	Fertilizers, biomass burning
Tsukuba	36.05°N	$140.13^{\circ}$ E	31	2014 - 2022	Fertilizers, biomass burning
Los Angeles	$34.20^{\circ}N$	$118.17^{\circ}$ W	345	1985-2024	Livestock, local sources
Hefei	$31.90^{\circ}N$	$117.17^{\circ}E$	30	2017 - 2022	Fertilizers, biomass burning
Izana	$28.30^{\circ}N$	$16.48^{\circ}$ W	2367	2000-2022	High altitude, biomass burning, transport
Mexico City	19.32°N	$99.17^{\circ}$ W	2280	2012 - 2022	Large local sources
Altzomoni	$19.11^{\circ}N$	98.65°W	3985	2012 - 2022	High altitude, biomass burning, transport
Paramaribo	$5.75^{\circ}N$	55.20°W	23	2018 - 2019	Biomass burning, local sources
Porto Velho	8.77°S	63.87°W	87	2019	Fertilizers, biomass burning
Reunion St. Denis	$20.90^{\circ}$ S	$55.50^{\circ}$ E	85	2004 - 2011	Fertilizers, biomass burning
Reunion Maido	$21.10^{\circ}$ S	$55.40^{\circ}$ E	2155	2013 - 2023	High altitude, fertilizers, biomass burning
Wollongong	$34.41^{\circ}S$	150.88°E	30	2007 - 2022	Fertilizers, biomass burning, industry
Lauder	$45.04^{\circ}\mathrm{S}$	169.68°W	370	1996-2022	Fertilizers, livestock

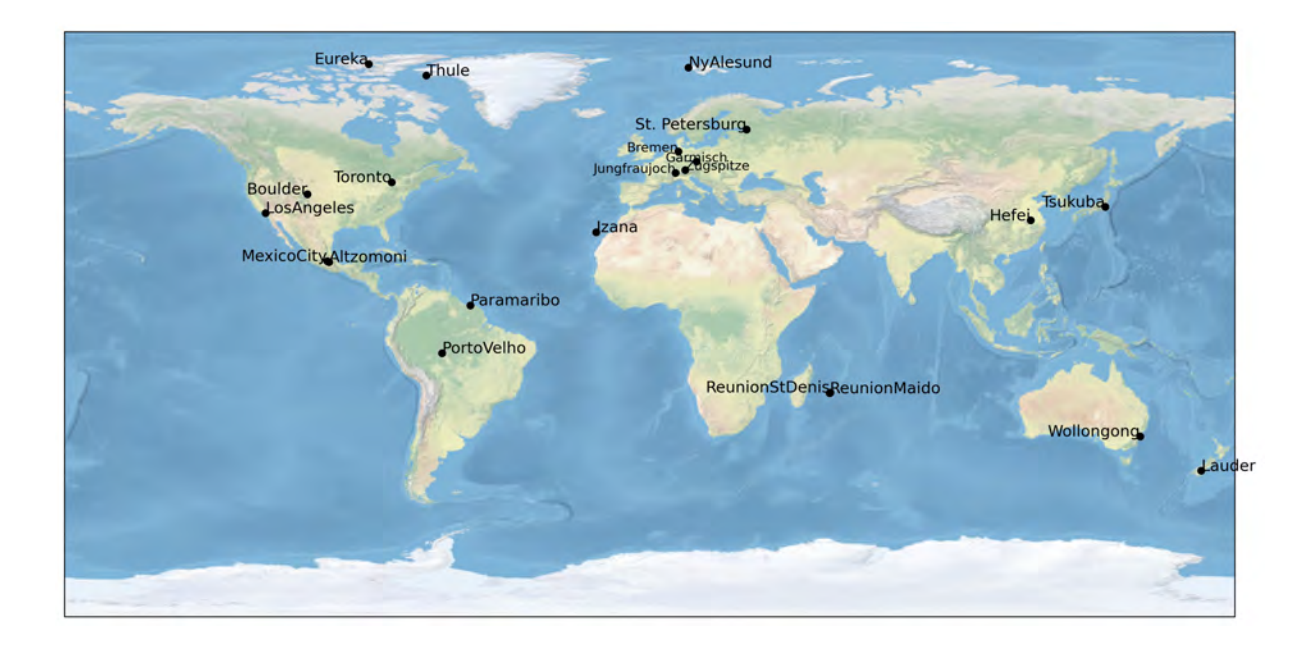


Figure 4.1: Location of the 22 ground-based Fourier transform infrared spectrometer sites used in this study.

# FTIR NH<sub>3</sub> Retrieval Strategy

The retrieved NH<sub>3</sub> total columns presented in this work were obtained following the strategy described in Section 2.1.5. For most sites, the solar FTIR spectra were analyzed using the SFIT4 retrieval algorithm (https://wiki.ucar.edu/display/sfit4/) version 0.9.4.4 to obtain the NH<sub>3</sub> total columns; except for Garmisch, Zugspitze, and Izana, which used PROFFIT9 (Hase et al., 2004), and GFIT for Los Angeles. The average DOFS for all sites was  $1.07 \pm 0.15$ . The total error on the NH<sub>3</sub> total columns was calculated as the square root sum of the squares of all systematic and statistical errors (García et al., 2021), with an average value for all sites of 0.93  $\pm$   $1.30 \times 10^{15}$  molec. cm<sup>-2</sup>.

# 4.2.2 Simulations of NH<sub>3</sub>

### **GEOS-Chem**

NH<sub>3</sub> total column simulations from the GCHP CTM between 2003 and 2021 were used. The horizontal resolution is C48 resolution ( $\approx 2^{\circ} \times 2.5^{\circ}$ ). The modeled fields were archived at a temporal resolution of 2 h for comparison with the FTIR observations. The details of this simulation are described in Section 2.2.1.

### TCR-2

NH<sub>3</sub> total column simulations from TCR-2 between 2005 and 2018 were used. The product has a horizontal resolution of  $1.1^{\circ} \times 1.1^{\circ}$  and was archived at a temporal resolution of two hours. The TCR-2 product was described in Section 2.2.2.

# 4.2.3 Trend Analysis

To derive the long-term trends for the time series, we used a linear trend model with fitted Fourier series to account for seasonality, and bootstrap resampling methods to derive the 95% confidence intervals following the methodology of Friedrich et al. (2020). The trend model is described as follows:

$$y_t = d_t + s_t + u_t \tag{4.1}$$

where  $y_t$  are NH<sub>3</sub> measurements at time t,  $d_t$  is the unknown trend,  $s_t$  is the intraannual seasonal pattern, and  $u_t$  is the error term.  $s_t$  is described by Fourier terms given by:

$$s_{t} = \sum_{j=1}^{S} a_{j} cos(2j\pi t) + b_{j} sin(2j\pi t)$$
(4.2)

where  $a_j$  and  $b_j$  are the Fourier series parameters.

The seasonal variability is relevant for trends in atmospheric gases, and previous

studies have shown that this variability is well captured by using the Fourier series of order 3 (S=3) (Gardiner et al., 2008; Franco et al., 2016; Prignon et al., 2019; Yamanouchi et al., 2021; Friedrich et al., 2020; Wizenberg et al., 2024). For this study, we apply Fourier series fitting of S=3 to the daily means of the NH<sub>3</sub> total column time-series data from the FTIR sites, GCHP, and TCR-2, to the sites with more than 150 data points to ensure a good fit of the linear trend model. In addition, to estimate the uncertainty, we used bootstrap resampling methods, with a bootstrap population of 5000 as recommended in Gardiner et al. (2008), and an autoregressive wild bootstrap method (AWB) as recommended by Friedrich et al. (2020) to obtain the corresponding 95% confidence intervals (CI). The latter is more suitable for analyzing geophysical time series as it is specifically designed to account for missing observations, autocorrelation, and seasonal effects in the datasets. Trends for which the CI does not include zero are considered statistically significant.

# 4.3 FTIR Results

# 4.3.1 Time Series

The retrieved total column time series of NH<sub>3</sub> from the 22 FTIR sites are shown in Figure 4.2. The NH<sub>3</sub> time series are very diverse across all sites, with Thule, Zugspitze, Toronto, Los Angeles, Izana, and Lauder, the only sites with more than 20 years of data. Most of the sites have between ten and 20 years of data, and only five sites have less than three years of data. The largest total columns of NH<sub>3</sub> are seen in Hefei, Bremen, Toronto, Mexico City and Porto Velho. These sites are in urban areas influenced by nearby agricultural activities, local sources, and biomass burning events. In contrast, the smallest total columns of NH<sub>3</sub> are mainly at the Arctic sites, where the NH<sub>3</sub> sources are limited, and in Reunion Maido and Jungfraujoch, two high-altitude sites that most likely were measuring NH<sub>3</sub> background concentrations.

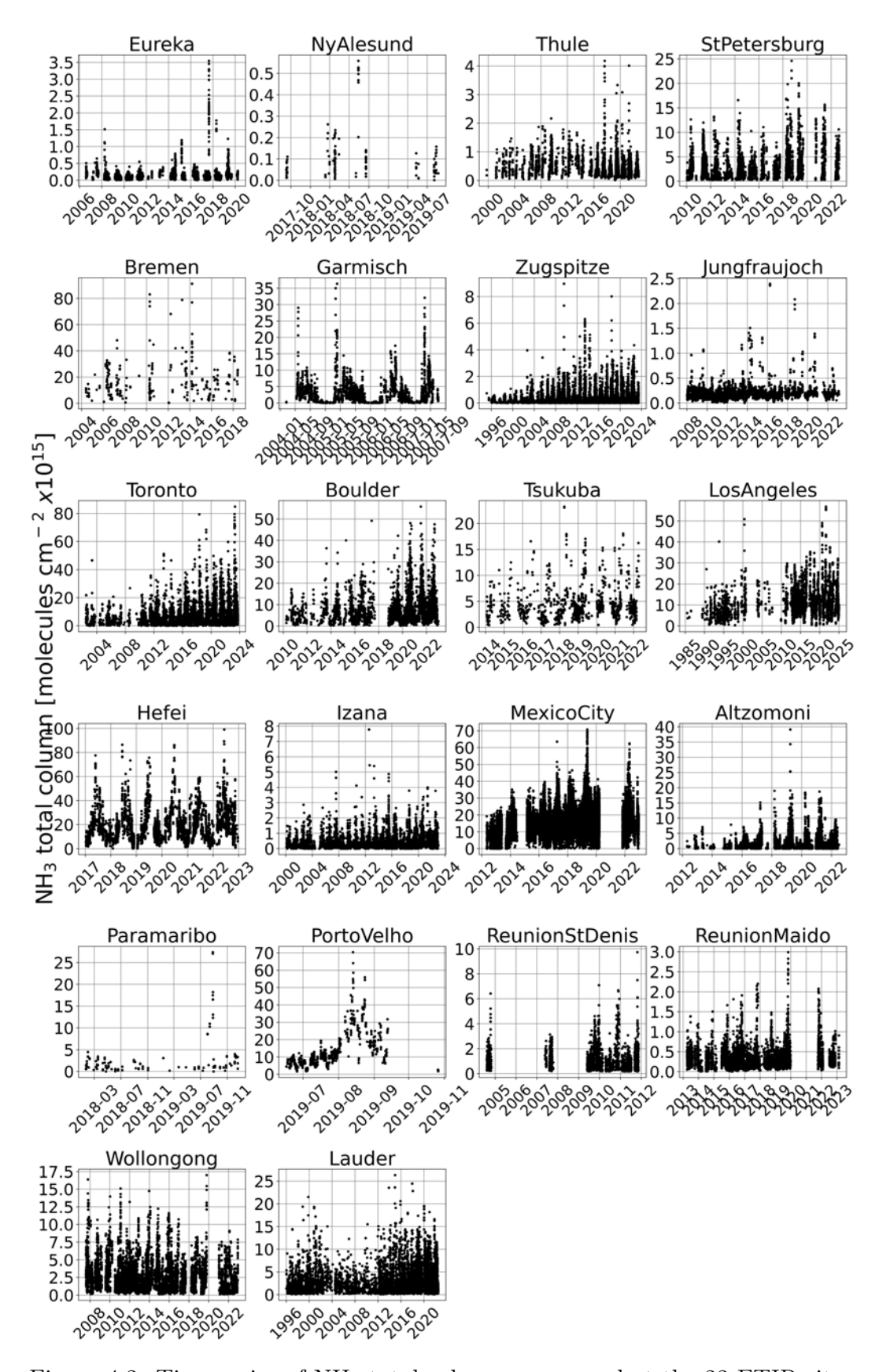


Figure 4.2: Time series of NH<sub>3</sub> total columns measured at the 22 FTIR sites.

However, some noticeable enhancements can be observed at some of the sites, such as Eureka, Thule, Izana, Los Angeles, Mexico City, Altzomoni, Paramaribo, Porto Velho and Reunion Maido, mainly attributed to biomass burning events. The NH<sub>3</sub> enhancements at Eureka and Thule were linked to the 2017 Canadian wildfires by Lutsch et al. (2019). A large fire that occurred in the Amazon that reached several regions, analyzed by Bencherif et al. (2020), potentially reached Porto Velho and Paramaribo in August 2019. The  $NH_3$  enhancements in late 2019 at the Reunion Maido site could be from biomass burning plumes from Africa and even the Amazon region (Callewaert et al., 2022). Simultaneous enhancements of NH<sub>3</sub> and CO at Porto Velho and Reunion Maido during 2019 are shown in Figures B.1 and B.2 in the Appendix B, as CO is largely emitted by fires with a longer lifetime than NH<sub>3</sub> and can be used as a reference species (Whitburn et al., 2017). For Mexico City, the simultaneous enhancements of NH<sub>3</sub> and CO are also shown in Figure C.1 during May 2019; this enhancement was part of a pollution event further discussed in Chapter 5. Unfortunately, there are no simultaneous measurements of CO at Altzomoni during the enhancement observed in late March 2019; however, a few fires in the surrounding areas were detected by the Aqua-MODIS instrument (https://wvs.earthdata.nasa.gov). Similarly, for the Los Angeles site, NH<sub>3</sub> and CO enhancements are observed during 2020 and 2021 (Figure B.3, which can be attributed to the exceptional California fires (Keeley and Syphard, 2021; Safford et al., 2022; Ayars et al., 2023).

For the Izana site, the enhancements observed in 2012 are from the Tenerife Island fire that reached the site in July 2012 (Santamarta Cerezal, 2013). In addition, in September 2021, a volcanic eruption on the island of La Palma (Canary Islands) affected the Izana site (García et al., 2023; Campeny et al., 2023). Studies on NH<sub>3</sub> emissions from volcanic eruptions are limited, but simultaneous enhancements of NH<sub>3</sub> and SO<sub>2</sub> from volcanoes has been reported (Uematsu et al., 2004; Adams et al., 2017), Figure B.4 shows SO<sub>2</sub> and NH<sub>3</sub> enhancements during the Tajogaite eruption from 19

September 2021 to 13 December 2021 during which volcanic plume reached the Izana site.

For the analysis in the following sections, the sites are divided into three categories: Arctic (Eureka, Ny Alesund, Thule), Northern Hemisphere (St. Petersburg, Bremen, Garmisch, Zugspitze, Jungfraujoch, Toronto, Boulder, Tsukuba, Los Angeles, Hefei, Izana, Mexico City, Altzomoni and Paramaribo), and Southern Hemisphere (Porto Velho, Reunion St. Denis, Reunion Maido, Wollongong, and Lauder).

# 4.3.2 Seasonal Variability

The seasonal variability in NH<sub>3</sub> total columns corresponding to the monthly means calculated across all years is shown in Figure 4.3. The seasonal patterns present similarities across most sites, with a few exceptions. In addition, the monthly means are seen to increase for the most recent years for most sites. The monthly mean total columns vary between 2.66 and  $6.92 \times 10^{15}$  molec. cm<sup>-2</sup> for all sites, with the maximum during spring and summer and the minimum in winter. For the Arctic sites, the variability of NH<sub>3</sub> across the year (between February and October due to the lack of Sunlight during the Arctic winter) is small. The columns are between 0.06 and  $0.70 \times 10^{15}$  molec. cm<sup>-2</sup> with the minimum in March and the maximum in August at all three sites, and an average of  $0.40 \times 10^{15}$  molec. cm<sup>-2</sup>, mainly due to NH<sub>3</sub> being transported from large biomass burning events in northern latitudes, such as the August wildfires in 2017 (Lutsch et al., 2019). According to Riddick et al. (2012), the seabird colonies near Thule are larger than those near Eureka, and the difference in the magnitude of the NH<sub>3</sub> columns between these sites is attributed to this source as shown by Lutsch et al. (2019), mainly due to the presence of seabird colonies on the Greenland coast (Murphy et al., 2025).

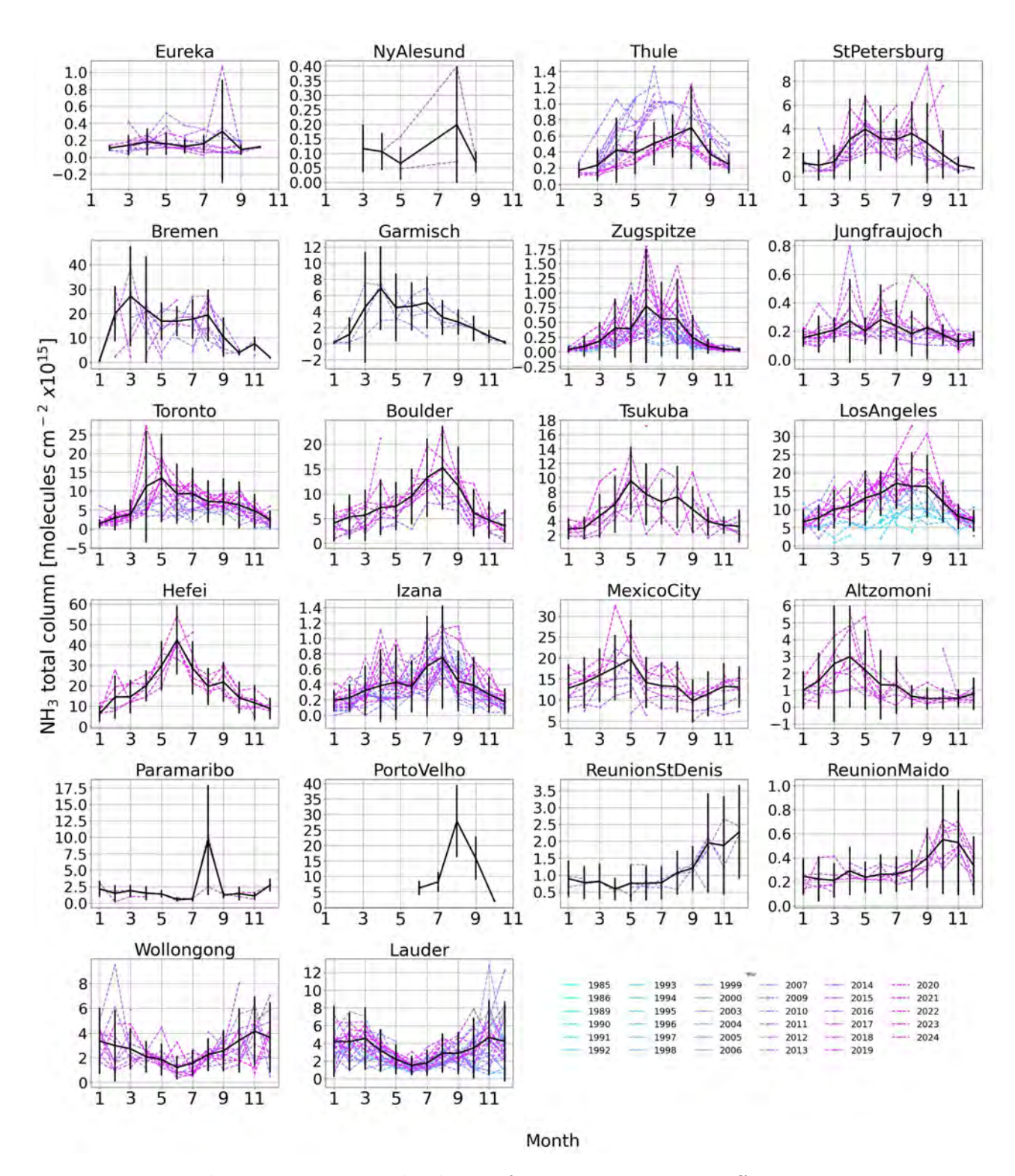


Figure 4.3: Monthly mean NH<sub>3</sub> total columns for each FTIR site. Different years are shown in different colours, with the most recent years in pink shades and older years in blue shades. The thick black line with error bars is the mean for all years  $\pm 1\sigma$ .

For the sites located in the Northern Hemisphere, excluding the Arctic sites, the monthly mean NH<sub>3</sub> total columns vary between 2.80 and  $8.77 \times 10^{15}$  molec. cm<sup>-2</sup>, with the largest values observed between April and August and the smallest values during December and January. For most sites, NH<sub>3</sub> has a maximum in April and May, then decreases with another maximum in August in a few cases. However, the maximum monthly mean was found at Hefei in June (42.38  $\times$  10<sup>15</sup> molec. cm<sup>-2</sup>) and the minimum at Zugspitze in December (0.03  $\times$  10<sup>15</sup> molec. cm<sup>-2</sup>). The observed pattern could reflect the influence of the meteorological conditions, mainly related to the NH<sub>3</sub> temperature sensitivity, warmer temperatures favour the conditions for NH<sub>3</sub> volatilization (Sutton et al., 2013).

Figure B.5 shows the monthly means of surface temperature derived from GCHP. However, at some sites such as Boulder, a maximum was observed later in the year, probably due to the fertilizer application season and agricultural practices. For Toronto, Mexico City, and Altzomoni, the seasonal patterns were directly compared with those reported in Yamanouchi et al. (2021) and Herrera et al. (2022) as those studies also used these FTIR datasets. For Toronto, the previously reported means were calculated between 2002 and 2018, while this study extends the time series up to 2023; the patterns are very similar with the maximum in May and the minimum in January, however, the columns are larger for April and June in the present study. For Mexico City and Altzomoni, the previously reported time series ended in 2020, while this study extends the time series up to 2022; the patterns are similar with a small increase in the total column means in this study.

For the sites in the Southern Hemisphere, a similar pattern is seen, with more NH<sub>3</sub> during the warmest months, in this case during the last months of the year, with overall monthly mean total columns between  $1.26 - 6.87 \times 10^{15}$  molec. cm<sup>-2</sup>. The maximum values were found at Porto Velho in August  $(27.82 \times 10^{15} \text{ molec. cm}^{-2})$ 

and the minimum at Reunion Maido during March  $(0.21 \times 10^{15} \text{ molec. cm}^{-2})$ . For Porto Velho, it is difficult to isolate a seasonal pattern due to the limited observations, however, it is clear that August is the month with more NH<sub>3</sub>, potentially influenced by Amazonian biomass burning events, in agreement with a study by Whitburn et al. (2015), and specifically for 2019 when an exceptional wildfire event took place in the southern portion of the Amazon during August (Bencherif et al., 2020). Plumes from this fire event could have reached Paramaribo, explaining the enhancements in this site. Overall, the reported seasonal patterns are in agreement with other studies such as Van Damme et al. (2015), which used satellite data. However, this study provides details for the specific sites.

### 4.3.3 Diurnal Variability

One advantage of the FTIR measurements, compared to satellite data, is their frequency, which allows diurnal cycles to be derived by calculating the hourly means as shown in Figure 4.4 in local hours for the 22 sites. In this case, similar to the monthly means, larger columns are observed for the most recent years for most sites, however, the diurnal variability is very different across the sites, with hourly means between 0.20 and  $6.74 \times 10^{15}$  molec. cm<sup>-2</sup>. Of the three Arctic sites, Thule showed the most complete diurnal cycle, while very little diurnal fluctuation is observed at these sites, with a mean of  $0.31 \times 10^{15}$  molec. cm<sup>-2</sup> and a variation of less than  $0.5 \times 10^{15}$  molec. cm<sup>-2</sup> during the day. This pattern is expected as there are limited sources in the Arctic region that change daily NH<sub>3</sub> concentrations. For the other sites located in the Northern Hemisphere, the diurnal means were between 0.06 and  $9.01 \times 10^{15}$  molec. cm<sup>-2</sup> with the larger values in the afternoon between 16h and 17h and the minimum in the early morning.

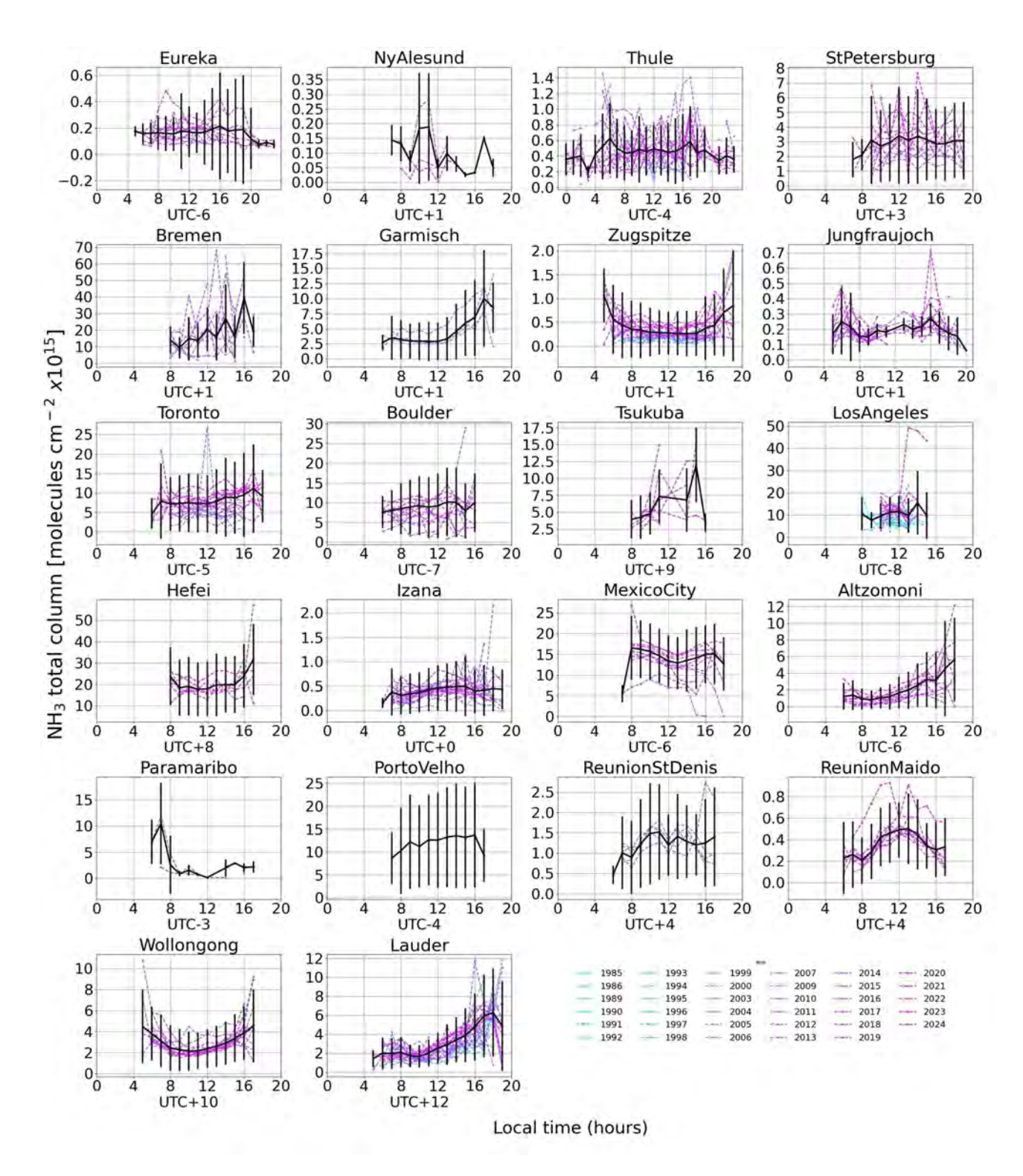


Figure 4.4: Hourly mean NH<sub>3</sub> total columns in local time (hours, with offset from UTC for each site indicated on each panel) for each FTIR site. Different years are shown in different colours with the most recent years in pink shades and older years in blue shades. The thick black line with error bars is the mean for all years  $\pm 1\sigma$ .

For the Southern Hemisphere, the diurnal means were between 1.64 and  $4.76 \times 10^{15}$  molec. cm<sup>-2</sup>, smaller values than in the Northern Hemisphere, with no consistent patterns across the sites; however, Lauder presents a pattern similar to Altzomoni, with columns increasing steadily during the day until reaching a peak in the late afternoon. The variability of Altzomoni was explored in more detail in Chapter 3 and Herrera et al. (2022), where this pattern was attributed to NH<sub>3</sub> transported from surrounding urban areas. The high-altitude sites also present very little variability throughout the day, except for Altzomoni.

The reasons for the observed patterns vary depending on each site. Diurnal variations in the NH<sub>3</sub> total columns can be associated with vertical variations of the relative humidity and temperature profiles (Kutzner et al., 2021), as changes in these conditions as well as in the pH can lead to phase changes between NH<sub>3</sub> in the gas and particulate phase (Pye et al., 2020). In addition, transport from the surrounding regions plays a major role in the variability for some sites. Finally, for the sites located in urban areas, traffic emissions during rush hour have an impact on the diurnal variability of NH<sub>3</sub> (Kotnala et al., 2019; Osada et al., 2019; Herrera et al., 2022; Gu et al., 2022; Viatte et al., 2023).

#### 4.3.4 FTIR Trends

Long-term trends in the daily mean NH<sub>3</sub> total column are calculated using Eqs. 4.1 and 4.2. The FTIR trends, the period used for the trend estimation, and confidence intervals for all sites are summarized in Table 4.2 and plotted in Figure 4.5. The mean trend for all sites is  $19.43 \ (14.18-24.68) \times 10^{13} \ \text{molec.} \ \text{cm}^{-2} \ \text{yr}^{-1} \ \text{driven}$  by the large trends at Hefei and Mexico City. Most of the sites present positive and significant trends. Only two sites present negative trends, Thule and Wollongong. Most of the trends are in agreement with trends reported by Van Damme et al. (2021) using ten

years of satellite data. The drivers behind these trends vary between sites, and can be due to a change in  $NH_3$  emissions, a change in meteorological conditions, or a change in the lifetime of  $NH_3$  due to changes in  $NO_x$  and  $SO_2$  abundances.

For the Arctic sites, Thule presents the largest and most significant trend, although it is negative. As mentioned in Section 4.3.2, seabird colonies are an important source of NH<sub>3</sub> at this site, so changes in the seabird population could impact the trend, such as the reported global decline in seabird population of 69.7% between 1950 and 2010 (Paleczny et al., 2015).

Europe is one of the few regions where actions towards the reduction of NH<sub>3</sub> emissions have been implemented. Zugspitze is located in Germany, where according to the European Environment Agency (EAP) National Emission Reduction Commitments Directive reporting status 2022 (European Environment Agency, 2023), there have been reductions in NH<sub>3</sub>, NOx, and SO<sub>2</sub> emissions. However, the FTIR time series at the five European sites don't show this reduction, suggesting that more efforts focused on reducing NH<sub>3</sub> from the agricultural sector are needed. Trends in reduced N have been previously reported in North America (Yao and Zhang, 2016; Yamanouchi et al., 2021; Benish et al., 2022; Herrera et al., 2022). In Canada, significant reductions in emissions of  $SO_x$  (79%) and  $NO_x$  (41%) between 1990 and 2021 have been reported (Government of Canada, 2023). In the US, the Acid Rain Program requires major emissions reductions in  $SO_2$  and  $NO_x$  and has delivered annual  $SO_2$  reductions of over 95% and  $NO_x$  reductions of over 89% (U.S. Environmental Protection Agency, 2024). These changes could be increasing the atmospheric lifetime of NH<sub>3</sub> over Toronto, Boulder, and Los Angeles, resulting in the positive NH<sub>3</sub> trends. Mexico City has the largest positive and significant trend; this may be due to Mexican policies to regulate  $NO_x$  and  $SO_2$  that (similar to Boulder and Toronto) could be affecting the lifetime of  $NH_3$ .

Table 4.2: NH<sub>3</sub> mean total columns and  $\pm 1\sigma$  and absolute trends with 95% confidence intervals for the FTIR sites. Bold indicates a significant trend.

	TATOME OTTOTTO	NH3 Mean 10tal Column	$NH_3$ Trend and 95%	nd 95% CI
	Period	$(\text{molec. cm}^{-2}) \times 10^{15}$	(molec. $\text{cm}^{-2} \text{ yr}^{-1}) \times 10^{13}$	%
Eureka	2006 - 2020	$0.17 \pm 0.24$	$0.58\ (0.13-1.02)$	<b>3.0</b> $(0.73 - 5.21)$
Ny Alesund	2017 - 2019	$0.12 \pm 0.12$		ı
Thule	1999 - 2022	$0.46 \pm 0.34$	<b>-2.10</b> (-2.501.70)	<b>-7.7</b> (-9.1 – -6.25)
St. Petersburg	2010 - 2022	$3.07 \pm 2.85$	<b>11.70</b> $(3.54 - 19.60)$	$4.67\; (1.44 - 7.81)$
Bremen	2004 - 2018	$16.80 \pm 14.70$	$28.20 \; (-8.20 - 63.80)$	3.55 (-1.03 - 8.02)
Garmisch	2004 - 2007	$3.56 \pm 3.97$	$31.10 \; (-13.80 - 76.20)$	$10.64 \; (-6.39 - 28.04)$
Zugspitze	1995 - 2023	$0.32 \pm 0.55$	$0.84\; (0.58-1.10)$	$2.13\ (1.43 - 2.84)$
Jungfraujoch	2008 - 2023	$0.20\pm0.16$	$0.38\ (0.13-0.63)$	$1.89 \ (0.66 - 3.07)$
Toronto	2002 - 2023	$7.98 \pm 8.53$	<b>28.40</b> $(21.20 - 35.40)$	<b>4.68</b> $(3.53 - 5.82)$
Boulder	2010 - 2022	$9.00 \pm 7.42$	$37.30 \; (26.30 - 48.30)$	$5.93\; (4.11 - 7.75)$
Tsukuba	2014 - 2022	$4.64 \pm 3.45$	<b>19.10</b> $(7.02 - 31.40)$	5.16 (1.82 - 8.46)
Los Angeles	1985-2024	$11.31\pm7.07$	<b>23.4</b> $(19.60 - 27.40)$	$4.86\; (4.07 - 5.69)$
Hefei	2017 - 2022	$19.20 \pm 13.50$	<b>73.80</b> $(16.60 - 132)$	<b>4.36</b> $(0.78 - 7.90)$
Izana	2000 - 2022	$0.42\pm0.47$	$0.38\;(0.03-0.74)$	$0.88\; (0.07-1.69)$
Mexico City	2012 - 2022	$14.50 \pm 6.89$	$93.0 \; (78.8 - 107)$	<b>12.8</b> $(10.86 - 14.79)$
Altzomoni	2012 - 2022	$1.63 \pm 2.36$	$7.08\; (2.56-11.50)$	$10.73\; (3.94 - 17.46)$
Paramaribo	2018 - 2019	$3.02 \pm 4.85$	I	I
Porto Velho	2019	$11.80 \pm 9.82$	l	I
Reunion St. Denis	2004 - 2011	$1.21 \pm 1.04$	ı	I
Reunion Maido	2013 - 2023	$0.34 \pm 0.29$	$0.16 \; (-0.53 - 0.84)$	0.49  (-1.73 - 2.59)
Wollongong	2007-2022	$2.62 \pm 2.12$	<b>-3.78</b> (-7.100.35)	<b>-0.93</b> (-1.79 – -0.08)
Lauder	1996 - 2022	$3.15 \pm 2.95$	$2.37\; (0.86 - 3.85)$	$1.63\; (0.60-2.61)$
Mean for all sites	I	I	<b>19.43</b> $(14.18 - 24.68)$	$3.82\ (3.29 - 4.35)$

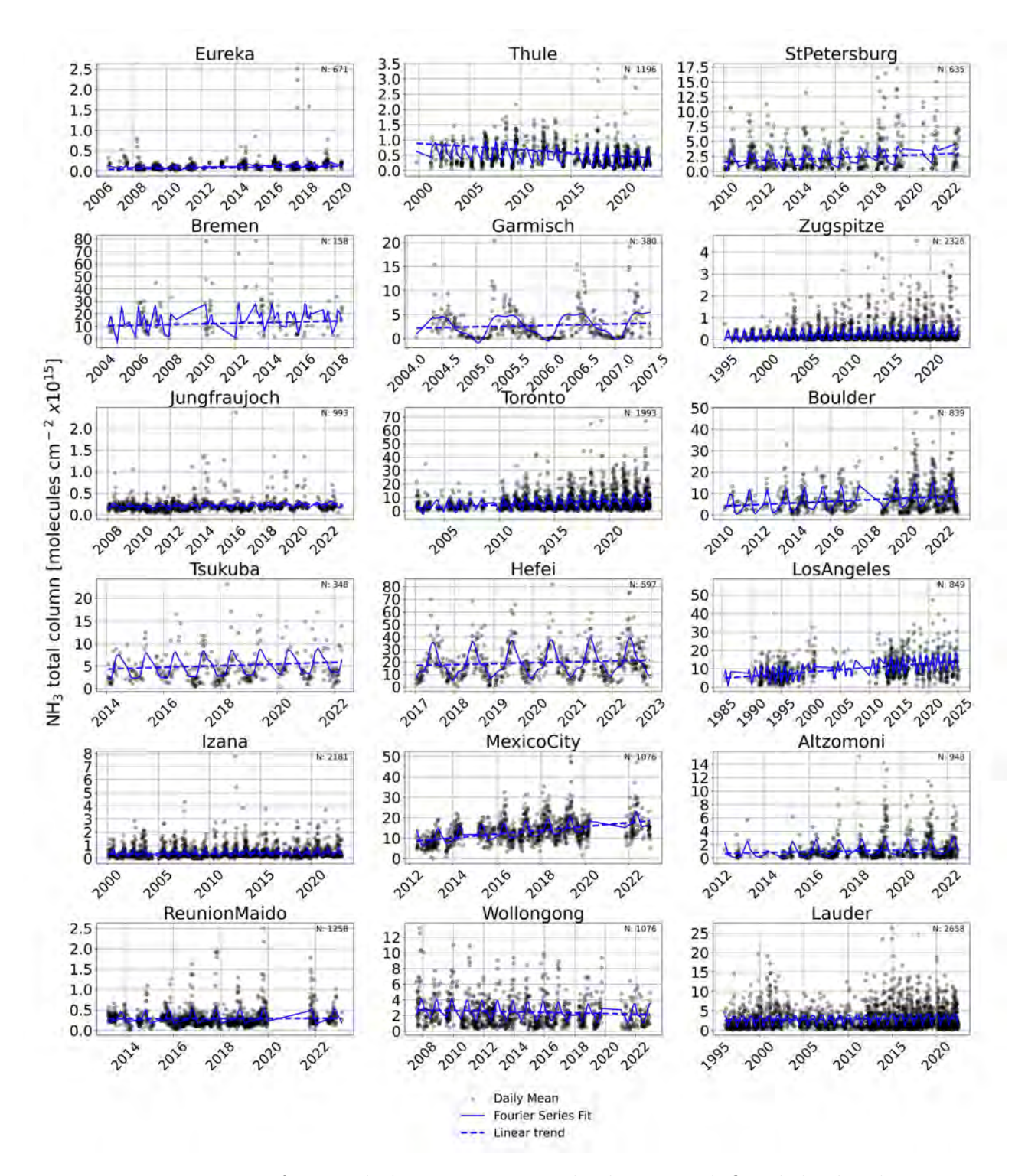


Figure 4.5: Time series of FTIR daily mean NH<sub>3</sub> total columns with fitted third-order Fourier series (solid blue line) and linear trends (dashed blue line) for the sites with sufficient data density to derive trends.

For the Southern Hemisphere, the largest trend is from Wollongong, and it is negative. There have been recent efforts in Australia to improve agricultural practices to mitigate emissions of different gases, based on the implementation of technology and a best management practices approach (Panchasara et al., 2021). For NH<sub>3</sub>, the focus is on reducing the emissions from volatilization by improving the irrigation methods, use of urease inhibitors, and use of ammonium-based fertilizers instead of urea (Pan et al., 2016). Zhang et al. (2022) emphasized the cost and benefits of NH<sub>3</sub> abatement in this region because the mitigation potential of NH<sub>3</sub> emissions from agricultural sources is around 32%. Similarly to Wollongong, several approaches to mitigate NH<sub>3</sub> emissions have been investigated for New Zealand (Jarvis and Ledgard, 2002; Parfitt et al., 2008; Saggar et al., 2013). Despite this, the trend for Lauder is positive and significant. Around 50% of Australia's and New Zealand's land area is used for agriculture. However, there are substantial differences in their agricultural sectors and diversity, with more diversification in Australia and dominance of livestock grazing and dairy production in New Zealand (Pannell and Rogers, 2022). Dairy farms involve several emission sources, such as grazing, fertilizer application, housed animals, and stored and applied excreta (Jarvis and Ledgard, 2002). Implementing strategies to mitigate emissions from several sources is more challenging, and this could be related to Lauder's positive trend. A more detailed discussion of similarities and differences in policy approaches regarding the agricultural situation in New Zealand and Australia is discussed in Pannell and Rogers (2022).

# 4.4 Comparison of Simulated NH<sub>3</sub> Total Columns

The FTIR measurements were used to evaluate the simulations of NH<sub>3</sub> by GCHP and TCR-2. Long-term time series of NH<sub>3</sub> total columns were extracted from the previously described GCHP model and TCR-2 product at the grid point closest to the latitude and longitude of each FTIR station. The total columns from GCHP and TCR-2 were smoothed using the FTIR averaging kernels (AVKs) and a priori profiles for each site following the methodology of Rodgers and Connor (2003). The temporal coincidence criterion for matching the simulation and the FTIR observations was 2 h. The time series of NH<sub>3</sub> total columns from FTIR, GCHP and TCR-2 are shown in Figure B.6 of the Appendix.

To compare the simulated and FTIR total columns, correlations for the simulationmeasurement pairs were performed, in addition to the calculation of simulation minus measurement relative differences (RD) as defined by Equation 4.3 according to Dammers et al. (2016), where  $TC_{S,i}$  and  $TC_{F,i}$  are the total columns for the simulations and FTIR, respectively. The mean is calculated to obtain the mean relative difference (MRD) used to compare the simulation's performance with the FTIR measurements:

$$MRD = \frac{1}{N} \sum_{i=1}^{N} RD = \frac{1}{N} \sum_{i=1}^{N} \left( \frac{TC_{S,i} - TC_{F,i}}{TC_{F,i}} \right) \times 100.$$
 (4.3)

The normalized root mean square error (NRMSE) was calculated with Equation 4.4, where N is the total number of model-measurement pairs, and  $\sigma_F$  is the standard deviation of the FTIR data, following Kärnä and Baptista (2016) and Flood et al. (2024):

$$NRMSE = \frac{1}{\sigma_F} \sqrt{\sum_{i=1}^{N} (TC_{S,i} - TC_{F,i})^2}.$$
 (4.4)

A NRMSE close to 1 indicates a RMSE comparable to  $\sigma_F$ , NRMSE > 1 indicates a RMSE >  $\sigma_F$  and poor fit, and NRMSE < 1 indicates a RMSE <  $\sigma_F$  and a better agreement of the simulation with respect to the FTIR. Linear regressions were fitted to the scatter plot data of the GCHP and TCR-2 outputs versus the FTIR measurements, without forcing the intercept to zero. The results are summarized in Table 4.3, including the correlation coefficient R, the fitted slope, the MRD, and the NRMSE. Figure 4.6 shows the correlations between both datasets and the FTIR data at each station.

The comparisons vary from site to site and differ between GCHP and TCR-2. For GCHP, R varies from a minimum of 0.02 at Eureka, to a maximum of 0.85 at Porto Velho. For TCR-2, R varies from a minimum of -0.02 at Reunion St. Denis, to a maximum of 0.85 at Ny Alesund. GCHP overestimates NH<sub>3</sub> at two of the three Arctic sites, with poor correlations, high NRMSE, and large columns in the lower range of FTIR, while TCR-2 underestimates NH<sub>3</sub> at all three sites, but with better correlations and NRMSE. For the other Northern Hemisphere sites, the correlation coefficients for GCHP improved, with larger R = 0.65 for Toronto. GCHP underestimates NH<sub>3</sub> for all sites except Garmisch and Zugspitze, where it significantly overestimates the NH<sub>3</sub> column with large NRMSE values. For TCR-2, the correlations are mostly smaller than those for GCHP, with negative MRDs, a maximum R of 0.46 for Boulder, and a minimum of -0.04 at Izana, while the highest NRMSE are for Hefei and Mexico City. For the Southern Hemisphere, GCHP correlation coefficients are between R=0.85and 0.22, with the best correlation for Porto Velho and the lowest value for Reunion St. Denis, with negative MRDs and NRMSE values close to one. For TCR-2, similarly to the Northern Hemisphere sites, the correlations are small between R=0.25 for

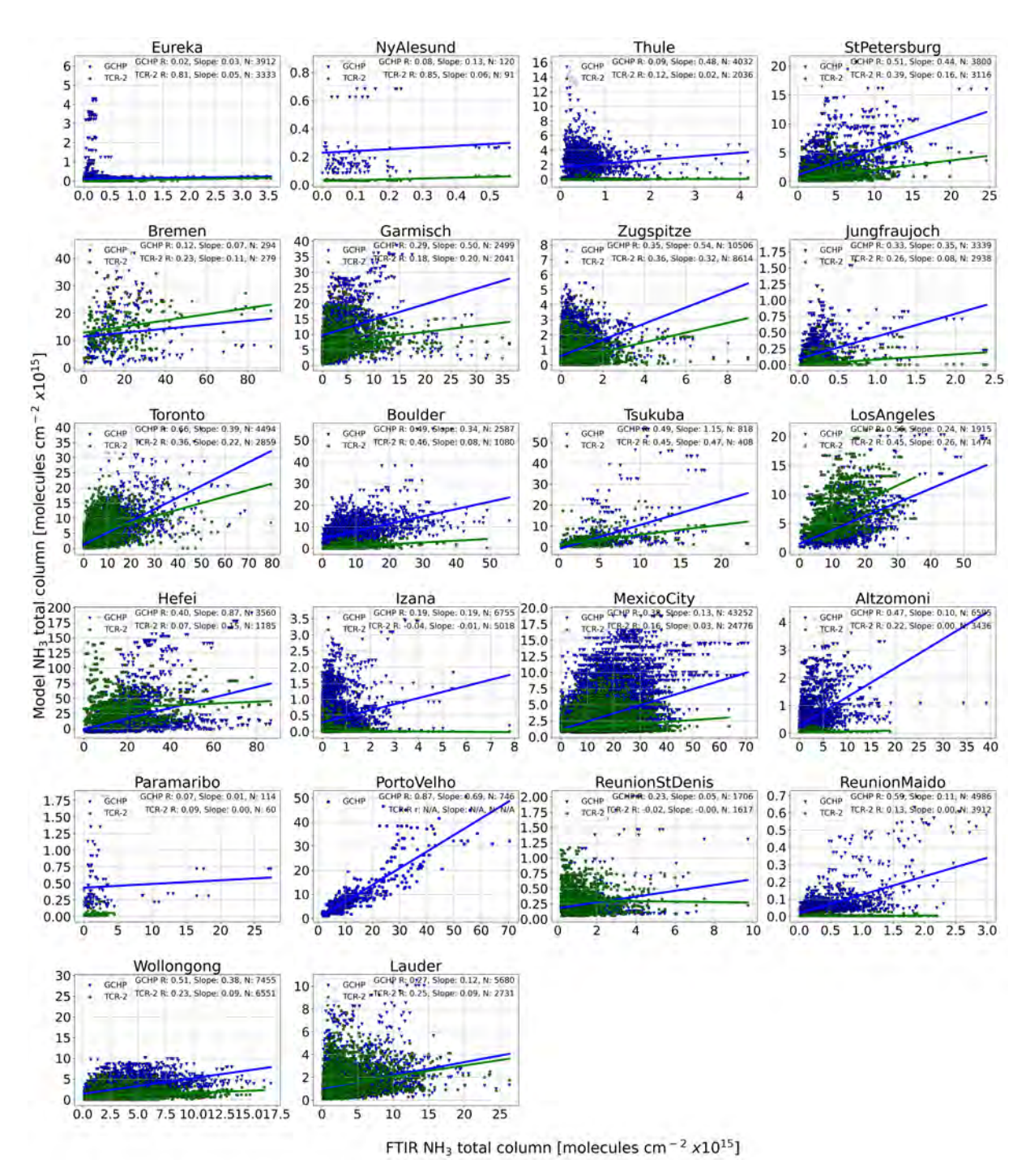


Figure 4.6: Scatter plots of GCHP and TCR-2 vs.FTIR  $\mathrm{NH_3}$  total columns. The lines show the individual regression results for each dataset. Note that for Porto Velho only the correlation between FTIR and GCHP is shown, as there are no TCR-2 data available for this site.

Table 4.3: Results of the NH<sub>3</sub> total column comparisons of GCHP and TCR-2 with FTIR measurements.

				-				
Station		GCHP				TCR-2		
	R	Slope	$\operatorname*{MRD}_{\widetilde{\widetilde{\alpha}}}$	NRMSE	R	Slope	$\underset{\widetilde{\mathbb{R}}}{\operatorname{MRD}}$	NRMSE
		$(\text{molec. cm}^{-2}) \times 10^{19}$	%			(molec. $cm^{-2}) \times 10^{19}$	%	
Eureka	0.02	0.03	-30.18	1.97	0.81	0.05	-97.23	1.14
Ny Alesund	0.07	0.12	105.93	2.13	0.85	0.06	-73.63	1.19
Thule	0.09	0.47	316.31	09.9	0.12	0.02	-97.63	1.59
St. Petersburg	0.51	0.45	-18.63	0.96	0.39	0.16	-67.73	1.19
Bremen	0.12	0.07	-24.40	1.14	0.23	0.11	-14.45	1.02
Garmisch	0.28	0.50	217.42	2.64	0.18	0.20	111.83	1.66
${ m Zugspitze}$	0.34	0.55	137.42	1.75	0.36	0.32	-0.32	1.07
Jungfraujoch	0.32	0.34	-19.19	1.23	0.26	0.08	-91.97	1.46
Toronto	0.65	0.39	-44.90	0.88	0.36	0.22	-16.74	0.98
Boulder	0.50	0.34	-18.96	0.92	0.46	0.08	-88.03	1.40
Tsukuba	0.48	1.16	-5.65	2.11	0.45	0.47	-23.64	1.12
Los Angeles	0.55	0.24	-64.47	1.37	0.45	0.26	-42.63	1.20
Hefei	0.40	0.86	-18.78	1.96	0.07	0.15	97.18	2.56
Izana	0.18	0.19	-16.12	0.61	-0.04	0.11	-96.18	0.65
Mexico City	0.38	0.13	-79.02	1.89	0.16	0.03	-88.09	2.13
Altzomoni	0.49	0.11	-73.93	1.04	0.22	0.00	-96.01	1.21
Paramaribo	0.08	0.01	-85.00	1.13	0.09	0.00	-97.06	1.72
Porto Velho	0.85	0.68	-31.02	0.64	NA	NA	NA	NA
Reunion St. Denis	0.22	0.05	-80.41	1.34	-0.02	0.00	-74.63	1.33
Reunion Maido	0.59	0.11	-83.87	1.33	0.13	0.00	-98.86	1.60
Wollongong	0.49	0.37	-11.36	0.91	0.23	0.09	-62.69	1.26
Lauder	0.28	0.12	-56.70	1.15	0.25	0.09	-55.49	1.13
Mean for all sites	0.35	0.33	3.76	1.63	0.28	0.11	-51.57	1.37

Lauder and R = -0.020 for Reunion St. Denis. TCR-2 continues underestimating NH<sub>3</sub> with negative MRDs and NRMSE > 1.

Using all the available coincidences for all sites, there is an overall correlation coefficient of R=0.36 and a slope of 0.27 ( $\pm 0.002$ ) for GCHP and R=0.28 and a slope of 0.22 ( $\pm 0.003$ ) for TCR-2 as shown in Figure B.7 of the Appendix. Figure 4.6 shows that the GCHP and TCR-2 total columns are larger than the FTIR measurements at the lower range of values, with larger columns from TCR-2 than GCHP. Both model datasets performed similarly at the higher range of values, with lower columns than the FTIR values.

### 4.4.1 Seasonal Variability

Figure 4.7 shows the FTIR, GCHP, and TCR-2 monthly mean NH<sub>3</sub> total columns, including the temporally matched FTIR and models data (solid lines) and the complete time series (dashed lines) between 2003-2021 for GCHP and 2005-2018 for TCR-2. The RD was calculated for each month for each site; then, using the monthly means, the MRD was obtained as reported in Table 4.4. Overall, no major differences were observed between the dashed and solid lines in Figure 4.7. Both GCHP and TCR-2 captured similar variability as the FTIRs; however, there are some sites where the differences are more noticeable.

Using data for all sites, the analysis suggested a monthly MRD = 0.41% for GCHP and -49.25% for TCR-2. For the Arctic sites, GCHP mainly overestimates and TCR-2 consistently underestimates NH<sub>3</sub> compared to the FTIR observations, while GCHP captures more variability than TCR-2. For the rest of the Northern Hemisphere sites, the best agreements were for Jungfraujoch, Boulder, and Tsukuba for GCHP, and Bremen, Zugspitze, Toronto, and Tsukuba for TCR-2, respectively, but overall, both datasets mainly underestimate NH<sub>3</sub> at all sites. For the Southern Hemisphere, GCHP

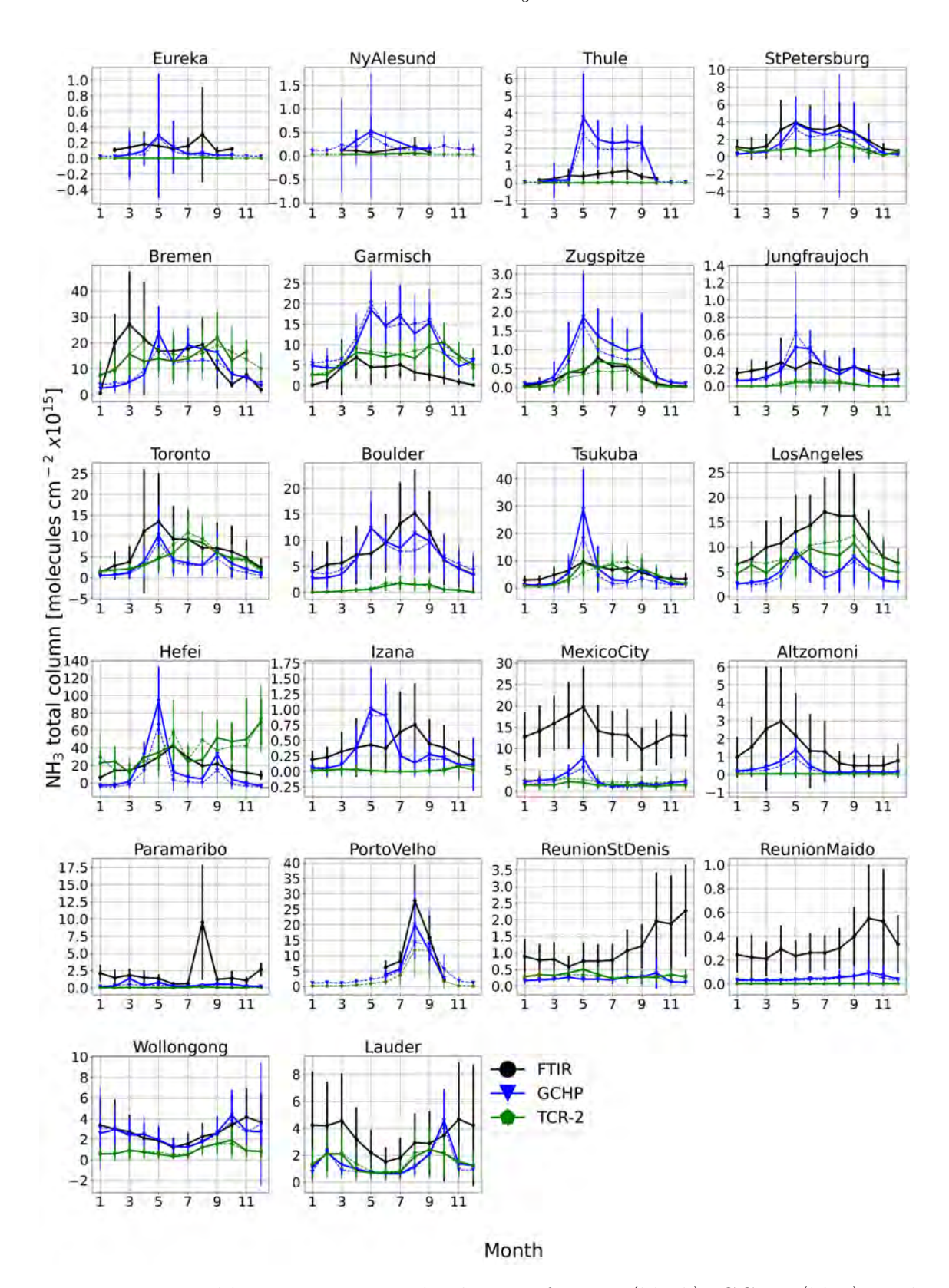


Figure 4.7: Monthly mean NH<sub>3</sub> total columns of FTIR (black), GCHP (blue), and TCR-2 (green). The thick solid lines represent the temporally matched FTIR measurements and GCHP and TCR-2 datasets; the dashed lines represent the complete time series from each dataset. Vertical lines represent the standard deviation  $(\pm 1\sigma)$ .

Table 4.4: MRD for monthly means of GCHP and TCR-2  $\rm NH_3$  total columns compared to FTIR measurements at each site.

Station	GCHP MRD	TCR-2 MRD
	%	%
Eureka	-41.87	-97.06
Ny Alesund	128.64	-77.99
Thule	265.41	-97.81
St. Petersburg	-23.21	-59.97
Bremen	-21.95	-5.84
Garmisch	233.47	132.21
Zugspitze	140.81	-2.19
Jungfraujoch	-9.88	-90.98
Toronto	-46.41	-18.35
Boulder	-18.12	-88.79
Tsukuba	1.46	-15.92
Los Angeles	-62.78	-42.66
Hefei	-22.92	93.02
Izana	-21.63	-87.18
Mexico City	-80.06	-87.98
Altzomoni	-72.85	-95.62
Paramaribo	-78.99	-96.05
Porto Velho	-28.12	NA
Reunion St. Denis	-80.81	-72.30
Reunion Maido	-84.11	-98.80
Wollongong	-11.69	-66.89
Lauder	-55.28	-57.11
All sites	0.41	-49.25

and TCR-2 presented similar results. For Porto Velho, GCHP and TCR-2 captured the NH<sub>3</sub> maximum between August and September; moreover, GCHP was able to capture the August 2019 enhancement. Both datasets underestimated NH<sub>3</sub> and barely captured the variability for Reunion St. Denis and Reunion Maido. For Wollongong, GCHP is in good agreement with FTIR, while TCR-2 captures the variability but with an underestimation, as in Lauder, where both datasets represented the variability but underestimated the monthly means.

### 4.4.2 Diurnal Variability

The NH<sub>3</sub> simulations do not have diurnal variation in anthropogenic emissions; however, in this section, comparisons of the hourly means were performed to see the ability of GCHP and TCR-2 to capture diurnal variability based on all the other processes involved in the simulations, such as the chemistry, transport, and meteorology variations. The hourly means are plotted in Figure 4.8; the RD was calculated for the matching hours for each site, then the MRD of these hourly means was obtained as shown in Table 4.5. There are large differences between the simulated and the observed total columns, as both GCHP and TCR-2 struggled to capture the diurnal variability of NH<sub>3</sub>, with an hourly MRD for all sites of 25.47% for GCHP and -47.84% for TCR-2. For the Arctic sites, TCR-2 doesn't capture any diurnal variability, while GCHP seems to capture some variability but with large overestimations, mainly at Ny Alesund and Thule. GCHP performed better at St. Petersburg and Wollongong and TCR-2 at Zugspitze where both datasets effectively reproduced the diurnal cycles, however, in most of the cases, there are large negative biases as observed in Figure 4.6 and Table 4.5, except for TCR-2 at Hefei and Garmisch where there is overestimation for the matching time series but better agreement with the full time series. The 24-hour variability from GCHP and TCR-2 could be relevant for some sites, but overall both simulations are unable to capture the diurnal variability of the FTIR instruments.

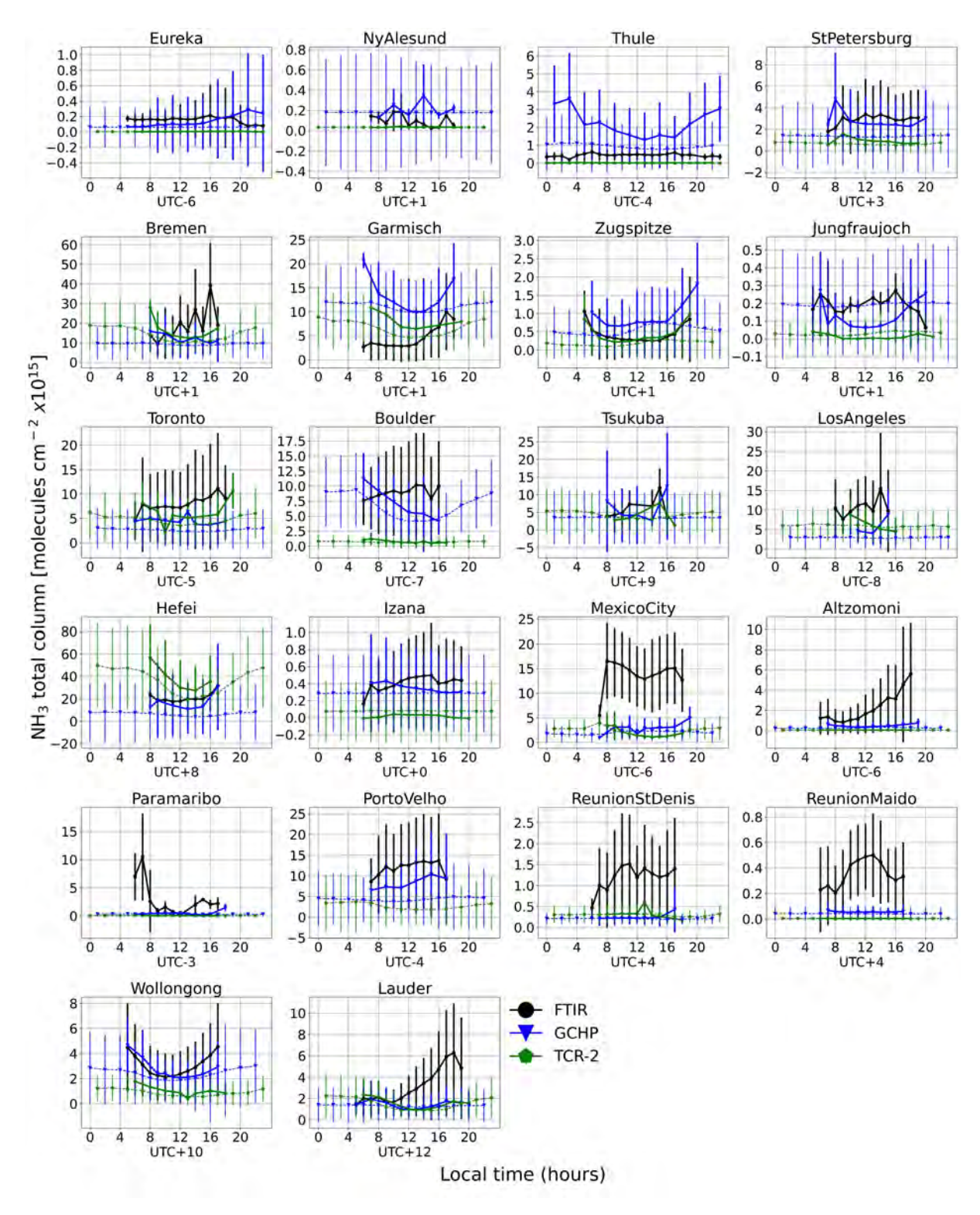


Figure 4.8: Hourly mean NH<sub>3</sub> total columns of FTIR (black), GCHP (blue), and TCR-2 (green) in local time (hours, with offset from UTC for each site indicated on each panel) for each site. The thick solid lines represent the temporally matched datasets between the FTIR measurements and GCHP and TCR-2 datasets; the dashed lines represent the complete time series from each dataset. Vertical lines represent the standard deviation  $(\pm 1\sigma)$ .

Table 4.5: MRD for diurnal means of GCHP and TCR-2 NH<sub>3</sub> total columns compared to FTIR measurements at each site.

Station	GCHP MRD	TCR-2 MRD
	%	%
Eureka	19.91	-96.83
Ny Alesund	234.15	-46.67
Thule	494.09	-97.13
St. Petersburg	9.50	-58.29
Bremen	-35.23	21.35
Garmisch	261.96	109.41
Zugspitze	122.25	-2.38
Jungfraujoch	-36.98	-88.93
Toronto	-40.25	-23.19
Boulder	-16.39	-87.80
Tsukuba	70.75	-35.75
Los Angeles	-42.38	-42.61
Hefei	-22.83	92.72
Izana	-21.35	-96.05
Mexico City	-80.67	-84.95
Altzomoni	-73.51	-96.00
Paramaribo	-39.68	-94.66
Porto Velho	-26.96	NA
Reunion St. Denis	-79.91	-71.91
Reunion Maido	-83.98	-98.71
Wollongong	-9.89	-64.02
Lauder	-42.25	-42.21
All sites	25.47	-47.84

## 4.4.3 Sensitivity Tests

Overall, GCHP NH<sub>3</sub> total columns agree better with the FTIR measurements than does TCR-2 for most sites, despite TCR-2 having higher spatial resolution and assimilated observations of relevant tropospheric species. Regardless of the optimization of the emissions and concentrations of various trace gases performed by TCR-2, NH<sub>3</sub> is not among the species that were assimilated. Consequently, the emissions of the TCR-2 NH<sub>3</sub> product in this work are not optimized, and its concentration is only indirectly improved by optimizing species related to the NH<sub>3</sub> chemistry, such as  $NO_x$  and  $SO_2$ .

One difference between TCR-2 and GCHP is the a priori input emissions inventory used in the CTMs: CEDS for GCHP and HTAP for TCR-2 as described in Sections 2.2.1 and 2.2.2. To explore the impact of the emissions inventory, we performed sensitivity tests for GCHP by running the model using HTAP emissions for one month (February 2013). In addition, the stand-alone input emissions from HTAP and CEDS were analyzed independently. The MRD difference for the GCHP-CEDS vs. GCHP-HTAP NH<sub>3</sub> total columns and between CEDS and HTAP NH<sub>3</sub> total emissions are presented in Table 4.6 and were calculated using:

$$RD = \frac{1}{N} \sum_{i=1}^{N} RD = \frac{1}{N} \sum_{i=1}^{N} \left( \frac{HTAP_{TC/Emissions,i} - CEDS_{TC/Emissions,i}}{CEDS_{TC/Emissions,i}} \right) \times 100.$$

$$(4.5)$$

The results show that the GCHP-HTAP NH<sub>3</sub> total columns were, on average 58.90% larger than the respective GCHP-CEDS columns for all sites. The sites with negative HTAP-CEDS MRD in the total columns were Eureka, Tsukuba, and all sites with a latitude south of Izana, while Bremen, Garmisch, Zugstpitze, Jungfraujoch, Toronto, Boulder and Los Angeles presented large positive MRD for the total columns.

The total HTAP NH<sub>3</sub> emissions are 10.85% larger than the total CEDS emissions for all sites, with the biggest differences for Los Angeles, Eureka, Hefei, Boulder and St. Petersburg. Among the emissions, the contribution from anthropogenic and seabird emissions the most different sectors.

This sensitivity test suggests that the larger underestimation in the NH<sub>3</sub> total columns from TCR-2 compared with GCHP does not solely due to the a priori input emissions, since the total columns of GCHP-HTAP were, on average, larger than GCHP-CEDS despite the HTAP emissions being lower than the CEDS emissions. The systematic negative bias in TCR-2 relative to the FTIR measurements can be related to persistent challenges common to many CTMs. Bian et al. (2017) highlighted that negative

Table 4.6: GCHP-HTAP vs GCHP-CEDS NH<sub>3</sub> total columns and NH<sub>3</sub> total emissions with HTAP and CEDS emissions based on Equation 4.5 during February 2013.

Station	MRD columns	MRD emissions
	%	%
Eureka	-12.01	-99.34
Ny Alesund	9.87	-0.93
Thule	9.00	0.60
St. Petersburg	21.81	-55.79
Bremen	195.69	49.56
Garmisch	210.17	20.45
Zugspitze	210.17	20.45
Jungfraujoch	175.00	27.16
Toronto	121.30	26.21
Boulder	220.52	81.03
Tsukuba	-12.66	-39.37
Los Angeles	213.70	267.64
Hefei	19.87	98.17
Izana	14.31	-67.71
Mexico City	-4.82	-4.11
Altzomoni	-4.82	-4.11
Paramaribo	-14.53	-27.20
Porto Velho	-14.93	-14.77
Reunion St. Denis	-19.20	-7.29
Reunion Maido	-19.20	-7.29
Wollongong	-13.19	-12.05
Lauder	-8.50	-12.64
All sites	58.98	10.85

biases in NH<sub>3</sub> simulations can result from significant uncertainties in the wet deposition process, where the effective Henry's Law constant for NH<sub>3</sub> varies significantly among different global models, up to 6 orders of magnitude, depending on what was considered in each model for its calculation (Bian et al., 2017). Additionally, the lack of NH<sub>3</sub> recycling between the atmosphere and soil further contributes to these biases. The implementation of a bi-directional flux scheme has been shown to mitigate these biases, as demonstrated in Zhu et al. (2015) and Cao et al. (2022) for the GEOS-Chem adjoint model. However, this scheme is not included in many CTMs, including the forecast model of TCR-2, limiting its ability to correct for such biases. In the TCR-2 framework, positive model biases in sulfate and nitric acid could also lead

to an underestimation of the ratio of gaseous ammonia to particulate ammonium. This issue is partially addressed by optimizing  $SO_2$  and  $NO_x$  emissions through data assimilation (Miyazaki et al., 2020a; Sekiya et al., 2023). To further improve the representation of  $NH_3$  in the data assimilation framework, the most effective approach would be to incorporate improved model schemes while simultaneously assimilating  $SO_2$ ,  $NO_2$ , along with  $NH_3$  observations.

### 4.4.4 Trend Comparison

Long-term trends were derived from the FTIR, GCHP, and TCR-2 datasets using temporally matched daily means as shown in Table 4.7. The FTIR trends using only the matching data do not indicate major changes compared with the trends in Table 4.2. The overall GCHP trend is 7.30 (-2.45 – 17.04)×10<sup>13</sup> molec. cm<sup>-2</sup> yr<sup>-1</sup>, smaller than the corresponding FTIR value, while the TCR-2 trend is 36.28 (-7.00 – 79.57)×10<sup>13</sup> molec. cm<sup>-2</sup> yr<sup>-1</sup>, larger than the FTIR trend, mainly due to the large TCR-2 trend at Hefei. For GCHP, the trend magnitudes are similar to the FTIR trends; however, there are changes in the statistical significance, with the largest differences for the Arctic and Southern Hemisphere sites. For TCR-2, most of the trends were positive but only two were significant. Both GCHP and TCR-2 have differences with the FTIR trends; however, the performance of GCHP is more consistent with the FTIR results than that of TCR-2.

The NH<sub>3</sub> total column trends derived from the full-time series of GCHP and TCR-2 for all sites are shown in Table 4.8. Overall, most of the GCHP trends are positive and significant, while for TCR-2, there are more negative and fewer significant trends. In addition, GCHP trends are much larger in magnitude than those for TCR-2, and there are differences compared to the trends in Table 4.7. For GCHP, all the trends for the Arctic sites are small, positive and non-significant; for the Northern Hemisphere

all trends were positive and significant, including Hefei; for the Southern Hemisphere only Porto Velho presented a negative trend that is non-significant, while the other sites presented positive trends, including Wollongong. For the Arctic sites, TCR-2 trends are very small and non-significant; for the Northern Hemisphere sites the trends are small and just a few of them are significant, including the negative trend for Mexico City; finally for the Southern Hemisphere, the trend for Porto Velho is also negative but non-significant, while the trend for Wollongong is negative, significant and similar to the FTIR trend.

Table 4.7: Trends in daily mean NH<sub>3</sub> total column from GCHP and TCR-2 along with the FTIR trends corresponding to the

Station		NH <sub>3</sub> Trends an	$NH_3$ Trends and 95% CI (molec. cm <sup>-2</sup> yr <sup>-1</sup> )×10 <sup>13</sup>	$^{-2} \text{ yr}^{-1}) \times 10^{13}$	ಎ	
	Time	FTIR	GCHP	Time	$\operatorname{FTIR}$	TCR-2
Eureka	2006-2020	$0.58\; (0.13-1.01)$	$1.12 \; (-0.31 - 2.58)$	2006 -2018	$0.48 \; (-0.10 - 1.07)$	$0.02 \; (-0.01 - 0.05)$
Thule	2003 - 2021	<b>-2.25</b> (-2.72 – -1.78)	$-1.22 \; (-2.91 - 0.44)$	2005 - 2018	<b>-2.44</b> (-3.21 – -1.67)	$0.06 \; (-0.01 - 0.14)$
St. Petersburg	2010 - 2021	$15.1 \; (5.52 - 24.3)$	$9.72\; (1.34-18.4)$	2010 - 2018	$6.83 \; (-3.27 - 15.7)$	$-3.34 \; (-7.34 - 0.60 \; )$
Bremen	2004 - 2018	$28.2 \; (-8.12 - 64.4)$	<b>45.1</b> $(17.2 - 74.5)$	2005-2018	$18.4\;(\text{-}19.6-58.1)$	$-6.88 \left(-30.5 - 16.5\right)$
Garmisch	2004 - 2007	$30.1  \left( -17.3 - 76.6 \right)$	62.2  (-17.9 - 145)	2005-2007	$50.7\;( ext{-}2.67-130)$	$56.4 \; (-8.59 - 122)$
${ m Zugspitze}$	2003 - 2021	$0.82\; (0.40-1.25)$	$3.30\; (2.64 - 3.98)$	2005-2018	$1.32 \; (0.68 - 1.95)$	$0.18\left(\text{-}0.34-0.70\right)$
Jungfraujoch	2008 - 2021	$0.52\; (0.21 - 0.82)$	<b>1.61</b> $(1.29 - 1.94)$	2008-2018	$0.49\ (0.09-0.88)$	0.09  (-0.05 - 0.23)
Toronto	2003 - 2021	$31.7\ (24.7 - 38.8)$	$17.5\; (13.1 - 21.8)$	2005-2018	$30.6\; (19.5-41.6)$	$4.20\; (\textbf{-}1.54 \; 9.86)$
Boulder	2010 - 2021	$45.3\; (30.5-59.6)$	$21.7\; (11.8 - 31.6)$	2010-2018	$30.6\; (5.92 - 55.9)$	$1.07 \ (-3.27 - 5.42)$
Tsukuba	2014 - 2021	<b>16.1</b> $(2.66 - 29.1)$	12.6(-14.5-40.6)	2014-2018	$-6.09 \; (-33.3 - 21.9)$	<b>25.1</b> $(3.45 - 45.8)$
Los Angeles	2003 - 2021	$20.9\; (3.64 - 3.85)$	$16.0\; (9.24 - 22.9)$	2005-2018	$34.0 \; (8.07 - 59.4)$	9.09 (-6.18 - 24.30)
7.75 5.24 10.20 Hefei	2017 - 2021	$67.8\left(\text{-}2.02-135\right)$	$-74.8 \; (-213 - 64.7)$	2017-2018	$93.9\;(-207-395)$	$564\left(\text{-}154-1310\right)$
Izana	2003 - 2021	$0.32 \; (-0.17 - 0.82)$	$1.69\; \big(1.30-2.10\big)$	2005-2018	0.35(-0.37-1.16)	$-0.01 \ (-0.14 - 0.10)$
Mexico City	2012 - 2021	$107\ (90.2-124)$	6.70(-0.02-13.7)	2012-2018	119 $(100 - 137)$	$1.88 \ (-1.63 - 5.46)$
Altzomoni	2012 - 2021	$10.7 \; (5.80 - 15.6)$	0.98(-0.06-2.03)	2012-2018	$\textbf{-0.07} \; (\textbf{-6.64} - 6.45)$	$0.05\;(\text{-}0.02-0.12)$
Reunion Maido	2013 - 2021	$0.17 \; (-0.75 - 1.11)$	$0.26\; (0.08-0.45)$	2013-2018	<b>-1.27</b> (-2.17 – -0.34)	$0.005\; (0.001-0.01)$
Wollongong	2007 - 2021	$-3.34 \; (-7.17 - 0.52)$	<b>4.17</b> $(1.38 - 7.02)$	2007-2018	$\textbf{-4.35} \; (\textbf{-9.15} - 0.63)$	0.92(-0.93-2.80)
Lauder	2003 - 2021	$2.07 \; (-0.26 - 4.42)$	$2.95\ (1.75 - 4.16)$	2005-2018	<b>8.81</b> $(4.96 - 12.6)$	$0.26 \ (-1.23 - 1.75)$
Mean all	,	<b>20 66</b> $(15.09 - 26.30)$	$7.30 (0.045 \pm 17.04)$		91 18 (9 65 30 71)	36 38 (700 70 87)

Table 4.8: GCHP and TCR-2 trends confidence intervals. Bold indicates a s	Table 4.8: GCHP and TCR-2 trends in $\mathrm{NH}_3$ total confidence intervals. Bold indicates a significant trend	al columns derived fre end.	in NH $_3$ total columns derived from the full-time series of each model along with 95% significant trend.	ach model along with 95%
Station	GCHP (2003–2021) $NH_3$ trends and 95%	trends and 95% CI	TCR-2 (2005-2018) NI	NH <sub>3</sub> trends and 95% CI
	(molec. $\text{cm}^{-2} \text{ yr}^{-1}) \times 10^{13}$	%	(molec. $\text{cm}^{-2} \text{ yr}^{-1}) \times 10^{13}$	%
Eureka	$0.87\left(  ext{-}0.42 - 2.19  ight)$	$1.99 \; (-0.97 - 5.01)$	$0.03 \; (\text{-}0.01 - 0.07)$	$72.90 \; (-11.00 - 156.00)$
Ny Alesund	$0.90\ (0.12-1.67)$	$3.42  \left( 0.44 - 6.38 \right)$	$0.05 \; (-0.01 - 0.11)$	$29.64 \; (-3.90 - 62.00)$
Thule	$0.81  \left( -0.24 - 1.91 \right)$	$1.05 \; (-0.31 - 2.47)$	$0.03\ (0.00-0.07)$	$31.11 \; (2.06 - 58.90)$
St. Petersburg	<b>3.02</b> (1.69 - 4.27)	<b>4.09</b> $(2.29 - 5.79)$	<b>-1.12</b> (-2.13 – -0.14)	<b>-1.77</b> $(-3.360.21)$
Bremen	<b>43.80</b> $(39.60 - 48.30)$	$6.34 \; (5.73 - 6.98)$	$5.46\;(0.98-9.99)$	$0.59\; (0.11-1.08)$
Garmisch	<b>19.10</b> $(16.80 - 21.70)$	<b>4.23</b> $(3.72 - 4.79)$	<b>4.10</b> $(0.97 - 7.16)$	<b>0.92</b> (0.22-1.60)
${ m Zugspitze}$	<b>19.10</b> $(16.80 - 21.50)$	<b>4.23</b> $(3.70 - 4.76)$	<b>3.58</b> (0.68-6.38)	$0.90\; (0.17-1.61)$
Jungfraujoch	<b>25.30</b> $(21.80 - 28.60)$	$4.74\ (4.10-5.36)$	$1.38 \; (-1.36 - 4.22)$	$0.37\left( -0.36 - 1.12  ight)$
Toronto	$12.20\; (10.50-14.00)$	<b>10.14</b> $(8.73 - 11.60)$	$2.58 \; (-0.01 - 5.12)$	$0.68\; (0.00-1.35)$
Boulder	<b>12.50</b> $(10.90 - 14.30)$	$6.40\ (5.54-7.29)$	$0.30\;(-0.30-0.91)$	0.54(-0.54-1.62)
Tsukuba	$8.18\; (5.50-11.00)$	$3.80\ (2.55-5.10)$	<b>12.80</b> $(9.49 - 16.10)$	$5.04\ (3.74-6.34)$
Los Angeles	<b>7.75</b> $(5.24 - 10.20)$	$2.66 \; (1.80 - 3.50)$	$-1.55  \left(-4.85 - 1.81 ight)$	$-0.26  \left(-0.80 - 0.30 ight)$
Hefei	<b>41.20</b> $(27.70 - 54.40)$	$5.48\ (3.69-7.24)$	<b>23.70</b> $(9.56 - 37.20)$	$1.50\; (0.61 - 2.36)$
Izana	<b>3.91</b> $(2.99 - 4.81)$	$8.58\; (6.57-10.60)$	$-0.19  \left( -0.51 - 0.12 \right)$	$-1.59  \left(-4.38 - 1.05 ight)$
Mexico City	$6.20\ (4.41-7.98)$	$3.62\ (2.57-4.66)$	<b>-1.77</b> (-2.37 – -1.18)	<b>2.58</b> (-3.46 – -1.72)
Altzomoni	<b>6.16</b> $(4.32 - 7.95)$	$3.60\ (2.52-4.64)$	<b>-1.77</b> (-2.37 – -1.15)	<b>2.58</b> (-3.46 – -1.68)
Paramaribo	<b>0.64</b> (0.32-0.95)	$1.24  \left(0.62 - 1.84\right)$	<b>-0.13</b> $(-0.210.05)$	$-2.10 \; (-3.420.81)$
Porto Velho	<b>-5.84</b> (-10.601.12)	<b>-1.36</b> (-2.470.26)	$-5.55 \; (-11.00 - 0.03)$	$-1.63 \; (-3.23 - 0.01)$
Reunion St. Denis	$0.11 \; (0.04 - 0.19)$	$0.67\ (0.21-1.12)$	$1.09\ (0.94-1.24)$	$6.51\; (5.61-7.43)$
Reunion Maido	$0.11 \; (0.04 - 0.18)$	<b>0.65</b> (0.21-1.09)	$1.09\ (0.94-1.24)$	$6.51\; (5.61-7.44)$
Wollongong	<b>2.69</b> (0.29 - 5.17)	<b>1.60</b> $(0.17 - 3.08)$	<b>-1.65</b> $(-2.460.85)$	<b>-1.95</b> (-2.901.01)
Lauder	$4.42\; (3.31-5.54)$	$3.36\ (2.52 - 4.22)$	-0.02  (-0.74 - 0.68)	-0.02 $\left( -0.59 - 0.54 \right)$
Mean for all sites	<b>10.11</b> $(9.31 - 10.91)$	$3.66\ (3.35-3.97)$	$1.93\ (1.11-2.75)$	$6.49\; (2.00-10.98)$

The NH<sub>3</sub> partitioning at each site was derived using GCHP total columns of NH<sub>3</sub> and NH<sub>4</sub><sup>+</sup> to calculate the NH<sub>3</sub>/NH<sub>4</sub><sup>+</sup> ratio and explore which was the predominant species in the chemical equilibrium. In addition, correlations of NH<sub>3</sub> total columns with total columns of SO<sub>2</sub> and NO<sub>x</sub>, and surface temperature were calculated. These results are shown in Table 4.9.

Table 4.9: GCHP  $NH_3/NH_4^+$  total column ratio and correlation coefficients for  $NH_3$  total columns vs.  $SO_2$ ,  $NO_x$  total columns and surface temperature. The calculations were made using GCHP variables from 2003 to 2021.

-	Ratio	Corre	lation co	pefficient $R$ for $NH_3$ with
Station	$\mathrm{NH_3/NH_4^+}$	$SO_2$	$NO_x$	Surface Temperature
Eureka	0.08	-0.03	0.13	0.08
Ny Alesund	0.08	0.00	0.07	-0.02
Thule	0.20	-0.17	0.48	0.39
St. Petersburg	0.14	-0.06	0.10	0.32
Bremen	0.57	0.02	-0.18	0.56
Garmisch	0.56	-0.15	-0.02	0.63
Zugspitze	0.56	-0.15	-0.02	0.63
Jungfraujoch	0.50	-0.13	-0.19	0.58
Toronto	0.22	-0.15	-0.04	0.39
Boulder	0.52	-0.03	0.39	0.56
Tsukuba	0.16	0.00	-0.06	0.10
Los Angeles	0.59	0.03	0.22	0.40
Hefei	0.23	-0.25	-0.25	0.23
Izana	0.19	0.09	0.30	0.08
Mexico City	0.24	0.40	0.09	0.23
Altzomoni	0.24	0.40	0.09	0.23
Paramaribo	0.92	0.01	-0.07	0.00
Porto Velho	2.93	0.91	0.77	0.27
Reunion St. Denis	0.21	-0.01	-0.14	-0.11
Reunion Maido	0.21	-0.01	-0.14	-0.11
Wollongong	0.55	0.37	0.63	0.30
Lauder	1.20	-0.10	0.17	0.15

The NH<sub>3</sub>/NH<sub>4</sub><sup>+</sup> ratio is less than one for all sites except Porto Velho and Lauder, meaning that NH<sub>3</sub> prevails in the particulate phase. This suggests that the previously described model trends might be underestimated, as they were calculated for NH<sub>3</sub> in the gas phase. Most of the correlations with SO<sub>2</sub> and NO<sub>x</sub> are very small, with a few exceptions. For Porto Velho, the NH<sub>3</sub>/NH<sub>4</sub><sup>+</sup> ratio is 2.93 with R = 0.91 for SO<sub>2</sub>

and R = 0.77 for  $NO_x$ . This suggests that for Porto Velho, the NH<sub>3</sub> trends are due to changes in the emission sources rather than a reduction in the emissions of  $SO_2$  and  $NO_x$ . The correlation coefficients between surface temperature and NH<sub>3</sub> total columns were > 0.5 only for Bremen, Garmisch, Zugspitze, Jungfraujoch, and Boulder, suggesting that for these sites, temperature changes could have a greater impact on NH<sub>3</sub> concentrations than for other sites.

### 4.5 Conclusions

Using NH<sub>3</sub> total columns from ground-based FTIR spectrometers at 22 globally distributed sites and from a global CTM (GCHP) and a reanalysis product (TCR-2), this work examined the variability and trends of atmospheric NH<sub>3</sub>. The FTIR time series revealed that NH<sub>3</sub> is present even in the most remote areas, and it can show significant enhancements mainly due to biomass burning events. The seasonal patterns were similar across most sites, ranging between 2.66 and  $6.92 \times 10^{15}$  molec. cm<sup>-2</sup>, and are in agreement with previous studies mainly using satellite data. The patterns are influenced by meteorological conditions such as temperature and rain, seasons of fertilizer application, and fire season. Overall, both NH<sub>3</sub> simulations captured the seasonality of the FTIR measurements with some differences, mainly underestimations for the Northern and Southern Hemisphere sites and GCHP overestimations in the Arctic.

The diurnal variability of NH<sub>3</sub> total columns was shown for the first time for most of the FTIR sites, with variations between 0.20 and  $6.74 \times 10^{15}$  molec. cm<sup>-2</sup> and large differences between sites. In general, the diurnal patterns differ significantly and depend on the characteristics of each site, as well as the influence of local sources such as vehicular emissions and NH<sub>3</sub> transported from surrounding areas in the late afternoon. Both models struggled to capture the diurnal variability of the measurements,

mainly due to the lack of diurnal variation in the anthropogenic emissions used in the NH<sub>3</sub> simulations.

Most NH<sub>3</sub> FTIR trends are positive and significant, ranging from 0.38 to 93 ×  $10^{13}$  molec. cm<sup>-2</sup> yr<sup>-1</sup> for all sites. The largest trends were for Mexico City, Boulder, and Toronto. The equivalent trends calculated using GCHP and the TCR-2 product were, in general, smaller for both GCHP and TCR-2. The trends using the full time series for GCHP are  $10.11 (9.31 - 10.91) \times 10^{13}$  molec. cm<sup>-2</sup> yr<sup>-1</sup> between 2003 and 2021 and  $1.93 (1.11 - 2.75) \times 10^{13}$  molec. cm<sup>-2</sup> yr<sup>-1</sup> for TCR-2 between 2005 – 2018. The drivers behind these trends depend on each location, and they involve a combination of changes in the NH<sub>3</sub>, NO<sub>x</sub>, and SO<sub>2</sub> emissions and changes in the meteorology. According to GCHP, NH<sub>3</sub> prevails in the particulate form NH<sub>4</sub><sup>+</sup> at most sites, suggesting that the model trends presented in this work might be underestimated.

Overall, GCHP exhibited a generally better agreement with the FTIR observations than TCR-2, with the largest differences at the Arctic sites and Mexico City. Sensitivity tests regarding the a priori emissions were performed, finding that the differences in the emissions used in GCHP and TCR-2 are not driving the larger underestimation observed in the TCR-2 product. The persistent negative bias in TCR-2 can be related to the lack of a bi-directional exchange flux scheme in its framework and to persistent positive model biases in sulfate and nitric acid. Further, sensitivity tests and direct assimilation of NH<sub>3</sub> from satellite observations are recommended to improve the TCR-2 NH<sub>3</sub> product.

# Chapter 5

# $NH_3$ and $PM_{2.5}$ over Mexico City

### 5.1 Introduction

This chapter presents a case study of pollution events due to high levels of O<sub>3</sub> and PM<sub>2.5</sub> reported in Mexico City during May 2019. Simultaneous enhancements of NH<sub>3</sub> and PM<sub>2.5</sub> were identified in May 2019 from ground-based measurements of NH<sub>3</sub> total columns and surface PM<sub>2.5</sub>. In addition, preliminary comparisons of NH<sub>3</sub> and PM<sub>2.5</sub> spatial distributions over Mexico City during the pollution events are presented. The spatial distributions were obtained from model simulations of two CTMs, both at a resolution of approximately 32 km: the regional model WRF-Chem and the GCHP stretched grid configuration. Comparisons between total columns from GCHP and GCHP stretched grid simulations were also performed.

According to the World Health Organization (WHO), air pollution is among the ten threats to global health, and was even considered the greatest environmental risk to health in 2019 by this organization. The air quality issue of most urgent concern around the world could be pollution from particulate matter (Fuzzi et al., 2015). As

mentioned in Chapter 1, Sections 1.1 and 1.2.1, NH<sub>3</sub> plays a key role in the formation of PM<sub>2.5</sub>. This role is particularly important in urban and densely populated areas, where pollution episodes due to particulate matter are recurrent. For example, Behera and Sharma (2010) made in situ measurements of PM<sub>2.5</sub>, NH<sub>3</sub>, SO<sub>2</sub> and NOx in the city of Kanpur, India and confirmed atmospheric NH<sub>3</sub> as a precursor of 30% of the mass of SIA such as (NH<sub>4</sub>)<sub>2</sub>SO<sub>4</sub> or NH<sub>4</sub>NO<sub>3</sub> in the PM<sub>2.5</sub>, and seasonal patterns with higher levels of NH<sub>3</sub> during the summer. Several studies of the efficiency in controlling PM<sub>2.5</sub> by reducing NH<sub>3</sub> emissions have been performed in Chinese megacities, as this region faces environmental challenges due to haze pollution with high levels of PM<sub>2.5</sub> (Wang et al., 2023; Xiao et al., 2025). Viatte et al. (2020), found in Paris, a city with frequent PM<sub>2.5</sub> episodes during springtime, simultaneous enhancements of PM<sub>2.5</sub> and NH<sub>3</sub>, and identified low temperatures, thin boundary layer, low precipitation, and winds from the north-east as the meteorological driving parameters of PM formation in the presence of atmospheric NH<sub>3</sub> over this region.

In terms of pollution episodes, the Mexico City Metropolitan Area presents many days of poor air quality due to  $O_3$  and particulate mmater ( $PM_{2.5}$  and  $PM_{10}$ ) (Molina et al., 2020) and some severe pollution events during the warm-dry season, with high levels of  $PM_{2.5}$  (Calderón-Ezquerro et al., 2020). From March to June, the warm-dry season is characterized by intense solar radiation and high-pressure systems, inducing hot days with low winds and clear skies; biomass burning events and dust during this season could further increase PM concentrations (Molina et al., 2020). Notably, from March to May, an atmospheric blockage with low relative humidity, small temperature fluctuations, and weak wind has been reported to trigger environmental contingency of pollutants such as  $O_3$  (Silva-Quiroz et al., 2019). More details about Mexico City are found Section 3.2.1. In particular, between 11 and 16 May 2019, Mexico City experienced several days of extremely poor air quality due to  $PM_{2.5}$  and  $O_3$ , with levels of  $PM_{2.5}$  exceeding the 99th percentile of the official dataset (2005-2019) (Rios

et al., 2023). This pollution event was attributed to a combination of factors, such as regional transport of emissions from biomass burning aggravated by meteorological conditions. The fire season in Mexico peaks in May (Ríos and Raga, 2017); the 2019 fire season was particularly intense due to extremely dry environmental conditions (Rios et al., 2023), contributing to the emission of several pollutants, including NH<sub>3</sub>, during the pollution event.

The results of the variability and trends analysis in Chapter 4 show that GCHP and TCR-2 severely underestimate NH<sub>3</sub> in some sites. One site of large underestimation was Mexico City, which has a challenging topography and emissions, as described in Section 3.2.1. The results in Table 4.3 for Mexico City showed MRD of -79.02% for GCHP and -88.09% for TCR-2, indicating that the modeled emissions are strongly underestimating NH<sub>3</sub>, potentially due to missing urban sources. In addition, the use of different emission inventories in GCHP, as described in Section 4.4.3, did not significantly impact the magnitude of the NH<sub>3</sub> total column. Thus, the coarse resolution of the GCHP simulation ( $\sim$ 198 km) might be affecting the performance of the model against the FTIR measurements, suggesting that the performance of higher resolution simulations should be investigated. The motivation for this study is thus to examine simultaneous enhancements of NH<sub>3</sub> and PM<sub>2.5</sub> during the May 2019 pollution event in Mexico City, to evaluate the model capabilities during periods when concentrations of both are greatly increased.

## 5.2 Materials and Methods

#### 5.2.1 Pollution Events

The identification of the NH<sub>3</sub> and PM<sub>2.5</sub> pollution events was done by applying Fourier series of order 3 on the daily means of the desired dataset, to account for the sea-

sonality in the time series. Events that are above  $2\sigma$  of this natural variability are considered pollution events (Yamanouchi et al., 2021; Viatte et al., 2022). For NH<sub>3</sub>, the FTIR total column time series from Chapter 4 between 2012 and 2022 was used. In the case of PM<sub>2.5</sub>, daily means of surface PM<sub>2.5</sub> data from Mexico City's Atmospheric Monitoring Network (RAMA, by its Spanish acronym), collected between 2015 and 2023, were used. RAMA uses PM sampling methods that include instruments that perform gravimetric or beta attenuation analysis, which are in compliance with the reference methods described by the US EPA. The identification of simultaneous enhancements of NH<sub>3</sub> and PM<sub>2.5</sub> in Mexico City was focused on May 2019. Using the time series of NH<sub>3</sub> total column and PM<sub>2.5</sub> surface concentration between 2003 and 2021, from the GCHP long-term simulation described in Section 2.2.1 and referred to in this Chapter as GCHP-C48, pollution events were identified too.

### 5.2.2 Modeled $NH_3$ and $PM_{2.5}$

The spatial distribution of NH<sub>3</sub> total column and surface PM<sub>2.5</sub> during the May 2019 pollution events over Mexico City was obtained from two model simulations of similar horizontal resolution. Using the stretched grid feature in GCHP, with a stretched factor of 6.5, the resolution was increased from approximately 198 km (GCHP-C48) to 32 km (GCHP-SF) for Mexico City. The details of this simulation are described at the end of Section 2.2.1 and it will be referred to as GCHP-SF in this chapter. Similarly, simulations for May 2019 from the regional model WRF-Chem with a domain over Mexico at a resolution of 32 km were used. The details of this simulation were described in Section 2.2.3. For comparisons presented in Section 5.3.3 and in Figure C.1, CO and formaldehyde (HCHO) FTIR total columns for the Mexico City site were obtained upon request; O<sub>3</sub> was not available. Unfortunately, there were no CO, HCHO, or O<sub>3</sub> FTIR measurements in May 2019 for Altzomoni.

To add a reference to the spatial distribution of NH<sub>3</sub> during the pollution event, NH<sub>3</sub> total columns from IASI (ANNI-NH<sub>3</sub>-v4, (Clarisse et al., 2023)) between May 11 and 16, 2019, were used. Satellite data from MetOp-A and MetOp-B, referred to in this Chapter as IASI A+B, were combined to have more satellite observations over Mexico during this event. Only IASI observations with adequate sensitivity to NH<sub>3</sub>, based on the quality flag of the product, were used. IASI measurements are described in Section 2.1.6.

### 5.3 Results and Discussion

### 5.3.1 Pollution Events

Figure 5.1 shows the NH<sub>3</sub> pollution events identified during 2019 in Mexico City. For the NH<sub>3</sub> FTIR measurements, 17 pollution events were identified, with seven events in May, as shown in Table 5.1.

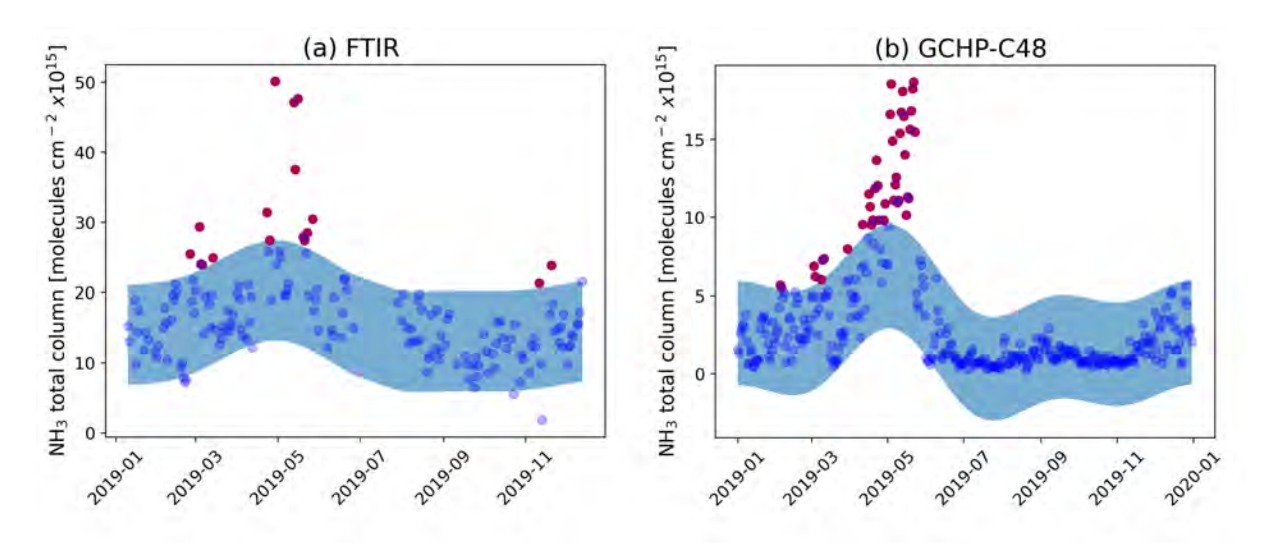


Figure 5.1: Daily mean NH<sub>3</sub> total columns in Mexico City from (a) ground-based FTIR measurements and (b) GCHP-C48 simulations. In red are the identified pollution events; note the spike in May. The blue shading represents  $2\sigma$  from the Fourier fit as described in Section 5.2.1.

From Figure 5.1, it can be observed that the most significant pollution events were in May, with NH<sub>3</sub> total columns of almost  $50 \times 10^{15}$  molec. cm<sup>-2</sup>. In contrast, from the GCHP-C48 data, a total of 40 pollution events were identified, with 21 of them occurring in May. However, the largest columns are of almost  $20 \times 10^{15}$  molec. cm<sup>-2</sup>, 60% smaller than the FTIR total columns.

Table 5.1: NH<sub>3</sub> pollution events over Mexico City during May 2019 from ground-based measurements and model simulations.

NH		$n \text{ (molec. cm}^{-2}$	$1 \times 10^{15}$
Date	FTIR NH <sub>3</sub>	Date	GCHP-C48 NH <sub>3</sub>
$2019-05-13^a$	47.08	2019-05-03	16.61
2019-05-14	37.53	2019-05-04	18.54
2019-05-16	47.63	2019-05-05	14.89
2019-05-20	27.92	2019-05-06	11.08
2019-05-21	27.36	2019-05-07	12.09
2019-05-23	28.47	2019-05-08	12.55
2019-05-27	30.42	2019-05-09	10.93
		2019-05-10	11.08
		2019-05-11	15.38
		2019-05-12	16.73
		$2019 \text{-} 05 \text{-} 13^a$	18.07
		2019-05-14	16.49
		2019-05-15	14.00
		2019-05-16	10.13
		2019-05-17	11.29
		2019-05-18	11.22
		2019-05-19	15.65
		2019-05-20	16.83
		2019-05-21	18.24
		2019-05-22	18.66
		2019-05-23	15.46

 $<sup>^{\</sup>rm a}$  Coincident date for simultaneous enhancements of NH $_3$  from FTIR measurements and GCHP-C48 simulations, and PM $_{2.5}$  from RAMA measurements and GCHP-C48 simulations.

Table 5.1 shows the seven and 21 NH<sub>3</sub> pollution events from FTIR and GCHP-C48, respectively. Despite the pollution event of interest being from 11 to 16 May, pollution events after this date were found. However, it can be observed that for the FTIR NH<sub>3</sub> pollution events, the magnitude of those before May 16 is considerably higher

than the later events.

Table 5.2:  $PM_{2.5}$  pollution events over Mexico City during May 2019 from surface measurements and model simulations.

-	Surface Pl	$\rm M_{2.5}~in~\mu g~m^{-3}$	
Date	RAMA $PM_{2.5}$	Date	GCHP-C48 $PM_{2.5}$
2019-05-04	39.90	2019-05-01	34.48
2019-05-05	38.04	2019-05-05	33.64
2019-05-06	40.25	2019-05-06	37.82
2019-05-07	35.67	2019-05-07	33.33
2019-05-09	37.02	2019-05-12	34.62
2019-05-10	41.86	2019-05-13	37.18
2019-05-11	67.38	2019-05-15	53.11
2019-05-12	76.17	2019-05-16	54.16
2019-05-13	78.86	2019-05-17	51.74
2019-05-14	65.99	2019-05-18	35.34
2019-05-15	66.32	2019-05-24	36.88
2019-05-16	65.26	2019-05-31	33.25
2019-05-17	34.58		
2019-05-28	32.72		

 $<sup>^{\</sup>rm a}$  Coincident date for simultaneous enhancements of PM $_{2.5}$  from RAMA measurements and GCHP-C48 simulations, and NH $_3$  from FTIR measurements and GCHP-C48 simulations.

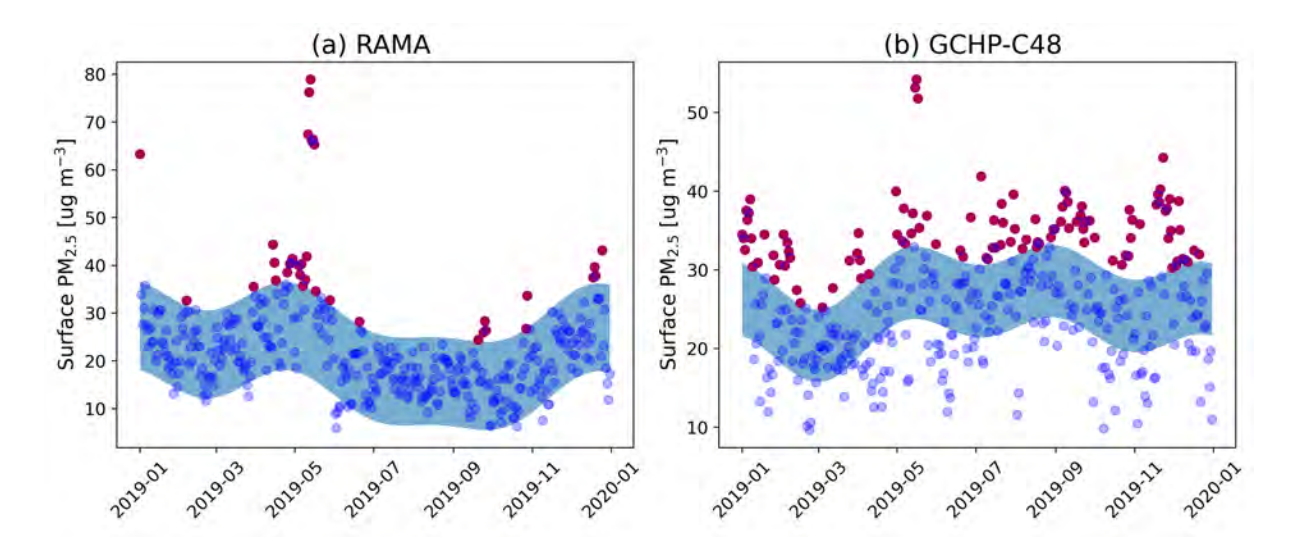


Figure 5.2: Daily mean surface  $PM_{2.5}$  in Mexico City from (a) in situ measurements and (b) GCHP-C48 simulations. In red are the identified pollution events; note the spike in May. The blue shading represents  $2\sigma$  from the Fourier fit as described in Section 5.2.1.

For the PM<sub>2.5</sub> pollution events, Figure 5.2 shows the events derived from the RAMA measurements and GCHP-C48 simulations, Table 5.2 shows the values of the pollution events in May for RAMA and GCHP-C48. In total, using the RAMA surface measurements of PM<sub>2.5</sub>, 35 events were identified, 14 of them in May, with concentrations up to almost 80  $\mu g$  m<sup>-3</sup>, as observed in Figure 5.2. The distribution of the RAMA pollution events is similar to the NH<sub>3</sub> pollution events, with most of the enhancements during the warm-dry season. The GCHP-C48  $PM_{2.5}$  pollution events are shown in Figure 5.2, with a total of 108 events through the year and only 12 of them in May. Compared to the other pollution events figures, the distribution of the GCHP-C48 PM<sub>2.5</sub> pollution events is spread through the year, showing both above and below the  $2\sigma$  events with similar frequency. In addition, the maximum PM<sub>2.5</sub> concentrations are around 54  $\mu g m^{-3}$ , almost 40% smaller than the respective RAMA measurement. According to the 2005 WHO Air Quality guidelines, the PM<sub>2.5</sub> level for short-term or 24-hour average exposure was 25  $\mu g$  m<sup>-3</sup>, which was further reduced in the 2021 guidelines to 15  $\mu \mathrm{g}$  m<sup>-3</sup>. Compared to the WHO level, the PM<sub>2.5</sub> levels are exceeded most of the year in Mexico City with both RAMA and GCHP-C48.

## 5.3.2 Spatial Distribution of $NH_3$ and $PM_{2.5}$

Here we compare the spatial distribution at a similar horizontal resolution ( $\sim$ 32 km) of NH<sub>3</sub> and PM<sub>2.5</sub> in GCHP-SF and WRF-Chem. From Tables 5.1 and 5.2, it can be observed that May 13th is the only date with coincident pollution events from all datasets. Thus, the spatial distribution over Mexico City and its surroundings was investigated under enhanced NH<sub>3</sub> and PM<sub>2.5</sub> conditions on this day. Figure 5.3 provides some context for the location of the biomass burning events that affected the PM<sub>2.5</sub> and NH<sub>3</sub> concentrations at Mexico City.



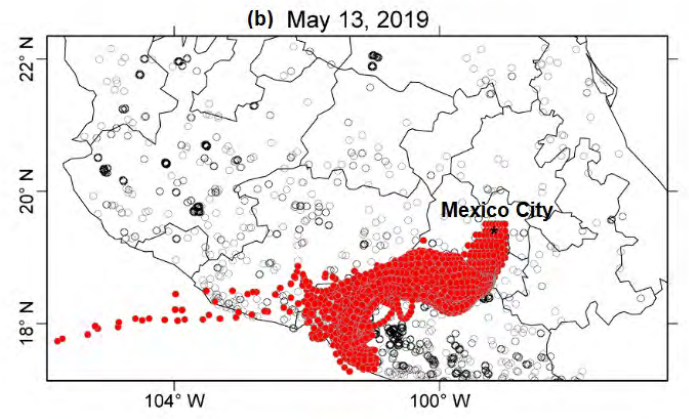


Figure 5.3: (a) Snapshot of Mexico's fire events on May 13, 2019, from the Aqua MODIS instrument with true colour corrected reflectance and resolution of 1 km, obtained from NASA Worldview Snapshots (https://earthdata.nasa.gov). The red dots show the fire events. The location of Mexico City is shown in red. (b) Hourly backward trajectories from HYSPLIT on May 13, 2019, initiated in Mexico City at 100 m (each dot corresponds to 1 h). Adapted from Rios et al. (2023).

The PM<sub>2.5</sub> spatial distribution over Central Mexico is presented in Figures 5.4 and 5.5. For GCHP-SF, the PM<sub>2.5</sub> distribution shows the largest concentrations towards the north, with values around 50  $\mu$ g m<sup>-3</sup>. The PM<sub>2.5</sub> values in the city are around 40  $\mu$ g m<sup>-3</sup>, approximately 50% smaller than the RAMA values from Table 5.2 but consistent with the GCHP-C48 values from the same table. To add more context about the spatial distribution of NH<sub>3</sub> and PM<sub>2.5</sub> over Mexico during the pollution events, plots of the complete target face from the GCHP-SF simulation are presented in Appendix C. The WRF-Chem model shows values of surface PM<sub>2.5</sub> between 25

and 30  $\mu$ g m<sup>-3</sup> in Mexico City, approximately 60% smaller than the RAMA value. However, contrary to GCHP-SF, WRF-Chem PM<sub>2.5</sub> concentrations are smaller at the north and larger at the bottom of the plot, southeast of the city, with values around 35  $\mu$ g m<sup>-3</sup>.

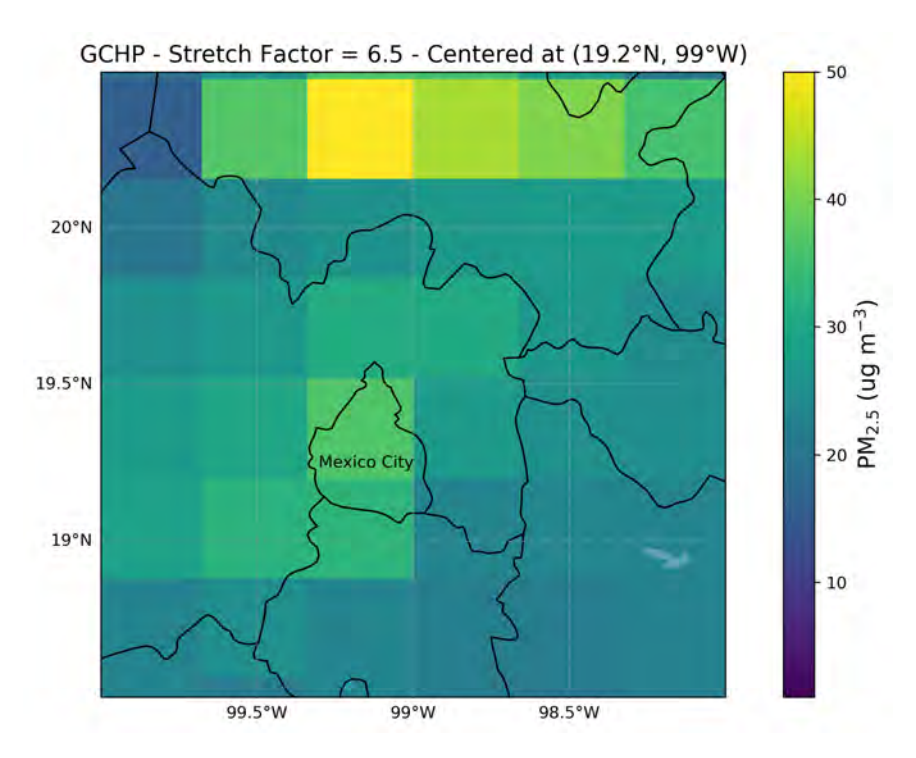


Figure 5.4: Spatial distribution of mean  $PM_{2.5}$  surface concentration during May 13, 2019, over central Mexico from the GCHP-SF stretched grid simulation.

Figure 5.6 shows the spatial distribution of NH<sub>3</sub> total column from the GCHP-SF simulation centered at Mexico City and its surroundings. The NH<sub>3</sub> total columns in the city are between 15 and 20×10<sup>15</sup> molec. cm<sup>-2</sup>, between 30 and 40% smaller than the FTIR values from Table 5.1, but comparable to the value from GCHP-C48. Not much variation is seen across the city and the surrounding states, except for the largest columns in the north, mainly for columns with values around 30×10<sup>15</sup> molec. cm<sup>-2</sup> in the northeast. In contrast, the spatial distribution from WRF-Chem is shown in Figure 5.7. It has NH<sub>3</sub> total columns in the city between 4 and 5×10<sup>15</sup> molec. cm<sup>-2</sup>, four times smaller than GCHP, and more than 10 times smaller than the FTIR value. Contrary to GCHP-SF, the largest NH<sub>3</sub> total columns are in the southeast of the city,

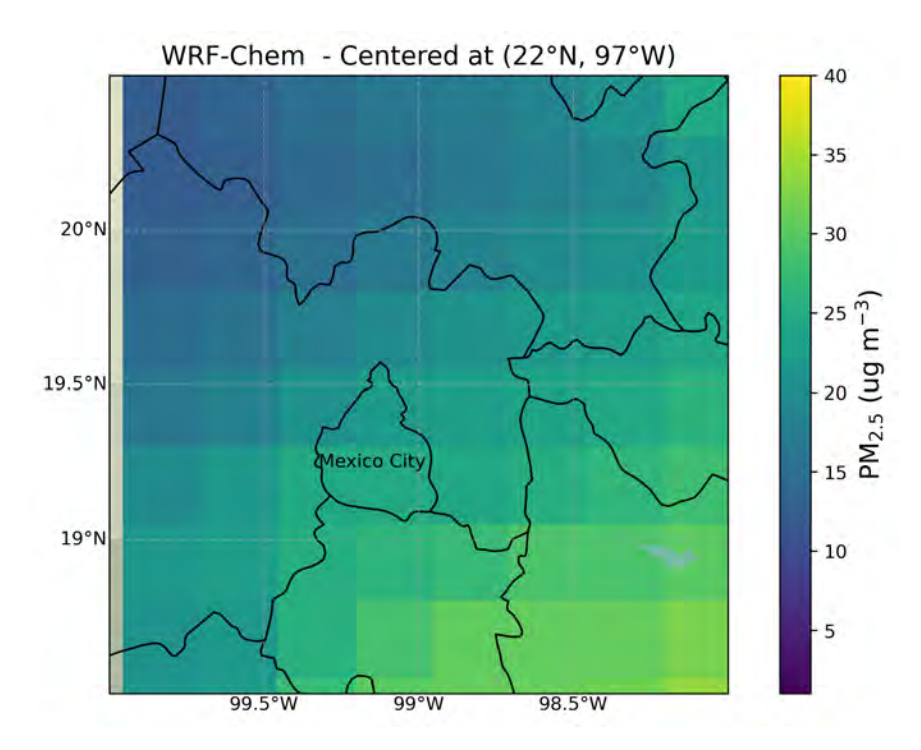


Figure 5.5: Spatial distribution of mean  $PM_{2.5}$  surface concentration during May 13, 2019, over central Mexico from the WRF-Chem simulation.

but the values are still small.

According to Rios et al. (2023), emissions from biomass burning were a major contributor to the May 2019 pollution episode, with fires coming from the south. Simultaneous enhancements of CO and NH<sub>3</sub> were found in the FTIR measurements and GCHP-SF (Figures C.1 and C.2), suggesting that the enhancements are from biomass burning emissions. The models used different emission inventories for biomass burning, GFAS for GCHP-SF and FINN for WRF-Chem, as described in Sections 2.2.1 and 2.2.3. According to the location of the fire events shown in Figure 5.3, it seems that, for this event, emissions from FINN are giving more accurate results regarding the spatial distribution of NH<sub>3</sub> and PM<sub>2.5</sub>. Still, the emissions from GFAS might be more precise in magnitude.

In addition, Figure 5.8 shows the spatial distribution of NH<sub>3</sub> total columns during the pollution event from May 11 to May 16, from GCHP-SF and WRF-Chem simulations

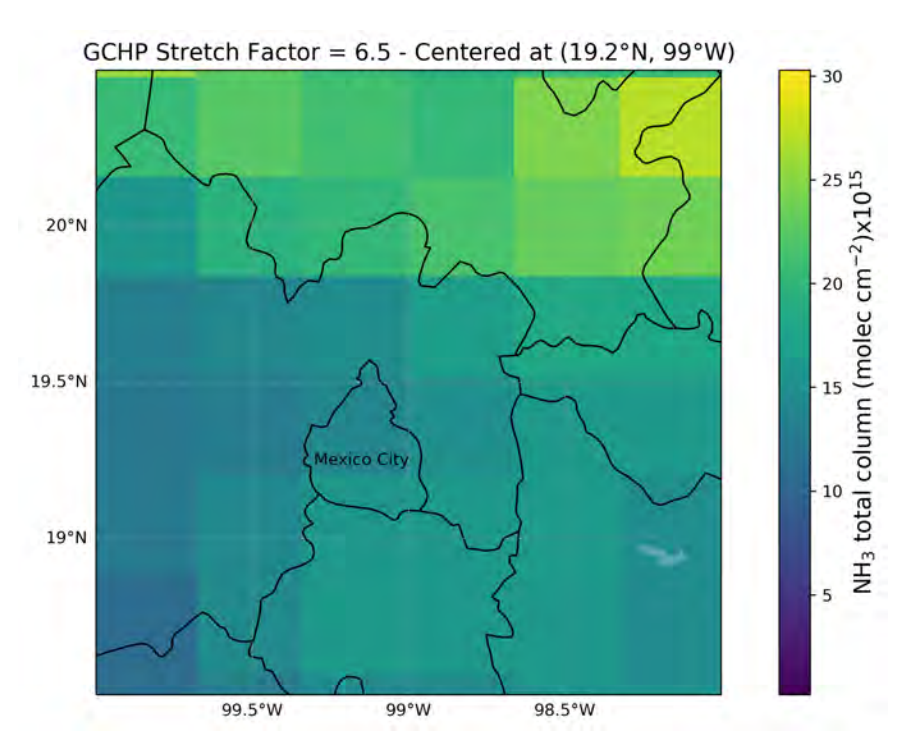


Figure 5.6: Spatial distribution of daily mean  $NH_3$  total columns during May 13, 2019, over central Mexico from the GCHP-SF stretched grid simulation.

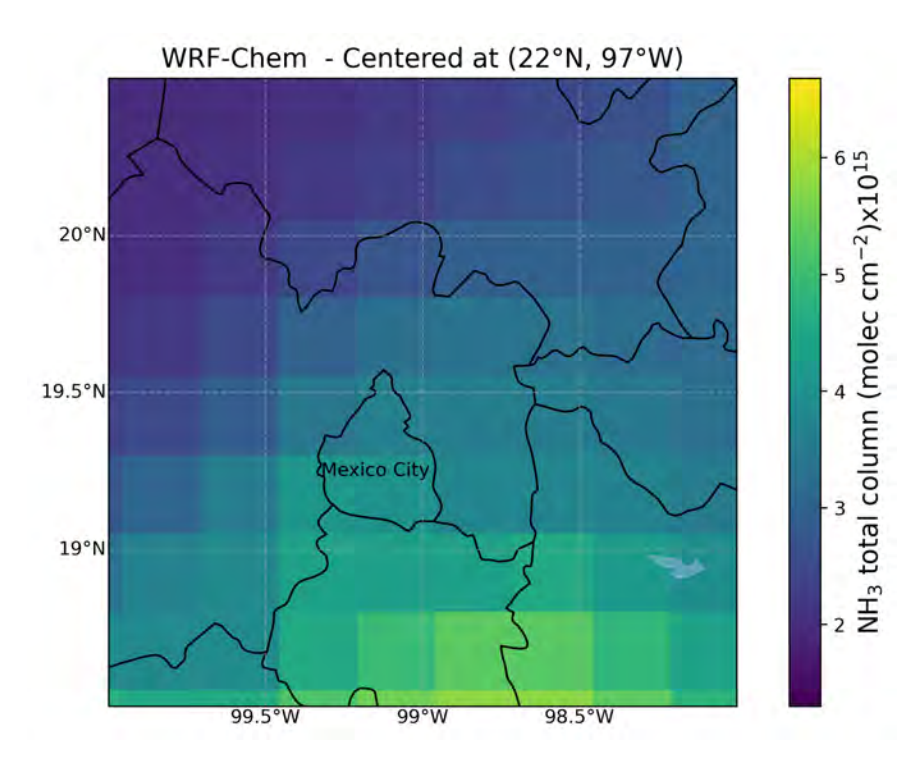


Figure 5.7: Spatial distribution of mean  $\rm NH_3$  total columns during May 13, 2019, over central Mexico from the WRF-Chem simulation.

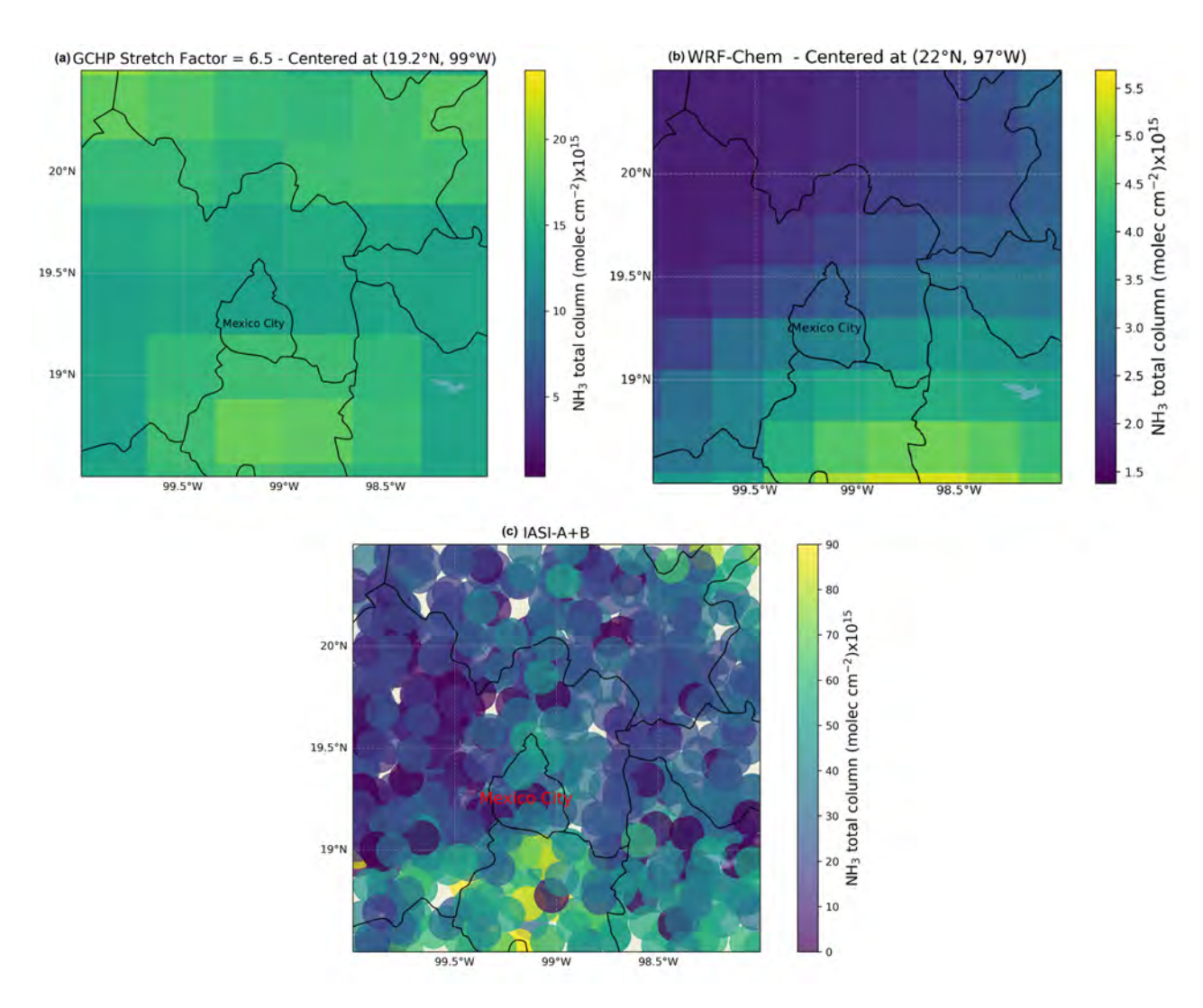


Figure 5.8: Spatial distribution of NH<sub>3</sub> total columns between 11 and 16 May 2019, over central Mexico from (a) GCHP-SF, (b) WRF-Chem, and (c) IASI A+B.

and IASI satellite data. The total NH<sub>3</sub> columns from IASI are much larger than those from GCHP-SF and WRF-Chem, with values between 40 and  $50\times10^{15}$  molec. cm<sup>-2</sup> in the city and  $90\times10^{15}$  molec. cm<sup>-2</sup> at the south and northeast of the city, more in agreement with the NH<sub>3</sub> total column from FTIR measurements at the Mexico City site, shown in Figure C.1, with values up to  $70\times10^{15}$  molec. cm<sup>-2</sup>. Both models underestimated the NH<sub>3</sub> total column compared to IASI values, and this negative bias is more prominent in WRF-Chem. The spatial distribution of NH<sub>3</sub> total columns from IASI over a larger region of Mexico is shown in Figure C.3, where large enhancements

of NH<sub>3</sub> are observed at the south, in agreement with Figure 5.3, and at the norteast and east of the city, reaching the Gulf of Mexico, probably due to long-range transport.

#### 5.3.3 GCHP-SF vs. GCHP-C48

This section presents comparisons between GCHP-C48 and GCHP-SF. The focus is on comparisons using GCHP-SF only, as at the time of the analysis, WRF-Chem outputs for Mexico City were not in the appropriate format to fully compare with GCHP and FTIR observations at Mexico City and Altzomoni. Equation 5.1 was used to calculate the relative difference of the results:

$$RD = \left(\frac{V_{GCHP-SF} - V_{GCHP-C48}}{V_{GCHP-C48}}\right) \times 100 \tag{5.1}$$

where  $V_{GCHP-SF}$  and  $V_{GCHP-C48}$  are the mean NH<sub>3</sub> total columns or surface PM<sub>2.5</sub> values for GCHP-SF and GCHP-C48 respectively.

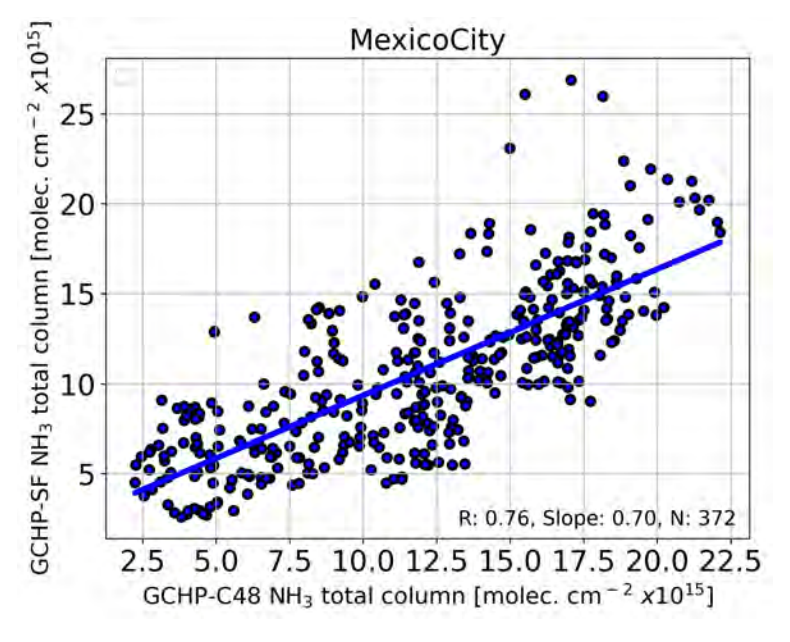


Figure 5.9: Scatter plots of GCHP-SF vs. GCHP-C48 NH<sub>3</sub> total columns for Mexico City during May 2019.

Figure 5.9 shows the scatter plot between the NH<sub>3</sub> total columns of GCHP-C48 and GCHP-SF for Mexico City during May 2019. It can be observed that there is consistency between the datasets, with a correlation coefficient R = 0.76 and a slope = 0.70. However, the GCHP-SF columns have a negative bias compared to GCHP-C48. For Mexico City, the mean NH<sub>3</sub> total columns  $\pm 1\sigma$  in May 2019 were 11.78  $\pm$  5.00  $\times 10^{15}$  molec. cm<sup>-2</sup> for GCHP-C48 and 10.64  $\pm$  4.61  $\times 10^{15}$  molec. cm<sup>-2</sup> for GCHP-SF, with a RD of -10.02%.

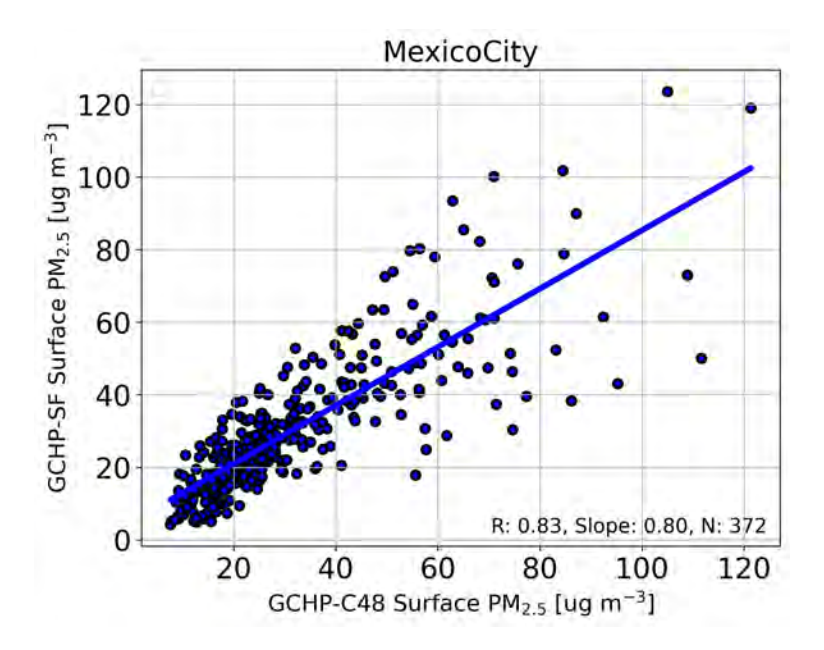


Figure 5.10: Scatter plots of GCHP-SF vs. GCHP-C48 surface  $\rm PM_{2.5}$  for Mexico City during May 2019.

The correlation for PM<sub>2.5</sub> in Figure 5.10 shows a better consistency, with R=0.83 and slope = 0.80, GCHP-SF values are generally smaller than GCHP-C48 above 40  $\mu$ g m<sup>-3</sup>. The mean PM<sub>2.5</sub> surface concentrations were 31.11  $\pm$  19.33  $\mu$ g m<sup>-3</sup> for GCHP-C48 and 29.92  $\pm$  18.67  $\mu$ g m<sup>-3</sup> for GCHP-SF with a RD of -3.81%.

For Altzomoni, Figure 5.11 shows a similar correlation to that found at Mexico City, with R=0.79 and slope = 0.73. The mean NH<sub>3</sub> total columns were 11.78  $\pm$  5.00  $\times 10^{15}$  molec. cm<sup>-2</sup> for GCHP-C48 and 11.30  $\pm$  4.63  $\times 10^{15}$  molec. cm<sup>-2</sup> for GCHP-

SF, with a RD of -4.14%. The mean NH<sub>3</sub> total columns for GCHP-C48 at Altzomoni are the same as for Mexico City, due to the coarse resolution of the model.

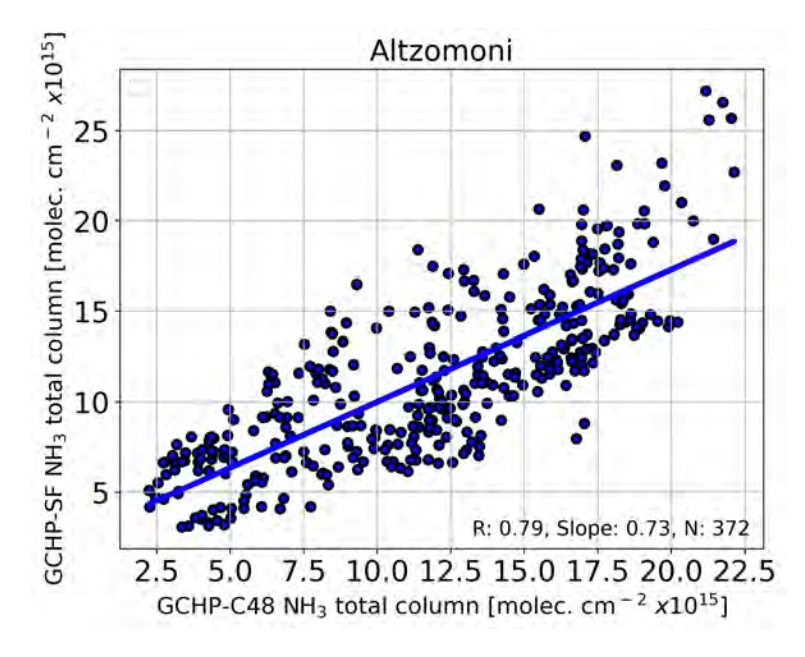


Figure 5.11: Scatter plots of GCHP-SF vs. GCHP-C48 NH<sub>3</sub> total columns for Altzomoni during May 2019.

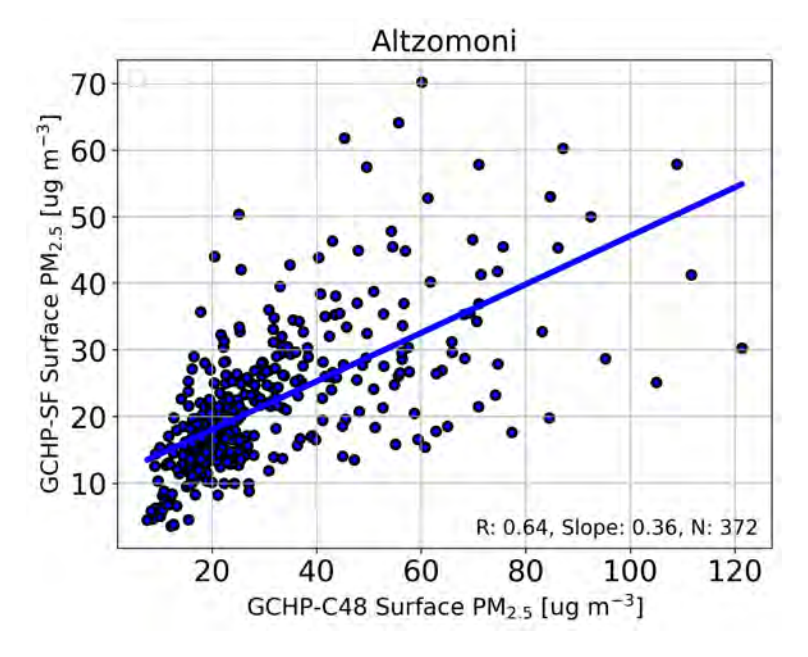


Figure 5.12: Scatter plots of GCHP-SF vs. GCHP-C48 surface  $PM_{2.5}$  for Altzomoni during May 2019.

The PM<sub>2.5</sub> correlations at Altzomoni are shown in Figure 5.12. In this case, the consistency was better below 20  $\mu$ g m<sup>-3</sup>, beyond which the underestimation in GCHP-SF for large values of GCHP-C48 is more evident, with a correlation R=0.64 and a slope of only 0.36. The mean surface PM<sub>2.5</sub> was 31.11  $\pm$  19.33  $\mu$ g m<sup>-3</sup> for GCHP-C48 and 22.06  $\pm$  10.93  $\mu$ g m<sup>-3</sup> for GCHP-SF, with a RD of -29.07%.

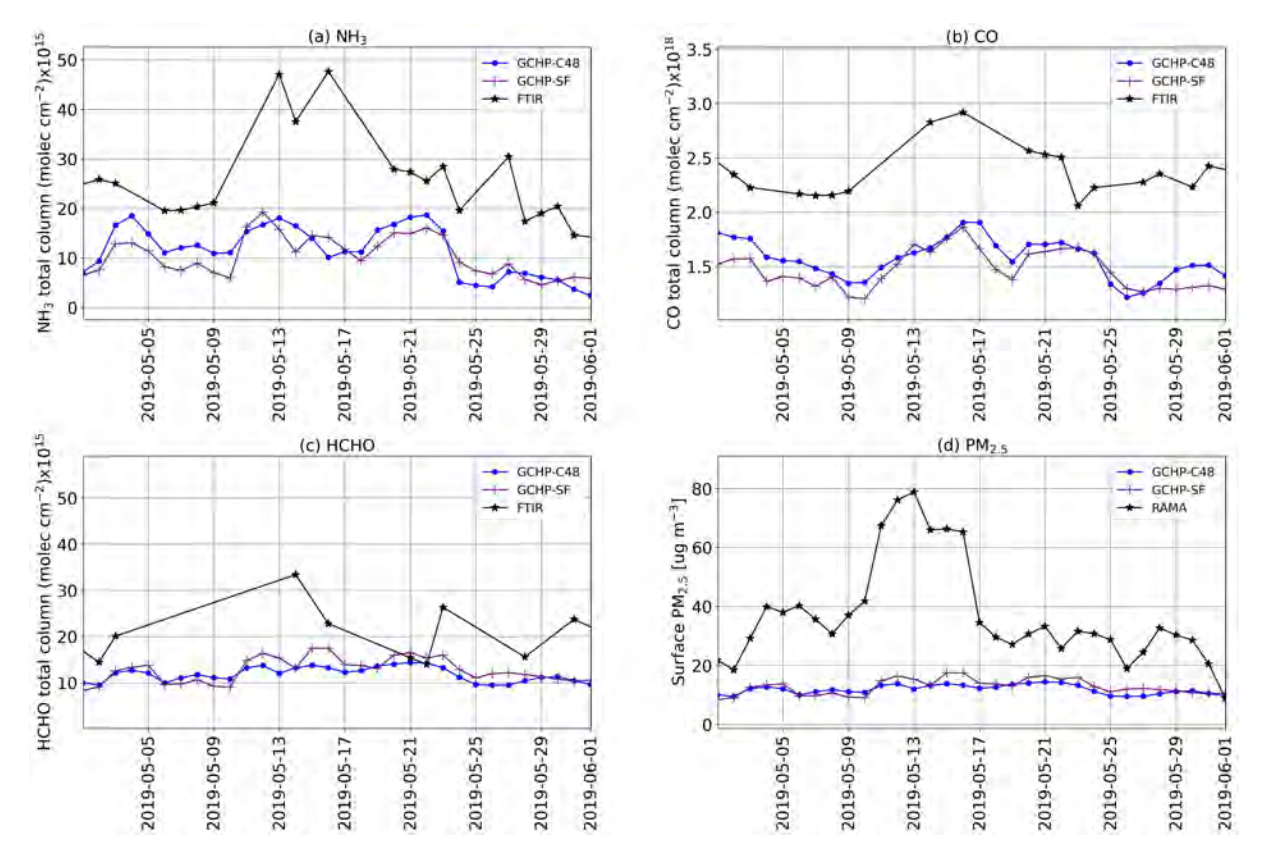


Figure 5.13: Daily means of (a)  $NH_3$ , (b) CO, (c) HCHO total columns and (d) surface  $PM_{2.5}$  for Mexico City during May 2019 from measurements (FTIR and RAMA), GCHP-C48, and GCHP-SF.

Comparisons between GCHP and the measurements were also performed. Figure 5.13 shows the time series of NH<sub>3</sub>, CO, and HCHO from FTIR measurements at the Mexico City site. CO and HCHO were included as they are species emitted from biomass burning events, with CO having a longer lifetime than NH<sub>3</sub>, to analyze the performance of the model simulations with those different gases. The figure shows that in general, GCHP-SF total columns seem to be capturing more variability than

GCHP-C48, however, with a more negative bias for the three species, mainly during the pollution event in mid-May. For PM<sub>2.5</sub>, both GCHP-SF and GCHP-C48 were able to capture the enhancements in mid-May, but the daily means of GHCP-C48 and GCHP-SF are considerably smaller than the RAMA values.

## 5.4 Summary

Mexico City's air quality can be detrimental throughout the year, mainly during the warm-dry season from March to June, with frequent episodes of high O<sub>3</sub> and PM<sub>2.5</sub> levels. During May 2019, several days of extremely poor air quality were recorded, with substantial contributions of emissions from unusually intense biomass burning events exacerbated by meteorological conditions. NH<sub>3</sub> can be emitted from biomass burning, a key precursor for PM<sub>2.5</sub>. Thus, two different models were evaluated under enhanced NH<sub>3</sub> and PM<sub>2.5</sub> conditions.

NH<sub>3</sub> and PM<sub>2.5</sub> pollution events were detected over Mexico City during May 2019 using GCHP-C48 data: on 21 days for NH<sub>3</sub> and 12 days for PM<sub>2.5</sub>. These events were confirmed using ground-based observations: seven for NH<sub>3</sub> and 14 for PM<sub>2.5</sub>. The magnitude of the pollution events from GCHP-C48 was smaller than the magnitude from the measurements, by 40% for NH<sub>3</sub> and 60% for PM<sub>2.5</sub>. The model representation of the pollution events was more accurate for NH<sub>3</sub> than for PM<sub>2.5</sub>. To further evaluate the participation of NH<sub>3</sub> in the PM<sub>2.5</sub> formation during this pollution event, the contribution of ammonium should be quantified via PM<sub>2.5</sub> speciation (% in total mass) derived from GCHP results.

In Chapter 4, it was observed that GCHP underestimates NH<sub>3</sub>, and Mexico City was one of the most affected sites. To evaluate if increasing the model's resolution will improve the representation of NH<sub>3</sub>, two models of higher and similar resolution were

selected ( $\sim 32$  km). May 13th was the only date with pollution events from the model and the measurements for both NH<sub>3</sub> and PM<sub>2.5</sub>; therefore, this day was selected to evaluate the spatial distribution of PM<sub>2.5</sub> and NH<sub>3</sub> from a regional model (WRF-Chem) and a global model but with a feature to increase the resolution over a target region by decreasing resolution in the areas that aren't of interest (GCHP-SF). For PM<sub>2.5</sub>, both models show similar surface PM<sub>2.5</sub> values, both smaller than the RAMA value. However, GCHP-SF presented larger values in the north and WRF-Chem in the southeast. The GCHP-SF NH<sub>3</sub> total column was larger than the WRF-Chem results, and more similar to the reference FTIR value. However, the spatial distribution from WRF-Chem was more accurate, with larger column values in the south, where the fire events originated. Large values of NH<sub>3</sub> total column from IASI were located south of and northeast of the city. Comparisons of the spatial distribution over a non-polluted day are recommended to evaluate the model's performance under low NH<sub>3</sub> and PM<sub>2.5</sub> concentrations. The GCHP analysis presented here should also be extended to include other biomass burning inventories, such as GFED and the Quick Fire Emissions Dataset (QFED).

Despite using a regional model and higher resolution, substantial underestimation of NH<sub>3</sub> for Mexico City remains. In the case of GCHP-SF, even though the resolution significantly increases from GCHP-C48, it seems that the resolution and quality of the emissions used are still a limiting factor to fully improve the model simulation over Mexico City. Comparisons with the spatial distribution of NH<sub>3</sub> from satellite measurements are recommended. For PM<sub>2.5</sub>, the RAMA network has stations distributed around the City; these measurements could be used to generate a matrix to visualize the spatial distribution of PM<sub>2.5</sub> over the city to evaluate the models.

Finally, a comparison was performed between GCHP-C48 and GCHP-SF total columns and  $PM_{2.5}$  for Mexico City and Altzomoni. In general, there is a good agreement be-

tween GCHP-SF and GCHP-C48. However, GCHP-SF total column and surface PM<sub>2.5</sub> values were consistently smaller for NH<sub>3</sub> and PM<sub>2.5</sub> at Mexico City (-10.02% for NH<sub>3</sub> and -3.81% for PM<sub>2.5</sub>) and Altzomoni (-4.14% for NH<sub>3</sub> and -29.07% for PM<sub>2.5</sub>). The largest difference was presented for the PM<sub>2.5</sub> surface values at Altzomoni. GCHP-C48 and GCHP-SF underestimates NH<sub>3</sub>, CO, HCHO, and PM<sub>2.5</sub>. However, the increase in the resolution of GCHP-SF allowed for better differentiation between Mexico City and Altzomoni stations. Although biomass burning was a major factor driving the pollution events, it would be valuable to rerun the GCHP simulations with higher resolution anthropogenic emission inventories to better assess the model fidelity in simulating the observations at Mexico City and Altzomoni.

## Chapter 6

## Conclusions and Future Work

## 6.1 Conclusions

Atmospheric ammonia is a pollutant that is getting more attention due to its environmental impact and participation in several chemical reactions, including the formation of fine particulate matter, which poses a threat to global human health. Ammonia is present in a variety of environments, ranging from agricultural regions to megacities and remote areas such as the Arctic. Despite this, there are still large uncertainties regarding its emissions. Ground-based measurements, such as the FTIR total columns presented in this work, provide information about the spatial and temporal distributions of this gas in the atmosphere and can be used to improve estimates of emission inventories. In this thesis, the total column time series of NH<sub>3</sub> from 22 globally distributed FTIR sites were combined with satellite observations, atmospheric models, and a reanalysis product to address the scientific objectives presented in Chapter 1, which were:

- To investigate the spatial and temporal variability of NH<sub>3</sub> over Mexico City by using satellite data and ground-based measurements from remote and urban sites.
- 2. To quantify the variability and long-term trends of atmospheric NH<sub>3</sub> using measurements and model simulations at globally distributed sites.
- 3. To investigate simultaneous enhancements of NH<sub>3</sub> and PM<sub>2.5</sub> in Mexico City during an extreme pollution event, and to assess the ability of models to characterize this event.

To address the first objective, the temporal and spatial variability of NH<sub>3</sub> over Mexico City was characterized from FTIR measurements at an urban and a remote site, and IASI satellite observations. The NH<sub>3</sub> total column at the urban site were considerably higher than that at the remote station with a clear difference in the diurnal cycle but similar seasonal variability. Most of the NH<sub>3</sub> measured at the urban station was attributed to local urban sources, while the NH<sub>3</sub> observed at the remote site was most likely transported from the surroundings and was influenced by biomass burning events. The IASI ANNI-NH<sub>3</sub>-v3 data product underestimated the NH<sub>3</sub> total columns over Mexico City, with a mean relative difference of 32% over the period 2008-2018, but showed a similar temporal variability and a good correlation with FTIR measurements. The NH<sub>3</sub> spatial distribution from satellite observations showed the highest NH<sub>3</sub> columns in the northeast part of the city.

To address the second objective, the time series of NH<sub>3</sub> from 22 FTIR sites, most of them affiliated with the NDACC IRWG, were acquired and analyzed to derive the seasonal and diurnal variability. The sites are globally dispersed in both hemispheres, ranging from 45°S to 80°N. Different retrieval strategies were tested for the Eureka, Toronto, Altzomoni, and Mexico City sites, with the chosen parameters summarized

in Table 2.1. For the other sites, the recommended retrieval strategy was followed to the extent possible at each site. The seasonal variability was obtained by calculating the monthly means for each site. It was found that the seasonal patterns were similar across most sites, ranging between 2.43 and  $6.47 \times 10^{15}$  molec. cm<sup>-2</sup>, and were consistent with previous studies that mainly used satellite data. For the diurnal variability, hourly means at local time for each site were calculated. The diurnal variability of NH<sub>3</sub> total columns was shown for the first time for most of the FTIR sites, with variations between 0.20 and  $6.74 \times 10^{15}$  molec. cm<sup>-2</sup> and significant differences between sites. The variability was compared to simulations of NH<sub>3</sub> from the GEOS-Chem High Performance CTM and the Tropospheric Chemistry Reanalysis product. Both NH<sub>3</sub> simulations captured the seasonality of the FTIR measurements, with a mainly negative bias for the Northern and Southern Hemisphere sites and a positive bias in the Arctic for GCHP. However, GCHP and TCR-2 poorly reproduced the diurnal variability of the measurements. This suggests that potential underestimation of local sources and lack of diurnal variations in the anthropogenic emissions used in the simulations are crucial for most sites to reproduce the diurnal variability better.

Long-term trends were derived from the FTIR time series and the NH<sub>3</sub> simulations. The trends were determined by fitting Fourier series to account for seasonality, and the 95% confidence intervals were obtained using an autoregressive wild bootstrap method, to account for missing observations, autocorrelation, and seasonal effects in the datasets. Most of the sites presented positive trends, with the largest trends at sites located in urban areas, and the smallest trends at Arctic and high-altitude sites. The mean value of the trends obtained for all sites is 19.43 (14.18 – 24.68)×10<sup>13</sup> molec. cm<sup>-2</sup> yr<sup>-1</sup> for the FTIR measurements. Trends were also derived from long-term NH<sub>3</sub> simulations, with a mean value from 2003 to 2021 of 10.11 (9.31 – 10.91)×10<sup>13</sup> molec. cm<sup>-2</sup> yr<sup>-1</sup> for the GCHP, and 1.93 (1.11 – 2.75)×10<sup>13</sup> molec. cm<sup>-2</sup> yr<sup>-1</sup> for TCR-2 from 2005 to 2018. In general, the trends calculated

using GCHP and the TCR-2 product were smaller than the FTIR results at each site. In addition, significant NH<sub>3</sub> enhancements were located in the time series for Eureka, Thule, Los Angeles, Izana, Mexico City, Altzomoni, Paramaribo, Porto Velho and Reunion Maido, and attributed to biomass burning events. NH<sub>3</sub> emissions from volcanic eruptions were also identified at Izana during the volcanic eruption of La Palma in 2021. This highlights the importance of biomass burning as a source of NH<sub>3</sub>.

Finally, to address the third objective, a pollution episode with enhanced PM<sub>2.5</sub> in May 2019 was selected to evaluate the model's performance and the role of NH<sub>3</sub> in PM<sub>2.5</sub> formation. Mexico City was one of the 22 FTIR sites where GCHP and TCR-2 exhibited larger negative biases relative to the FTIR NH<sub>3</sub> columns. Simulations of NH<sub>3</sub> and PM<sub>2.5</sub> from two CTMs with a 32 km horizontal resolution, the GCHP stretched-grid configuration and WRF-Chem regional model, were evaluated. Simultaneous enhancements of PM<sub>2.5</sub> and NH<sub>3</sub> at Mexico City were identified during May 2019. Both models' representation of NH<sub>3</sub> was better than that for PM<sub>2.5</sub>. However, compared to satellite and ground-based data, a substantial underestimation of NH<sub>3</sub> for Mexico City remains for both models, suggesting that the resolution and quality of the emissions used in the models are still limiting factors in fully improving the model performance over Mexico City.

 $\mathrm{NH_3}$  is a short-lived and highly variable atmospheric trace gas present in urban and remote areas, with consequences for the Earth's radiative forcing balance, ecosystems, and human health, including its role as  $\mathrm{PM_{2.5}}$  precursor. Atmospheric  $\mathrm{NH_3}$  concentrations have been rising since the early 1900s with the introduction of synthetic fertilizers and they continue to increase globally. The lack of global regulation regarding  $\mathrm{NH_3}$  emissions, changes in meteorology, and emissions of other species such as  $\mathrm{NOx}$  and  $\mathrm{SO_2}$  are some of the factors contributing to this. It is important to

continue and expand the monitoring of NH<sub>3</sub> using ground-based and satellite instruments to extend the time series of this gas, analyze trends, and reduce uncertainties in the emissions and simulations. Such measurements could help inform the development of global regulations and policies that are needed to reduce the atmospheric concentration of NH<sub>3</sub> and its effects.

## 6.2 Future Work

Regarding the FTIR measurements, there are a few suggestions for future work. First, continuing the ongoing measurements at the different NDACC IRWG sites will expand the current time series. As shown in this work, NH<sub>3</sub> can be retrieved at the NDACC FTIR sites; however, it is not among the routine products provided by the network. Future work on this could include improvements in the retrieval strategy across all sites, such as the complete implementation of the new SFIT4 version v1.0.21, instead of version v0.9.4.4; updating the linelist from HITRAN 2008 to HITRAN 2020 with the H<sub>2</sub>O lines from ATM 2020, updating the recommended a priori profiles by creating new ones using the long-term simulation (2003-2021) from GCHP. For sites where there are substantial differences in NH<sub>3</sub> concentrations through the year due to significant changes in temperature between warm and cold seasons or sites that are strongly impacted by biomass burning season, the use of a changing a priori profile could be explored. Having an improved retrieval for NH<sub>3</sub> adopted by a significant number of NDACC FTIR sites could be helpful in proposing this gas to be added to the list of standard data products for the NDACC IRWG. FTIR measurements of NH<sub>3</sub> have been used to validate satellite products such as IASI or CrIS. However, those validations were performed using data from less than ten FTIR sites; thus, having a standard NDACC NH<sub>3</sub> product could be useful for validation of future satellite NH<sub>3</sub> products. Such a product could be valuable for continuously evaluating regional and global atmospheric models.

Regarding GCHP and TCR-2 performance, a similar analysis to the one performed in Chapter 4 could be done using another gas that preferably has a longer lifetime than NH<sub>3</sub> and less uncertainty in the retrieved total column. Among the standard NDACC products, CO and O<sub>3</sub> could be a good option to evaluate the model performance in some of the FTIR sites where larger biases were found. TCR-2 optimizes the emissions and concentrations of various trace gases through data assimilation of satellite observations. To improve the TCR-2 NH<sub>3</sub> product, it is recommended to assimilate satellite observations of NH<sub>3</sub> from instruments such as TES or CrIS, from which other products, such as O<sub>3</sub>, are already being assimilated by TCR-2. This is planned for the next version of TCR, TCR-3 (Kazuyuki Miyazaki, personal communication). This new TCR-3 NH<sub>3</sub> product should then be validated against the global FTIR measurements.

In addition, it could be helpful to rerun the GCHP simulations with higher-resolution anthropogenic emissions for Mexico City. Comparisons against FTIR observations should be performed using the WRF-Chem data to further assess the performance of both models over this region. To evaluate the differences in the chemistry mechanisms in the models, a simulation using WRF-GC (WRF coupled with GEOS-Chem chemistry) could be performed at the same resolution as the WRF-Chem simulation.

# Appendix A

# Supplemental Figures and Information for Chapter 2

## A.1 NH<sub>3</sub> Retrieval

Table A.1: Summary of FTIR  $NH_3$  retrieval parameters used at Eureka between 2006 and 2020.

$NH_3$ a priori	Lutsch (2019)	$GC \times 2.5$
Mean total column (molec. cm <sup>-2</sup> )	$2.27 \times 10^{14}$	$1.50 \times 10^{14}$
DOFS	1.01	0.96
RMS(%)	0.57	0.65
# retrievals converged	8763	6355

Table A.2: Summary of FTIR  $\mathrm{NH}_3$  retrieval parameters used at Toronto during 2021.

$\mathrm{NH_{3}}$ a priori	Yamanouchi (2021)	$GC \times 3$
Mean total column (molec. cm <sup>-2</sup> )	$9.54 \times 10^{15}$	$9.05 \times 10^{15}$
DOFS	1.15	1.43
RMS(%)	1.29	1.28
# retrievals converged	693	693

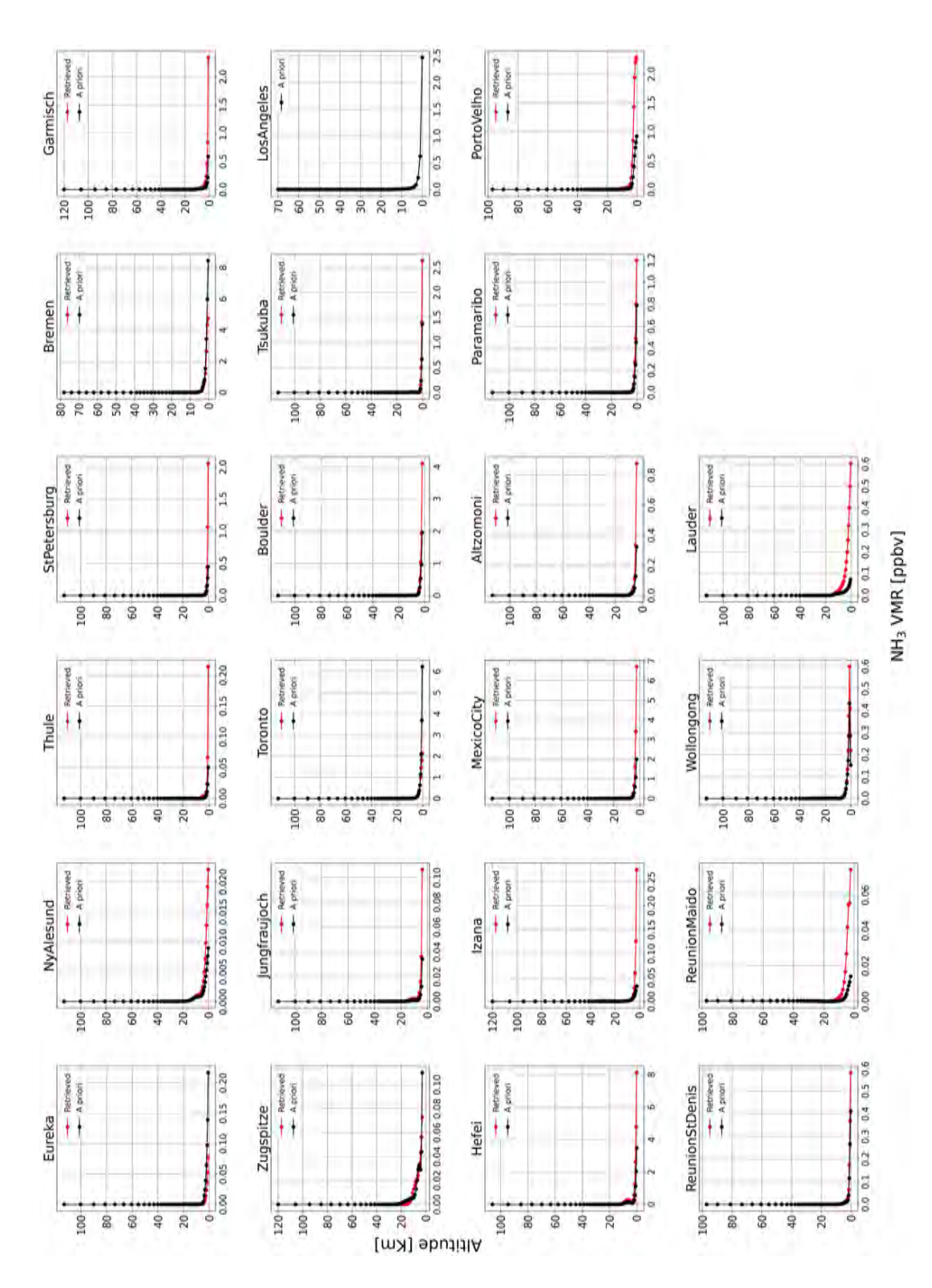


Figure A.1: Mean retrieved NH<sub>3</sub> VMR profiles (red) and a priori profiles (black) at the 22 FTIR sites. The retrieved profiles are the means over the years indicated in Table 2.2. The circle markers indicate the layer centers of the FTIR vertical retrieval grid. The shaded region indicates ± the standard deviation from the mean. For the Los Angeles site, only the a priori VMR profile is shown as GFIT scaling retrievals do not contain more vertical information than the total column amount.

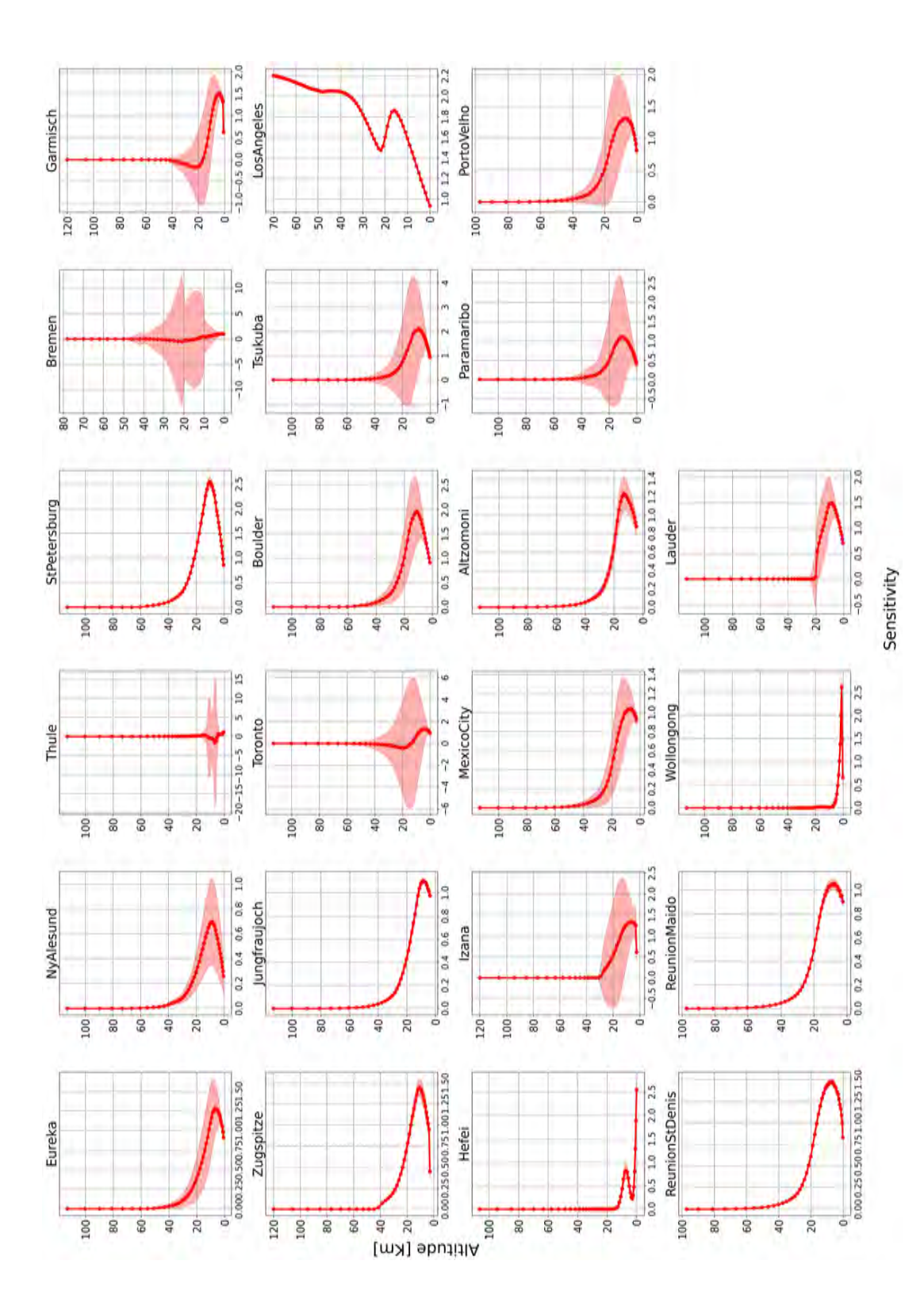


Figure A.2: Mean sensitivity for NH<sub>3</sub> retrieval at the 22 FTIR sites taken over the years indicated in Table 2.2. The circle markers indicate the layer centers of the FTIR vertical retrieval grid. The shaded region indicates ± the standard deviation from the mean. The standard deviation for the Los Angeles site was not available.

## A.2 Total Columns From GCHP

Below are the general steps followed to calculate the  $\rm NH_3$  total column in molecules  $\rm cm^{-2}$  from GCHP simulations. These GCHP outputs are used:

- SpeciesConcVV\_NH3, which is the NH3 in mol NH3/mole dry air;
- $\bullet$  MetAIRDEN, which is the dry air density in kg  $\mathrm{m}^{-3};$  and
- MetBXHEIGHT, which is the grid box height in m.

We define a constant c that includes Avogadro's constant (N<sub>A</sub> = 6.022x10<sup>23</sup> molecules NH<sub>3</sub> mole<sup>-1</sup>), the molecular mass of dry air ( $M_{dry} = 0.028964$  kg mole<sup>-1</sup>), and a conversion factor from m<sup>-2</sup> to cm<sup>-2</sup>:

$$c = \frac{N_A}{M_{dry}} \cdot \left(\frac{1}{100}\right)^2 = -2.079132716x10^{21} \left[\frac{\text{mole air} \cdot \text{molecules} \cdot \text{m}^2}{\text{kg} \cdot \text{mole NH}_3 \cdot \text{cm}^2}\right]. \tag{A.1}$$

The GCHP partial columns are given by:

$$PC_{NH3} = \text{SpeciesConcVV\_NH3} \cdot \text{MetAIRDEN} \cdot \text{MetBXHEIGHT} \cdot c$$
  
= partial column in  $\left[\frac{\text{molecules NH}_3}{\text{cm}^2}\right]$ . (A.2)

The total columns are calculated by taking the sum of the partial columns:

$$TC_{NH3} = \sum_{i=1}^{N} PC_{NH3,i}.$$
 (A.3)

## A.3 Total Columns From TCR-2

The TCR-2 product contains the following variables: latitude, longitude, level in millibars, time, and NH<sub>3</sub> VMR in pptv. The steps to calculate the total columns in NH<sub>3</sub> molec.  $cm^{-2}$  from TCR-2 outputs are as follows:

First, convert the NH<sub>3</sub> VMR from pptv to moles of NH<sub>3</sub>/moles of dry air using 1 pptv =  $1 \times 10^{12}$  mole NH<sub>3</sub>/mole air. Then, assuming dry-air conditions, the hydrostatic equation, and constant g, and using the molecular mass of dry air, the molar partial column is given by:

$$\frac{-\Delta P}{g M_{\rm dry}} = \frac{\rho \Delta z}{M_{\rm dry}}.$$
 (A.4)

where  $-\Delta P$  is the difference between adjacent pressure levels in the models in Pa; it is calculated using pressure values from a separate output from the MIROC-CHASER model. Similar to the GCHP total column calculation, a conversion factor k is defined as:

$$k = \frac{-N_A}{g \cdot M_{\text{dry}}} \cdot \left(\frac{1}{100}\right)^2 = -3.51943 \left[\frac{\text{s}^2 \cdot \text{mole}}{\text{m} \cdot \text{kg}}\right].$$

The partial columns are given by:

$$PC_{NH3} = NH_3 VMR \cdot \Delta P \cdot k = partial column in \left[ \frac{molecules NH_3}{cm^2} \right]$$
 (A.5)

The total columns are again calculated by taking the sum of the partial columns.

# Appendix B

# Supplemental Figures for Chapter 4

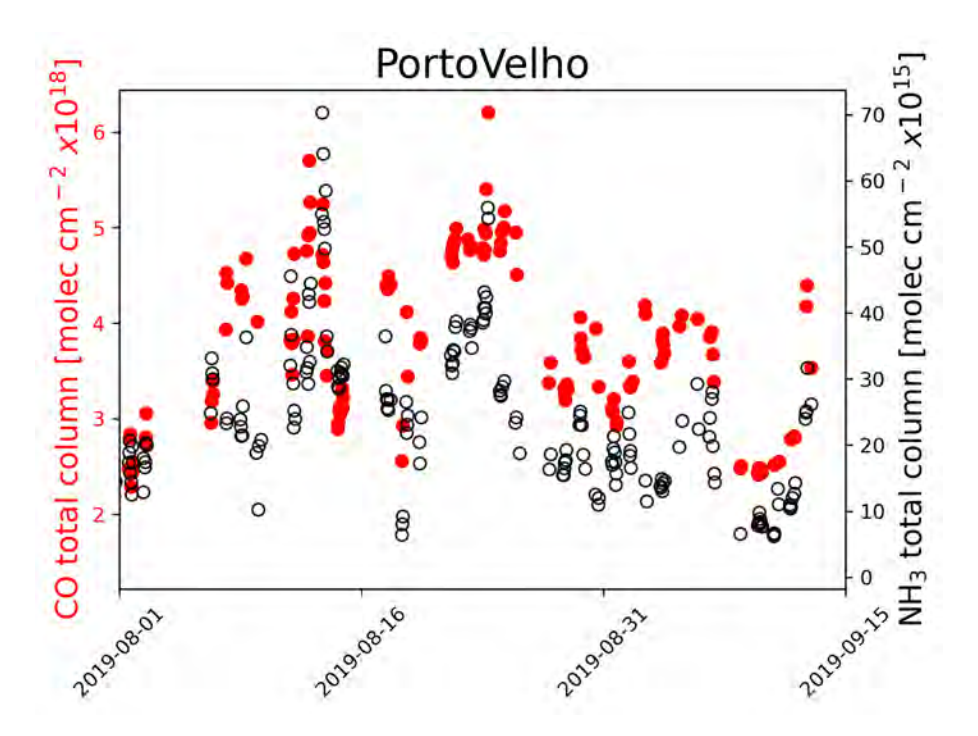


Figure B.1: Comparison of  $NH_3$  and CO total columns measured at Porto Velho between July and September 2019. Simultaneous enhancements can be observed, attributed to biomass burning events.

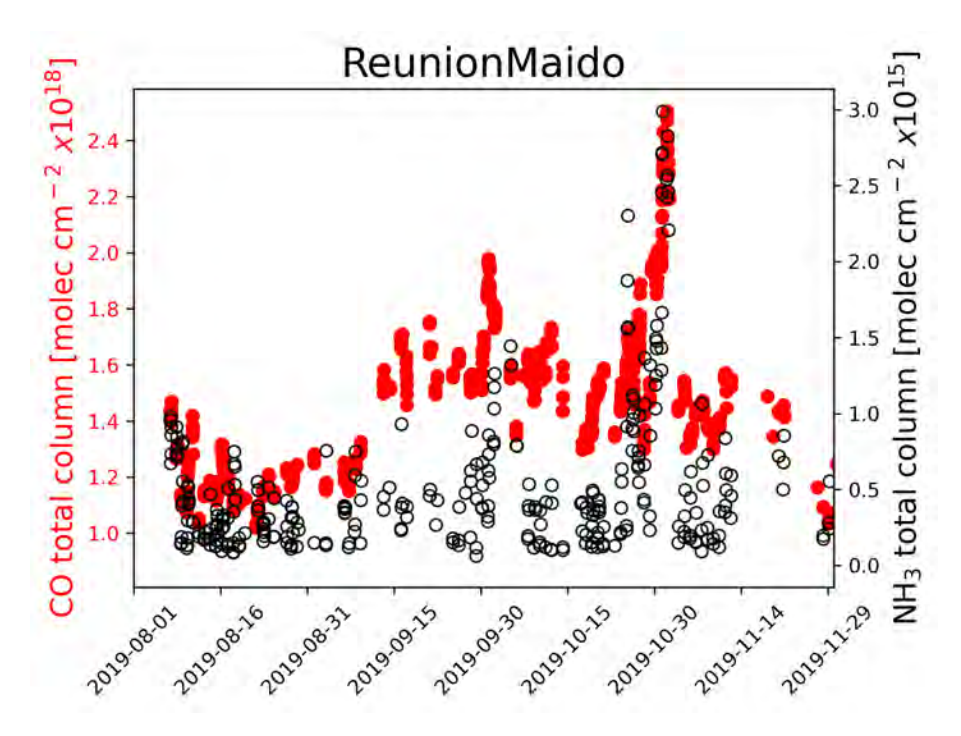


Figure B.2: Comparison of  $NH_3$  and CO total columns measured at Reunion Maido between August and November 2019. Simultaneous enhancements can be observed, attributed to biomass burning events.

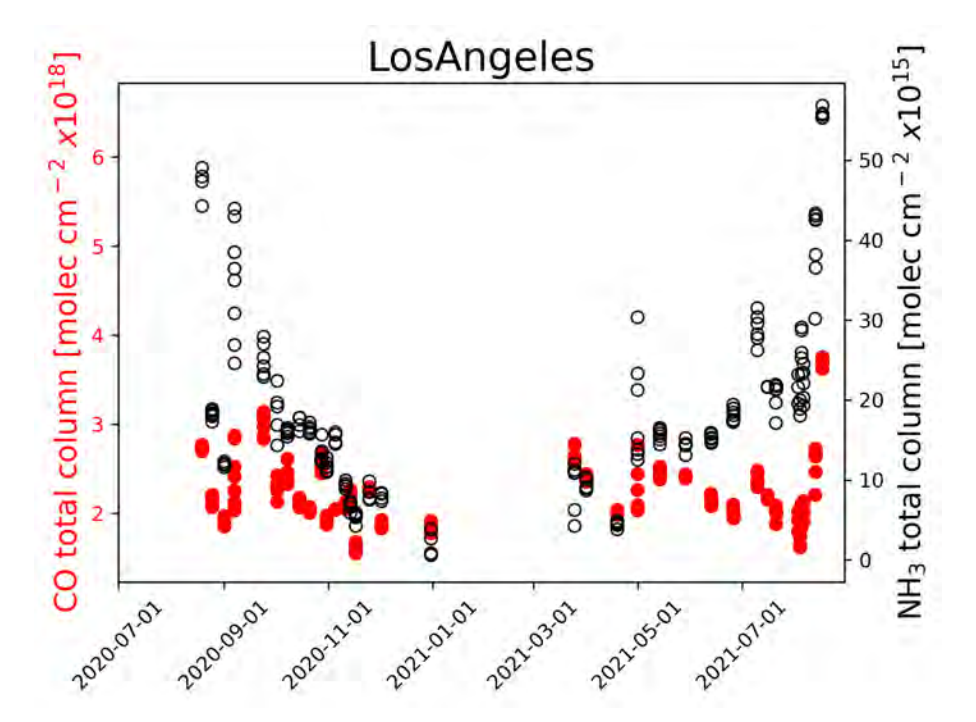


Figure B.3: Comparison of  $\rm NH_3$  and CO total columns measured at Los Angeles between July 2020 and August 2021. Simultaneous enhancements can be observed, attributed to wildfires.

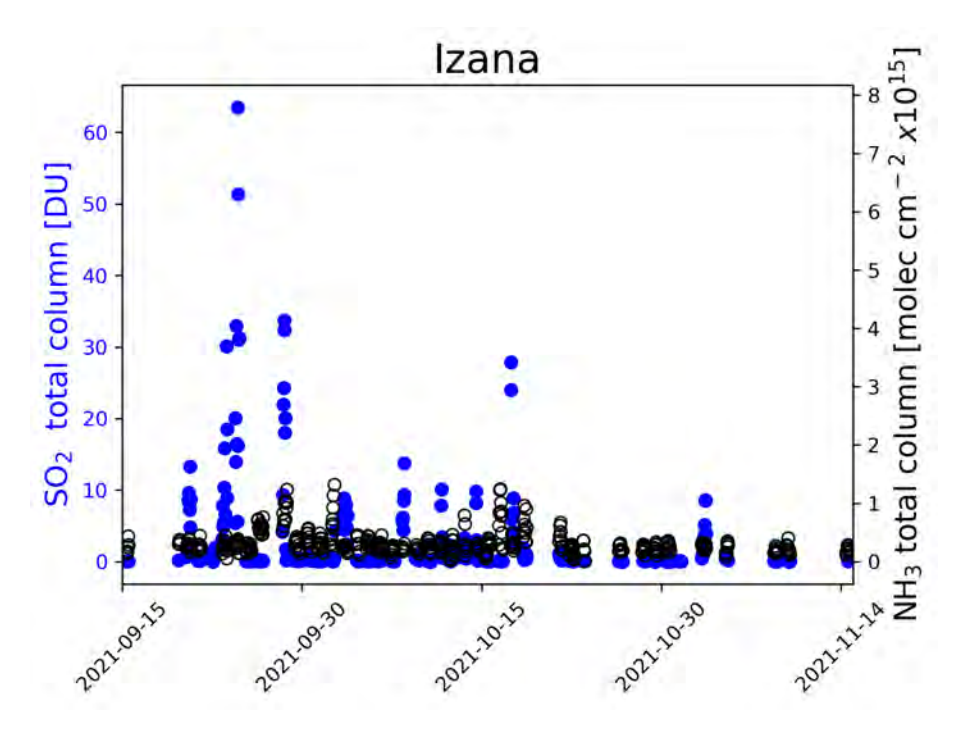


Figure B.4: Comparison of  $NH_3$  and  $SO_2$  total columns measured at Izana between September and November 2021 during the Tarjogaite volcanic eruption that reached the Izana site. Simultaneous enhancements can be observed.

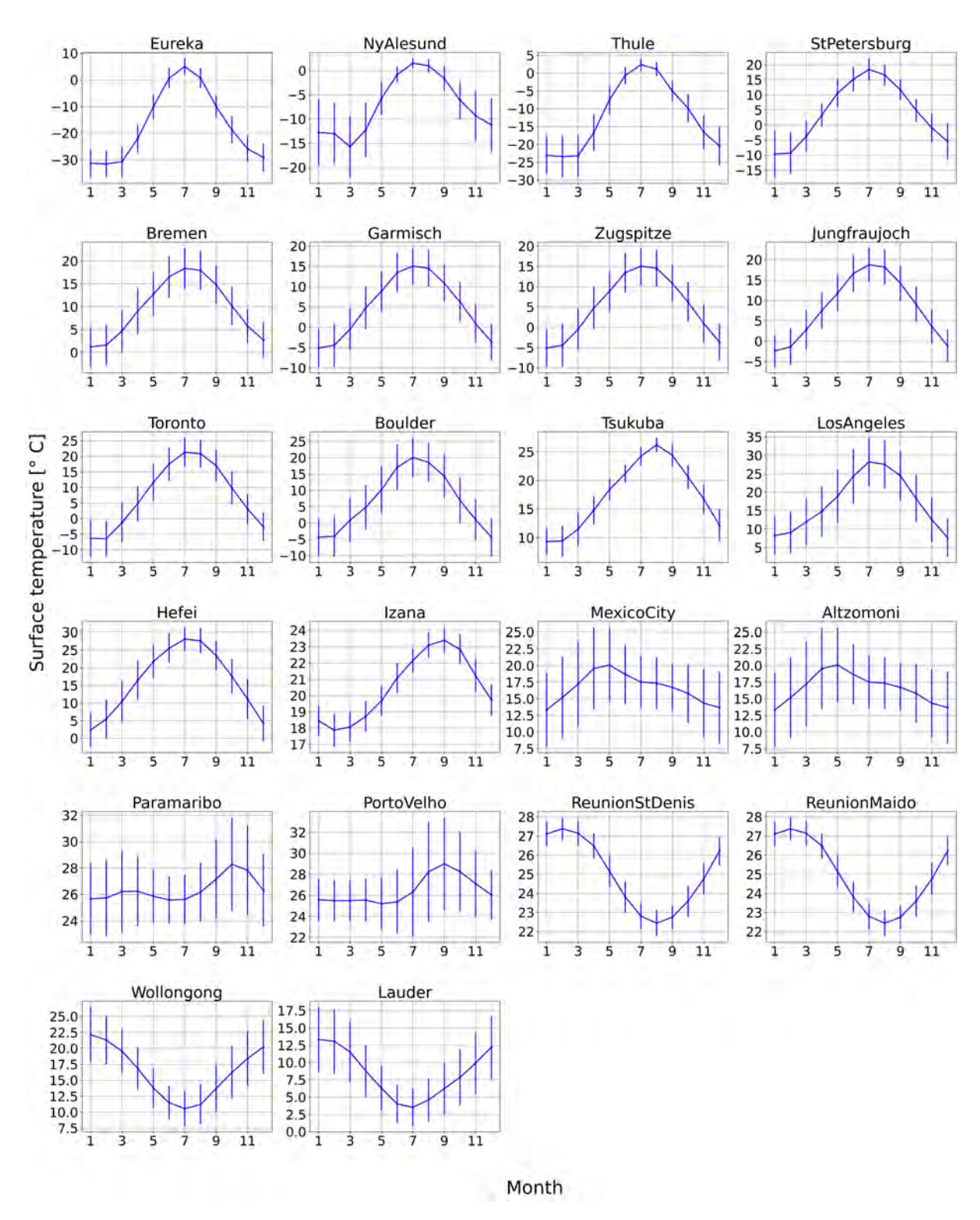


Figure B.5: Monthly mean GCHP surface temperature at each FTIR site between 2003 and 2021. Vertical lines represent the standard deviation  $(\pm 1\sigma)$ .

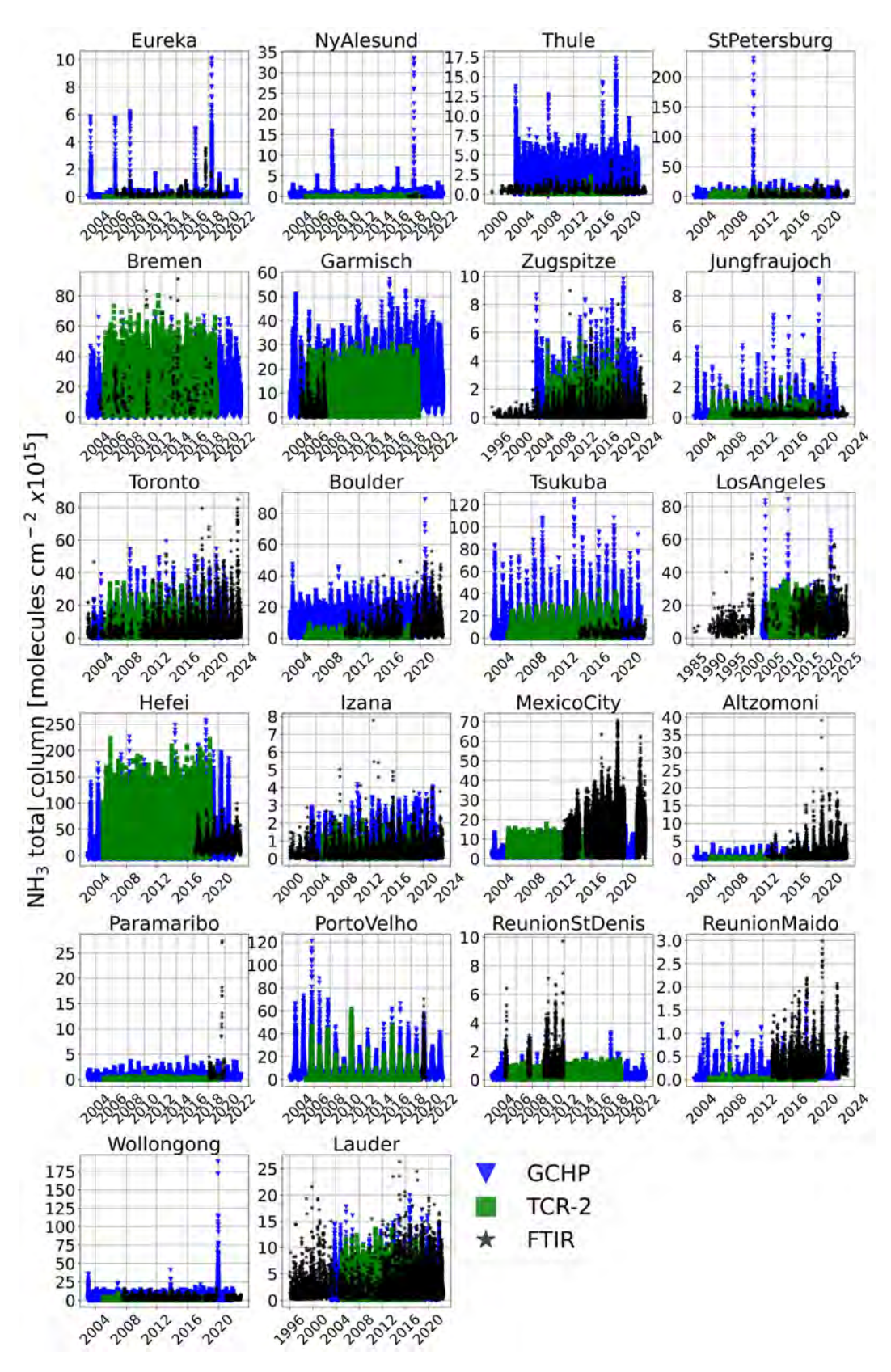


Figure B.6: Comparison of the time series of NH<sub>3</sub> total columns from FTIR measurements (black) versus GCHP (blue) and TCR-2 (green) at the 22 FTIR sites.

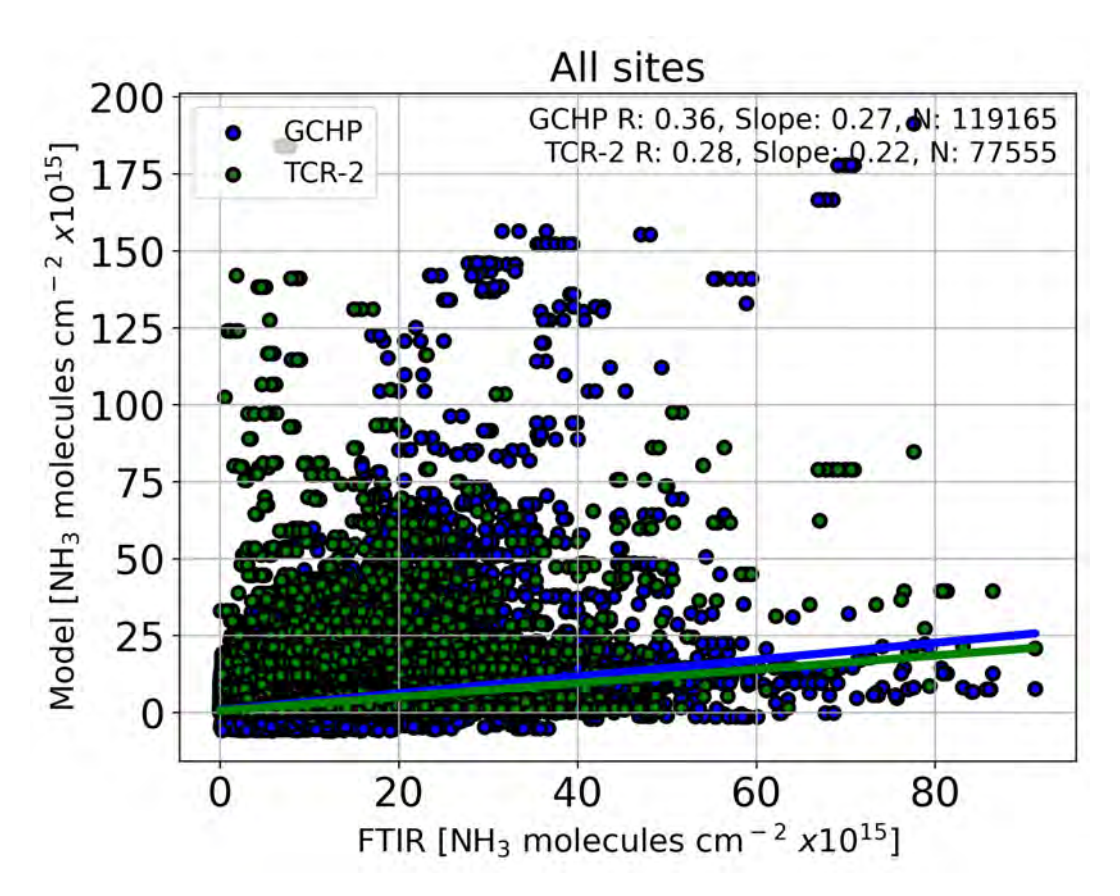


Figure B.7: Scatter plot of GCHP and TCR-2 vs. FTIR temporally matched  $\rm NH_3$  total columns. The lines show the regression results for each model.

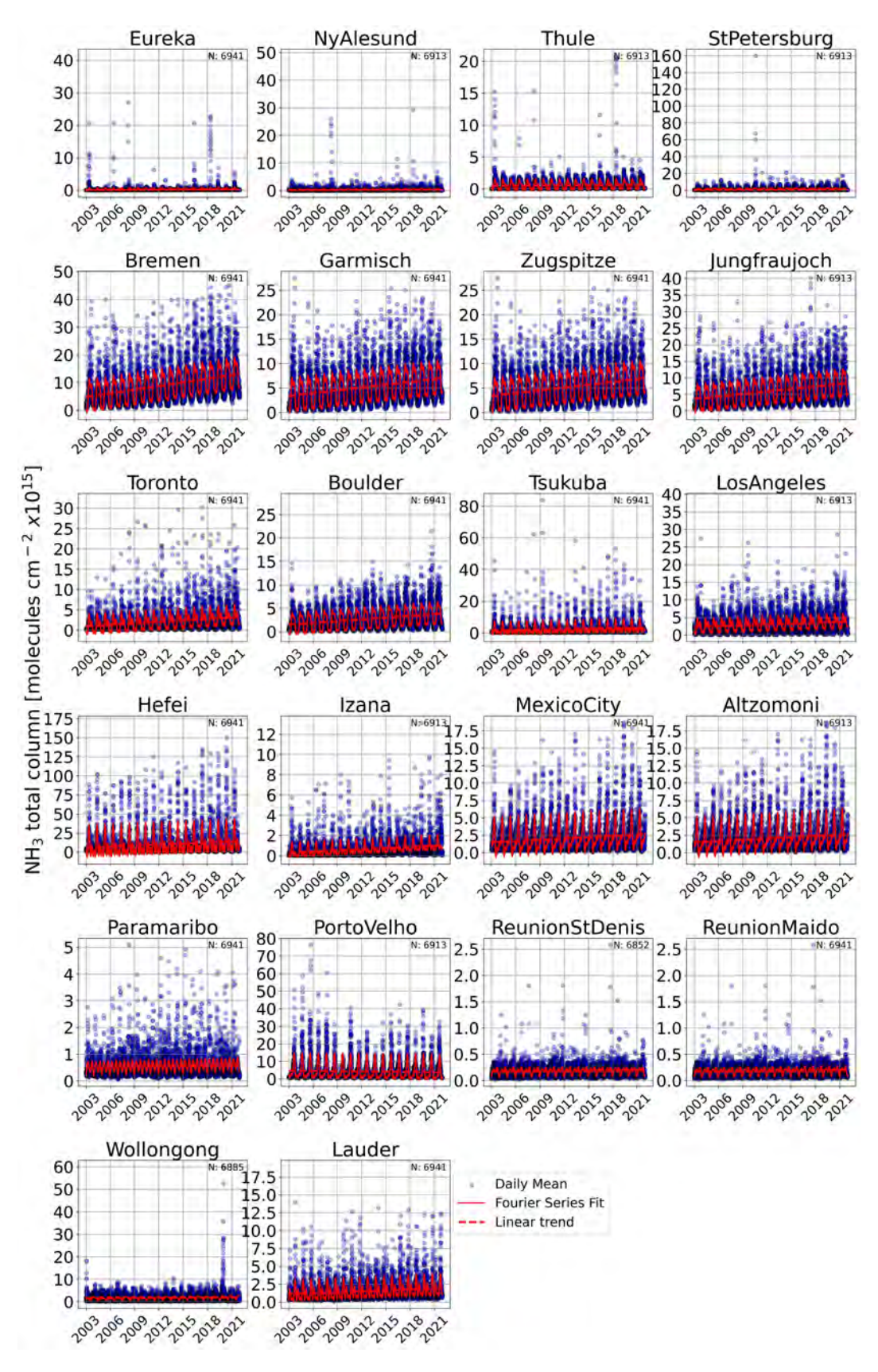


Figure B.8: Time series of GCHP daily mean  $NH_3$  total columns between 2003 and 2021 with fitted third-order Fourier series (solid red line) and linear trends (dashed red line) for the 22 FTIR sites.

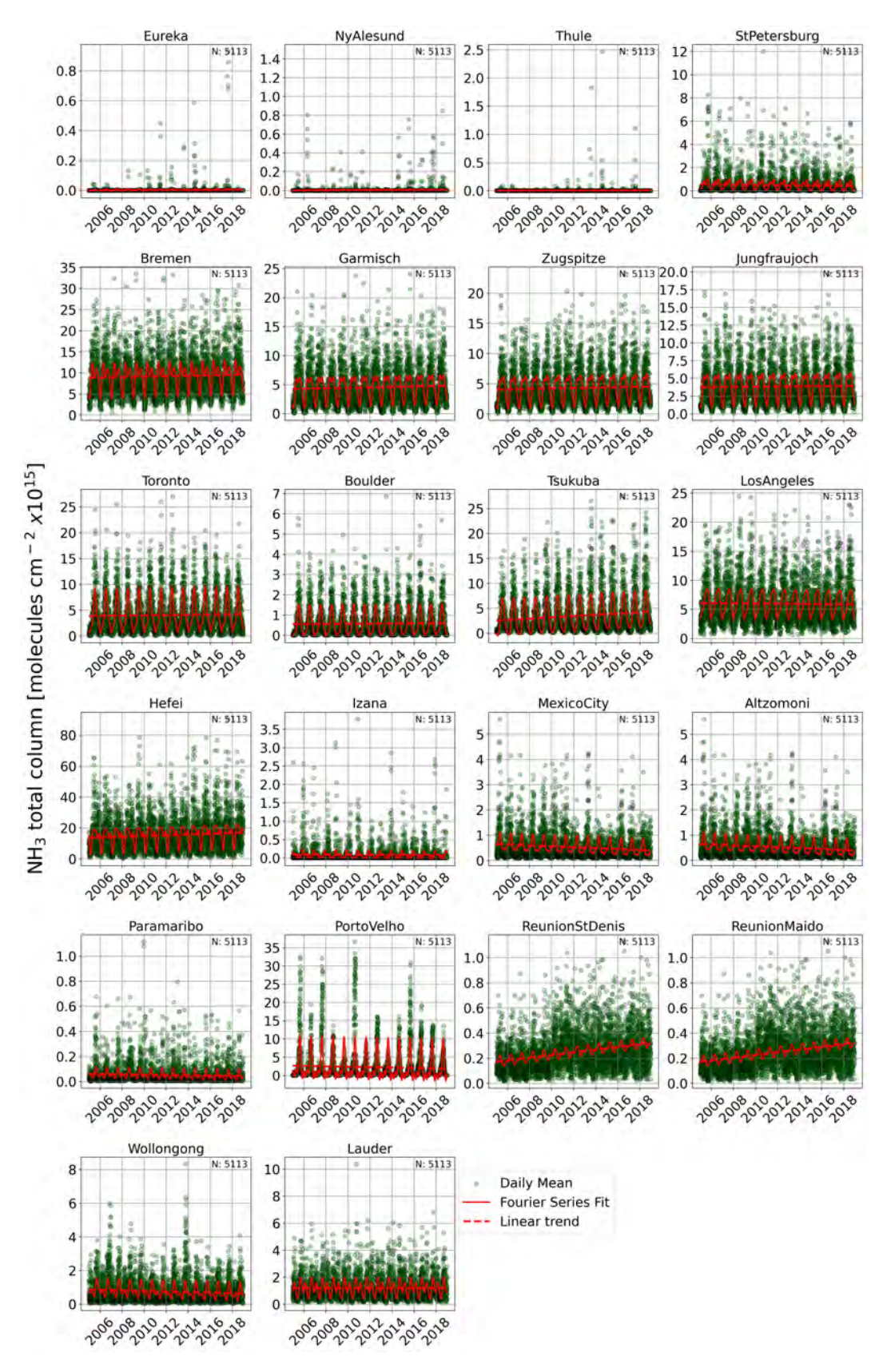


Figure B.9: Time series of TCR-2 daily mean  $NH_3$  total columns between 2005 and 2018 with fitted third-order Fourier series (solid red line) and linear trends (dashed red line) for the 22 FTIR sites.

# Appendix C

# Supplemental Figures for Chapter 5

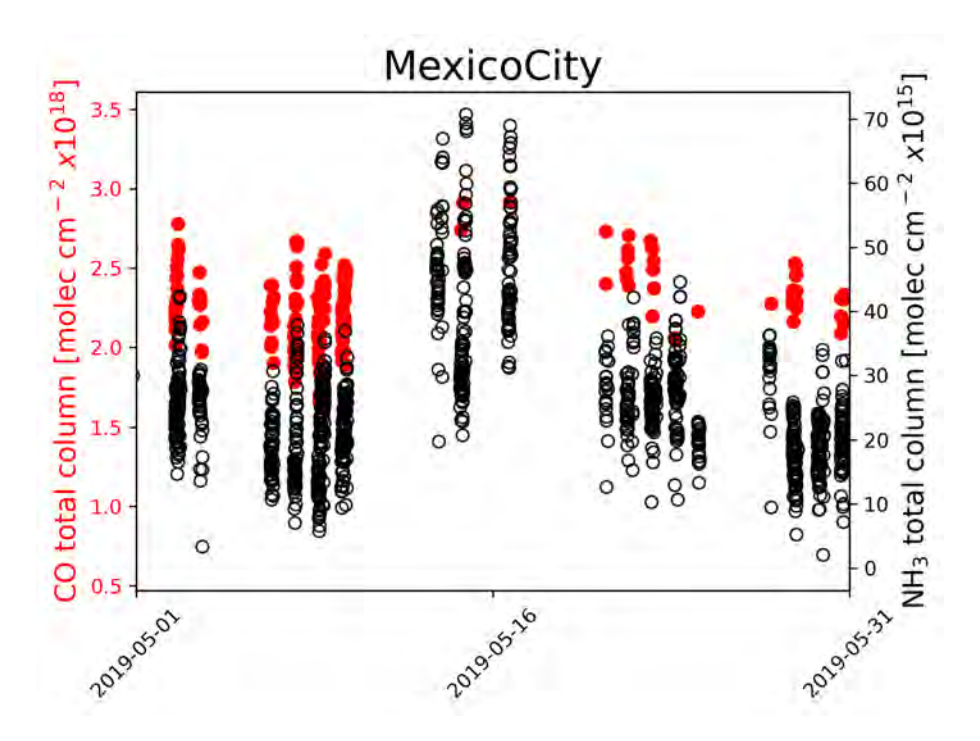


Figure C.1: Comparison of NH<sub>3</sub> and CO total columns measured at Mexico City during May 2019. Simultaneous enhancements can be observed, attributed to biomass burning events.

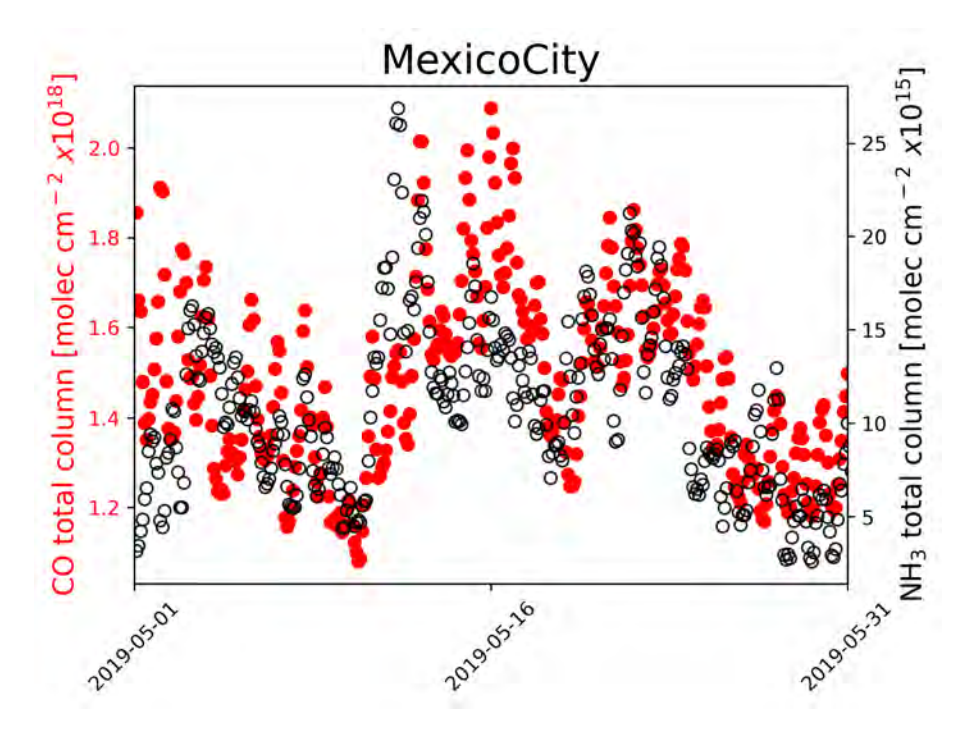


Figure C.2: Comparison of  $\rm NH_3$  and CO total columns from GCHP-SF during May 2019. Simultaneous enhancements can be observed, attributed to biomass burning events.

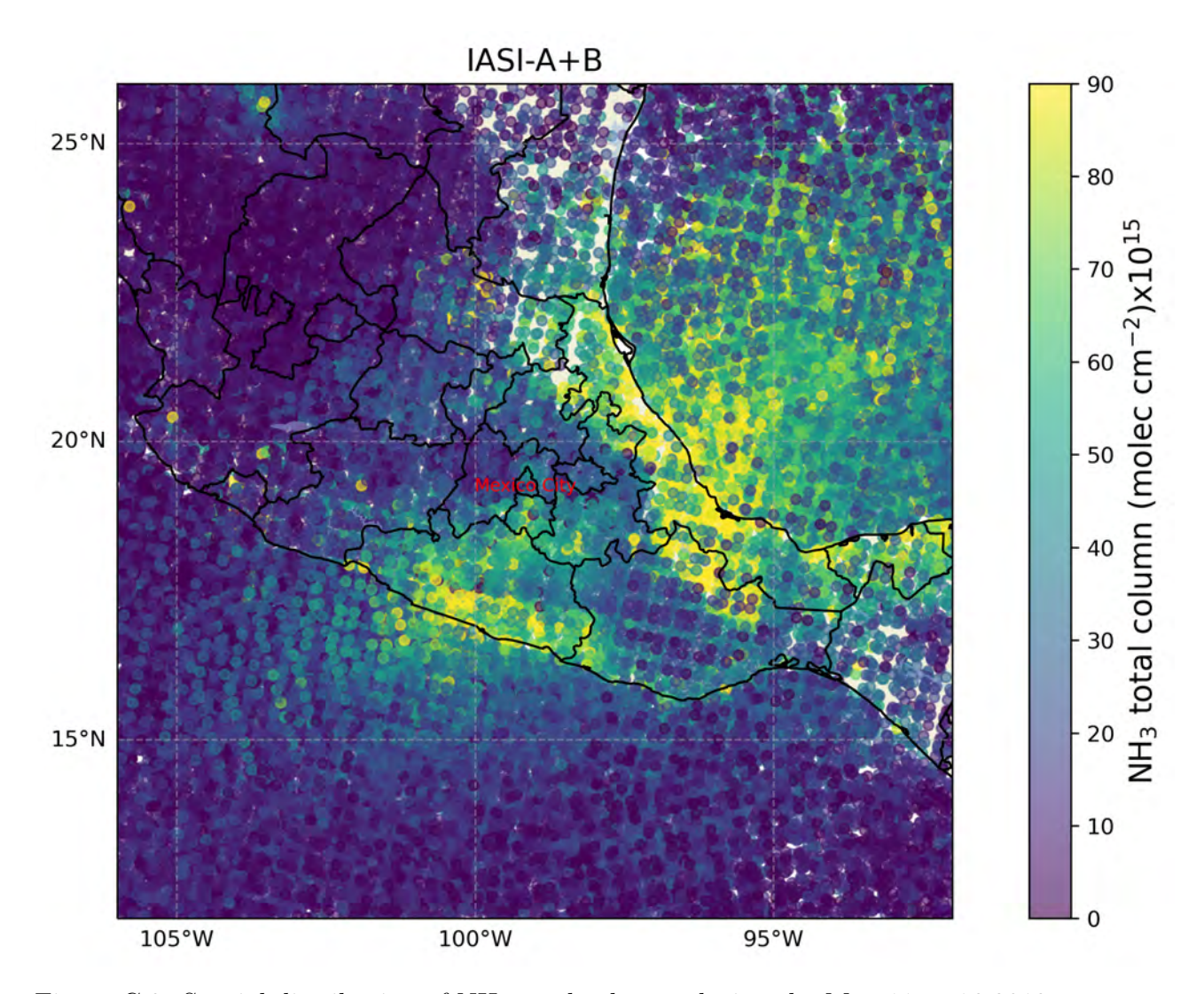


Figure C.3: Spatial distribution of  $NH_3$  total columns during the May 11 to 16 2019, pollution event over Mexico from IASI A and B.

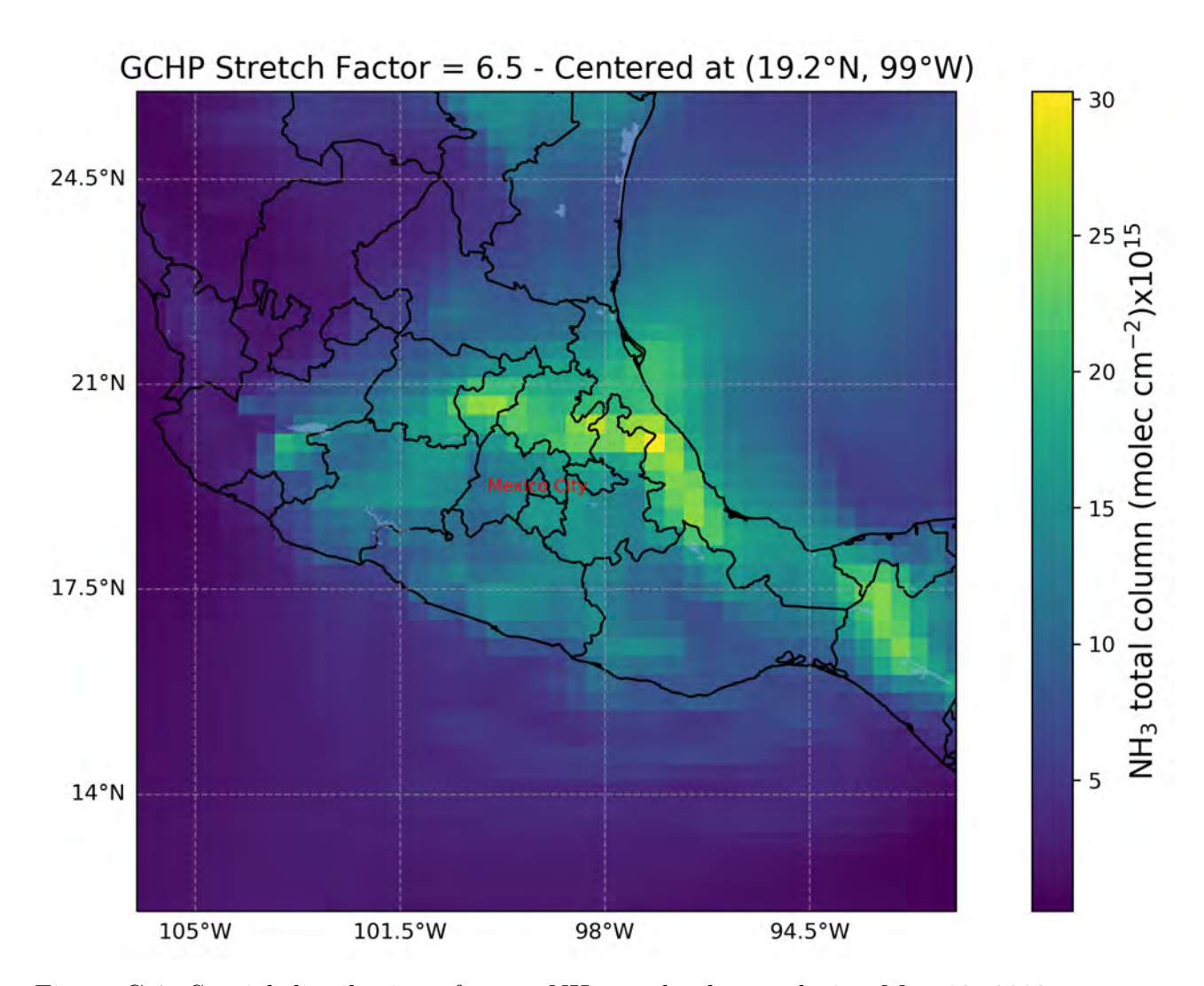


Figure C.4: Spatial distribution of mean  $\rm NH_3$  total columns during May 13, 2019, over Mexico from the target cube-face from the GCHP-SF stretched grid simulation.

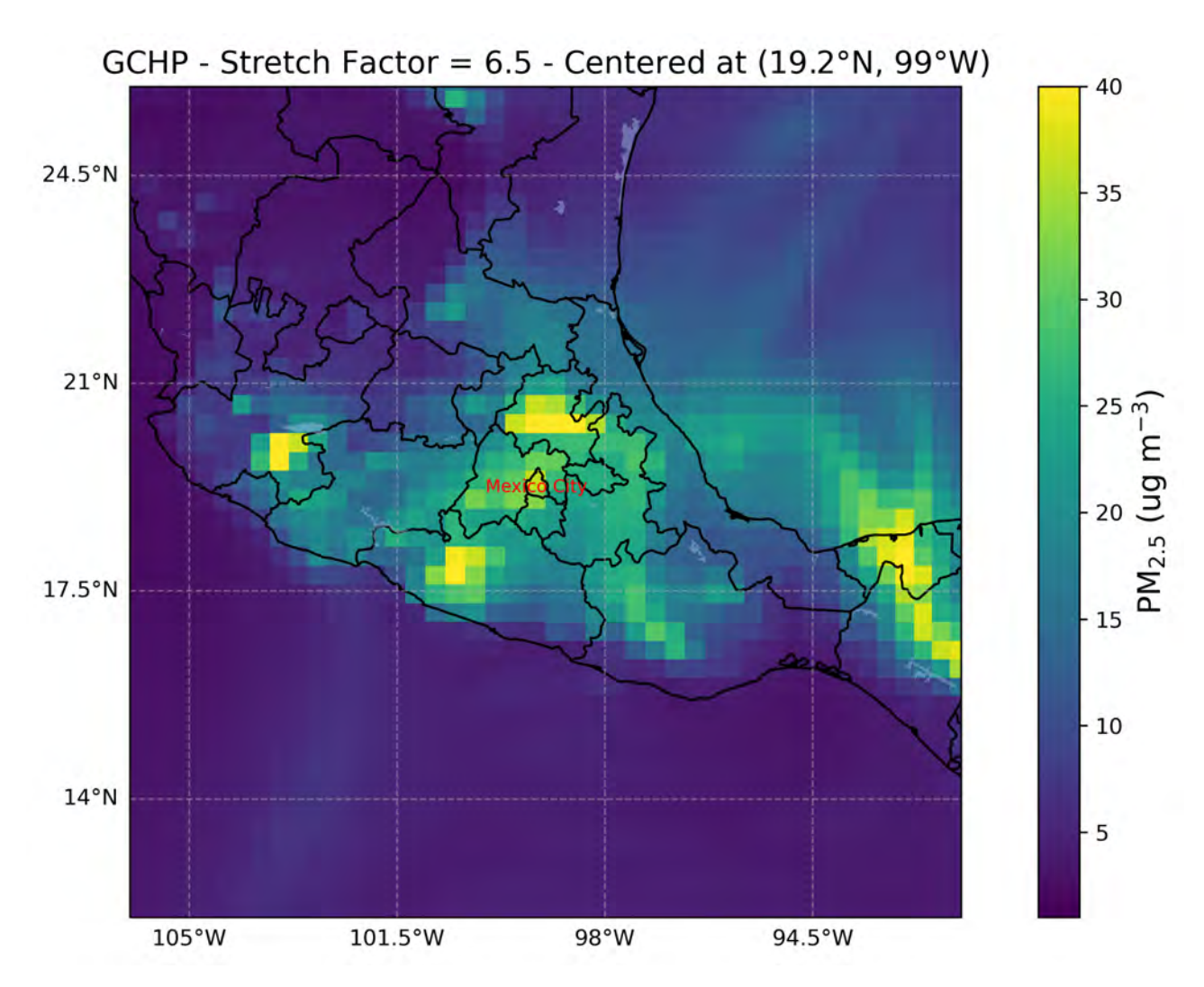


Figure C.5: Spatial distribution of mean  $PM_{2.5}$  surface concentration during May 13, 2019, over Mexico from the target cube-face from the GCHP stretched grid simulation.

## **Bibliography**

- Adams, P. M., Lynch, D. K., Buckland, K. N., Johnson, P. D., and Tratt, D. M. (2017). Sulfate mineralogy of fumaroles in the Salton Sea Geothermal Field, Imperial County, California. *Journal of Volcanology and Geothermal Research*, 347:15–43.
- Asman, W. A. H., Sutton, M. A., and Schørring, J. K. (1998). Ammonia: emission, atmospheric transport and deposition. *The New Phytologist*, 139(1):27–48.
- Ayars, J., Kramer, H. A., and Jones, G. M. (2023). The 2020 to 2021 California megafires and their impacts on wildlife habitat. *Proceedings of the National Academy of Sciences*, 120(48):e2312909120.
- Bader, W., Bovy, B., Conway, S., Strong, K., Smale, D., Turner, A. J., Blumenstock,
  T., Boone, C., Collaud Coen, M., Coulon, A., Garcia, O., Griffith, D. W. T., Hase,
  F., Hausmann, P., Jones, N., Krummel, P., Murata, I., Morino, I., Nakajima, H.,
  O'Doherty, S., Paton-Walsh, C., Robinson, J., Sandrin, R., Schneider, M., Servais,
  C., Sussmann, R., and Mahieu, E. (2017). The recent increase of atmospheric
  methane from 10 years of ground-based NDACC FTIR observations since 2005.
  Atmospheric Chemistry and Physics, 17(3):2255–2277.
- Battye, W., Aneja, V. P., and Roelle, P. A. (2003). Evaluation and improvement of ammonia emissions inventories. *Atmospheric Environment*, 37(27):3873–3883.

Battye, W., Aneja, V. P., and Schlesinger, W. H. (2017). Is nitrogen the next carbon? Earth's Future, 5(9):894–904.

- Baumgardner, D., Grutter, M., Allan, J., Ochoa, C., Rappenglueck, B., Russell, L. M., and Arnott, P. (2009). Physical and chemical properties of the regional mixed layer of Mexico's Megapolis. Atmospheric Chemistry and Physics, 9(15):5711–5727.
- Baylon, J. L., Stremme, W., Grutter, M., Hase, F., and Blumenstock, T. (2017). Background CO<sub>2</sub> levels and error analysis from ground-based solar absorption IR measurements in central Mexico. *Atmospheric Measurement Techniques*, 10(7):2425–2434.
- Beer, R., Shephard, M. W., Kulawik, S. S., Clough, S. A., Eldering, A., Bowman, K. W., Sander, S. P., Fisher, B. M., Payne, V. H., Luo, M., Osterman, G. B., and Worden, J. R. (2008). First satellite observations of lower tropospheric ammonia and methanol. *Geophysical Research Letters*, 35(9):L09801.
- Behera, S. N. and Sharma, M. (2010). Investigating the potential role of ammonia in ion chemistry of fine particulate matter formation for an urban environment. Science of the Total Environment, 408(17):3569–3575.
- Behera, S. N., Sharma, M., Aneja, V. P., and Balasubramanian, R. (2013). Ammonia in the atmosphere: A review on emission sources, atmospheric chemistry and deposition on terrestrial bodies. *Environmental Science and Pollution Research*, 20(11):8092–8131.
- Bencherif, H., Bègue, N., Kirsch Pinheiro, D., du Preez, D. J., Cadet, J.-M.,
  da Silva Lopes, F. J., Shikwambana, L., Landulfo, E., Vescovini, T., Labuschagne,
  C., Silva, J. J., Anabor, V., Coheur, P.-F., Mbatha, N., Hadji-Lazaro, J., Sivakumar, V., and Clerbaux, C. (2020). Investigating the long-range transport of aerosol

plumes following the Amazon fires (August 2019): A multi-instrumental approach from ground-based and satellite observations. *Remote Sensing*, 12(22):3846.

- Benish, S. E., Bash, J. O., Foley, K. M., Appel, K. W., Hogrefe, C., Gilliam, R., and Pouliot, G. (2022). Long-term regional trends of nitrogen and sulfur deposition in the United States from 2002 to 2017. Atmospheric Chemistry and Physics, 22(19):12749–12767.
- Bernath, P. F. (2025). Spectra of Atoms and Molecules. Oxford University Press, 5th edition.
- Bey, I., Jacob, D. J., Yantosca, R. M., Logan, J. A., Field, B. D., Fiore, A. M., Li, Q., Liu, H. Y., Mickley, L. J., and Schultz, M. G. (2001). Global modeling of tropospheric chemistry with assimilated meteorology: Model description and evaluation. *Journal of Geophysical Research: Atmospheres*, 106(D19):23073–23095.
- Bezanilla, A., Krüger, A., Stremme, W., and de la Mora, M. G. (2014). Solar absorption infrared spectroscopic measurements over Mexico City: Methane enhancements. *Atmósfera*, 27(2):173–183.
- Bian, H., Chin, M., Hauglustaine, D. A., Schulz, M., Myhre, G., Bauer, S. E., Lund, M. T., Karydis, V. A., Kucsera, T. L., Pan, X., Pozzer, A., Skeie, R. B., Steenrod, S. D., Sudo, K., Tsigaridis, K., Tsimpidi, A. P., and Tsyro, S. G. (2017). Investigation of global particulate nitrate from the AeroCom phase III experiment. Atmospheric Chemistry and Physics, 17(21):12911–12940.
- Bindle, L., Martin, R. V., Cooper, M. J., Lundgren, E. W., Eastham, S. D., Auer, B. M., Clune, T. L., Weng, H., Lin, J., Murray, L. T., Meng, J., Keller, C. A., Putman, W. M., Pawson, S., and Jacob, D. J. (2021). Grid-stretching capabil-

ity for the GEOS-Chem 13.0.0 atmospheric chemistry model. Geoscientific Model Development, 14(10):5977–5997.

- Blackall, T. D., Wilson, L. J., Theobald, M. R., Milford, C., Nemitz, E., Bull, J., Bacon, P. J., Hamer, K. C., Wanless, S., and Sutton, M. A. (2007). Ammonia emissions from seabird colonies. Geophysical Research Letters, 34(10):L10801.
- Bouwman, A. F., Lee, D. S., Asman, W. A. H., Dentener, F. J., Van Der Hoek, K. W., and Olivier, J. G. J. (1997). A global high-resolution emission inventory for ammonia. Global Biogeochemical Cycles, 11(4):561–587.
- Boyer, M., Quéléver, L., Brasseur, Z., McManus, B., Herndon, S., Agnese, M., Nelson, D., Roscioli, J., Weis, F., Sel, S., Marincovich, G. L., Quarin, F. J., Buchholz, A., Xavier, C., Perchivale, P. J., Kerminen, V.-M., Kulmala, M., Petäjä, T., He, X.-C., Sofieva-Rios, S., Timonen, H., Aurela, M., Barreira, L., Virkkula, A., and Sipilä, M. (2025). Penguin guano is an important source of climate-relevant aerosol particles in Antarctica. *Communications Earth & Environment*, 6(1):368.
- Brasseur, G. P. and Jacob, D. J. (2017). *Modeling of Atmospheric Chemistry*. Cambridge University Press, 3rd edition.
- Bruker Optics (2006). Vertex 80 User Manual. Technical report. URL: https://www.bruker.com/en/products-and-solutions/infrared-and-raman/ft-ir-research-spectrometers/vertex-research-ft-ir-spectrometer/vertex-80-80v-ft-ir-spectrometer.html?page\_1=1. Last access: February, 2025.
- Buchholz, R. R., Emmons, L. K., Tilmes, S., and Team, T. C. D. (2019). CESM2.1/CAM-chem Instantaneous Output for Boundary Conditions. UCAR/NCAR Atmospheric Chemistry Observations and Modeling Laboratory.

Cadle, S., Nebel, G., and Williams, R. (1979). Measurements of unregulated emissions from General Motors' light-duty vehicles. SAE Transactions, 88:2381–2401.

- Cady-Pereira, K. E., Payne, V. H., Neu, J. L., Bowman, K. W., Miyazaki, K., Marais, E. A., Kulawik, S., Tzompa-Sosa, Z. A., and Hegarty, J. D. (2017). Seasonal and spatial changes in trace gases over megacities from Aura TES observations: Two case studies. Atmospheric Chemistry and Physics, 17(15):9379–9398.
- Calderón-Ezquerro, M. C., Serrano-Silva, N., and Brunner-Mendoza, C. (2020).
  Metagenomic characterisation of bioaerosols during the dry season in Mexico City.
  Aerobiologia, 36(3):493–505.
- Callewaert, S., Brioude, J., Langerock, B., Duflot, V., Fonteyn, D., Müller, J.-F., Metzger, J.-M., Hermans, C., Kumps, N., Ramonet, M., Lopez, M., Mahieu, E., and De Mazière, M. (2022). Analysis of CO<sub>2</sub>, CH<sub>4</sub>, and CO surface and column concentrations observed at Réunion Island by assessing WRF-Chem simulations. *Atmospheric Chemistry and Physics*, 22(11):7763–7792.
- Campeny, M., Menéndez, I., Ibáñez-Insa, J., Rivera-Martínez, J., Yepes, J., Álvarez Pousa, S., Méndez-Ramos, J., and Mangas, J. (2023). The ephemeral fumarolic mineralization of the 2021 Tajogaite volcanic eruption (La Palma, Canary Islands, Spain). Scientific Reports, 13(1):6336.
- Cao, H., Henze, D. K., Zhu, L., Shephard, M. W., Cady-Pereira, K., Dammers, E., Sitwell, M., Heath, N., Lonsdale, C., Bash, J. O., Miyazaki, K., Flechard, C., Fauvel, Y., Kruit, R. W., Feigenspan, S., Brümmer, C., Schrader, F., Twigg, M. M., Leeson, S., Tang, Y. S., Stephens, A. C. M., Braban, C., Vincent, K., Meier, M., Seitler, E., Geels, C., Ellermann, T., Sanocka, A., and Capps, S. L. (2022). 4D-Var Inversion of European NH<sub>3</sub> Emissions Using CrIS NH<sub>3</sub> Measurements and GEOS-

Chem Adjoint With Bi-Directional and Uni-Directional Flux Schemes. *Journal of Geophysical Research: Atmospheres*, 127(9):e2021JD035687.

- CENAPRED (2021). Centro nacional de prevención de desastres incendios forestales. URL: http://www.cenapred.gob.mx/es/Publicaciones/archivos/159-FASCCULOINCENDIOSFORESTALES.PDF. Last access: February, 2025.
- Chin, M., Ginoux, P., Kinne, S., Torres, O., Holben, B. N., Duncan, B. N., Martin, R. V., Logan, J. A., Higurashi, A., and Nakajima, T. (2002). Tropospheric Aerosol Optical Thickness from the GOCART Model and Comparisons with Satellite and Sun Photometer Measurements. *Journal of the Atmospheric Sciences*, 59(3):461–483.
- Christian, T. J., Yokelson, R. J., Cárdenas, B., Molina, L. T., Engling, G., and Hsu, S.-C. (2010). Trace gas and particle emissions from domestic and industrial biofuel use and garbage burning in central Mexico. Atmospheric Chemistry and Physics, 10(2):565–584.
- Clarisse, L., Clerbaux, C., Dentener, F., and Co-authors (2009). Global ammonia distribution derived from infrared satellite observations. *Nature Geoscience*, 2(7):479–483.
- Clarisse, L., Franco, B., Van Damme, M., Di Gioacchino, T., Hadji-Lazaro, J., Whitburn, S., Noppen, L., Hurtmans, D., Clerbaux, C., and Coheur, P. (2023). The IASI NH<sub>3</sub> version 4 product: averaging kernels and improved consistency. Atmospheric Measurement Techniques, 16(21):5009–5028.
- Clarisse, L., Shephard, M. W., Dentener, F., Hurtmans, D., Cady-Pereira, K., Karagulian, F., Van Damme, M., Clerbaux, C., and Coheur, P.-F. (2010). Satellite moni-

toring of ammonia: A case study of the San Joaquin Valley. *Journal of Geophysical Research*, 115:D13302.

- Clarisse, L., Van Damme, M., Clerbaux, C., and Coheur, P.-F. (2019). Tracking down global NH<sub>3</sub> point sources with wind-adjusted superresolution. *Atmospheric Measurement Techniques*, 12(10):5457–5473.
- Clerbaux, C., Boynard, A., Clarisse, L., George, M., Hadji-Lazaro, J., Herbin, H., Hurtmans, D., Pommier, M., Razavi, A., Turquety, S., Wespes, C., and Coheur, P.-F. (2009). Monitoring of atmospheric composition using the thermal infrared IASI/MetOp sounder. Atmospheric Chemistry and Physics, 9(16):6041–6054.
- Croft, B., Martin, R. V., Leaitch, W. R., Burkart, J., Chang, R. Y.-W., Collins, D. B.,
  Hayes, P. L., Hodsase, A. L., Huang, L., Kodros, J. K., Moravek, A., Mungall,
  E. L., Murphy, J. G., Sharma, S., Tremblay, S., Wentworth, G. R., Willis, M. D.,
  Abbatt, J. P. D., and Pierce, J. R. (2019). Arctic marine secondary organic aerosol
  contributes significantly to summertime particle size distributions in the Canadian
  Arctic Archipelago. Atmospheric Chemistry and Physics, 19(5):2787–2812.
- Croft, B., Wentworth, G. R., Martin, R. V., Leaitch, W. R., Murphy, J. G., Murphy, B. N., Kodros, J. K., Abbatt, J. P. D., and Pierce, J. R. (2016). Contribution of Arctic seabird-colony ammonia to atmospheric particles and cloud-albedo radiative effect. *Nature Communications*, 7(1):13444.
- Dammers, E., McLinden, C. A., Griffin, D., Shephard, M. W., Van Der Graaf, S., Lutsch, E., Schaap, M., Gainairu-Matz, Y., Fioletov, V., Van Damme, M., Whitburn, S., Clarisse, L., Cady-Pereira, K., Clerbaux, C., Coheur, P. F., and Erisman, J. W. (2019). NH<sub>3</sub> emissions from large point sources derived from CrIS and IASI satellite observations. Atmospheric Chemistry and Physics, 19(19):12261–12293.

Dammers, E., Palm, M., Van Damme, M., Vigouroux, C., Smale, D., Conway, S., Toon, G. C., Jones, N., Nussbaumer, E., Warneke, T., Petri, C., Clarisse, L., Clerbaux, C., Hermans, C., Lutsch, E., Strong, K., Hannigan, J. W., Nakajima, H., Morino, I., Herrera, B., Stremme, W., Grutter, M., Schaap, M., Wichink Kruit, R. J., Notholt, J., Coheur, P.-F., and Erisman, J. W. (2016). An evaluation of IASI-NH<sub>3</sub> with ground-based FTIR measurements. *Atmospheric Chemistry and Physics*, 16(16):10351–10368.

- Dammers, E., Shephard, M. W., Palm, M., Cady-Pereira, K., Capps, S., Lutsch, E., Strong, K., Hannigan, J. W., Ortega, I., Toon, G. C., Stremme, W., Grutter, M., Jones, N., Smale, D., Siemons, J., Hrpcek, K., Tremblay, D., Schaap, M., Notholt, J., and Erisman, J. W. (2017). Validation of the CrIS fast physical NH<sub>3</sub> retrieval with ground-based FTIR. Atmospheric Measurement Techniques, 10(7):2645–2667.
- Dammers, E., Vigouroux, C., Palm, M., Mahieu, E., Warneke, T., Smale, D., Langerock, B., Franco, B., Van Damme, M., Schaap, M., Notholt, J., and Erisman, J. W. (2015). Retrieval of ammonia from ground-based FTIR solar spectra. Atmospheric Chemistry and Physics, 15(22):12789–12803.
- De Mazière, M., Thompson, A. M., Kurylo, M. J., Wild, J. D., Bernhard, G., Blumenstock, T., Braathen, G. O., Hannigan, J. W., Lambert, J.-C., Leblanc, T., McGee, T. J., Nedoluha, G., Petropavlovskikh, I., Seckmeyer, G., Simon, P. C., Steinbrecht, W., and Strahan, S. E. (2018). The Network for the Detection of Atmospheric Composition Change (NDACC): history, status and perspectives. Atmospheric Chemistry and Physics, 18(7):4935–4964.
- Delwiche, C. C. (1970). The nitrogen cycle. Scientific American, 223(3):137–146.
- Dentener, F. and Crutzen, P. (1994). A three-dimensional model of the global ammonia cycle. *Journal of Atmospheric Chemistry*, 19:331–369.

Draxler, R. R. and Hess, G. D. (1997). Description of the HYSPLIT4 modeling system. NOAA Tech. Memo. ERL ARL224, NOAA Air Resources Laboratory, Silver Spring, MD.

- Draxler, R. R., Stunder, B., Rolph, G., Stein, A., and Taylor, A. (2021). HYSPLIT User's Guide. Technical report, NOAA Air Resources Laboratory, Silver Spring, Maryland, USA.
- Eastham, S. D., Long, M. S., Keller, C. A., Lundgren, E., Yantosca, R. M., Zhuang, J., Li, C., Lee, C. J., Yannetti, M., Auer, B. M., Clune, T. L., Kouatchou, J., Putman, W. M., Thompson, M. A., Trayanov, A. L., Molod, A. M., Martin, R. V., and Jacob, D. J. (2018). GEOS-Chem High Performance (GCHP v11-02c): A next-generation implementation of the GEOS-Chem chemical transport model for massively parallel applications. Geoscientific Model Development, 11(7):2941–2953.
- Emmons, L. K., Schwantes, R. H., Orlando, J. J., Tyndall, G., Kinnison, D., Lamarque, J.-F., Marsh, D., Mills, M. J., Tilmes, S., Bardeen, C., Buchholz, R. R., Conley, A., Gettelman, A., Garcia, R., Simpson, I., Blake, D. R., Meinardi, S., and Pétron, G. (2020). The Community Earth System Model Version 2 (CESM2). *Journal of Advances in Modeling Earth Systems*, 12(2):e2019MS001882.
- Emmons, L. K., Walters, S., Hess, P. G., Lamarque, J.-F., Pfister, G. G., Fillmore, D., Granier, C., Guenther, A., Kinnison, D., Laepple, T., Orlando, J., Tie, X., Tyndall, G., Wiedinmyer, C., Baughcum, S. L., and Kloster, S. (2010). Description and evaluation of the Model for Ozone and Related chemical Tracers, version 4 (MOZART-4). Geoscientific Model Development, 3:43–67.
- European Environment Agency (2023). National Emission Reduction Commitments Directive 2023. URL: https://www.eea.europa.eu/publications/

national-emission-reduction-commitments-directive-2023. Last access: February, 2025.

- Evangeliou, N., Balkanski, Y., Eckhardt, S., Cozic, A., Van Damme, M., Coheur, P.-F., Clarisse, L., Shephard, M. W., Cady-Pereira, K. E., and Hauglustaine, D. (2021). 10-year satellite-constrained fluxes of ammonia improve performance of chemistry transport models. Atmospheric Chemistry and Physics, 21(6):4431–4451.
- Eyring, V., Waugh, D. W., Bodeker, G. E., Cordero, E., Akiyoshi, H., Austin, J.,
  Beagley, S. R., Boville, B. A., Braesicke, P., Brühl, C., Butchart, N., Chipperfield,
  M. P., Dameris, M., Deckert, R., Deushi, M., Frith, S. M., Garcia, R. R., Gettelman,
  A., Giorgetta, M. A., Kinnison, D. E., Mancini, E., Manzini, E., Marsh, D. R.,
  Matthes, S., Nagashima, T., Newman, P. A., Nielsen, J. E., Pawson, S., Pitari,
  G., Plummer, D. A., Rozanov, E., Schraner, M., Scinocca, J. F., Semeniuk, K.,
  Shepherd, T. G., Shibata, K., Steil, B., Stolarski, R. S., Tian, W., and Yoshiki, M.
  (2007). Multimodel projections of stratospheric ozone in the 21st century. Journal of Geophysical Research: Atmospheres, 112(D16303).
- Farquhar, G. D., Firth, P. M., Wetselaar, R., and Weir, B. (1980). On the gaseous exchange of ammonia between leaves and the environment: Determination of the ammonia compensation point. *Plant Physiology*, 66(4):710–714.
- Farr, T. G., Rosen, P. A., Caro, E., Crippen, R., Duren, R., Hensley, S., Kobrick, M., Paller, M., Rodriguez, E., Roth, L., Seal, D., Shaffer, S., Shimada, J., Umland, J., Werner, M., Oskin, M., Burbank, D., and Alsdorf, D. (2007). The Shuttle Radar Topography Mission. Reviews of Geophysics, 45(2):2005RG000183.
- Finlayson-Pitts, B. J. and Pitts, J. N., editors (2000). Chemistry of the Upper and Lower Atmosphere. Academic Press, San Diego.

Flechard, C. R. and Fowler, D. (1998). Atmospheric ammonia at a moorland site. I: The meteorological control of ambient ammonia concentrations and the influence of local sources. Quarterly Journal of the Royal Meteorological Society, 124(547):733–757.

- Flood, V. A., Strong, K., Whaley, C. H., Walker, K. A., Blumenstock, T., Hannigan, J. W., Mellqvist, J., Notholt, J., Palm, M., Röhling, A. N., Arnold, S., Beagley, S., Chien, R.-Y., Christensen, J., Deushi, M., Dobricic, S., Dong, X., Fu, J. S., Gauss, M., Gong, W., Langner, J., Law, K. S., Marelle, L., Onishi, T., Oshima, N., Plummer, D. A., Pozzoli, L., Raut, J.-C., Thomas, M. A., Tsyro, S., and Turnock, S. (2024). Evaluating modelled tropospheric columns of CH<sub>4</sub>, CO, and O<sub>3</sub> in the Arctic using ground-based Fourier transform infrared (FTIR) measurements. Atmospheric Chemistry and Physics, 24(2):1079–1118.
- Fortems-Cheiney, A., Dufour, G., Foret, G., Siour, G., Van Damme, M., Coheur, P.-F., Clarisse, L., Clerbaux, C., and Beekmann, M. (2022). Understanding the Simulated Ammonia Increasing Trend from 2008 to 2015 over Europe with CHIMERE and Comparison with IASI Observations. *Atmosphere*, 13(7):1101.
- Fountoukis, C. and Nenes, A. (2007). ISORROPIA II: a computationally efficient thermodynamic equilibrium model for K<sup>+</sup>-Ca<sup>2+</sup>-Mg<sup>2+</sup>-NH<sub>4</sub><sup>+</sup>-Na<sup>+</sup>-SO<sub>4</sub><sup>2-</sup>-NO<sub>3</sub><sup>-</sup>-Cl<sup>-</sup>-H<sub>2</sub>O aerosols. Atmospheric Chemistry and Physics, 7:4639–4659.
- Fowler, D., Coyle, M., Skiba, U., Sutton, M. A., Cape, J. N., Reis, S., Sheppard,
  L. J., Jenkins, A., Grizzetti, B., Galloway, J. N., Vitousek, P., Leach, A., Bouwman,
  A. F., Butterbach-Bahl, K., Dentener, F., Stevenson, D., Amann, M., and Voss,
  M. (2013). The global nitrogen cycle in the twenty-first century. *Philosophical Transactions of the Royal Society B: Biological Sciences*, 368(1621):20130164.
- Franco, B., Marais, E. A., Bovy, B., Bader, W., Lejeune, B., Roland, G., Servais,

C., and Mahieu, E. (2016). Diurnal cycle and multi-decadal trend of formaldehyde in the remote atmosphere near 46° N. Atmospheric Chemistry and Physics, 16(6):4171–4189.

- Franklin, J. (2015). Solar absorption spectroscopy at the Dalhousie Atmospheric Observatory. PhD thesis, Dalhousie University, Halifax, Canada.
- Fraser, M. P. and Cass, G. R. (1998). Detection of excess ammonia emissions from in-use vehicles and the implications for fine particle control. *Environmental Science* and *Technology*, 32(8):1053 1057.
- Friedrich, M., Beutner, E., Reuvers, H., Smeekes, S., Urbain, J.-P., Bader, W., Franco, B., Lejeune, B., and Mahieu, E. (2020). A statistical analysis of time trends in atmospheric ethane. Climatic Change, 162(1):105–125.
- Fuzzi, S., Baltensperger, U., Carslaw, K., Decesari, S., Denier van der Gon, H., Facchini, M. C., Fowler, D., Koren, I., Langford, B., Lohmann, U., Nemitz, E., Pandis, S., Riipinen, I., Rudich, Y., Schaap, M., Slowik, J. G., Spracklen, D. V., Vignati, E., Wild, M., Williams, M., and Gilardoni, S. (2015). Particulate matter, air quality and climate: lessons learned and future needs. Atmospheric Chemistry and Physics, 15(14):8217–8299.
- Galloway, J. N., Dentener, F. J., Capone, D. G., Boyer, E. W., Howarth, R. W., Seitzinger, S. P., Asner, G. P., Cleveland, C. C., Green, P. A., Holland, E. A., Karl, D. M., Michaels, A. F., Porter, J. H., Townsend, A. R., and Vöosmarty, C. J. (2004). Nitrogen cycles: past, present, and future. *Biogeochemistry*, 70(2):153–226.
- García, O. E., Schneider, M., Sepúlveda, E., Hase, F., Blumenstock, T., Cuevas, E., Ramos, R., Gross, J., Barthlott, S., Röhling, A. N., Sanromá, E., González, Y., Gómez-Peláez, A. J., Navarro-Comas, M., Puentedura, O., Yela, M., Redondas,

A., Carreño, V., León-Luis, S. F., Reyes, E., García, R. D., Rivas, P. P., Romero-Campos, P. M., Torres, C., Prats, N., Hernández, M., and López, C. (2021). Twenty years of ground-based NDACC FTIR spectrometry at Izaña Observatory – overview and long-term comparison to other techniques. *Atmospheric Chemistry and Physics*, 21(20):15519–15554.

- García, R. D., García, O. E., Cuevas-Agulló, E., Barreto, Á., Cachorro, V. E., Marrero, C., Almansa, F., Ramos, R., and Pó, M. (2023). Spectral Aerosol Radiative Forcing and Efficiency of the La Palma Volcanic Plume over the Izaña Observatory. *Remote Sensing*, 15(1):173.
- Gardiner, T., Forbes, A., de Mazière, M., Vigouroux, C., Mahieu, E., Demoulin, P., Velazco, V., Notholt, J., Blumenstock, T., Hase, F., Kramer, I., Sussmann, R., Stremme, W., Mellqvist, J., Strandberg, A., Ellingsen, K., and Gauss, M. (2008). Trend analysis of greenhouse gases over Europe measured by a network of ground-based remote FTIR instruments. Atmospheric Chemistry and Physics, 8(22):6719–6727.
- Gelaro, R., McCarty, W., Suárez, M. J., Todling, R., Molod, A., Takacs, L., Randles, C. A., Darmenov, A., Bosilovich, M. G., Reichle, R., Wargan, K., Coy, L., Cullather, R., Draper, C., Akella, S., Buchard, V., Conaty, A., Da Silva, A. M., Gu, W., Kim, G.-K., Koster, R., Lucchesi, R., Merkova, D., Nielsen, J. E., Partyka, G., Pawson, S., Putman, W., Rienecker, M., Schubert, S. D., Sienkiewicz, M., and Zhao, B. (2017). The Modern-Era Retrospective Analysis for Research and Applications, Version 2 (MERRA-2). Journal of Climate, 30(14):5419–5454.
- Giannakis, E., Kushta, J., Bruggeman, A., and Lelieveld, J. (2019). Costs and benefits of agricultural ammonia emission abatement options for compliance with European air quality regulations. *Environmental Sciences Europe*, 31(1):93.

Gomez, D. (2018). GACETA: LXIV/1PPO-56/86584. Gaceta del Senado. URL: https://www.senado.gob.mx/64/gaceta\_del\_senado/documento/86584. Last access: February, 2025.

- Government of Canada (2023). Air Pollutant Emissions. URL: https://www.canada.ca/en/environment-climate-change/services/environmental-indicators/air-pollutant-emissions.html. Last access: February, 2025.
- Graedel, T. E., Bates, T. S., Bouwman, A. F., Cunnold, D., Dignon, J., Fung, I., Jacob, D. J., Lamb, B. K., Logan, J. A., Marland, G., Middleton, P., Pacyna, J. M., and Placet, M.and Veldt, C. (1993). A compilation of inventories of emissions to the atmosphere. *Global Biogeochemical Cycles*, (7):1–26.
- Grell, G. A., Peckham, S. E., Schmitz, R., McKeen, S. A., Frost, G., Skamarock, W. C., and Eder, B. (2005). Fully coupled "online" chemistry within the WRF model. Atmospheric Environment, 39(37):6957–6975.
- Griffiths, P. R. and De Haseth, J. A. (2007). Fourier Transform Infrared Spectrometry. Wiley, 1st edition.
- Gu, M., Pan, Y., Walters, W. W., Sun, Q., Song, L., Wang, Y., Xue, Y., and Fang, Y. (2022). Vehicular Emissions Enhanced Ammonia Concentrations in Winter Mornings: Insights from Diurnal Nitrogen Isotopic Signatures. *Environmental Science & Technology*, 56(3):1578–1585.
- Hargreaves, R. J., Li, G., and Bernath, P. F. (2011). Hot NH<sub>3</sub> spectra for astrophysical applications. *The Astrophysical Journal*, 735(2):111.
- Harris, D. C. and Bertolucci, M. D. (1978). Symmetry and Spectroscopy: An Introduction to Vibrational and Electronic Spectroscopy. Oxford University Press.

Hase, F., Hannigan, J., Coffey, M., Goldman, A., Höpfner, M., Jones, N., Rinsland, C., and Wood, S. (2004). Intercomparison of retrieval codes used for the analysis of high-resolution, ground-based FTIR measurements. *Journal of Quantitative Spectroscopy and Radiative Transfer*, 87(1):25–52.

- Hauglustaine, D. A., Balkanski, Y., and Schulz, M. (2014). A global model simulation of present and future nitrate aerosols and their direct radiative forcing of climate. Atmospheric Chemistry and Physics, 14(20):11031–11063.
- Herrera, B., Bezanilla, A., Blumenstock, T., Dammers, E., Hase, F., Clarisse, L., Magaldi, A., Rivera, C., Stremme, W., Strong, K., Viatte, C., Van Damme, M., and Grutter, M. (2022). Measurement report: Evolution and distribution of NH<sub>3</sub> over Mexico City from ground-based and satellite infrared spectroscopic measurements. Atmospheric Chemistry and Physics, 22(21):14119–14132.
- Hertel, O., Skjøth, C. A., Reis, S., Bleeker, A., Harrison, R. M., Cape, J. N., Fowler,
  D., Skiba, U., Simpson, D., Jickells, T., Kulmala, M., Gyldenkærne, S., Sørensen,
  L. L., Erisman, J. W., and Sutton, M. A. (2012). Governing processes for reactive
  nitrogen compounds in the European atmosphere. Biogeosciences, 9(12):4921–4954.
- Hoesly, R. M., Smith, S. J., Feng, L., Klimont, Z., Janssens-Maenhout, G., Pitkanen, T., Seibert, J. J., Vu, L., Andres, R. J., Bolt, R. M., Bond, T. C., Dawidowski, L., Kholod, N., Kurokawa, J.-I., Li, M., Liu, L., Lu, Z., Moura, M. C. P., O'Rourke, P. R., and Zhang, Q. (2018). Historical (1750–2014) anthropogenic emissions of reactive gases and aerosols from the Community Emissions Data System (CEDS). Geoscientific Model Development, 11(1):369–408.
- Huai, T., Durbin, T. D., Miller, J. W., Pisano, J. T., Sauer, C. G., Rhee, S. H., and Norbeck, J. M. (2003). Investigation of NH<sub>3</sub> Emissions from New Technology

Vehicles as a Function of Vehicle Operating Conditions. *Environmental Science* and *Technology*, 37(21):4841 – 4847.

- Huijnen, V., Miyazaki, K., Flemming, J., Inness, A., Sekiya, T., and Schultz, M. G. (2020). An intercomparison of tropospheric ozone reanalysis products from CAMS, CAMS interim, TCR-1, and TCR-2. Geoscientific Model Development, 13(3):1513–1544.
- Janssens-Maenhout, G., Crippa, M., Guizzardi, D., Dentener, F., Muntean, M., Pouliot, G., Keating, T., Zhang, Q., Kurokawa, J., Wankmüller, R., Denier van der Gon, H., Kuenen, J. J. P., Klimont, Z., Frost, G., Darras, S., Koffi, B., and Li, M. (2015). HTAP v2.2: a mosaic of regional and global emission grid maps for 2008 and 2010 to study hemispheric transport of air pollution. Atmospheric Chemistry and Physics, 15(19):11411–11432.
- Jarvis, S. and Ledgard, S. (2002). Ammonia emissions from intensive dairying: a comparison of contrasting systems in the United Kingdom and New Zealand. *Agriculture, Ecosystems & Environment*, 92(1):83–92.
- Kaiser, J. W., Heil, A., Andreae, M. O., Benedetti, A., Chubarova, N., Jones, L.,
  Morcrette, J.-J., Razinger, M., Schultz, M. G., Suttie, M., and van der Werf,
  G. R. (2012). Biomass burning emissions estimated with a Global Fire Assimilation
  System based on observed fire radiative power. *Biogeosciences*, 9(1):527–554.
- Keeley, J. E. and Syphard, A. D. (2021). Large California wildfires: 2020 fires in historical context. Fire Ecology, 17(22).
- Khan, M., Lowe, D., Derwent, R., Foulds, A., Chhantyal-Pun, R., McFiggans, G., Orr-Ewing, A., Percival, C., and Shallcross, D. (2020). Global and regional model simulations of atmospheric ammonia. *Atmospheric Research*, 234:104702.

Kotnala, G., Sharma, S., and Mandal, T. K. (2019). Influence of vehicular emissions (NO, NO<sub>2</sub>, CO and NMHCs) on the mixing ratio of atmospheric ammonia (NH<sub>3</sub>) in Delhi, India. Archives of Environmental Contamination and Toxicology, 78:79–85.

- Krupa, S. (2003). Effects of atmospheric ammonia (NH<sub>3</sub>) on terrestrial vegetation: A review. *Environmental Pollution*, 124(2):179–221.
- Kutzner, R. D., Cuesta, J., Chelin, P., Petit, J.-E., Ray, M., Landsheere, X., Tournadre, B., Dupont, J.-C., Rosso, A., Hase, F., Orphal, J., and Beekmann, M. (2021). Diurnal evolution of total column and surface atmospheric ammonia in the megacity of Paris, France, during an intense springtime pollution episode. Atmospheric Chemistry and Physics, 21(15):12091–12111.
- Kärnä, T. and Baptista, A. M. (2016). Evaluation of a long-term hindcast simulation for the Columbia River estuary. *Ocean Modelling*, 99:1–14.
- Laughner, J. L., Toon, G. C., Mendonca, J., Petri, C., Roche, S., Wunch, D., Blavier, J.-F., Griffith, D. W. T., Heikkinen, P., Keeling, R. F., Kiel, M., Kivi, R., Roehl, C. M., Stephens, B. B., Baier, B. C., Chen, H., Choi, Y., Deutscher, N. M., Di-Gangi, J. P., Gross, J., Herkommer, B., Jeseck, P., Laemmel, T., Lan, X., McGee, E., McKain, K., Miller, J., Morino, I., Notholt, J., Ohyama, H., Pollard, D. F., Rettinger, M., Riris, H., Rousogenous, C., Sha, M. K., Shiomi, K., Strong, K., Sussmann, R., Té, Y., Velazco, V. A., Wofsy, S. C., Zhou, M., and Wennberg, P. O. (2024). The Total Carbon Column Observing Network's GGG2020 data version. Earth System Science Data, 16(5):2197–2260.
- Li, M., Weschler, C. J., Bekö, G., Wargocki, P., Lucic, G., and Williams, J. (2020).
  Human ammonia emission rates under various indoor environmental conditions.
  Environmental Science & Technology, 54(9):5419–5428.

Lin, H., Jacob, D. J., Lundgren, E. W., Sulprizio, M. P., Keller, C. A., Fritz, T. M., Eastham, S. D., Emmons, L. K., Campbell, P. C., Baker, B., Saylor, R. D., and Montuoro, R. (2021). Harmonized emissions component (HEMCO) 3.0 as a versatile emissions component for atmospheric models: Application in the GEOS-Chem, NASA GEOS, WRF-GC, CESM2, NOAA GEFS-aerosol, and NOAA UFS models. Geoscientific Model Development, 14(9):5487–5506.

- Liou, K.-N. (2002). An Introduction to Atmospheric Radiation. Academic Press, 2 edition.
- Luo, Z., Zhang, Y., Chen, W., Van Damme, M., Coheur, P.-F., and Clarisse, L. (2022). Estimating global ammonia (NH<sub>3</sub>) emissions based on IASI observations from 2008 to 2018. *Atmospheric Chemistry and Physics*, 22(15):10375–10388.
- Lutsch, E., Dammers, E., Conway, S., and Strong, K. (2016). Long-range transport of NH<sub>3</sub>, CO, HCN, and C<sub>2</sub>H<sub>6</sub> from the 2014 Canadian Wildfires. Geophysical Research Letters, 43(15):8286–8297.
- Lutsch, E., Strong, K., Jones, D. B. A., Ortega, I., Hannigan, J. W., Dammers, E.,
  Shephard, M. W., Morris, E., Murphy, K., Evans, M. J., Parrington, M., Whitburn,
  S., Van Damme, M., Clarisse, L., Coheur, P.-F., Clerbaux, C., Croft, B., Martin,
  R. V., Pierce, J. R., and Fisher, J. A. (2019). Unprecedented Atmospheric Ammonia
  Concentrations Detected in the High Arctic from the 2017 Canadian Wildfires.
  Journal of Geophysical Research: Atmospheres, 124(14):8178–8202.
- Lutsch, E. M. (2019). The Influence of Biomass Burning on the Arctic Atmosphere.PhD thesis, University of Toronto, Toronto, Canada.
- Marsh, D. R., Mills, M. J., Kinnison, D. E., Lamarque, J.-F., Calvo, N., and Polvani,

L. M. (2013). Climate Change from 1850 to 2005 Simulated in CESM1(WACCM).

Journal of Climate, 26(19):7372 – 7391.

- Martin, R. V., Eastham, S. D., Bindle, L., Lundgren, E. W., Clune, T. L., Keller, C. A., Downs, W., Zhang, D., Lucchesi, R. A., Sulprizio, M. P., Yantosca, R. M., Li, Y., Estrada, L., Putman, W. M., Auer, B. M., Trayanov, A. L., Pawson, S., and Jacob, D. J. (2022). Improved advection, resolution, performance, and community access in the new generation (version 13) of the high-performance GEOS-Chem Global atmospheric chemistry model (GCHP). Geoscientific Model Development, 15(23):8731–8748.
- Miyazaki, K., Bowman, K. W., Sekiya, T., Eskes, H., Boersma, F., Worden, H., Livesey, N., Payne, V. H., Sudo, K., Kanaya, Y., Takigawa, M., and Ogochi, K. (2020a). Updated tropospheric chemistry reanalysis and emission estimates, TCR-2, for 2005–2018. *Earth System Science Data*, 12(3):2223–2259.
- Miyazaki, K., Bowman, K. W., Yumimoto, K., Walker, T., and Sudo, K. (2020b). Evaluation of a multi-model, multi-constituent assimilation framework for tropospheric chemical reanalysis. *Atmospheric Chemistry and Physics*, 20(2):931–967.
- Miyazaki, K., Eskes, H. J., and Sudo, K. (2015). A tropospheric chemistry reanalysis for the years 2005–2012 based on an assimilation of OMI, MLS, TES, and MOPITT satellite data. *Atmospheric Chemistry and Physics*, 15(14):8315–8348.
- Miyazaki, K., Eskes, H. J., Sudo, K., Takigawa, M., van Weele, M., and Boersma, K. F. (2012). Simultaneous assimilation of satellite NO<sub>2</sub>, O<sub>3</sub>, CO, and HNO<sub>3</sub> data for the analysis of tropospheric chemical composition and emissions. *Atmospheric Chemistry and Physics*, 12(20):9545–9579.
- Molina, L. T., Lei, W., Zavala, M., Almanza, V., Garcia, A., Saide, P., and Mena-

Carrasco, M. (2020). Atmospheric Pollution: Experience from Mexico City and Santiago de Chile. In Mensink, C., Gong, W., and Hakami, A., editors, *Air Pollution Modeling and its Application XXVI*, pages 127–138. Springer International Publishing, Cham.

- Molina, L. T., Retama, A., and Zavala, M. (2023). Diagnosis of Current Knowledge of the Scientific Bases for Air Quality Management in the Megalopolis. Technical report, Molina Center for Strategic Studies in Energy and the Environment, Boston, MA, USA.
- Moya, M., Grutter, M., and Báez, A. (2004). Diurnal variability of size-differentiated inorganic aerosols and their gas-phase precursors during january and February of 2003 near downtown Mexico City. *Atmospheric Environment*, 38(33):5651–5661.
- Munasinghe-Arachchige, S. P. and Nirmalakhandan, N. (2020). Nitrogen-fertilizer recovery from the centrate of anaerobically digested sludge. *Environmental Science & Technology Letters*, 7(7):450–459.
- Murphy, J. G., Wentworth, G. R., Moravek, A., Collins, D. B., and Sharma, S. (2025). Processes regulating the sources and sinks of ammonia in the Canadian Arctic. *Faraday Discuss*.
- Möller, D. and Schieferdecker, H. (1985). A relationship between agricultural NH<sub>3</sub> emissions and the atmospheric SO<sub>2</sub> content over industrial areas. *Atmospheric Environment* (1967), 19(5):695–700.
- Nair, A. A. and Yu, F. (2020). Quantification of atmospheric ammonia concentrations:

  A review of its measurement and modeling. *Atmosphere*, 11(10):1092.
- Neirynck, J. and Ceulemans, R. (2008). Bidirectional ammonia exchange above a mixed coniferous forest. *Environmental Pollution*, 154(3):424–438.

Nemitz, E., Milford, C., and Sutton, M. A. (2001). A two-layer canopy compensation point model for describing bi-directional biosphere-atmosphere exchange of ammonia. *Quarterly Journal of the Royal Meteorological Society*, 127(573):815–833.

- Nenes, A., Pandis, S. N., and Pilinis, C. (1998). ISORROPIA: A new thermodynamic equilibrium model for multiphase multicomponent inorganic aerosols. *Aquatic Geochemistry*, 4:123–152.
- Nguyen, H. V. L., Gulaczyk, I., Kreglewski, M., and Kleiner, I. (2021). Large amplitude inversion tunneling motion in ammonia, methylamine, hydrazine, and secondary amines: From structure determination to coordination chemistry. *Coordination Chemistry Reviews*, 436:213797.
- Norman, M. and Leck, C. (2005). Distribution of marine boundary layer ammonia over the Atlantic and Indian Oceans during the Aerosols99 cruise. *Journal of Geophysical Research: Atmospheres*, 110(D16302).
- Olabi, A., Abdelkareem, M. A., Al-Murisi, M., Shehata, N., Alami, A. H., Radwan, A., Wilberforce, T., Chae, K.-J., and Sayed, E. T. (2023). Recent progress in green ammonia: Production, applications, assessment; barriers, and its role in achieving the sustainable development goals. *Energy Conversion and Management*, 277:116594.
- Osada, K., Saito, S., Tsurumaru, H., and Hoshi, J. (2019). Vehicular exhaust contributions to high NH<sub>3</sub> and PM<sub>2.5</sub> concentrations during winter in Tokyo, Japan.

  Atmospheric Environment, 206:218–224.
- Paleczny, M., Hammill, E., Karpouzi, V., and Pauly, D. (2015). Population Trend of the World's Monitored Seabirds, 1950-2010. PLOS ONE, 10(6):e0129342.
- Pan, B., Lam, S. K., Mosier, A., Luo, Y., and Deli, C. (2016). Strategies for mitigating

ammonia emissions from agroecosystems. In Proceedings of the 2016 International Nitrogen Initiative Conference. URL: https://agronomyaustraliaproceedings.org/images/sampledata/ini2016/pdf-papers/INI2016\_Pan\_Baobao.pdf. Last access: February, 2025.

- Panchasara, H., Samrat, N. H., and Islam, N. (2021). Greenhouse Gas Emissions Trends and Mitigation Measures in Australian Agriculture Sector A Review. Agriculture, 11(2):85.
- Pannell, D. and Rogers, A. (2022). Agriculture and the Environment: Policy Approaches in Australia and New Zealand. Review of Environmental Economics and Policy, 16(1):126–145.
- Parfitt, R. L., Baisden, W. T., Schipper, L. A., and and, A. D. M. (2008). Nitrogen inputs and outputs for New Zealand at national and regional scales: past, present and future scenarios. *Journal of the Royal Society of New Zealand*, 38(2):71–87.
- Paulot, F. and Jacob, D. J. (2014). Hidden Cost of U.S. Agricultural Exports: Particulate Matter from Ammonia Emissions. *Environmental Science & Technology*, 48(2):903–908.
- Paulot, F., Jacob, D. J., Pinder, R. W., Bash, J. O., Travis, K., and Henze, D. K. (2014). Ammonia emissions in the United States, European Union, and China derived by high-resolution inversion of ammonium wet deposition data: Interpretation with a new agricultural emissions inventory (MASAGE\_NH<sub>3</sub>). *Journal of Geophysical Research: Atmospheres*, 119(7):4343–4364.
- Philip, S., Martin, R. V., and Keller, C. A. (2016). Sensitivity of chemistry-transport model simulations to the duration of chemical and transport operators: A case study with GEOS-chem V10-01. *Geoscientific Model Development*, 9(5):1683–1695.

Pougatchev, N. S., Connor, B. J., and Rinsland, C. P. (1995). Infrared measurements of the ozone vertical distribution above Kitt Peak. *Journal of Geophysical Research*, 100(D8):16689–16697.

- Prignon, M., Chabrillat, S., Minganti, D., O'Doherty, S., Servais, C., Stiller, G., Toon, G. C., Vollmer, M. K., and Mahieu, E. (2019). Improved FTIR retrieval strategy for HCFC-22 (CHClF<sub>2</sub>), comparisons with in situ and satellite datasets with the support of models, and determination of its long-term trend above Jungfraujoch. Atmospheric Chemistry and Physics, 19(19):12309–12324.
- Pye, H. O. T., Nenes, A., Alexander, B., Ault, A. P., Barth, M. C., Clegg, S. L., Collett Jr., J. L., Fahey, K. M., Hennigan, C. J., Herrmann, H., Kanakidou, M., Kelly, J. T., Ku, I.-T., McNeill, V. F., Riemer, N., Schaefer, T., Shi, G., Tilgner, A., Walker, J. T., Wang, T., Weber, R., Xing, J., Zaveri, R. A., and Zuend, A. (2020). The acidity of atmospheric particles and clouds. Atmospheric Chemistry and Physics, 20(8):4809–4888.
- Pöschl, U. (2005). Atmospheric aerosols: Composition, transformation, climate and health effects. *Angewandte Chemie International Edition*, 44(46):7520–7540.
- Quinn, P. K., Bates, T. S., Johnson, J. E., Covert, D. S., and Charlson, R. J. (1990).
  Interactions between the sulfur and reduced nitrogen cycles over the central Pacific
  Ocean. Journal of Geophysical Research: Atmospheres, 95(D10):16405–16416.
- Randerson, J., Van Der Werf, G., Giglio, L., Collatz, G., and Kasibhatla, P. (2017). Global Fire Emissions Database, Version 4.1 (GFEDv4).
- Reizer, M. and Orza, J. A. G. (2018). Identification of PM10 air pollution origins at a rural background site. *E3S Web of Conferences*, 28:01031.
- Riddick, S., Dragosits, U., Blackall, T., Daunt, F., Wanless, S., and Sutton, M. (2012).

The global distribution of ammonia emissions from seabird colonies. *Atmospheric Environment*, 55:319–327.

- Rios, B., Díaz-Esteban, Y., and Raga, G. B. (2023). Smoke emissions from biomass burning in Central Mexico and their impact on air quality in Mexico City: May 2019 case study. *Science of The Total Environment*, 904:166912.
- Rios, B. and Estrada, F. (2022). Reduction in Crop Yield in Mexico Due to Ozone Associated with Emissions from Biomass Burning. Water, Air, & Soil Pollution, 233(10):407.
- Roche, S., Strong, K., Wunch, D., Mendonca, J., Sweeney, C., Baier, B., Biraud, S. C., Laughner, J. L., Toon, G. C., and Connor, B. J. (2021). Retrieval of atmospheric CO<sub>2</sub> vertical profiles from ground-based near-infrared spectra. Atmospheric Measurement Techniques, 14(4):3087–3118.
- Rodgers, C. D. (2000). Inverse Methods for Atmospheric Sounding: Theory and Practice (Series on Atmospheric, Oceanic and Planetary Physics). World Scientific.
- Rodgers, C. D. and Connor, B. J. (2003). Intercomparison of remote sounding instruments. *Journal of Geophysical Research: Atmospheres*, 108(D3):4116.
- Rothman, L., Gordon, I., Barbe, A., Benner, D., Bernath, P., Birk, M., Boudon,
  V., Brown, L., Campargue, A., Champion, J.-P., Chance, K., Coudert, L., Dana,
  V., Devi, V., Fally, S., Flaud, J.-M., Gamache, R., Goldman, A., Jacquemart, D.,
  Kleiner, I., Lacome, N., Lafferty, W., Mandin, J.-Y., Massie, S., Mikhailenko, S.,
  Miller, C., Moazzen-Ahmadi, N., Naumenko, O., Nikitin, A., Orphal, J., Perevalov,
  V., Perrin, A., Predoi-Cross, A., Rinsland, C., Rotger, M., Šimečková, M., Smith,
  M., Sung, K., Tashkun, S., Tennyson, J., Toth, R., Vandaele, A., and Vander

Auwera, J. (2009). The HITRAN 2008 molecular spectroscopic database. *Journal of Quantitative Spectroscopy and Radiative Transfer*, 110(9-10):533–572.

- Ríos, B. and Raga, G. B. (2017). Spatio-temporal distribution of burned areas by ecoregions in Mexico and Central America. *International Journal of Remote Sens*ing, 39(4):949–970.
- Safford, H. D., Paulson, A. K., Steel, Z. L., Young, D. J. N., and Wayman, R. B. (2022). The 2020 California fire season: A year like no other, a return to the past or a harbinger of the future? Global Ecology and Biogeography, 31(10):2005–2025.
- Saggar, S., Singh, J., Giltrap, D., Zaman, M., Luo, J., Rollo, M., Kim, D.-G., Rys, G., and van der Weerden, T. (2013). Quantification of reductions in ammonia emissions from fertiliser urea and animal urine in grazed pastures with urease inhibitors for agriculture inventory: New Zealand as a case study. Science of The Total Environment, 465:136–146.
- Santamarta Cerezal, J., editor (2013). Avances en la investigación de los recursos hídricos en islas y terrenos volcánicos. Universidad de La Laguna. Reunión científica nacional sobre el estudio de los recursos hídricos en islas volcánicas, Nov 2012, Tenerife.
- Schreier, F., Milz, M., Buehler, S. A., and von Clarmann, T. (2018). Intercomparison of three microwave/infrared high resolution line-by-line radiative transfer codes.

  Journal of Quantitative Spectroscopy and Radiative Transfer, 211:64–77.
- SEDEMA (2018). Secretaría del Medio Ambiente de la Ciudad de México Inventario de Emisiones de la Ciudad de México 2016. Dirección General de Gestión de la Calidad del Aire, Dirección de Programas de Calidad del Aire e Inventario de Emisiones, Ciudad de México. URL: http://www.aire.cdmx.gob.

mx/descargas/publicaciones/flippingbook/inventario-emisiones-2016/mobile/inventario-emisiones-2016.pdf. Last access: February, 2025.

- SEDEMA (2021). Secretaría del Medio Ambiente de la Ciudad de México Inventario de Emisiones de la Zona Metropolitana del Valle de México 2018. Dirección General de Gestión de la Calidad del Aire, Dirección de Proyectos de Calidad del Aire, Ciudad de México. URL: <a href="http://www.aire.cdmx.gob.mx/descargas/publicaciones/flippingbook/memoria-inventario-emisiones-2018/memoria\_inventario\_emisiones\_2018.">http://www.aire.cdmx.gob.mx/descargas/publicaciones/flippingbook/memoria-inventario-emisiones-2018/memoria\_inventario\_emisiones\_2018.</a>
- Sekiya, T., Miyazaki, K., Eskes, H., Bowman, K., Sudo, K., Kanaya, Y., and Takigawa, M. (2023). The worldwide COVID-19 lockdown impacts on global secondary inorganic aerosols and radiative budget. *Science Advances*, 9(30):eadh2688.
- Sen, B., Toon, G. C., Blavier, J.-F., Fleming, E. L., and Jackman, C. H. (1996). Balloon-borne observations of midlatitude fluorine abundance. *Journal of Geophysical Research*, 101(D4):9045–9054.
- Sheikh, M., Harami, H. R., Rezakazemi, M., Cortina, J. L., Aminabhavi, T. M., and Valderrama, C. (2023). Towards a sustainable transformation of municipal wastewater treatment plants into biofactories using advanced NH<sub>3</sub>-N recovery technologies: A review. *Science of The Total Environment*, 904:166077.
- Shephard, M. W. and Cady-Pereira, K. E. (2015). Cross-track Infrared Sounder (CrIS) satellite observations of tropospheric ammonia. *Atmospheric Measurement Techniques*, 8(3):1323–1336.
- Shephard, M. W., Cady-Pereira, K. E., Luo, M., Henze, D. K., Pinder, R. W., Walker, J. T., Rinsland, C. P., Bash, J. O., Zhu, L., Payne, V. H., and Clarisse, L. (2011).

TES ammonia retrieval strategy and global observations of the spatial and seasonal variability of ammonia. *Atmospheric Chemistry and Physics*, 11(20):10743–10763.

- Silva-Quiroz, R., Rivera, A. L., Ordoñez, P., Gay-Garcia, C., and Frank, A. (2019).
  Atmospheric blockages as trigger of environmental contingencies in Mexico City.
  Heliyon, 5(7):e02099.
- Smil, V. (2000). Enriching the Earth: Fritz Haber, Carl Bosch, and the Transformation of World Food Production. The MIT Press.
- Stein, A. F., Draxler, R. R., Rolph, G. D., Stunder, B. J. B., Cohen, M. D., and Ngan,
  F. (2015). NOAA's HYSPLIT Atmospheric Transport and Dispersion Modeling
  System. Bulletin of the American Meteorological Society, 96(12):2059 2077.
- Stiller, G. P. (2000). The Karlsruhe optimized and precise radiative transfer algorithm (KOPRA). Technical report. Germany.
- Stremme, W., Grutter, M., Rivera, C., Bezanilla, A., Garcia, A. R., Ortega, I., George, M., Clerbaux, C., Coheur, P.-F., Hurtmans, D., Hannigan, J. W., and Coffey, M. T. (2013). Top-down estimation of carbon monoxide emissions from the Mexico Megacity based on FTIR measurements from ground and space. *Atmospheric Chemistry and Physics*, 13(3):1357–1376.
- Sun, K., Tao, L., Miller, D. J., Pan, D., Golston, L. M., Zondlo, M. A., Griffin, R. J., Wallace, H. W., Leong, Y. J., Yang, M. M., Zhang, Y., Mauzerall, D. L., and Zhu, T. (2017). Vehicle Emissions as an Important Urban Ammonia Source in the United States and China. *Environmental Science & Technology*, 51(4):2472–2481.
- Sutton, M. A. (1990). The surface/atmosphere exchange of ammonia. PhD thesis, University of Edinburgh. Edinburgh, U.K.

Sutton, M. A., Erisman, J. W., Dentener, F., and Möller, D. (2008). Ammonia in the environment: From ancient times to the present. *Environmental Pollution*, 156(3):583–604.

- Sutton, M. A., Reis, S., Riddick, S. N., Dragosits, U., Nemitz, E., Theobald, M. R., Tang, Y. S., Braban, C. F., Vieno, M., Dore, A. J., Mitchell, R. F., Wanless, S., Daunt, F., Fowler, D., Blackall, T. D., Milford, C., Flechard, C. R., Loubet, B., Massad, R., Cellier, P., Personne, E., Coheur, P. F., Clarisse, L., Van Damme, M., Ngadi, Y., Clerbaux, C., Skjøth, C. A., Geels, C., Hertel, O., Wichink Kruit, R. J., Pinder, R. W., Bash, J. O., Walker, J. T., Simpson, D., Horváth, L., Misselbrook, T. H., Bleeker, A., Dentener, F., and De Vries, W. (2013). Towards a climate-dependent paradigm of ammonia emission and deposition. *Philosophical Transactions of the Royal Society B: Biological Sciences*, 368(1621):20130166.
- Tan, J., Fu, J. S., and Seinfeld, J. H. (2020). Ammonia emission abatement does not fully control reduced forms of nitrogen deposition. *Proceedings of the National Academy of Sciences*, 117(18):9771–9775.
- Theobald, M. R., Crittenden, P. D., Hunt, A. P., Tang, Y. S., Dragosits, U., and Sutton, M. A. (2006). Ammonia emissions from a Cape fur seal colony, Cape Cross, Namibia. *Geophysical Research Letters*, 33(3).
- Toon, G. C. (1991). The JPL MkIV Interferometer. Optics and Photonics News, 2(10):19–21.
- Toon, G. C. (2022). Atmospheric voigt line list for the tccon 2020 data release (ggg2020.r0). CaltechDATA. Data set.
- Toon, G. C., Blavier, J.-F. L., and Sung, K. (2018). Measurements of atmo-

spheric ethene by solar absorption FTIR spectrometry. Atmospheric Chemistry and Physics, 18(7):5075–5088.

- Tournadre, B., Chelin, P., Ray, M., Cuesta, J., Kutzner, R. D., Landsheere, X., Fortems-Cheiney, A., Flaud, J.-M., Hase, F., Blumenstock, T., Orphal, J., Viatte, C., and Camy-Peyret, C. (2020). Atmospheric ammonia (NH<sub>3</sub>) over the Paris megacity: 9 years of total column observations from ground-based infrared remote sensing. Atmospheric Measurement Techniques, 13(7):3923–3937.
- Trivitayanurak, W., Adams, P. J., Spracklen, D. V., and Carslaw, K. S. (2008). Tropospheric aerosol microphysics simulation with assimilated meteorology: model description and intermodel comparison. *Atmospheric Chemistry and Physics*, 8:3149–3168.
- Uematsu, M., Toratani, M., Kajino, M., Narita, Y., Senga, Y., and Kimoto, T. (2004).
  Enhancement of primary productivity in the Western North Pacific caused by the eruption of the Miyake-Jima Volcano. Geophysical Research Letters, 31(6).
- United Nations (2018). The world's cities in 2018. World's Cities 2018 Data Booklet (ST/ESA/ SER.A/417). URL: https://www.un.org/en/development/desa/population/publications/pdf/urbanization/the\_worlds\_cities\_in\_2018\_data\_booklet.pdf. Last access: February, 2025.
- U.S. Environmental Protection Agency (2024). Acid Rain Program Results. URL: https://www.epa.gov/acidrain/acid-rain-program-results. Last access: February, 2025.
- Van Damme, M., Clarisse, L., Franco, B., Sutton, M. A., Erisman, J. W., Wichink Kruit, R., van Zanten, M., Whitburn, S., Hadji-Lazaro, J., Hurtmans, D., Clerbaux, C., and Coheur, P.-F. (2021). Global, regional and national trends

of atmospheric ammonia derived from a decadal (2008–2018) satellite record. Environmental Research Letters, 16(5):055017.

- Van Damme, M., Clarisse, L., Whitburn, S., Hadji-Lazaro, J., Hurtmans, D., Clerbaux, C., and Coheur, P.-F. (2018). Industrial and agricultural ammonia point sources exposed. *Nature*, 564(7734):99–103.
- Van Damme, M., Erisman, J. W., Clarisse, L., Dammers, E., Whitburn, S., Clerbaux, C., Dolman, A. J., and Coheur, P.-F. (2015). Worldwide spatiotemporal atmospheric ammonia (NH<sub>3</sub>) columns variability revealed by satellite. *Geophysical Research Letters*, 42(20):8660–8668.
- Van Damme, M., Whitburn, S., Clarisse, L., Clerbaux, C., Hurtmans, D., and Coheur, P.-F. (2017). Version 2 of the IASI NH<sub>3</sub> neural network retrieval algorithm: near-real-time and reanalysed datasets. Atmospheric Measurement Techniques, 10(12):4905–4914.
- Van Damme, M., Wichink Kruit, R. J., Schaap, M., Clarisse, L., Clerbaux, C., Coheur, P.-F., Dammers, E., Dolman, A. J., and Erisman, J. W. (2014). Evaluating 4 years of atmospheric ammonia (NH<sub>3</sub>) over Europe using IASI satellite observations and LOTOS-EUROS model results. *Journal of Geophysical Research: Atmospheres*, 119(15):9549–9566.
- Van Der Werf, G. R., Randerson, J. T., Giglio, L., Van Leeuwen, T. T., Chen, Y., Rogers, B. M., Mu, M., Van Marle, M. J. E., Morton, D. C., Collatz, G. J., Yokelson, R. J., and Kasibhatla, P. S. (2017). Global Fire Emissions Estimates during 1997–2016. Earth System Science Data, 9(2):697–720.
- Viatte, C., Abeed, R., Yamanouchi, S., Porter, W. C., Safieddine, S., Van Damme, M., Clarisse, L., Herrera, B., Grutter, M., Coheur, P.-F., Strong, K., and Clerbaux,

C. (2022). NH<sub>3</sub> spatiotemporal variability over Paris, Mexico City, and Toronto, and its link to PM<sub>2.5</sub> during pollution events. *Atmospheric Chemistry and Physics*, 22(19):12907–12922.

- Viatte, C., Guendouz, N., Dufaux, C., Hensen, A., Swart, D., Van Damme, M., Clarisse, L., Coheur, P., and Clerbaux, C. (2023). Measurement report: Ammonia in Paris derived from ground-based open-path and satellite observations. *Atmo-spheric Chemistry and Physics*, 23(24):15253–15267.
- Viatte, C., Wang, T., Van Damme, M., Dammers, E., Meleux, F., Clarisse, L., Shephard, M. W., Whitburn, S., Coheur, P. F., Cady-Pereira, K. E., and Clerbaux, C. (2020). Atmospheric ammonia variability and link with particulate matter formation: A case study over the Paris area. Atmospheric Chemistry and Physics, 20(1):577–596.
- Vigouroux, C., Blumenstock, T., Coffey, M., Errera, Q., García, O., Jones, N. B., Hannigan, J. W., Hase, F., Liley, B., Mahieu, E., Mellqvist, J., Notholt, J., Palm, M., Persson, G., Schneider, M., Servais, C., Smale, D., Thölix, L., and De Mazière, M. (2015). Trends of ozone total columns and vertical distribution from FTIR observations at eight NDACC stations around the globe. Atmospheric Chemistry and Physics, 15:2915–2933.
- Vohra, K., Vodonos, A., Schwartz, J., Marais, E. A., Sulprizio, M. P., and Mickley, L. J. (2021). Global mortality from outdoor fine particle pollution generated by fossil fuel combustion: Results from geos-chem. *Environmental Research*, 195:110754.
- von Bobrutzki, K., Braban, C. F., Famulari, D., Jones, S. K., Blackall, T., Smith, T. E. L., Blom, M., Coe, H., Gallagher, M., Ghalaieny, M., McGillen, M. R., Percival, C. J., Whitehead, J. D., Ellis, R., Murphy, J., Mohacsi, A., Pogany, A., Junninen, H., Rantanen, S., Sutton, M. A., and Nemitz, E. (2010). Field inter-comparison of

eleven atmospheric ammonia measurement techniques. Atmospheric Measurement Techniques, 3(1):91–112.

- Wallace, J. M. and Hobbs, P. V. (2006). Atmospheric Science (Second Edition).

  Academic Press, San Diego, second edition.
- Wang, Y., Wen, Y., Zhang, S., Zheng, G., Zheng, H., Chang, X., Huang, C., Wang, S., Wu, Y., and Hao, J. (2023). Vehicular Ammonia Emissions Significantly Contribute to Urban PM2.5 Pollution in Two Chinese Megacities. *Environmental Science & Technology*, 57(7):2698–2705.
- Ward, J. H. (1963). Hierarchical grouping to optimize an objective function. *Journal* of the American Statistical Association, 58(301):236–244.
- Wartewig, S. (2003). IR and Raman Spectroscopy. John Wiley & Sons, Ltd, 1st edition.
- Watanabe, S., Hajima, T., Sudo, K., Nagashima, T., Takemura, T., Okajima, H., Nozawa, T., Kawase, H., Abe, M., Yokohata, T., Ise, T., Sato, H., Kato, E., Takata, K., Emori, S., and Kawamiya, M. (2011). MIROC-ESM 2010: Model description and basic results of CMIP5-20c3m experiments. Geoscientific Model Development, 4(4):845–872.
- Wen, D., Lin, J. C., Zhang, L., Vet, R., and Moran, M. D. (2013). Modeling atmospheric ammonia and ammonium using a stochastic Lagrangian air quality model (STILT-Chem v0.7). *Geoscientific Model Development*, 6(2):327–344.
- Wentworth, G. R., Murphy, J. G., Croft, B., Martin, R. V., Pierce, J. R., Côté, J.-S., Courchesne, I., Tremblay, J.-E., Gagnon, J., Thomas, J. L., Sharma, S., Toom-Sauntry, D., Chivulescu, A., Levasseur, M., and Abbatt, J. P. D. (2016). Ammonia

in the summertime Arctic marine boundary layer: sources, sinks, and implications.

Atmospheric Chemistry and Physics, 16(4):1937–1953.

- Whitburn, S., Van Damme, M., Clarisse, L., Bauduin, S., Heald, C. L., Hadji-Lazaro, J., Hurtmans, D., Zondlo, M. A., Clerbaux, C., and Coheur, P. (2016a). A flexible and robust neural network IASI-NH<sub>3</sub> retrieval algorithm. *Journal of Geophysical Research: Atmospheres*, 121(11):6581–6599.
- Whitburn, S., Van Damme, M., Clarisse, L., Hurtmans, D., Clerbaux, C., and Coheur, P.-F. (2017). IASI-derived NH<sub>3</sub> enhancement ratios relative to CO for the tropical biomass burning regions. Atmospheric Chemistry and Physics, 17(19):12239–12252.
- Whitburn, S., Van Damme, M., Clarisse, L., Turquety, S., Clerbaux, C., and Coheur, P.-F. (2016b). Doubling of annual ammonia emissions from the peat fires in Indonesia during the 2015 El Niño. *Geophysical Research Letters*, 43(20):11,007–11,014.
- Whitburn, S., Van Damme, M., Kaiser, J., Van Der Werf, G., Turquety, S., Hurtmans, D., Clarisse, L., Clerbaux, C., and Coheur, P.-F. (2015). Ammonia emissions in tropical biomass burning regions: Comparison between satellite-derived emissions and bottom-up fire inventories. Atmospheric Environment, 121:42–54.
- Wiedinmyer, C., Akagi, S. K., Yokelson, R. J., Emmons, L. K., Al-Saadi, J. A., Orlando, J. J., and Soja, A. J. (2011). The Fire Inventory from NCAR (FINN): A high resolution global model to estimate the emissions from open burning. Geoscientific Model Development, 4(3):625–641.
- Wizenberg, T., Strong, K., Jones, D. B. A., Hannigan, J. W., Ortega, I., and Mahieu, E. (2024). Measured and modeled trends of seven tropospheric pollutants in the high Arctic from 1999 to 2022. *Journal of Geophysical Research: Atmospheres*, 129(12):e2023JD040544.

Xiao, H., Xiao, H.-W., Xu, Y., Zheng, N.-J., and Xiao, H.-Y. (2025). Control of combustion related ammonia emissions can be effective in mitigating PM<sub>2.5</sub> pollution in two megacities in Sichuan Basin, Southwest China. Atmospheric Research, 320:108059.

- Xie, Y., Wang, W., Chen, Y., Qian, Z., Chen, J., Tong, J., Li, L., Yue, Y., Chen, K., Chu, Z., and Hu, X. (2024). NH<sub>3</sub> Emissions and Lifetime Estimated by Satellite Observations with Differential Evolution Algorith. Atmosphere, 15(3):251.
- Yamanouchi, S. (2021). Long-term Analysis of Toronto-Area Atmospheric Composition. PhD thesis, University of Toronto, Toronto, Canada.
- Yamanouchi, S., Viatte, C., Strong, K., Lutsch, E., Jones, D. B. A., Clerbaux, C., Van Damme, M., Clarisse, L., and Coheur, P.-F. (2021). Multiscale observations of NH<sub>3</sub> around Toronto, Canada. Atmospheric Measurement Techniques, 14(2):905– 921.
- Yao, X. and Zhang, L. (2016). Trends in atmospheric ammonia at urban, rural, and remote sites across North America. *Atmospheric Chemistry and Physics*, 16(17):11465–11475.
- Yokelson, R. J., Urbanski, S. P., Atlas, E. L., Toohey, D. W., Alvarado, E. C., Crounse, J. D., Wennberg, P. O., Fisher, M. E., Wold, C. E., Campos, T. L., Adachi, K., Buseck, P. R., and Hao, W. M. (2007). Emissions from forest fires near Mexico City. Atmospheric Chemistry and Physics, 7(21):5569–5584.
- Zeng, Z.-C., Natraj, V., Xu, F., Chen, S., Gong, F.-Y., Pongetti, T. J., Sung, K., Toon, G., Sander, S. P., and Yung, Y. L. (2021). GFIT3: A full physics retrieval algorithm for remote sensing of greenhouse gases in the presence of aerosols. Atmospheric Measurement Techniques, 14(10):6483–6507.

Zhang, X., Sun, Y., Liang, X., Lam, S. K., Liu, L., Gu, B., and Chen, D. (2022).
Costs and benefits of ammonia abatement in Australia. Resources, Conservation and Recycling, 182:106318.

- Zhou, M., Deng, Z., Robert, C., et al. (2024). The First Global Map of Atmospheric Ammonia (NH<sub>3</sub>) as Observed by the HIRAS/FY-3D Satellite. *Advances in Atmospheric Sciences*, 41:379–390.
- Zhu, L., Henze, D., Bash, J., Jeong, G.-R., Cady-Pereira, K., Shephard, M., Luo, M., Paulot, F., and Capps, S. (2015). Global evaluation of ammonia bidirectional exchange and livestock diurnal variation schemes. Atmospheric Chemistry and Physics, 15(22):12823–12843.